THE ROLE OF THERMAL INPUT ON SQUAT TYPE DEFECTS IN RAILS

By:

Shahmir Hayyan Sanusi

A thesis submitted in partial fulfilment of the requirements for the degree of

Doctor of Philosophy

The University of Sheffield

Faculty of Engineering

Department of Mechanical Engineering

April 13, 2017

Abstract

The recently discovered squat type defect which is understood as a thermal defect has renewed interest in rolling contact fatigue damage in railway studies. These defects were reported to appear in several locations across the globe where the cost incurred for their removal leads to a major increase of track maintenance cost. While the growth mechanism for classical rolling contact fatigue squat is well understood, limited research has so far been undertaken for squat type defects leaving them poorly understood, especially in their initiation and propagation mechanism. The presence of white etching layer in all locations where these defects have been found strongly suggests that thermal input is responsible for their development rather than fluid assisted growth that is responsible for the development of classical rolling contact fatigue squats. In this thesis, research is reported that combines morphological analysis data with a boundary element model to understand the direct influence of these thermally transformed layers on the initiation and propagation of squat type defects in rail. Furthermore, the work has been extended to explore the possibilities for defect detection in rails reaching a positive proof of concept outcome. It is expected that this approach could serve as a basis for maintenance schedules in order to avoid rail failure due to inadequate understanding of this type of defect.

Acknowledgements

A special acknowledgement and sincere appreciation go to my main supervisor, Dr. David Fletcher for spending quality time to assist, guide, and keep me on track in order to accomplish this project. His enthusiasm and insightful suggestions have helped me a lot in this research.

I am also grateful to my second supervisor, Dr. Hassan Ghadbeigi for his interest in these studies.Many thanks to SBB and Dr. Stuart Grassie for initiating the project that led to this research.

Deepest gratitude goes to my wife Nur Daut and my lovely daughter Sofea Shahmir, my parents Sanusi Samid and Sadiah Ismail, and my supportive sisters for their support and encouragement throughout my university studies.

I would also like to express my appreciation to the project sponsors, Kementerian Pengajian Tinggi (KPT) and Universiti Tun Hussein onn Malaysia (UTHM). Without their financial support, this research would not have been possible.

Finally, I would like to dedicate my deepest gratitude to the University of Sheffield, Department of Mechanical Engineering, for giving me the opportunity and provide me with the best facilities for me to complete this work.

List of Abbreviations

2D	Two-dimensional
3D	Three-dimensional
BE	Boundary Element
BEM	Boundary Element Method
BFM	Body Force Method
BHN	Brinell Hardness Number
BS	British Standard
CCT	Continous Cooling Transformation
DIC	Digital Image Correlation
EDM	Electrical Discharge Machining
FE	Finite Element
FEM	Finite Element Method
K_{I}	Mode-I Stress Intensity Factor
K_{II}	Mode-II Stress Intensity Factor
K_{III}	Mode-III Stress Intensity Factor
LEFM	Linear Elastic Fracture Mechanics
LU	London Underground
NDT	Non Destructive Test
RCF	Rolling Contact Fatigue
ROI	Region of Interest
SBB	Swiss Federal Railways

SIF	Stress Intensity Factor
TTT	Time Transformation Temperature
UIC	International Union of Railways
UK	United Kingdom
UT	Ultrasonic Testing
WEL	White Etching Layer

Rail Direction Terminology

Longitudinal direction:	Along the rail
Lateral direction:	Across the rail
Vertical direction:	Normal to the rail

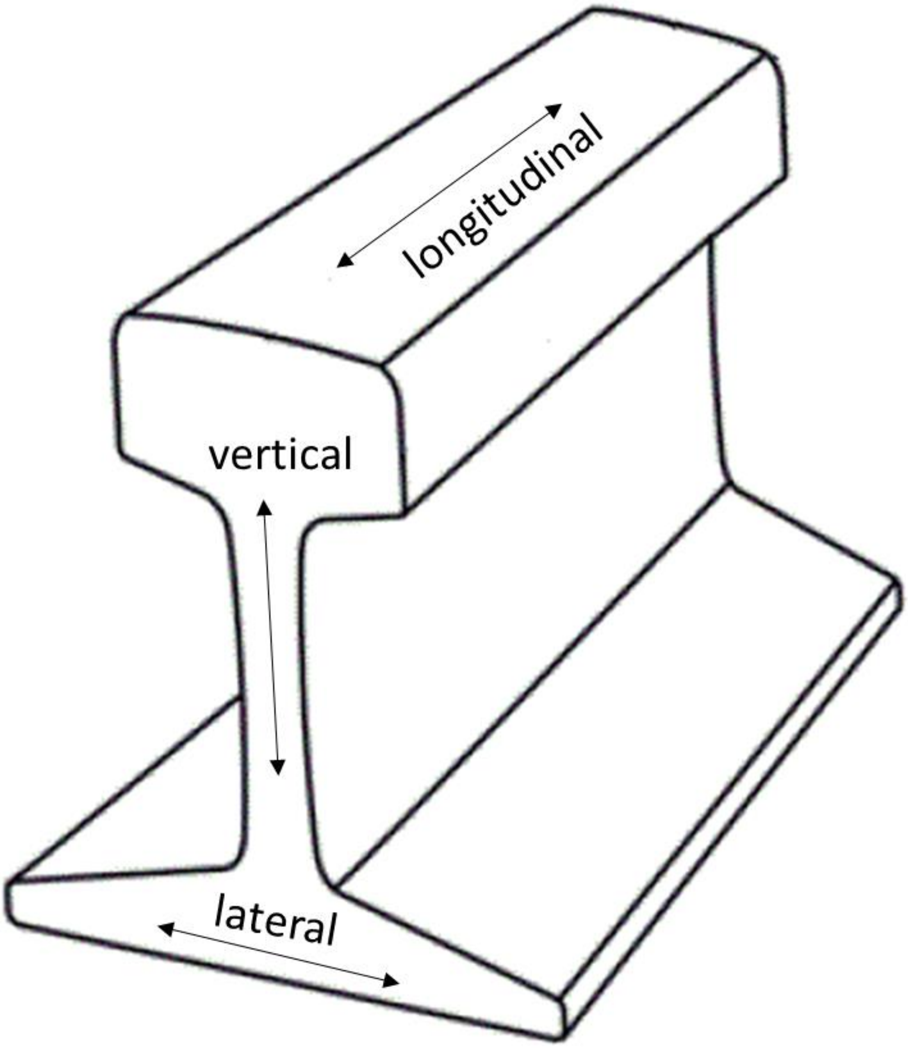

Contents

CHAPTER 1

INTRODUCTION

1.0 Introduction

Rail-wheel contact places extreme stress on the railway rail and with a growing transport demand, rail defects represent a cost and inconvenience to travellers and rail infrastructure managers. Squat type defects are a class of defects which were discovered in the year 2000 [1] and known as "studs" by some researchers. They have renewed interest in rolling contact fatigue (RCF) damage studies due to their superficial similarities to classical squat defects, but very different character. These defects look exactly like squats at a single glance, and the presence of subsurface damage which was considerably similar with classical squat was identified from ultrasonic scans. It is well known that subsurface damage may develop into transverse defects that can lead to rail fracture, yet there are no records associating rail fracture with studs. Even though studs can be considered as benign, surface depressions that typically develop from studs give rise to noise and vibration that affects riding quality. It was reported that London Underground had a problem with stud defects where £6M was spent to remove them by re-railing the affected locations.

The early research on studs mainly focussed on providing understanding to differentiate between the stud and classical squat defects through several field observations and metallurgical investigations. While most RCF defects including classical squat are quite well understood after almost five decades of extensive studies, there are still a lot of mysteries need to be solved for studs especially on its initiation and propagation mechanisms. Even though stud defects are not well understood, evidence exists that its initiation and growth pattern is very different to conventional RCF defects such as classical squats, head checks, and gauge corner cracking. The major difference between classical squat and studs defect is that, classical squat normally associated with surface plastic deformation and ratchetting, while studs are believed to be associated with thermally transformed material. Due to its similarity of appearance with classical squats, re-profiling the rail surface through the use of rail grinding is currently the main technique applied by rail infrastructure managers to combat the growth of these defects. However, it is essential to predict the right frequency of grinding in order to prevent over-maintenance and excess cost. Precise prediction of crack growth in rails via modelling can ensure system safety and reduce system infrastructure maintenance cost at the same time. In addition, alternative control measures can be designed once the growth pattern is fully understood to combat the growth of defects in rails.

The occurrence of a white etching layer (WEL) in all locations where studs have been found strongly suggests that thermal input might be responsible for the development of studs. Excessive thermal input followed by rapid cooling on the rail surface will result in the formation of metallurgical transformed layer with transformation from pearlite to martensite (WEL). Evidence exists to suggest that WEL appears in different forms/configuration (either continuous or patches) with a variety of lengths and thicknesses [2]. However, limited research [1], [3]–[6] has been undertaken to understand the direct influence of WEL on the initiation and propagation of subsurface cracks especially as observed with studs defect in rail.

1.1 Thesis aims and objectives

The work in this thesis aims to provide a better understanding of the role of thermal input on squat type defects (studs) in rail. This can be achieved by fulfilling the following objectives:

- To investigate the effect of metallurgical transformed layers on the growth of subsurface cracks
- To study the potential for supressing defect growth through tailoring rail thermo-mechanical properties
- To identify the effect of white etching layer configuration on a larger rail defects
- To explore the possibilities for defect detection in rails with the application of digital image correlation

1.2 Significance of study

At present, limited information is known about the role of thermal input on squat type defects in rail. The current research on squat type defects only focussed on metallurgical investigations and crack growth study without considering the effect of thermal input on already initiated defects. Furthermore, current practice to detect squat type defects in rail will result in delay and disruptions to the rail operation. Thus, this study will contribute mainly to the benefit of rail infrastructure managers in understanding squat type defects in detail, serve as a basis maintenance schedules to control the growth of the defects, and provide a method that could detect presence of defects in rail that will not results in disruptions and delay to the rail operations. In addition, this study will also benefit the rail manufacturers by providing insight to produce rails that could supress defect growth.

1.3 Thesis layout

This thesis is arranged in a series of 8 chapters in which each chapter cover a particular aspect of the investigation.

Chapter 2 presents a review of the fundamental principles behind the wheel-rail contact. This chapter begins with the historical review on the rail, its material and metallurgy, and recent advances in rail materials. The chapter then focuses on wheel-rail contact mechanics followed by the consequences of wheel-rail contact and damage phenomena that occur in the rail. Finally, it provides a review of several available methods to predict rail failure.

Chapter 3 provides understanding between classical squat and squat type defect based on results from field observation and metallurgical investigation. Possible mechanisms for the initiation of squat type defect in rail are discussed in this chapter.

Chapter 4 was written based on the paper with the title of “The potential for supressing rail defect growth through tailoring rail thermo-mechanical properties” [7], published in Journal of Wear. This chapterinvestigates the effect of a metallurgical transformed layer on the growth of subsurface cracks. A control measure to suppress the growth of the defect is introduced in this chapter.

Chapter 5 outlines how different configurations of the white etching layer will affect the growth of larger rail defects. The growth rate results predicted from the model are compared against wear rates from literature to identify which failure mechanism can be expected to dominate.

Chapter 6 describes a proof of concept for detection in rail with the application of digital image correlation. The results from the experimental work are compared with modelling results to explore the potential for the digital image correlation method to detect the presence of transverse defects in rail.

Chapter 7 summarises the main conclusions of the thesis and chapter 8 highlights suggestion for further work.

CHAPTER 2

LITERATURE REVIEW

2.0 Introduction

This chapter provides a historical review of rail materials and metallurgy, the fundamental principles behind wheel-rail contact, consequences of wheel-rail contact focusing on damage phenomena that occur on the rail, and review of popular methods available to predict rail failure.

2.1 Rail, materials, and metallurgy

The origin of rail tracks dates back into ancient civilization (6th B.C.) where the Greeks and Romans were the first to develop groove stone guides (Figure 2-1) for transporting carts and primitive wagons along a predetermined path which resembles our railway network nowadays [8]. During that period, animals were used to pull carts along the tracks (in the form of ruts) to transport supplies and goods easily without a need for steering, especially on uneven terrain. Ruts that are used to guide the wheel form the basis of the conventional railway concepts, and function to ensure the vehicle will remain on track.

In Great Britain, earliest records demonstrate rail usage began in the 17th century [9] where wooden-railed wagon-ways were used to transport minerals from coal mines to nearby rivers and harbours. The rails were initially made from soft woods such as pine which tends to wear quickly due to frequent passage of the wooden wheel. An improvement on the wear quality of the track was made later on where a malleable iron strip was placed on top of the wooden rail to overcome the wear issues. In 1776, the first iron rails known as plate rail was produced near Sheffield, England where the rails were cast in the form of L shape. Development of rail profile continued with the introduction of the edge rail (Figure 2-2) where the design was almost similar with present day rail section and was found to be many times stronger than its predecessor (the plate rail) [10].

However, the application of steam engine locomotives on the rail network unleashed some issues whereby the cast iron rail was too brittle and fractured easily due to repetitive passing movement of the heavy steam engine [11]. In 1856, the development of steel rails made through the Bessemer process [12] has led to the replacement of cast iron rails across the network and they lasted 16 years with 250 trains passed per day. Over the following 20 years, rail profiles developed similar to that used today.

The standard form of rail used around the world nowadays is the "flat bottom" rail (Figure 2-3) where UIC 60 and BS113A are the dominant rail profile used in the UK and can be found widely across the UK network. The production process (Figure 2-4) for the modern rail involves melting iron ore, adding alloying element such as carbon, manganese, and silicon to make the steel more durable, vacuum degassing process to reduce hydrogen content that could lead to formation of porosity, continuous casting process into a rectangle block called bloom, cooling process at different rates to produce different grades/type, and forming to its final shape through a consecutive series of rolling process. This production process leaves compressive residual stress in the rail where if it is carefully controlled, these can help suppress crack growth [12]–[14] which could lead to longevity life of a rail. To ensure durability life of a rail, selection of material is a crucial decision in order to produce a rail that could respond well to factors that could reduce its life such as fatigue, wear, and environmental conditions.

2.1.1 Materials and metallurgy

A typical rail steel should have a good hardness and should resist crack and wear phenomena. This can be achieved by controlling its composition (alloying elements) and its cooling rate during solidification. Many grades of rail exist with different compositions (alloying element such as Si, Mn, P, S, Cr, Al, V) and different properties [15] for a different application. Normal grade steels such as 260 grade (minimum tensile strength of 880 MPa) are commonly used on lines which operate under normal service conditions while high strength grade such as R 350 HT (minimum tensile strength between 1100-1200 MPa) are used on lines that experienced higher axle load and in extremely tightly curved track. In the past, the standard for rail grade was indicated by its tensile strength but presently was replaced by Brinell Hardness (BHN) value.

The form of steel called pearlite has been found efficacious for rails and it is widely used across the globe due to its ability to work hardened during the first cycle of load application which results in good resistance to wear. Pearlite steel typically has a Carbon level around 0.6% by weight and are composed of a layered structure of soft ductile Ferrite (α-Fe) and hard brittle Cementite (Fe_3C) as depicted in Figure 2-5. The mechanical properties of pearlite are strongly influenced by the distance between cementite lamellae (interlamellar spacing), its thickness, and the size of the grain. Different grades of rail steel have different spacing where finer spacing gives better wear resistance and higher hardness which could be controlled by manipulating the cooling rate as the hot rail cools (Figure 2-6). A refinement of the lamellae pearlite could be achieved through the heat treatment process where the cooling rate of the steel is controlled according to the time transformation temperature (TTT) diagram (Figure 2-7) or by increasing the weight content of Chromium in the steel [16].

2.1.2 Advancement in rail materials

The development of new material for rail steel is generally focussed on the material resistance against wear and cracks developed under wheel-rail contact. Head hardened rails (R350HT) were developed by Voestalpine Schienen GmbH in 1990 [17] where results to date showed that they have better wear and crack resistance compared to standard carbon rail (R260 grade) [18] due to their high hardness as a result from heat treatment process that reduced the inter-lamellar spacing. This type of rails has been applied widely to the heavy-haul network where the occurrence of RCF cracks and wear have significantly reduced especially in an area with tight radius curve.

In addition to head hardened, research in rail material has developed with the introduction of two-material rail. Instead of manufacturing the whole rail section with expensive high wear and RCF resistance material, a new material that composed of better resistance properties were coated on the railhead surface of standard carbon rail which acts as a protective barrier to combat against wear and RCF. Laser cladding is one of the widely used methods to produce coatings on the railhead where superior material with excellent mechanical and tribological properties can be welded to the top surface of the original substrate material.

Franklin et al. [19] performed a study to test the performance of this beneficial coating using a twin disc test where the base material for the discs was machined from a standard carbon rail (R260 grade) and coated using Duroc laser cladding techniques. Two types of coating materials (numbered as 222 and 508) were tested under different condition (high pressure, dry contact, lubricated contact) to determine whether the coating surface provides improved fatigue and wear resistance compared to the standard rail material. Based on their results, they observed that both coating materials have higher resistance against RCF damage compared to standard carbon rail. However, one of the coating materials (508) was vulnerable to crack initiation under prolonged (15,000) cycles while no crack initiation was observed for 222 coating material. In terms of wear performance, the 508 material proved to be better compared to 222 material under unlubricated conditions. Therefore it was proven that the coating surface provides improved fatigue and wear resistance compared to the standard rail material in which these advantages was brought into Chapter 4 to explore the possibilities of defect suppression.

In a recent investigation, Lewis et al. [20] performed a similar test but with a wider range of coating material where some of the disks were coated with a double layer of similar coating material. They observed that all of the coating specimens had higher RCF lives compared to the standard carbon rail specimen where the R260 specimen generally failed under 15,000 cycles while the clad specimens failed between 28,000 – 50,000 cycles. Based on their investigation, they concluded that the rail cladding techniques have the prospect to supress RCF crack initiation since the majority of the cladding surface showed almost no plastic deformation that could lead to crack initiation.

2.2 Wheel-rail contact

In general, the interface between wheel and rail involves rolling and sliding contact at high contact pressure. The contact pressure transmitted by the wheel usually surpass the yield strength of the rail material due to the small size of the contact which is approximately similar to the size of a 20 pence coin. The combination of rolling and sliding drives many expensive maintenance issues such as wear, rolling contact fatigue, and thermal damage. Therefore it is essential to understand the position, shape, size, and pressure of the contact in order to reduce damage from these issues.

The actual position of the contact between the wheel and the rail varies and depends on various factors such as bogie design, wheel-rail geometry, and track condition. According to Tournay [21], the contact between the wheel and the rail can be separated into three different regions (Figure 2-8) which involve wheel tread-rail contact (Region A), wheel flange-rail gauge corner contact (Region B), and field side wheel-rail contact (Region C). Wheel and rail contact typically happens in Region A (normally occurs on tangent track or greater curve radius) and Region B (tight radius curve such as switches and crossings) where different contact region will result in a different level of stresses and sizes of contact that could lead to undesirable phenomena such as wear.

Numerous studies have been done theoretically and experimentally to investigate the phenomena of the wheel-rail interface focusing in the contact area. Several attempts have been made experimentally to understand the wheel-rail contact problem that involves numerous techniques such as photo-elasticity methods, impression methods, and ultrasonic wave method [22]. The simplest way to determine the wheel rail contact area on a full scale rail is by rolling the wheel over the rail with carbon copy paper inserted at the wheel-rail interface which creates an impression of the contact shape and size [23]. However, this technique does not provide the pressure distribution resulting from the wheel-rail contact. More complex techniques exist where the shapes, sizes, and pressure distribution in the contact area can be determined using the ultrasonic method. Quantification of the shape and pressure distribution of the wheel rail contact using ultrasonic scan [24] under different loading conditions provides good comparative data where the results (overall contact shape and maximum pressure) show good correlation with existing numerical techniques (Figure 2-9).

Analytical methods derived from the Hertzian theory together with a numerical method such as Contact developed by Kalker [25] are among the most popular methods that were used to study the wheel-rail contact phenomena. Both methods were developed based on the assumption of half space and linear elastic material model that was found relevant for contact that occurs in Region A (wheel-tread rail contact). However, study on wheel-rail contact using finite element (FE) modelling [26] suggest that Hertz and Kalker’s method was found to be of lower precision for the gauge corner rail contact (Region B) where maximum contact pressure produced by both method was significantly larger than the FE solution while results for Region A contact shows very good agreement (Figure 2-10).

The Hertzian Method is a simple calculation because it idealized a simple geometry. While the centre of the rail is close to this geometry and gives good prediction, it is less good representation of Region B. Even though various techniques exist numerically and experimentally to describe the wheel-rail contact, only Hertzian method will be considered in this thesis since contact on the rail head (Region A) is the focus of the work.

2.2.1 Contact mechanics

Contact mechanics is the study of the relationship between stresses and deformation that happened when two surfaces of solid body are in contact. Its principle is widely used in many engineering applications such as gears, bearings, brakes and also in railway wheel-rail contact. The history of contact mechanics began in 1882 [27] when Heinrich Hertz published his paper "On the contact of elastic solids" [28] that forms a foundation to solve contact mechanics problem nowadays. Hertz theory has been applied by many researchers to solve problem that involves wheel-rail contact such as analysis to describe creep phenomena. Carter [29] has analyzed creep phenomena of a wheel-rail contact (see Section 2.2.2.1) based on Hertzian analysis to generate the expression for the creep coefficient by treating the case as two dimensional where he assumed the wheel-rail contact as two parallel cylinders rolling against each other. Hertz theory was also applied by Johnson [30] where he solved three dimensional creep problem by representing the wheel-rail contact as sphere rolling on an elastic plane. With the successful application of Hertzian Theory in solving wheel-rail contact problems, Hertz Theory will be applied in this thesis as an approximation to describe wheel-rail contact size, shape, and pressure distribution.

2.2.1.1 Hertzian Contact Theory

Hertzian Contact Theory has been extensively applied in the railway contact mechanics to determine the contact shape and local deformation that happened on the surface of a wheel-rail contact region. In his study on deformation of lenses under contact force, Hertz hypothesized that the contact area is elliptical in shape. Hertz Contact Theory is based on the assumptions as follow:

- Each body is regarded as an elastic half-space (i.e. a semi-infinite region) loaded only in a small elliptical region on its plane surface.
- Bodies must touch at a point which is small relative to their overall dimensions, and small relative to the radii of curvature of the surfaces.
- Surfaces were frictionless, the bodies are isotropic, and the surfaces were clean and free of lubricants.

Hertz contact theory represents an idealized situation whereas in practice (on the railways), wheel-rail contacts are unlikely to be clean and frictionless since the presence of lubricant is needed to control the friction values in the wheel-rail contact. However, this assumption can be satisfied since friction can be considered separately where extensions of the model for traction and friction are available. For the assumption of a small contact region relative to overall dimension, this condition is often violated in certain contact position especially at the gauge corner contact due to change surface curvature and plastic deformation. However, these issues can be neglected since the contact considered in this thesis is focused on the rail head region where the contact region is small compared with the radius of curvature of the undeformed surfaces. Two cases can be used to represent the contact at the rail head region based on Hertzian Contact Theory which is the three dimensional (3D) elliptical contact and the simplified line contact method.

2.2.1.1.1 Three dimensional elliptical contact

When the bodies in contact are more generally curved (Figure 2-11), the contact patch is elliptical where the surfaces initially touch at a point and will contact further over an elliptical area of semi axes a and b (Figure 2-12). By considering the case where the planes of principal curvature of the bodies are aligned against each other, three dimensional elliptical contact can be established based on Hertzian Contact Theory where the pressure distribution, p is defined by

$$p(x) = P_o\sqrt{1-\frac{x^2}{a^2}-\frac{y^2}{b^2}} \tag{2.1}$$

where P_o is the peak contact pressure and is given by

$$P_o = \frac{3P}{2\pi ab} \tag{2.2}$$

Where *P* is the normal load evaluated at any point in the contact. The contact half width dimensions *a* and *b* are given by

$$a = m \left[3 \frac{\pi}{4} P \left(\frac{k_1 + k_2}{A + B}\right)\right]^{\frac{1}{3}} \tag{2.3}$$

$$b = n \left[3 \frac{\pi}{4} P \left(\frac{k_1 + k_2}{A + B}\right)\right]^{\frac{1}{3}} \tag{2.4}$$

where *m* and *n* are the coefficients for Hertz theory (Table 2-1). The constant *A* and *B* are given by equation 2.5 and 2.6 while Θ is the constant to be used in Table 2-1.

$$A = \frac{1}{2}\left(\frac{1}{R_{1x}} + \frac{1}{R_{2x}}\right) \tag{2.5}$$

$$B = \frac{1}{2}\left(\frac{1}{R_{1y}} + \frac{1}{R_{2y}}\right) \tag{2.6}$$

$$\Theta = \cos^{-1}\left(\frac{B - A}{A + B}\right) \tag{2.7}$$

R_{1x} and R_{1y} are the radii curvature of the first body while R_{2x} and R_{2y} are the radii curvature of the second body in the lateral and longitudinal direction respectively (Figure 2-13). The elastic constants k_1 and k_2 are quantified using the following equations

$$k_1 = \frac{1 - v_1^2}{\pi E_1} \tag{2.8}$$

$$k_2 = \frac{1 - v_2^2}{\pi E_2} \tag{2.9}$$

where v_1 and v_2 are the Poisson's ration and E_1 and E_2 are Young's Modulus for the two contacting bodies

2.2.1.1.2 Line contacts

The complex geometry of 3D wheel-rail contact can be simplified as a 2D case by representing the contact as a cylinder running on a flat plane (Figure 2-14). For this case, only longitudinal and vertical force can be represented (not lateral force). The maximum pressure P_o which is located at the centre of the contact, is related to the applied load, cylindrical geometry, and material properties which is defined by

$$P_o = \sqrt{\frac{PE^*}{\pi L R^*}} \tag{2.10}$$

where P is the applied load, E^* is elastic contact modulus, L is contact length and R^* is effective radii of curvature. The elastic contact modulus E* is given by

$$\frac{1}{E^*} = \frac{1-v_1^2}{E_1} + \frac{1-v_2^2}{E_2} \tag{2.11}$$

where v is Poisson's ratio and E is young modulus (subscript refer to surface 1 and 2 respectively). The effective radii of curvature, R^* is defined by the following equation where R_1 and R_2 are the radii of the two contacting surfaces.

$$\frac{1}{R^*} = \frac{1}{R_1} + \frac{1}{R_2} \tag{2.12}$$

The contact half width a is given by

$$a = \sqrt{\frac{4PR^*}{\pi L E^*}} \tag{2.13}$$

The pressure distribution across the contact width is then given by

$$p(x) = P_o\sqrt{1 - \frac{x^2}{a^2}} \tag{2.14}$$

2.2.1.1.3 Sliding Hertzian contact

For a realistic two dimensional rolling-sliding contact, two components of forces exist between the wheel and the rail (normal forces and tangential forces) with the influence of friction between the contacting elements. The tangential forces, q(x) act in longitudinal direction along the length of the rail where its distribution due to relative sliding can be estimated from the Hertzian pressure distribution, p(x) [31]. The pressure distribution, q(x) and p(x) act simultaneously over the contact and the influence of frictional forces referred as coefficient of friction for full sliding contact is given by

$$q(x) = \mu p(x) \tag{2.15}$$

An example of the shear stress contour below a sliding Hertzian contact is displayed in Figure 2-15. The presence of tangential force has increased the maximum subsurface shear stress value and shifted the contour of maximum shear stress towards the surface and away from the vertical axis (z-axis). Without the presence of tangential force, the contour of shear stress below a Hertzian contact will be symmetrical about the vertical axis. With an increase in the frictional traction, the position of maximum shear stress moves towards the surface. Plastic strains can become larger at this point as the highly stressed material has lost the constraining effect of the surrounding material [32].

2.2.2 **Friction**

Friction can be defined as the force that hinders the movement of one body relative to another body. In railway operation, the movement of the train is dependent on the presence of frictional forces which is influenced by surface geometry, surface properties, running conditions, and lubricants. Sustaining good friction control is one of the important keys to ensure safety and reliability in a railway operation. During traction, low level of friction could lead to wheel slippage that will results in operation delay, while low friction in braking could result in a catastrophic incident. Furthermore, the level of friction forces plays a major role in the generation of failure on both the wheel and the rail, whereby low friction level will contribute to the formation of WEL either during acceleration or braking due to wheel spin or slip.

Different levels of frictions are maintained in different regions of the contact between the wheel and the rail. The term traction coefficient (ratio between friction force and normal force) is used to represent the level of friction experienced between the wheel and the rail surface. For contact that occurs at wheel tread-rail contact (Region A), the range of traction coefficient is typically between 0.2-0.4 while for the wheel flange-gauge corner contact (Region B), the value of traction coefficient is typically less than 0.2 [33]. In order to maintain the required level of friction at a certain region of contact, friction modifiers (e.g. sand or lubricants) are applied on the rail either to increase or decrease the level of friction. Generally, low friction modifiers are used to reduce wear while high friction modifiers act as a media to increase adhesion between the wheel and the rail. To determine the coefficient of friction between the wheel and the rail, various techniques can be used such as a tribometer, bogie on roller rig, or instrumented trains. An example of friction data measured under a wide range of conditions [34] is shown in Table 2-2. From these data, the adhesion coefficient value of 0.3 will be used in the modelling work to represent a dry rail condition.

2.2.2.1 Creep

In a wheel-rail contact, the relationship between the rolling speed of the wheel (due to tractive force) relative to pure rolling is known as Creep, γ where the term describe how much faster (or slower) the wheel is turning relative to pure rolling. Creep often expressed as a percentage, and usually plotted against the tractive force or coefficient of traction in a creep curve. A typical creep curve (Figure 2-16) provides information on the level of stick and slip that occurs within the contact patch between the wheel and the rail. Under pure rolling (zero creep), there is no traction transmitted by the contact and the whole contact patch is under stick region. As tractive force increase, rolling and sliding contact will occur due to the reduction of the stick region with an increase of the slip region. The stick region will fully disappear once the tractive force reaches its saturation point where the whole contact patch will experience a full slip. Under full slip condition, the level of traction is limited by the coefficient of friction with a maximum creep level between 1% to 2% under dry contact [35].

During traction or braking, it is desirable to achieve maximum acceleration or deceleration available. This can be achieved by ensuring the operation is close to the saturation point (partial slip) rather than full slip (Figure 2-17). Under acceleration, full slip condition will results in wheel spin while under braking, full slip induce wheel slide (locked wheel) event. Full slip condition (either wheel spin or wheel slide) will generate a lot of thermal input in a concentrated part of the wheel or rail which is likely to result in damage and failure. Therefore it is important for the traction control system to know how to approach full slip but not reach it.

2.2.3 Thermal aspect of wheel-rail contact

In the event of wheel slip, either a locked wheel during braking or spinning wheel during traction will generate thermal input to both the wheel and the rail. Excessive thermal input can result in the formation of white etching layer (WEL) on the steel rail surface where thermal transformation happens and change the steel phase from pearlite to martensite [36]–[38]. A martensite is a form of steel which is known to be hard but brittle. This form of steel is formed by heating a normal rail steel over 727°C, followed by rapid cooling [39].

The term white etching layer was given due to its resistance against etching and appears white and remain featureless under metallographic examination. An early investigation on WEL was conducted by Stead [36] where he discovered WEL formation on the surface of a used steel wire ropes. He interpreted the formation of WEL as martensite where the formation comes from frictional heating in service followed by rapid quenching [40]. Since then, the formation of WEL on the rail surface has become the subject of interest by many researchers [41]–[45] in order to understand its origin and mechanism.

It is thought that the formation of WEL would be beneficial to combat against wear phenomena due to its high microstructural hardness. However, the brittle surface layer can easily crack and once a small crack exists within the WEL region, it will propagate and grow down into the rail. A recent investigation by numerous researcher [46]–[48] has discovered that the formation of WEL has a detrimental effect in fatigue life due to its brittle nature where crack that initiates at the WEL surface will grow rapidly until it reaches the interface between WEL and the base material. In the current project, this is important because WEL was found on all of the samples as discussed in Chapter 3.

2.2.3.1 Metallurgical background

A rail steel with a carbon content of 0.6% in weight typically melts at around 1400°C. In order for WEL to form, the steel needs to be heated above its eutectoid temperature (727°C) and rapidly cooled within a tenth of second (cooling rate of 140°C/s) so that it will miss the nose of the curve of the austenite-to pearlite transformation (continuous cooling transformation diagram in Figure 2-18). If the steel cools more slowly within a cooling rate lower than 35°C/s (blue dashed) it will transform to the equilibrium pearlite and austenite structures. Once martensite is formed, its hard brittle structure is retained at room temperature.

The exact position of the continuous-cooling transformation curves varies with the composition of the steel. The existence of alloying elements in the rail (i.e. Si, Mn, P, S, Cr, Al, V) may results in alteration to the positions and shapes of the curves in the continuous cooling transformation (CCT) diagram where the nose of austenite to pearlite transformation has been shifted to longer times, thus decreasing the cool rate [49]. These changes can be seen from Figure 2-19 where the cooling rate to change the phase of alloy steel from austenite to martensite has decreased to 8.3°C/s compared to the rapid cooling rate of plain carbon steel (140°C/s) in Figure 2-18.

2.2.3.2 Possible mechanism for heat generation

Sufficient thermal input must be generated at the rail surface in order for WEL formation to take place. Knothe in his study suggests that a temperature around 600°C can be achieved under sliding contact with contact condition of 200 kN, 3% creep, and speed of 75 m/s [50]. However, it is implausible for such values to be achieved during normal running. Furthermore, the temperature of 600°C is far below the temperature required (727°C) for austenization to take place. A recent investigation by Takashi [51] has confirmed that the formation of WEL on the rail surface was based on martensitic transformation after rapid austenization. Temperature above 727°C could be achieved due to frictional heating that would result in a transformation of up to 60 µm in depth under contact condition of 98 kN axle load, dynamic friction coefficient of 0.4, and vehicle speed of 30 m/s. The transformation depth of 60 µm calculated by Takashi shows good agreement with field observation from another researcher [52] where the thickness of WEL that formed on the rail surface was observed between 50 to 125 µm. This finding identifies that it is possible for metallurgical transformation to take place with the influence of thermal input under certain contact conditions.

Heat could be generated on the rail surface when an extreme sliding event, due to locked wheel, will flash heat the rail surface (Figure 2-20). Assume that the rail and wheel are in such close contact that they are at the same temperature within the contact patch, the heat generated from the sliding wheel will be transfer to the rail surface where each point on the rail will be briefly heated to the same temperature as the wheel. Once the hot wheel moves away, the rail will then rapidly cool (heat dissipates along the length of the rail). The rail will be heated over a very shallow depth which serves as the perfect situation for forming a white etching layer on the rail. The depth of metallurgical transform region will depend on the sliding speed.

2.2.3.3 Effect of heat input

Despite the fact that excessive heat input could result in the formation of metallurgical transform layer on the rail surface, heat input generated from slippage effect could also lead to the formation of thermal or traction defects such as wheel burn defects and squat defects. This type of defects could result in spalling of the rail surface and also could result in rail fracture if the defect grows transversely into the rail material. Furthermore, the presence of this type of defect could block the signal of an ultrasonic wave during inspection that could prevent the detection of any subsurface defect that might present in the railhead.

A numerical method was developed by Fletcher [53] to investigate the effect of heat input on an embedded crack under combined thermal and contact loading. This investigation suggests that a crack opening stress is generated near the crack tip region under combined thermal and contact loading, yet these stresses were not present in the absence of thermal effects. It was concluded that the heat input provides crack opening effect which is similar to the crack opening effect of trapped fluid [54] in surface breaking crack.

In addition, Seo [46] has performed a numerical analysis to investigate the stresses and strains generated by the WEL that originates from heat input of sliding friction. The results demonstrate that the formation of the WEL due to heat input will encourage initiation of crack at the edge of WEL. Similar observation was also reported in [55] where significant residual tension was developed at WEL edges as a result of differential expansion. This suggests that heat input will result in the thermal transformation of the rail surface which in turn would be a potential site for a defect such as crack to develop.

2.3 Rolling contact fatigue

Over the last forty years, rolling contact fatigue (RCF) remains one of the major problems in the U.K. rail industry with the cost of their removal results in higher maintenance cost. Since the Hatfield derailment caused by rail fracture associated with RCF defects [56], RCF has become the subject of interest by many researchers. This includes investigations on growth mechanisms from a material aspect [57], control measures [58], failure prediction [59], and failure prevention [19]. In the railway context, the term rolling contact fatigue (RCF) is used to describe the development of cracks generated on both the wheel and the rail as a result of repeated high contact stresses.

2.3.1 Rail rolling contact fatigue defects

The presence of different contact forces such as compressive forces, shear forces, and lateral forces transmitted by the wheel to the rail, have major influences on the initiation location and growth direction of RCF defects. Defects may occur on the rail surface or within the subsurface where they take millions of wheel passes to grow. The type of RCF defects that attract major attention for removal include head checking, tache oval, and squats [60] and these defects can be found in almost all major line across the globe.

2.3.1.1 Head checks

Head checks can be described as a group of fine surface cracks that generally occur close to the rail crown. This group of cracks can also develop at the gauge corner especially in high rails with a tight curve radius. The term gauge corner cracks are used when they appear at the gauge corner instead of the rail crown. These fine and small cracks can develop into different type of shapes (nearly straight, V-Shape, C-shape) and are almost parallel to each other with a typical distance of 2-3 mm between cracks (Figure 2-21) [61]. In the earliest stage of development, head checks are hard to see due to their fine size but as they continue to develop, their appearances are more obvious due to shadows from slight surface depressions around them.

The formation of head checks on the rail surface could lead to complete rail failure since they grow down with a shallow angle below the rail surface where the crack might branch towards the rail surface (resulting in spalling), or in a worst case, they might branch transversely leading to rail breakage [62]. The development of head checks is normally associated with higher contact stresses (as a result of small contact region such as at the gauge corner contact) and higher creepages (continuous slight slippage) that are closely related to friction. Eadie et al. [63] suggested that development of surface cracks such as head checks can be controlled/reduced by reducing the friction coefficient at the wheel-rail contact with the application of friction modifier. At the present moment, two common practice have been employed for removal of head checks which involve preventive grinding maintenance (for a crack size up to 15 mm) and rail replacement (crack size above 15 mm) [61].

2.3.1.2 Tache Oval

Tache Oval or sometimes known as kidney shape cracks are a type of internal defects that initiate about 7 mm below the rail surface [64] which develop mainly downwards in the rolling direction. As the name suggests, the cracks have a form of kidney shape (Figure 2-22) with some grainy, granular material between the rail surface and the shiny face of the fatigue crack [65]. This type of defects generally initiates due to manufacturing defects that lead to pre-existing flaws such as hydrogen shatter cracks/cavities [66] and also with the presence of internal impurities in the rail material such as MnS inclusions that originate as a result of improper control during steel refinement process [67]. Furthermore, they can also occur from free manufacturing defect material where they could form in welds due to poor welding practice [68].

Tache Oval are of particular concern since it could not be detected by the naked eye (subsurface defect) and requires non-destructive technique such as ultrasonic inspection to detect its presence. In order to control the formation of tache oval, an improvement on the steelmaking process (vacuum degassing process) have greatly reduced hydrogen content in the rail steel which greatly reduces the occurrence of this defect type. Care must also be taken during the welding process such as preventing water entrapment in rails so that presence of excessive levels of hydrogen in the material could be reduced [21].

2.3.1.3 Squats

Squats was the first type of RCF defects that was recognized in the U.K. [61]. The term squat was given due to the indentation of two lobes with similar size (Figure 2-23) where "it looks as though a very heavy gnome has sat or squatted on the running band of the rail" [3]. This type of defects was first discovered in the 1960s in Japan which they were described as "black spots" and a similar observation was reported later in the U.K. around 1970s [69]. They generally initiated at the surface or near the surface of the rail [70] that takes place in either tangent or large curve radius track [71].

Squats normally categorized into three classes which known as light (class A), moderate (class B), and severe (class C). Field observations have shown that squats appeared on most type of tracks and lines including passenger lines, freight lines, high speed lines, and metro lines [72]. Currently, squat has become a major problem in railway network worldwide. From the viewpoint of railway infrastructure managers, squats will lead to accelerated rail deterioration, track deterioration owing to high frequency dynamic forces, wheel–rail impact noise, which will all results in an increase of track maintenance cost [73]. For preventive maintenance there exist only two solutions either by preventive grinding mechanism or by costly rail renewal [74].

The focus on squats research was mainly on the metallurgical investigation, crack growth, and also on preventive maintenance. Early records by British researchers described squats as surface initiated cracks that grew into the rail material under a shallow angle and normally branch downwards (Figure 2-24) which could lead to brittle fracture once they reach a critical size [75]. Similar defects known as "Shinkansen shelling" that appeared on the Japanese Shinkansen lines have been reported by Kondo [76] where he observed that the defects have an appearance of a dented black spot that formed on the rail surface with two types of cracks formation which were horizontal crack (develops at a depth of 3-6 mm in traffic direction) and transverse type crack (grow into the material and has potential to cause rail breakage). The formation of squats is normally associated with local plastic deformation and accumulation of strain that occurs on the railhead surface under rolling-sliding contact [77]. However, a recent study by Steenbergen [78] revealed that squats could also develop either by brittle fracture of the white etching layer or delamination at the edge of the white etching layer.

Stress and crack growth analysis on shallow angle rolling contact fatigue crack which has a similar characteristic with squats crack was carried out by Bogdanski et al. [79], [80]. They revealed that by modelling squat as plane oblique semi-elliptical crack, the influence of various contact conditions on the values of stress intensity factor at the crack front can be determined. They conclude that mixed mode fatigue crack growth takes place when fluid entrapment mechanism is introduced. The effect of fluid entrapment mechanism was further analysed in [81] to identify the effect of fluid viscosity on the growth of RCF crack using numerical study where it was concluded that liquid with a higher viscosity will dominate the growth rate even though the differences were small. A study by Fletcher et al. [82] has confirmed that liquid was able to penetrate into the cracks under loading or unloading condition and the effect of the liquid entry leads to modification of crack face friction which accelerates shear mode growth.

From the literature, two groups have worked on the squat problem where one group proposed that the mechanism for crack initiation comes from the detachment of the white etching layer [78] while the other group believed that plastic flow associated with high dynamic loads is accountable for crack initiation [83]. Even though disagreement exists particularly in the origination of squat defects, Grassie [3] conclude that squats initiated from severe shear deformation of the rail surface due to high traction forces. The Periodic spacing of squats defects might arise due to the presence of harder material between the wheel-rail surfaces that results in the indentation on the rail surface which serves as crack initiation point. Under the presence of fluid in the wheel-rail contact, the crack extends below the surface and might branch either towards the surface which leads to spalling or grow transversely leading to the formation of transverse defects.

2.3.1.4 Squat type defect/studs

In 2006, around 600 of rail defects that were mistaken as classical squats defects were identified lying on London Underground’s track in which around £6,000,000 was spent to eliminate them by re-railing the affected locations. These defects look exactly like squats at a single glance and the presence of subsurface damage which were considerably similar with classical squat was identified from ultrasonic scans. Even though both defects look alike, a closer observation on their initiation spot highlighted differences. While classical squats defect typically initiate close to the gauge corner of the running band (region B), these defects, on the other hand, initiate in or underneath the centre of the running band (region A) suggesting that different mechanisms might cause these two different defects to initiate at two different locations. Field observation (Figure 2-25) shows that this defect has an appearance of V-shaped surface-breaking crack (similar with classical squats defect) which take place in the centre of the running band. Gauge corner cracks were present near the location of the defects, however, there were no indication that the defects were connected with the surface cracks that appeared at the gauge corner (the way classical squats defect does). Since differences exist between these defects and classical squats defects, the term “studs” were proposed by Grassie et al. [84] as an alternate name for the squat type defects to clearly distinguish between studs (squat type defects) with classical squat defects.

According to Grassie et al. [84], studs does not present in tunnels and largely appeared near the signal location in which a lot of braking and accelerating would be expected. Cross section of rail containing major defects suggests that subsurface cracks present with a very minimal plastic flow, which is evidently different from conventional rolling contact fatigue defects where they generally initiate under severely sheared deformed layer. No sign of corrosion on the crack faces was observed suggesting that liquid entrapment mechanism was not responsible for crack propagation. Patches of WEL were observed near stud defects with minimal plastic flow suggesting that excessive heat input instead of excessive shear mechanism [85] might be responsible for the formation of the metallurgical transformed layer. In their study, Grassie et al. concluded that stud defects were clearly not the conventional RCF defects and their initiation are associated with thermal input due to wheelslip event as a result of poor adhesion. However, their study is limited to a small number of railways and only focussed on field observations and metallurgical investigations.The early research on studs mainly focussed on providing understanding between the studs and classical squat defect [3], field observation, and metallurgical investigation [84]. Its possible mechanism under wheelslip event was investigated by Scott et al. [52] where they predict that even under a low speed running condition, temperature rise above eutectoid temperature is possible which would aid in the formation of WEL that is responsible for studs initiation. To study the effect of surface temperature on the growth of near surface short crack (such as observed with studs), Fletcher [53] observed that thermal load provide crack opening stress which is similar to the opening stressed from trapped fluid observed by Bower [54] even though the crack analysed by Fletcher is located below the surface without any presence of fluid entrapment on the crack faces. This suggests that thermally initiated defect such as studs could develop under the influence of thermal load, supporting the hypothesis from Grassie [4] that studs possibly initiated from thermal events.

The research on rail defects conducted by both British [84] and Australian [86] researchers clearly suggest that their research subject was not conventional RCF defects even though both defects (studs and squats) look alike. In fact, studs are more benign than classical squats since no records of broken rail associated with transverse defects were reported. However, studs is still a potential risk since its development could mask the presence of transverse defect if they appear near to each other [4]. Evidence exists that studs commonly appear in the head hardened rail than the standard carbon rail [87]. This suggests that wear phenomena that happened on the softer rail might be beneficial to reduce the initiation of stud defects. Hence, preventative grinding maintenance should be scheduled properly especially on harder rails that are affected by studs defects.

2.3.2 Rolling contact fatigue crack initiation

A crack that has just initiated in a rail is hard to detect by eye even with non-destructive testing (NDT) method such as ultrasonic testing since the available inspection equipment can only detect a crack with a minimum size of 1.5 mm [88]. In the context of the railway, the rail is subjected to repeated loading as a result of repeated passing wheel. This repeated loading will induced stresses within the material that will drive the initiation of a crack. The Shakedown Theory [89] is commonly used in the rail industry to represent the response of material under repeated loading. This theory also describes how the wheel-rail contact operates above its yield point without accumulation of plastic damage. In the context of wheel-rail contact, the response of material under repeated loading [90] can be categorized into four cases (Figure 2-26). For the first case (Figure 2-26a): if the repeated stress transmitted by the wheel is below the elastic limit of the rail material, there will be no permanent deformation as the wheel moves away. If a failure occurs, generally the rail material will fail by high-cycle fatigue. For the second case (Figure 2-26b): if the wheel-rail contact pressure exceeds the elastic limit but still below the elastic shakedown limit, initial plastic flow will occur resulting in the development of protective residual stresses that will reduce the amount of plastic flow in subsequent wheel passes. This phenomenon describes the strain hardening process that occurs on pearlite rail in which during the first cycle of wheel passes, the load will be supported elastically due to changes in the material structure as a result of plastic flow. For the third case (Figure 2-26c): if the stress cycle exceeds the elastic shakedown limit but below the plastic shakedown limit, plastic flow will occur with each wheel passes that could results failure under low cyclic fatigue. For the final case (Figure 2-26d): for the case where the contact load is relatively high (exceeding the plastic shakedown limit), permanent plastic deformation will develop for each wheel passes leading to incremental plastic collapse or plastic ratchetting. The material's ductility will become exhausted which will lead to crack initiation.

Under wheel-rail contact, cracks can initiate either at the surface or below the surface of a rail. In the absence of thermal damage, the surface crack generally originates from plastic flow at the surface of the rail due to ratchetting process that happens when the contact stresses exceed the elastic shakedown limit. The surface material will become extruded and delaminates with each wheel passes which will results in crack initiation at the surface of the rail. On the other hand, subsurface cracks generally initiate due to the presence of inclusions (hard carbide inclusions) in the material as a result of poor rail manufacturing process. The inclusion generally de-bond from its matrix phase under repeated stress cycle, generating stress concentrator that will result in the formation of a subsurface crack.

2.3.3 Crack propagation

After initiation of defect, the wheel loads in railways are typically so high that defect will usually go on to grow (modelled in Chapter 4 and 5). In a wheel-rail contact, compressive forces are being transmitted by the wheel to the rail which will result in propagation of the crack. Even though it is thought that compressive forces generally will close the cracks and prevent them from growing, certain mechanisms that will lead to crack propagation can occur under compressive forces. The mechanisms that dominate the growth of RCF crack can be categorized into three different phases (phase I, II, and III) where a different growth mechanism dominates each phase (Figure 2-27). Phase 1 represents the early growth of RCF crack in a rail where the crack grows up to a size of hundred microns. The mechanism that mainly dominates this phase is the ratchetting process that develops defects in the heavily deformed material near the surface layer. Generally, the depth of the deformed layer corresponds to the length of the crack [91].

In a wheel-rail contact, fluid is generally present in a form of water (from rain) or lubricant such as flange lubricant. Even though lubricant is needed in certain conditions such as to reduce wear, the presence of fluid/lubricant also plays a major role in the growth of the crack in phase 2. Way [92] discovered that when fluid is trapped within the crack faces, the crack will propagate due to hydraulic pressurization as a result of pressure induce by the contact. The role of fluid in the growth of a crack is further studied by Bower [54] and Bogdanski [93] in which four mechanisms of fluid assisted growth can be considered:

- Shear driven crack growth (Figure 2-28a): Sliding between cracks faces generally occur as the compressive wheel approaches the crack. With the presence of fluid, friction between the crack faces will be reduced and the crack faces can slide more easily resulting in growth acceleration.

- Hydraulic pressure transmission (Figure 2-28b): The passing load force the fluid into the crack which provides a way for a tensile crack opening stress to take place even though the crack is loaded under compressive wheel force. As the wheel passes, fluid might squeeze out and might be trapped again with subsequent wheel passes.

- Fluid entrapment (Figure 2-28c): Fluid can become trapped and remain in the crack as the wheel contact closes the crack mouth. The trapped fluid will be pressurized with subsequent wheel passes generating tensile stress at the crack tip which will advance the growth of the crack.

- Squeeze film fluid action (Figure 2-28d): This mechanism originally developed to predict pressure as a result of repeated action of fluid entering and squeezing out from a gap (such as knee joints). As the fluid enters a gap and contact load from the wheel is applied, high pressure will be generated at the crack tip due to the fluid being compressed by the motion of crack faces. High pressure can still generate even if the crack is not sealed.

Rails can bend and twist under the action of multiple wheels and bogies. These stresses can drive large cracks to cause rapid failure. In phase 3, the crack is generally long with a size above 20 mm in length where individual wheel (contact stresses) have less influence on such long cracks. The mechanism of crack propagation in phase 3 is generally dominated by bending stress which will result in crack branching and rapid failure.

2.4 Wear

Wear can be categorized as progressive damage that involves displacement or material loss from a contacting surface as a result of relative motion. In the context of wheel-rail contact, wear happens due to the interaction between the wheel and the rail which involves rolling and sliding. There are several factors that affect the wear phenomena in both the wheel and the rail such as contact conditions, environmental conditions, and the presence of contaminants between the contacting surfaces. Wear is quantified in terms of volume of material lost (mm^3) per unit sliding distance (m). In the rail-wheel context, the main concern of wear lies on how much material is lost from the rail or wheel cross-section. Several mechanisms of wear can occur at the wheel-rail interface such as adhesive wear, fatigue wear, abrasive wear, oxidative wear, and delamination wear [94].

2.4.1 Wear mechanisms

Adhesive wear happens when two bodies with rough surfaces are in contact and slide against each other. Initially, these bodies will touch at a few irregular points. Local contact pressure at those points will become extremely high as compressive load is applied resulting in plastic deformation that will adhere them together. When the surfaces move, material from the softer surface will detach and adhere to the harder surface. This is often a problem in the wheel-rail contact since the surfaces of the wheel and the rail in service are not perfectly smooth which will result in adhesive wear.

Abrasive wear occurs when a harder particles are present at the interface between two sliding surfaces. The presence of these harder particles will abrade the softer surface leaving a groove along the sliding length. This phenomenon is quite common in wheel-rail contact since contaminants such as dirt, rocks, and sand are normally present at the wheel-rail interface.

Fatigue wear takes place when the surface is subjected to repeated contact loading. In the wheel-rail contact, degradation happens once particle spall away from either the wheel or the rail surfaces typically at a high number of cycle. Further deterioration might occurs rapidly following initial degradation. Normally, the wear particle produced by this mechanism are very much larger compared to abrasive and adhesive wear.

Oxidative wear occurs when debris layer of oxide particle is removed from a material surface due to sliding action of two bodies. Regeneration of oxide growth occurs rapidly on the rail surface after existing oxide layer is removed. The formation of oxide layer will inhibit metal to metal contact that could lead to low adhesion in the wheel-rail contact.

Under repeated sliding contact, subsurface plastic deformation accumulates which leads to the formation of cracks that initiate as ductility is exhausted. Further loading will cause the cracks to propagate and finally shear to the surface. Delamination wear happens when the surface of a material is damaged and then splits into thin layers resulting in loss of materials [95].

2.4.2 **Wear regimes**

In order to describe the severity of wear in a wheel-rail contact, two approaches can be used to model the wear process which is the Archard's Theory and also Tgamma (Tγ) wear number. Both methods require formulation of wear coefficients that could be determined from rolling and sliding wear experiments such as the Twin Disc machine. According to Archard [96], the severity of wear can be mapped by plotting the wear rates over the sliding distance against normal load (Figure 2-29) where the wear rate, W, depends on the normal load applied to the contact, N, wear coefficient, k, sliding distance, l, and material hardness, H given by

$$W = k\frac{Nl}{H} \tag{2.16}$$

According to Bolton [97], the wear rate (material lost) is proportional to the energy dissipated at the wheel-rail contact zone given by

$$W = T\gamma \tag{2.17}$$

Where W is Wear Number, T is the tangential force, and γ is the percentage difference between the speed of the wheel relative to the rail surface (creep). To identify the wear regimes, the wear data can be mapped by plotting the wear rate (mass loss per meter rolled of the wheel divide by the contact area, µg/m/mm^2) against the wear number over the contact area ($T\gamma/A$). Using the data produced by Bolton [97], Lewis and Olofsson [98] have plotted the wear data (Figure 2-30) to identify the wear regimes under rolling/sliding contact between different wheel and rail material. Three wear regimes have been identified from the twin disc test which was referred as mild, severe, and catastrophic.

Mild wear usually takes place under low creep (below 2%) resulting in a smooth surface that is generally smoother than the original surface. The wear debris produced is particularly small with a diameter around 0.1 µm [99]. Evidence of oxide particles from surface examination suggests that oxidative wear mechanism is the dominant mechanism during mild wear. In the wheel-rail contact, mild wear takes place at the rail head, in the region of wheel-tread rail contact.

Severe wear happens under medium creep (below 10%) resulting in a rough surface that is generally rougher than the original surface, forming ripple like surface topography. The wear debris produced is particularly larger than mild wear debris with a diameter around 10 µm. Analysis of wear particles revealed that adhesion wear mechanism might be responsible for causing debris particle adhere to the rolling surfaces. Severe wear that happens on the rail usually occurs at the flange-gauge corner contact.

Catastrophic wear generally occurs under high creep (above 10%) resulting in a massive increase in the wear rates as compared to the other wear regimes. Metallography analysis (Figure 2-31) suggest that huge amount of material have been scooped out under catastrophic wear regime. Cracks can develop at the surface and grow parallel to the deformation leading to severe delamination.

2.4.3 Wear – Rolling Contact Fatigue interaction

During each wheel-rail contact, both wear phenomena and crack initiation/propagation happen at the same time. Wear is not necessarily a bad thing as it can remove material from the surface that may contain small cracks, and also reduce the growth of larger cracks. Reducing the wear rate will results in the development of RCF cracks, therefore, both natural and artificial wear (grinding) play a major role in the development of RCF damage.

When the wear rate exceeds the crack tip advance rate, the surface of the rail will be worn faster compared to the propagation of the crack, thus resulting in a net shortening of the crack for each wheel pass. When the wear rate is lower than the crack propagation rate, the crack will grow faster compared to the rate of the worn surface in which the crack will further develop resulting in fatigue failures. A schematic of wear process and development of surface breaking crack that happened at the same time is shown in Figure 2-32. For each wheel pass, the crack tip advances into the rail by a small distance (da) and at the same time, wear of the rail surface truncates the top of the crack over a small length (dw). The net crack growth rate (da_{net}) can be estimated by subtracting the crack tip advance rate (da) with the wear rate (dw) given by:

$$da_{net} = da - dw \tag{2.18}$$

Where the wear rate (dw) is given by:

$$dw = \frac{d}{\sin\theta} \tag{2.19}$$

Where d is the wear depth and ϴ is the angle of the crack.

The interaction between wear and RCF in rails have been studied by some researcher focusing on rolling sliding contact equipment. Fletcher [100] carried out a test to investigate whether RCF cracks would still develop under prolong unlubricated contact in which he observed that RCF will dominate until approximately 10,000 cycles before equilibrium between crack growth and wear rate can be achieved. Donzella [101] on the other hand study the competitive role between wear and RCF crack in R900A rail steel using rolling sliding test machine. He observed that under pure rolling contact, RCF will predominate due to less material surface being removed under pure rolling. However, wear will dominate under rolling-sliding contact due to high material being removed from the surface that eliminates surface micro cracks.

2.5 Fracture mechanics

Even though many components are generally designed to be in service for an infinite life, there were still many tragic incidents reported that involve loss of life as a result of material failure. For instance, the Comet jetliners disintegrated in flight killing dozens of people in 1954 [102], the Union Oil Amine pressure vessel ruptured and exploded in 1984 killing seventeen people [103], the derailment of German Inter City Express in 1998 killing hundreds of people [104], in which all of these incidents happened due to material fracture caused by development of cracks in the material.

The theory of linear elastic fracture mechanics (LEFM) was established which provides a method to predict failure of materials due to the development of crack (fracture). The birth of LEFM theory started with the early work of Griffith [105] based on the forces between atoms in which he managed to explain why the observed strength of a material is considerably less than the theoretical strength. Griffith concluded that ‘real’ material must contain a small defect, and the strength of a material will be reduced when defects and crack exist in the material.

The presence of cracks will generate stress concentration as would exist for a general elliptic defect. As the minor axis of an elliptical defect approaching zero, the elliptical defect will become a crack. However, the stress at the crack tip will become infinity (based on elliptical defect stress concentration factor) which suggest that a material with a crack would not be able to withstand any applied forces and this theory can only be applied for brittle materials. Based on the original concept of Griffith, Irwin [106] suggested that plasticity is necessary for fracture of ductile materials such as metals. With some refinement of Griffith approach, LEFM has developed as an analytical approach to describe fracture in a material. The material fatigue and fracture properties can be represented in terms of a single parameter, either by energy or by stress intensity factor [107].

2.5.1 Stress Intensity Factor

Stress intensity factor, K can be described as failure criteria of a material due to fracture. It is generally used to predict the stress state around the crack front as a result of remote load or contact stresses. For central crack in an infinite plate (Figure 2-33), the elastic stress distribution near the crack tip are given by

$$\sigma_x = \frac{K}{(2\pi r)^{\frac{1}{2}}} \cos\left(\frac{\theta}{2}\right)\left\{1 - \sin\left(\frac{\theta}{2}\right)\sin\left(\frac{3\theta}{2}\right)\right\} \tag{2.20}$$

$$\sigma_y = \frac{K}{(2\pi r)^{\frac{1}{2}}} \cos\left(\frac{\theta}{2}\right)\left\{1 + \sin\left(\frac{\theta}{2}\right)\sin\left(\frac{3\theta}{2}\right)\right\} \tag{2.21}$$

$$\tau_{xy} = \frac{K}{(2\pi r)^{\frac{1}{2}}} \sin\left(\frac{\theta}{2}\right)\cos\left(\frac{\theta}{2}\right)\cos\left(\frac{3\theta}{2}\right) \tag{2.22}$$

Where r is the distance from the crack tip and ϴ is the angle from the reference axis (Figure 2-33). The stress intensity factor, K, is proportional to $(\pi a)^{1/2}$ where a is the half length of the crack. The relationship is given by

$$K = \sigma(\pi a)^{\frac{1}{2}} \tag{2.23}$$

Note that the above equation can only be applied for the case of central crack in an infinite plate. Different crack geometry and configuration (single edge crack, elliptical surface crack, infinite plate, finite plate) would have a different form of stress intensity factor [108]. Therefore the stress intensity factor is usually expressed in a more general form given by the following equation where Y is the geometry factor

$$K = Y\sigma(\pi a)^{\frac{1}{2}} \tag{2.24}$$

The stress intensity factor is generally referred as K_I, K_{II}, and K_{III} where the subscript represents modes of failure that cause the crack to deform and propagate. There are three types of mode (Figure 2-34) that could cause the crack to deform known as:

- Opening / tensile mode (mode I) - crack faces move directly apart due to direction of stress that acts normal to the plane of the crack

- Shearing/slide mode (mode II) - crack faces slide over against each other due to direction of stress that acts perpendicular to the crack tip
- Tearing mode (mode III) – crack faces move relative to one another due to direction of stress that acts parallel to the crack tip

2.5.1.1 Method for stress intensity factor calculation

The stress field generated below a typical wheel-rail contact is extremely complex since it involves many components of stresses that act in a different direction. Thus, predicting stress intensity factors (SIF) from scratch for particular loading conditions are often difficult since there might be a combination of different failure mode (mode I, II, and III) known as mixed mode that contributes to the deformation of the crack. For a range of common crack configurations, standard solutions are available where the value of the SIF can be acquired by inputting the applied load and crack size in a certain chart, equation or table [109]. For complex crack configurations, several numerical methods exist to predict SIF such as body force method, finite element analysis, and boundary element modelling.

2.5.1.1.1 Body force method

In 1968, the body force method (BFM) was first introduced by Nisitani [110] to quantify stress concentration factors of notches and SIF for cracks in linear elastic problem. It was developed based on the principle of superposition where point forces were superposed and transmitted along an imaginary boundary to satisfy the boundary condition. The mechanism responsible for the growth of an inclined surface under the effect of fluid pressurization were investigated by Kaneta et al. [111] where the BFM was applied to obtain the stress intensity factor. He assumed that the fluid pressure at the crack mouth being equal to the contact pressure and decrease linearly falling to zero at the crack tip. The prediction of the stress intensity factor has resulted in an exceedance on the shear mode threshold value for a small crack size in which he concluded that the opening / tensile mode is unlikely to happen and crack will develop under the effect of shear mode growth.

2.5.1.1.2 Finite element method

Finite element method (FEM) is among the most common numerical analysis techniques used for engineering practices. The basic principle in FEM is the process of discretization/meshing where the object of interest (model) is divided into smaller regions (elements and nodes) and a set of equation that describe the model is selected and solved. This method is useful to solve the problem of complex geometries and loadings such as crack propagation across deformed microstructure in which analytical solutions are hard to obtain.

Prediction of stress intensity factor using the FEM has been applied widely by many researchers especially to study crack propagation in rail. This includes the work by Bogdanski et al. [112] where they analysed the growth of squat defect under the effect of practical loading condition that exists in the wheel-rail contact such as bending, residual, and thermal stresses. The defect was represented as semi elliptical crack using three dimensional FEM where two sizes of defect (small and large) were considered. Based on the calculation of the SIF, they concluded that crack propagation is mainly dominated by mode II (shear) mechanism. Even though the range for mode I SIF increases with increasing crack size, the value is still low compared to the mode I threshold value suggesting that crack propagation under the opening/tensile mode does not present. It was also observed that the presence of stresses resulted from thermal, residual, and bending has very minimal effect on the range of SIF value.

Farjoo et al. [113] have performed an investigation on the effect of bending stress on squat crack propagation by using FEM. Their work was motivated by a study by Kerr et al. [114] where it was reported from field observation that squat developed widely on a rail supported under elastic foundation (timber sleepers) compared to a solid foundation (concrete sleepers). By considering two values of bending stresses (calculated with lower and higher stiffness) in their model, Farjoo et al. [113] concluded that the SIF range of a crack that formed under elastic foundation is extremely high compared to the solid foundation in which they suggested that consideration of bending stresses in the boundary condition of squat defect modelling is as important as fluid entrapment condition proposed by Bogdanski [115].

2.5.1.1.3 Boundary element method

Boundary element method (BEM) is a numerical method that solves partial differential equation of a domain/boundary where the material properties and boundary condition of the model were fitted into a system of boundary integral equations. This method is quite similar to the FEM where the geometry of a model is represented by meshing process (divided into elements and nodes). However, the difference lies in terms of solution process where in FEM, the entire domain is calculated for solution whereas, for BEM, only the boundary of the mesh is solved. In the application of crack growth analysis, the mesh is required to be extremely fine when using FEM to capture the high stress gradients ahead of the crack tip whereas, for BEM; only the interest regions (crack) need to have finer mesh while the other region can be mesh coarsely. This is a particular advantage especially for crack growth prediction in rails whereby numerous researcher has successfully produce crack growth prediction model using BEM techniques.

In railway studies, Akama and Mori [116] developed a two dimensional boundary element model to investigate the change of SIF at the crack tip of an inclined surface crack loaded under a moving Hertzian contact. In their model, they consider the presence of fluid which penetrates through the crack mouth resulting in a reduction of crack face friction which is similar to the model developed by Bower [54]. Based on the prediction of SIF, both mode I and mode II SIF results show very good agreement with findings in [54].

Fletcher et al. [117] also utilized the BEM technique to investigate the growth of surface breaking crack where the 3D model of a rail with actual geometry was developed instead of half assumptions model. Their model was based on mode II growth mechanism, controlled by variation of friction coefficient between the crack faces without considering fluid pressurization mechanism since previous investigations [118] suggested that presence of fluid reduced the friction coefficient between the crack faces that drive crack growth through mode II mechanism rather than by fluid pressurization mechanism. Their results (based on prediction of SIF) show good correlation with findings by Kaneta et al. [111] especially in determining peak shear SIF under different value of surface traction. Based on their results, they concluded that the growth rate for an inclined surface crack is inversely proportional to the coefficient of friction between the crack faces.

In a recent investigation, Fletcher [53] developed a two dimensional model based on BEM approach to investigate the effect of heat input on an embedded crack loaded under combined thermal and contact loading. He considered three different cases of thermal load which includes no thermal load (20°C), intermediate thermal load (500°C), and severe thermal load (1000°C). Based on his prediction of the SIF at the crack tip, he discovered that crack will develop under intermediate (500°C) and severe (1000°C) thermal load. He concluded that the intermediate and severe thermal load provide crack opening stress which is similar to the opening stressed from trapped fluid observed by Bower [54] in which this opening stress will help to unleash shear mode mechanism that will drive the crack to grow.

Technically, BEM is a lot faster and simpler to use compared to FEM, but it has some limitation whereby plasticity could not be modelled within BEM. However, BEM is very good for crack modelling because the stress field ahead of the crack is internal to the body so there is no need to model the whole body. Even though BFM has been primarily used by a particular group in Japan, but the math of it is not likely disseminated. Therefore BEM has been chosen as the primary method in this study to model and predicts crack growth since plasticity is not the main focus of the work.

2.5.2 Crack growth law

In a wheel-rail contact, crack growth in mode I can happen either by fluid pressurization, bending stresses, or by thermal stresses whereas shear mode (mode II) crack growth will follow as the wheel pass over the crack tip causing the crack faces to slide over each other. Due to the fact that mixed mode occurs in a wheel-rail contact, developing a crack growth law based on conventional compact test specimen [119] which involve cyclic loading of push-pull action (Figure 2-35) would be deficient to describe crack growth in rail.

Crack growth law that represents a combination of mixed mode mechanism has been developed by Wong et al. [120] by conducting a series of tests using cruciform fatigue specimen. The crack growth law was developed specifically for normal grade rail steel where the cruciform specimen was machined from a BS11 rail steel. Two growth laws were developed where each law is governed by different principal fatigue mechanism. If the principle fatigue mechanism is the mode I (upper bound) in nature, the growth law was given by:

$$\frac{da}{dN} = 0.000507\left(\Delta K_{eq}^{3.74} - 4^{3.74}\right) \quad (2.25)$$

Where K_{eq} is the equivalent SIF given by

$$\Delta K_{eq} = \sqrt{\Delta K_1^2 + \Delta K_2^2} \quad (2.26)$$

If the principle fatigue mechanism is mode II (lower bound) in nature [80], the growth law was given by:

$$\frac{da}{dN} = 0.000614\left(\Delta K_{eq}^{3.21} - 4^{3.21}\right) \quad (2.27)$$

Where da/dN is the growth rate given by nm/cycle, while the range of mode I and II stress intensity factor ΔK_I and ΔK_{II} are in $MPa.m^{0.5}$.

The significance of the SIF predictions for fatigue crack growth can be judged by comparing the predicted SIF with the fatigue threshold ranges of tensile ($\Delta K_{\sigma th}$) and shear ($\Delta K_{\tau th}$) mode growth. To predict crack growth under fatigue in rail during the passage of a wheel contact, either the tensile mode stress intensity ΔK_{σ} should exceed the tensile mode threshold value $\Delta K_{\sigma th}$, or the shear mode stress intensity ΔK_{τ} should exceed the shear mode threshold value $\Delta K_{\tau th}$. For a mixed mode case where both mode I and mode II stresses present, Otsuka et al. [121] discovered that a crack is more likely to grow by a tensile mechanism in preference to a shear mechanism since tensile growth tends to be faster. It was stated that for low carbon steel, the threshold stress intensity factor value for tensile and shear modes crack growth was $\Delta K_{\sigma th}$ = 6 $MPa.m^{0.5}$ and $\Delta K_{\tau th}$ = 1.5 $MPa.m^{0.5}$ respectively.

2.6 Tables and figures

Table 2-1 Coefficients for Hertzian Theory [122].

Ө	**30**	**35**	**40**	**45**	**50**	**55**	**60**	**65**	**70**	**75**	**80**	**85**	**90**
m	2.73	2.39	2.13	1.92	1.75	1.61	1.48	1.37	1.28	1.20	1.12	1.06	1.00
n	0.49	0.53	0.56	0.60	0.64	0.67	0.71	0.75	0.80	0.84	0.89	0.94	1.00

Table 2-2 friction data measured under a wide range of condition [34].

Condition of rail surface	**Adhesion coefficient**
Dry rail (clean)	0.25-0.30
Dry rail (with sand)	0.25-0.33
Wet rail (clean)	0.18-0.20
Wet rail (with sand)	0.22-0.25
Greasy rail	0.15-0.18
Moisture on rail	0.09-0.15
Light snow on rail	0.10
Light snow on rail (sand)	0.15
Wet leaves on rail	0.07

Figure 2-1 Paved track/ruts that guide the wheel so that the vehicle will remain on the track near Corinth, Greece [123].

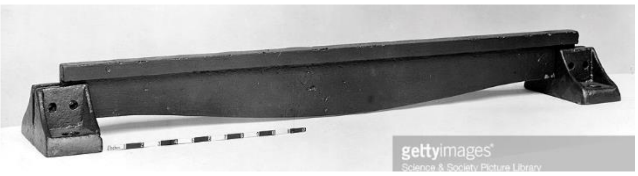

Figure 2-2 Edge rail [124].

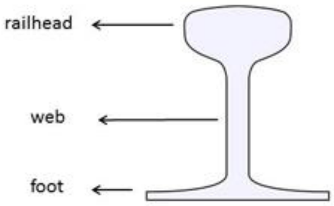

Figure 2-3 Cross section of flat bottom rail [125].

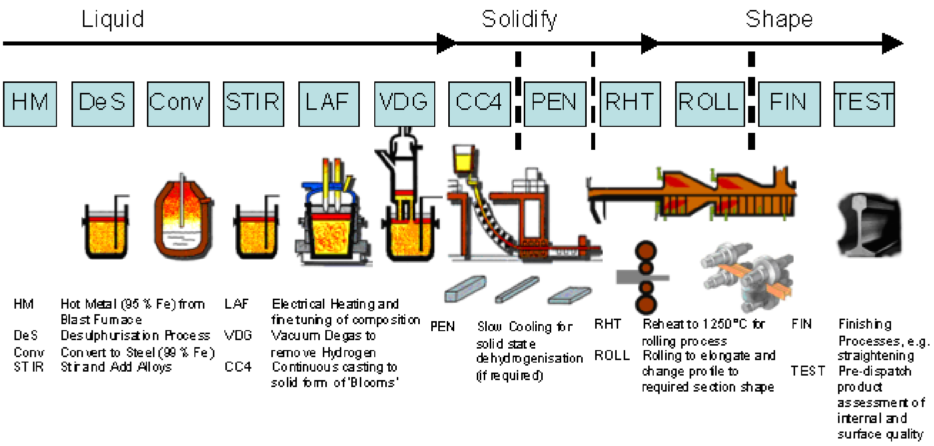

Figure 2-4 Rail manufacturing process [126].

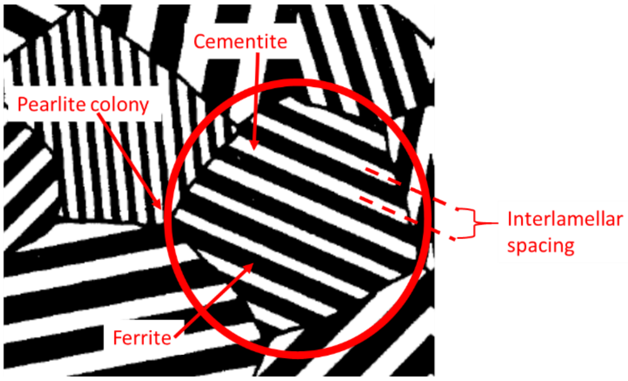

Figure 2-5 Sketch of pearlite microstructure

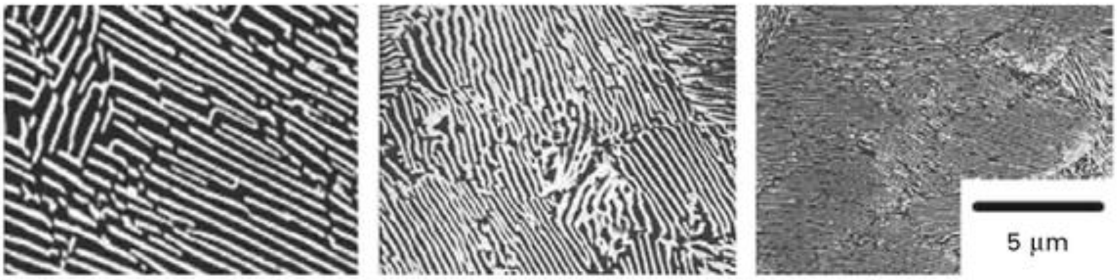

Figure 2-6 Pearlite lamellae structure for different rail grade. Left to right: R220, R260, R350 HT [127].

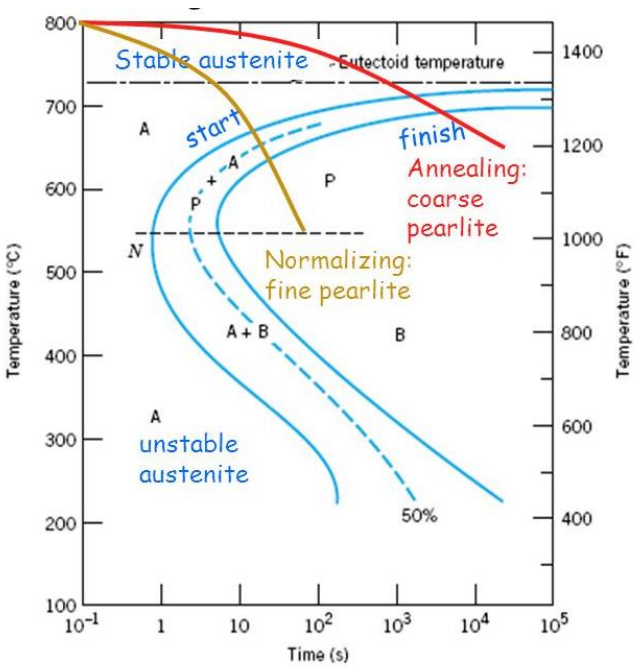

Figure 2-7 Time transformation temperature (TTT) diagram for eutectoid steel

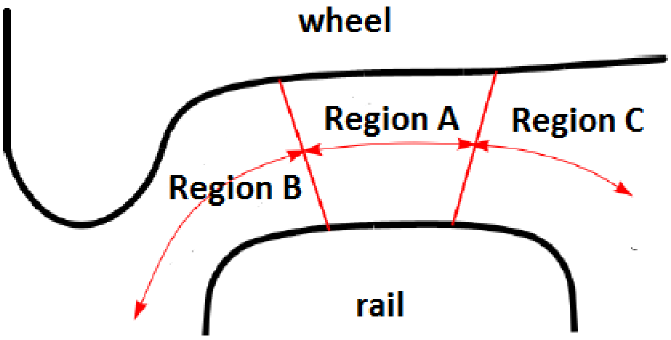

Figure 2-8 Wheel-rail contact regions

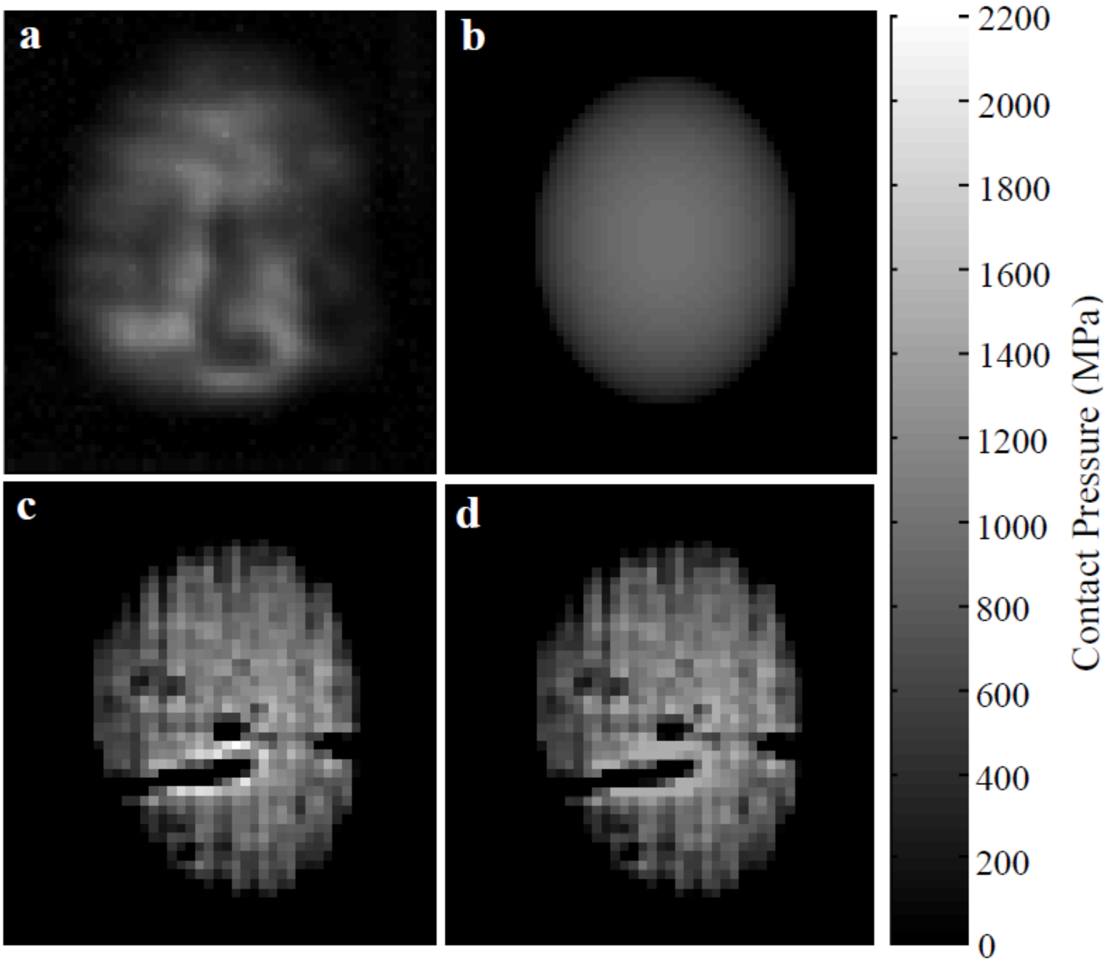

Figure 2-9 Contact Pressure Maps for a load of: 80 kN (a) Ultrasonic Measurement; (b) Hertzian; (c) Elastic Model; (d) Elastic-Plastic Model [24].

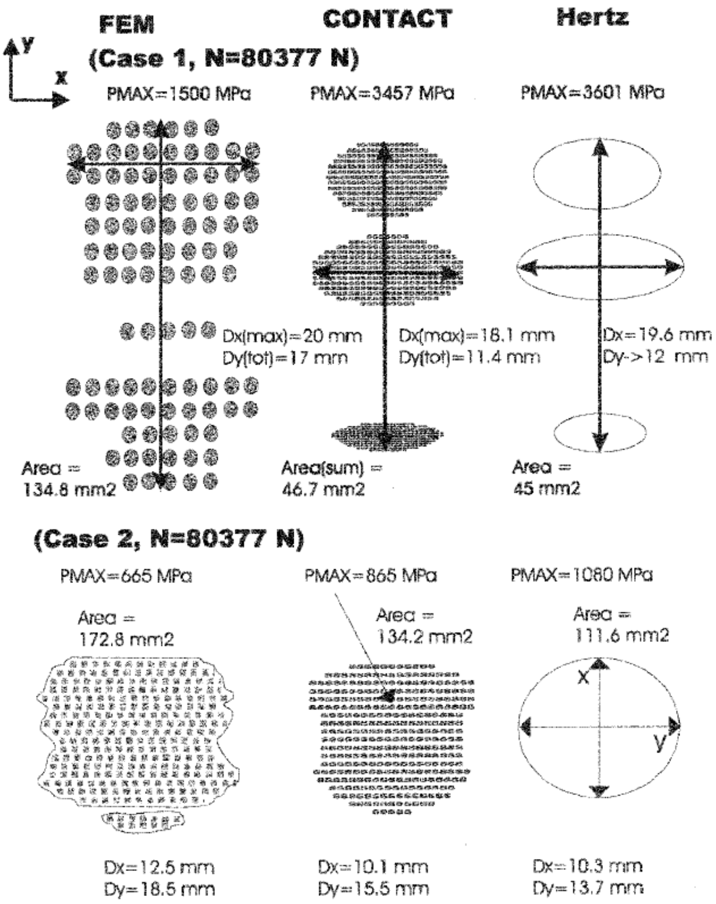

Figure 2-10 Comparison, with respect to maximum contact pressure and the contact area, between FEM, Contact, and Hertzian analysis [26].

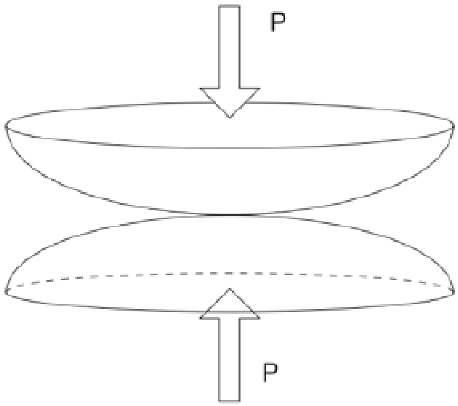

Figure 2-11 Contact of two curved body

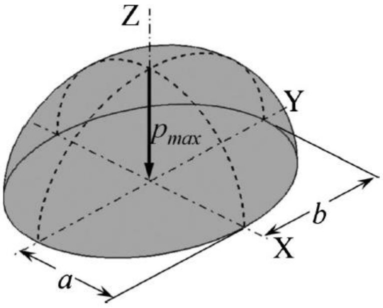

Figure 2-12 Hertzian elliptical pressure distribution formed by the contact of two curved bodies [128].

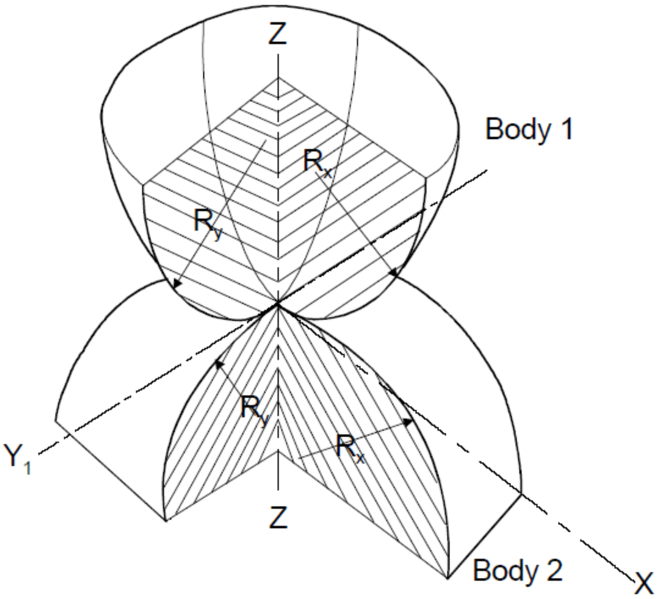

Figure 2-13 Contact between two curvature bodies with different radius [129]

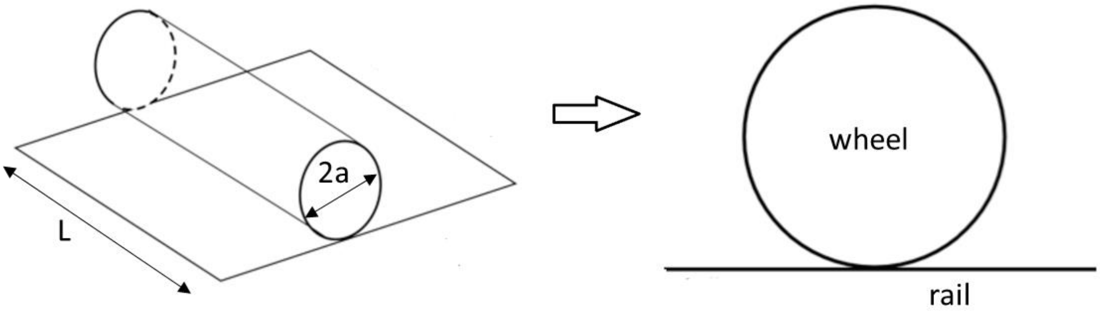

Figure 2-14 Representation of a simplified 2D wheel-rail contact

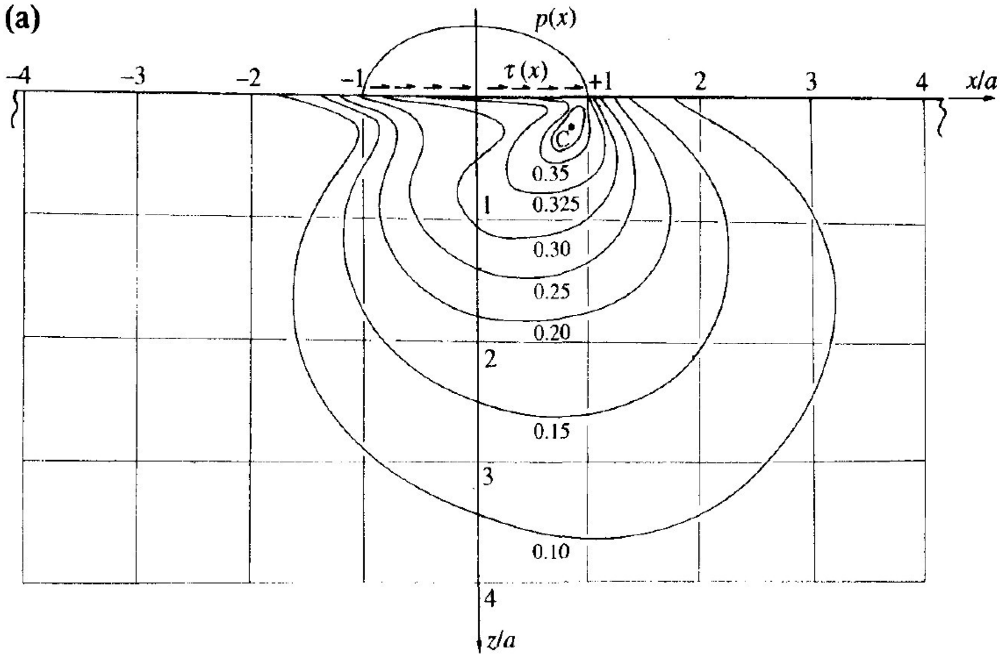

Figure 2-15 Contours of maximum shear stress below a sliding Hertzian contact. Traction is from left to right. Contour values represent friction coefficent [32].

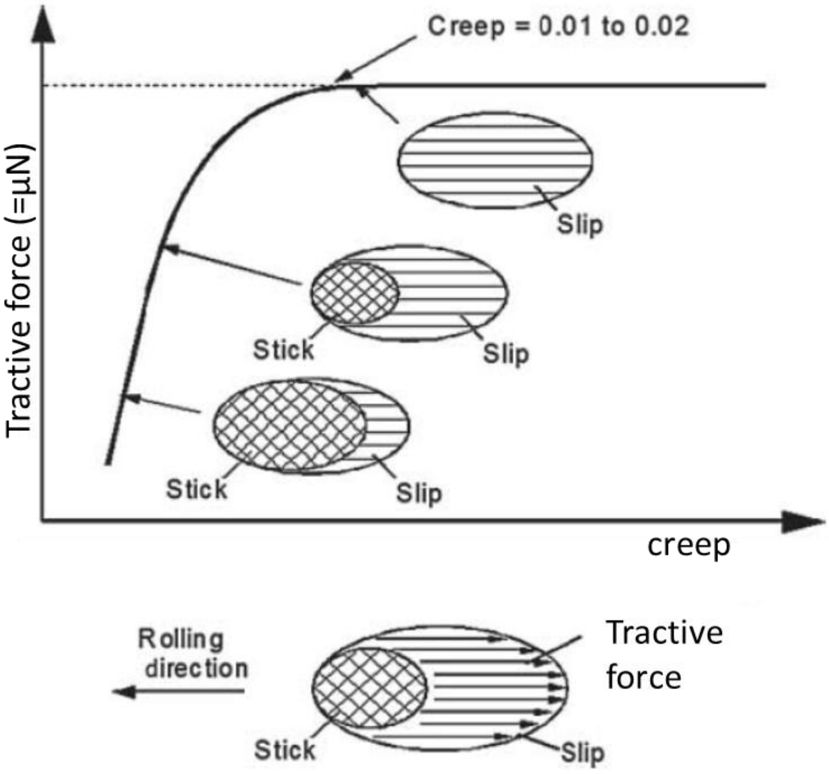

Figure 2-16 Typical creep curve under dry contact condition. Adapted from [99].

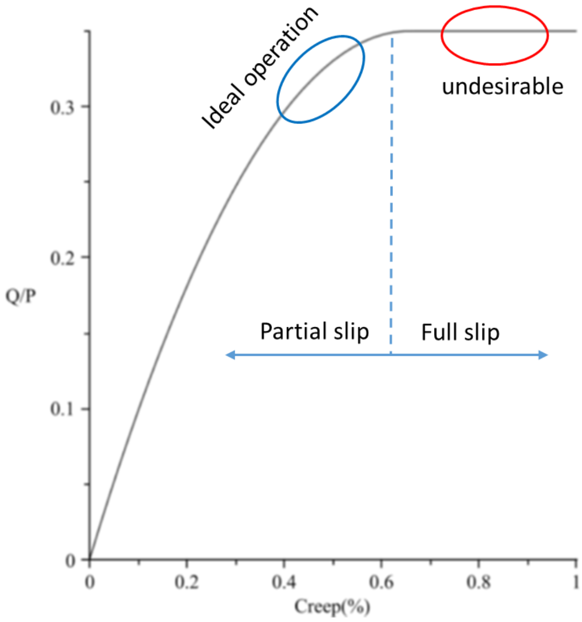

Figure 2-17 Typical creep curve displaying ideal operational conditions [130]

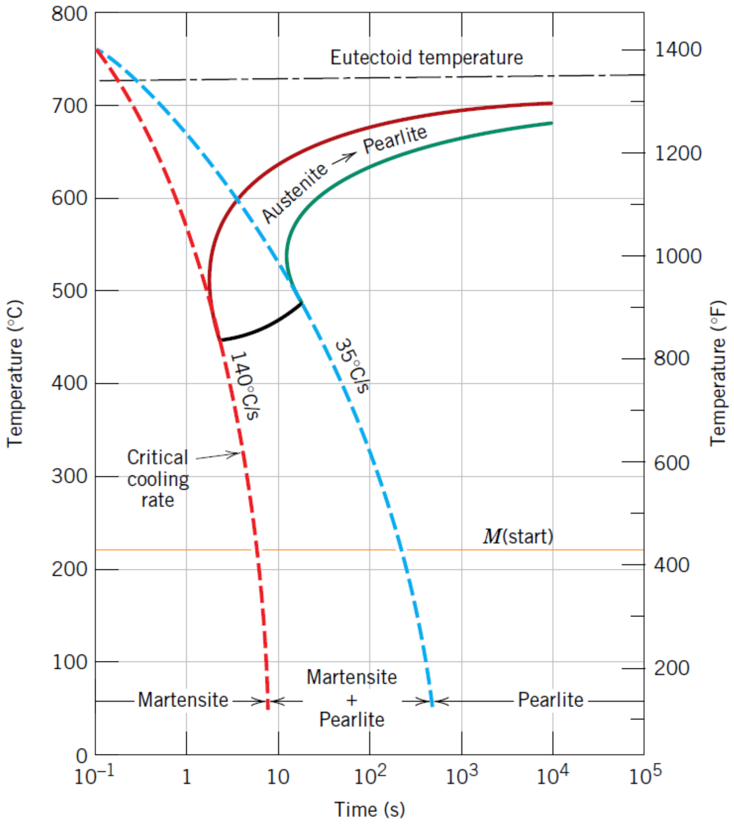

Figure 2-18 Continuous-cooling transformation diagram for a eutectoid iron–carbon alloy and superimposed cooling curves, demonstrating the dependence of the final microstructure on the transformations that occur during cooling [49].

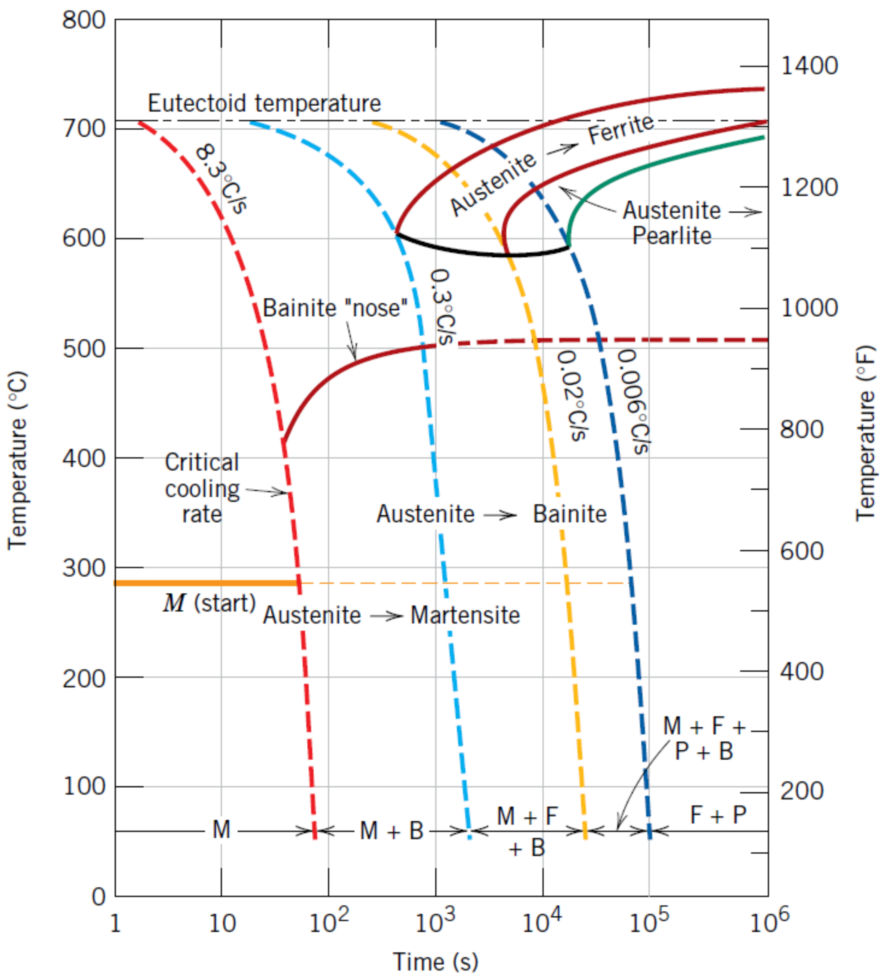

Figure 2-19 Continuous-cooling transformation diagram for an alloy steel (type 4340) and several superimposed cooling curves demonstrating the dependence of the final microstructure of this alloy on the transformations that occur during cooling [131].

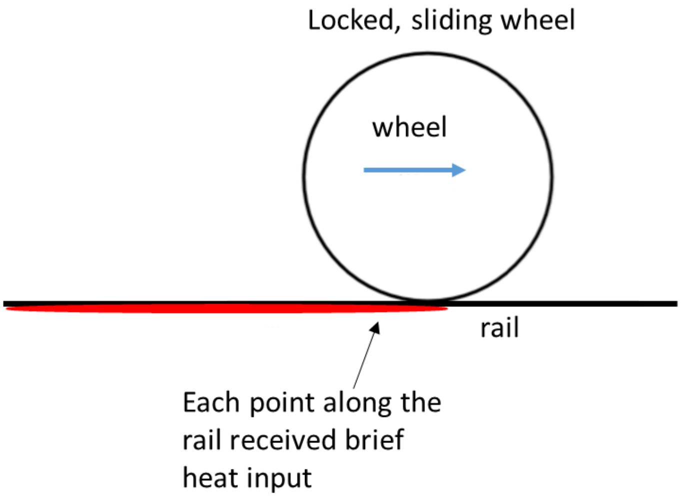

Figure 2-20 Flash heat of the rail surface due to sliding wheel.

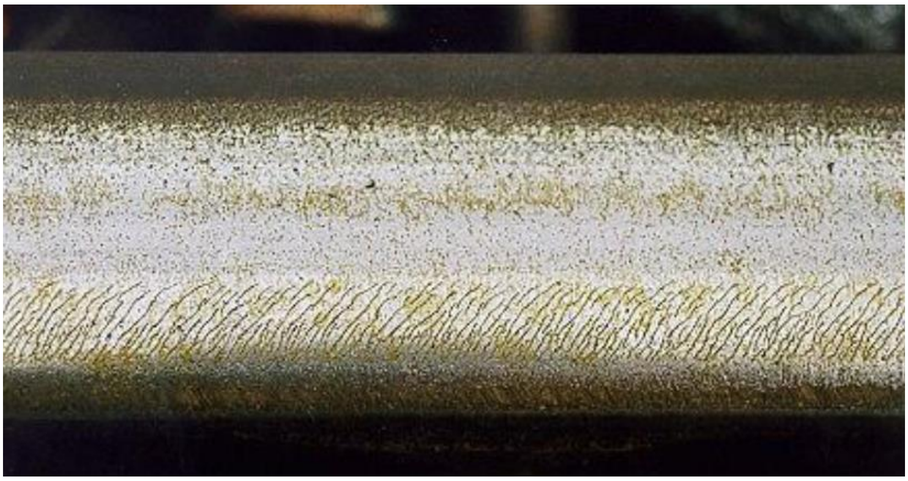

Figure 2-21 Typical appearances of head checks cracks [70]

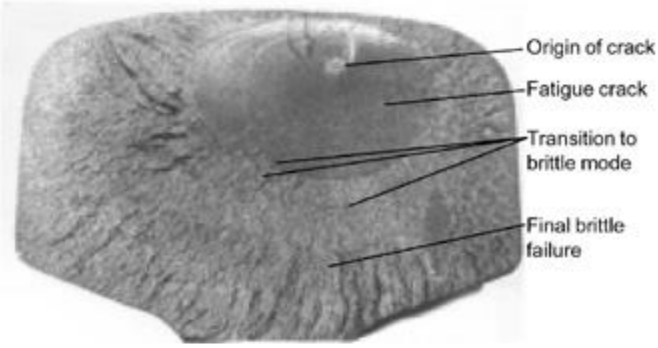

Figure 2-22 Example of tache oval (kidney shape crack) appearance that initiates in the subsurface region of the railhead [67].

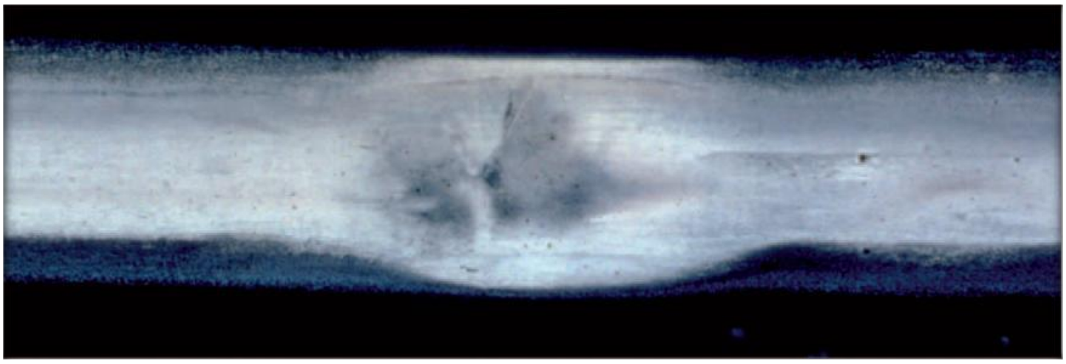

Figure 2-23 Squat appearance on rail [3]

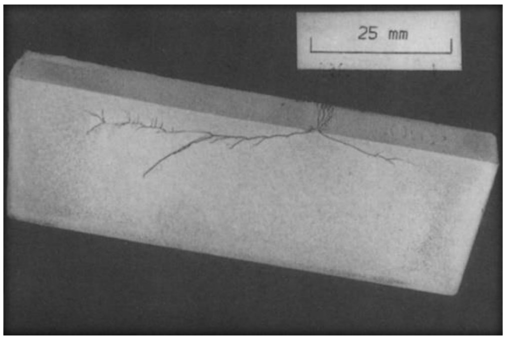

Figure 2-24 Longitudinal cross section of rail suffering from squats defect reveal that one of the crack branches grew in transverse direction [132].

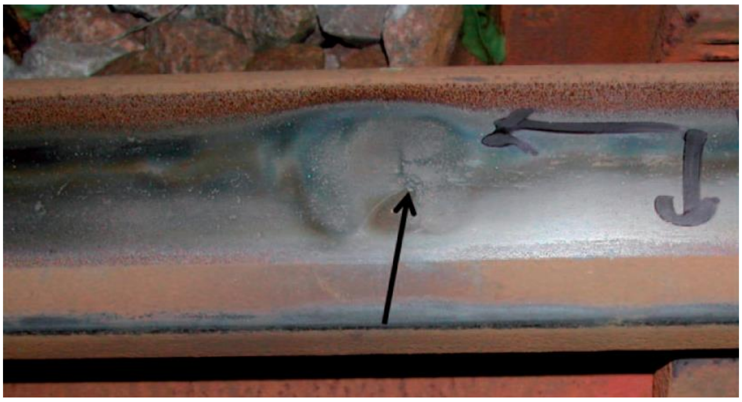

Figure 2-25 'Studs' defect appearance on rails. Arrows superposed on photos point to the apex of the 'V' shaped crack [84]

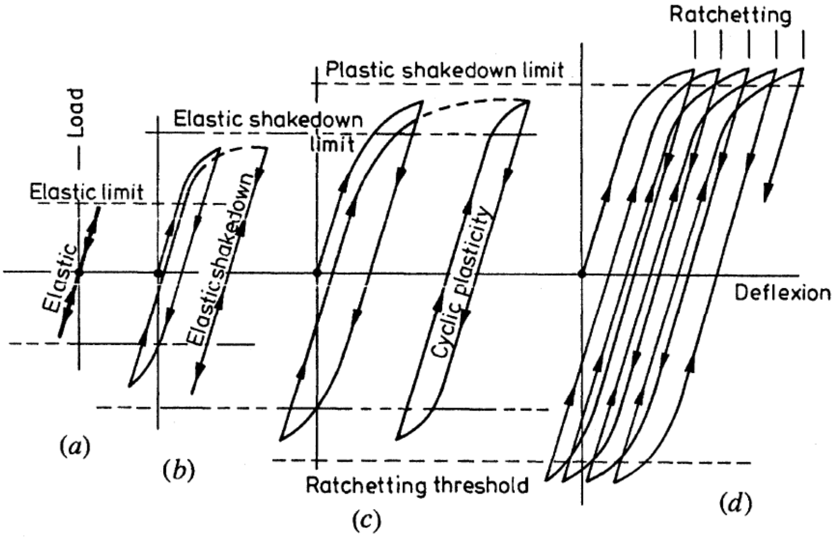

Figure 2-26 Material response to cyclic loading. (a) elastic (b) above the elastic limit, but below the shakedown limit (c) above the elastic shakedown limit, but below the plastic shakedown limit (d) above the plastic shakedown limit. Adapted from [90].

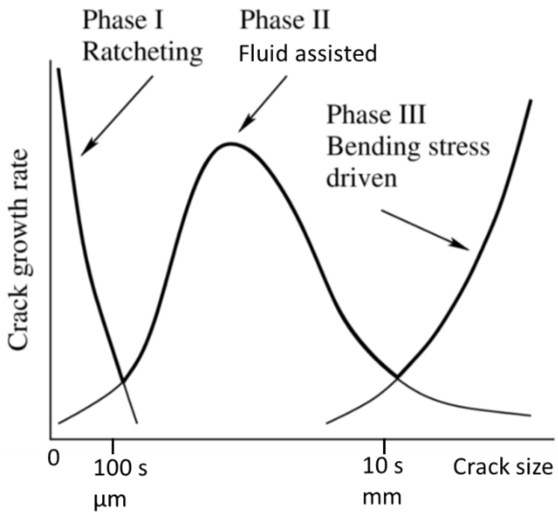

Figure 2-27 Rail crack growth and phases [133].

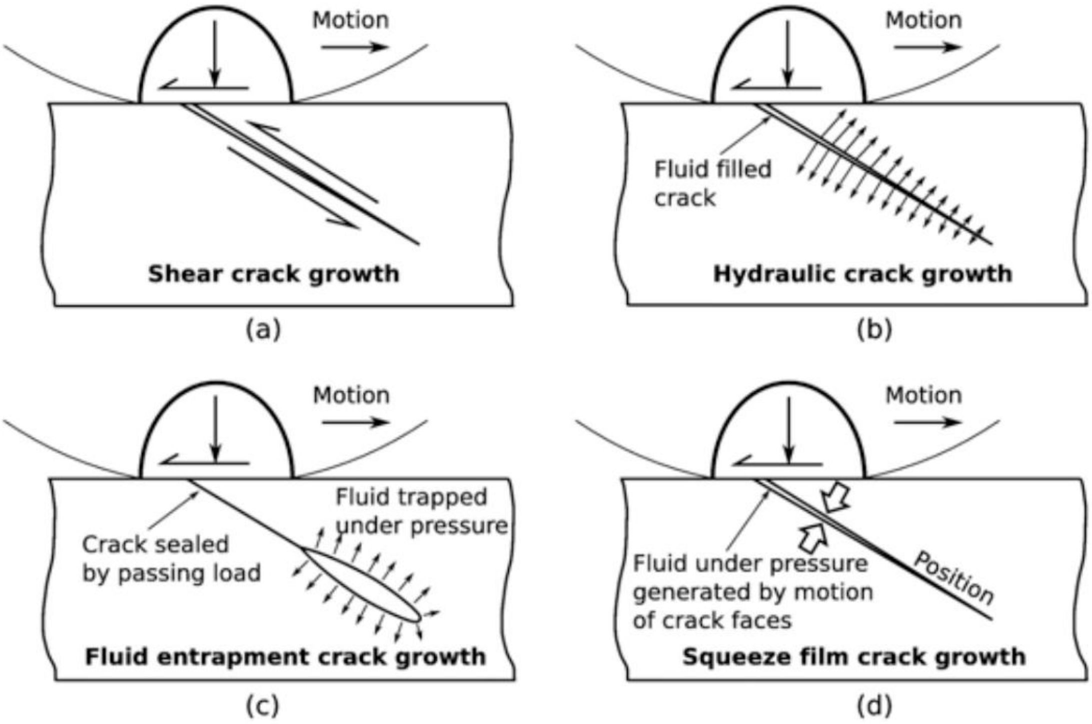

Figure 2-28 Schematic growth mechanism for phase II crack propagation. (a) Shear driven crack growth. (b) Hydraulic pressure transmission. (c) Fluid entrapment. (d) Squeeze film fluid action. [91]

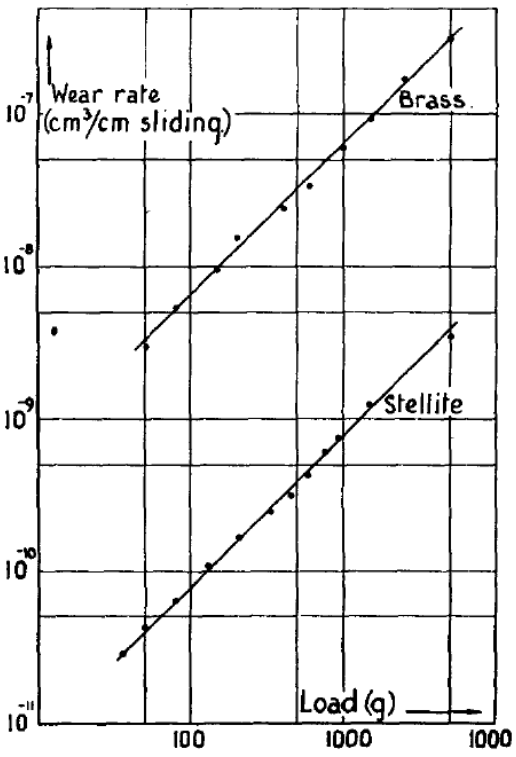

Figure 2-29 Wear map for brass and stellite pins rubbing on tool steel rings according to Archard Theory [96].

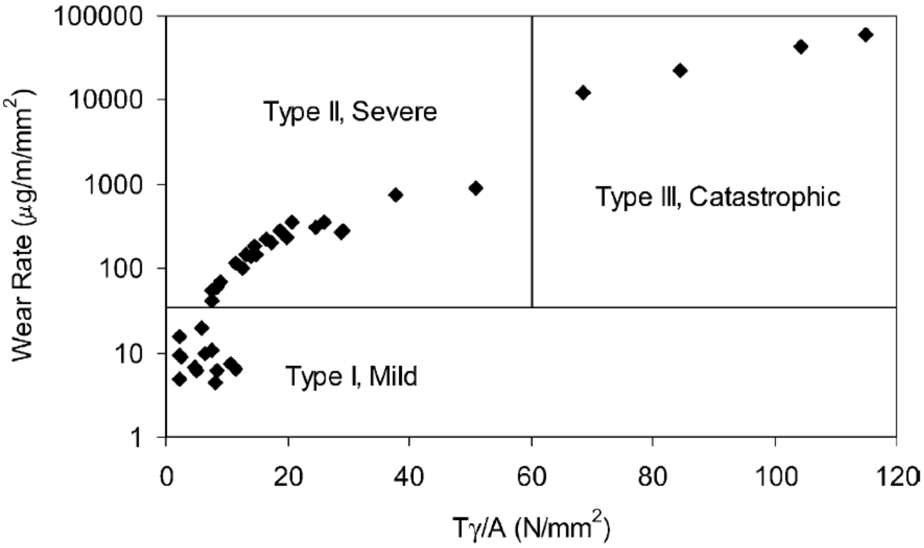

Figure 2-30 Wear regimes identified during twin disc testing of BS11 rail material vs. Class D tyre material [98].

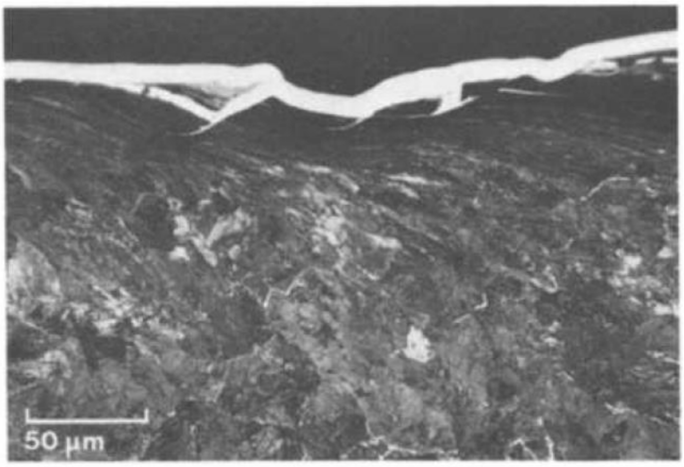

Figure 2-31 Optical micrograph of a longitudinal section through severe wear regime [97].

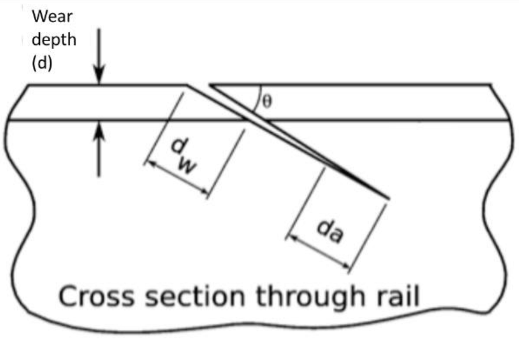

Figure 2-32 Schematic of wear process and development of surface breaking crack that happened at the same time. Net crack growth rate equals to crack tip advance rate (da) minus wear depth (dw) [91].

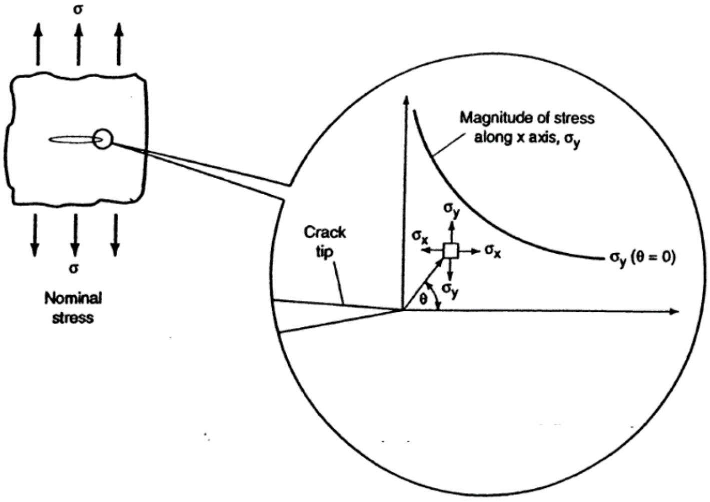

Figure 2-33 Distribution of stress near the crack tip of thin plate with an elliptical crack [108]

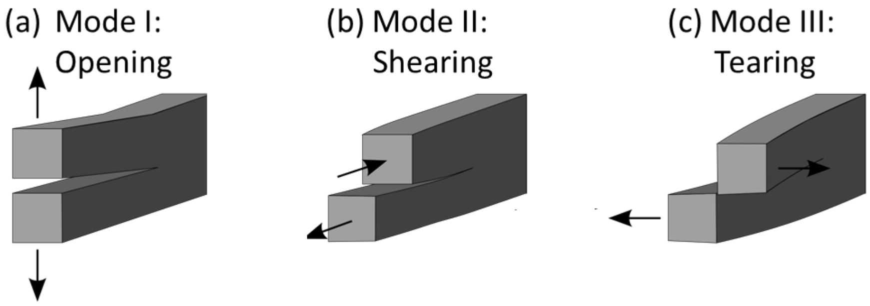

Figure 2-34 Fracture mechanics mode of failure. (a) Mode I – Opening mode. (b) Mode II – Shearing mode. (c) Mode III – Tearing mode.

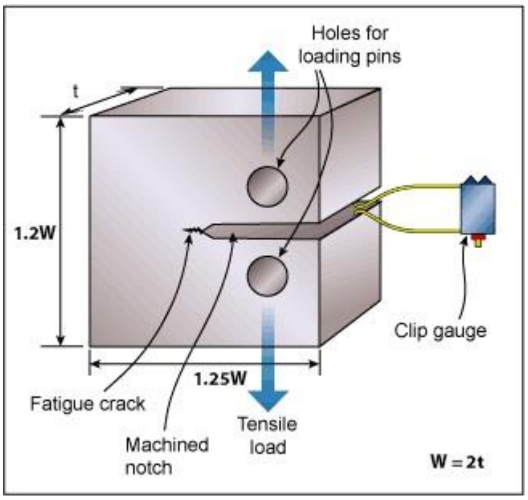

Figure 2-35 The conventional compact tension specimen [134].

CHAPTER 3

SQUAT TYPE DEFECTS: PHYSICAL EVIDENCE

3.0 Introduction

This chapter discusses several findings from an investigation of squat type defects in rails which involve visual observation and metallographical analysis that was undertaken in the preliminary stage of the research. The key features of the squat type defects that were reported elsewhere will also be discussed in this chapter to highlight the similarities between the author's experience and those of others.

3.1 Investigation of squat type defect in rail

Following ultrasonic detection of a rail defect in 2013, a rail with an approximate length of 600 mm was removed from mixed traffic line in Switzerland. The defects occurred in the open where the nearest signal is at least 5 km from the location of the defects. According to the records of Swiss Federal Railways (SBB), the line carries vehicles with Thyrister-controlled (AC traction) at speeds between 120-200 km/h. The rail was installed in 2002 and was re-profiled twice in 2004 and 2005. Following its removal, the rail was brought to the University of Sheffield for further investigation in which the author performed a series of investigation that involved visual observations and metallographical analysis. The purpose of this investigation was to extract information on what caused the ultrasonic detection and examined any additional defects to understand the cause of the damage.

3.1.1 Visual observation

Closer observation in the area of the ultrasonically detected defect revealed that the main defect (with the widening of the running band) was adjacent to two other surface breaking cracks (with a spacing between 40-50 mm from the main defect). The defects were referred to as defects A, B, and C which correspond to 195 mm, 245 mm and 285 mm respectively as shown in the scale of Figure 3-1. Pitting was observed scattered along the rail surface especially around the area where defects were located and multiple fine lateral cracks can be seen clearly on the gauge side of the running band.

Looking at individual defects, Figure 3-2 shows the main defect (defect A) in detail. Crack mouths were present at two different locations, Point X (centre of defect A depression) and Point Y (close to gauge corner). Detail observation of defect B revealed the formation of surface depression which was longitudinally aligned with defect A and defect C (Figure 3-3). Several small surface indentations and distinct crack mouth were observed, contained within the shallow depression. Defect C is shown in detail (Figure 3-4) where a surface ‘flap’ of material with pitting in the centre was formed on the rail surface. No surface depression was observed within defect C. From the observations, it was concluded at this point that the main defect (defect A) closely resembles a squat type defect due to the formation of surface depression, surface crack, and widening of the running band.

A nital etch solution (2% nitric acid in ethanol) was applied on the rail surface to identify the formation of white etching layer (WEL) on the rail surface especially around the area where defects were located. Nital etch solution will cause the pearlitic rail steel to turn dark in colour, whereas martensite (WEL) shows as white under natural light. The application of nital on the rail surface revealed that most of the running band area remained shiny (Figure 3-5) suggesting the presence of WEL on the rail surface.

3.1.2 Metallographic analysis

Since all three defects (A-C) lie on a longitudinal plane throughout the rail and can be viewed on a single sample, the rail was sectioned longitudinally to examine its internal geometry. An electrical discharge machining (EDM) wire cut machine was used to section the rail longitudinally to avoid excessive material loss. The rail was then divided into 3 samples where each sample contained cracks in the longitudinal plane as shown in Figure 3-6. Sample B and C were sectioned laterally to get more accurate details of the geometry along the lateral plane, while sample A was broken open to reveal the crack faces inside the defect. This will not affect the existing crack because brittle fracture will occur once the sample was broken open and has a different texture with fatigue fracture (existing crack). This was achieved by soaking Sample A in liquid nitrogen to make it brittle, followed by loading under a 3 point bend configuration. All of the samples were ground, polished to a 1 micron diamond paste finish, and etched with 2% nital for microstructural analysis. The crack morphology of any cracks observed was mapped, and the microstructure was examined to look for plastic flow and martensite formation (indicated by white etching layer on the rail surface).

The longitudinal cross sections revealed horizontal subsurface cracks with several branches on leading and trailing edge for sample A and B, while sample C contained two separate surface breaking cracks. Below the surface of the main defect (defect A), subsurface cracks of approximately 24 mm tip to tip with a maximum distance of approximately 4 mm from the rail surface were observed. The subsurface crack was initiated from a large void (2.9 mm long by 0.9 mm deep) that was located approximately 2 mm below the rail surface (Figure 3-7). Etching all the polished samples revealed the microstructure of the pearlite steel where the presence of WEL with different length and thickness was observed to have formed on the rail surface. The location of WEL for each defect (A, B, and C) is shown in Figure 3-8 to Figure 3-10 represented by the white dash line in each figure. Figure 3-11 shows the thickest WEL formed on the surface of sample A. Based on the deformation of the pearlitic microstructure on the surface, very little plastic deformation was observed in the upper 5 µm of the rail for all of the samples. The minor distortion (Figure 3-12) is less severe than ratchetting strain accumulation mechanism that is responsible for initiation of RCF crack. Results from longitudinal metallographic analysis are summarized in Table 3-1.

Lateral cross section of sample B (denoted by sample B2 in Figure 3-6) revealed 2 surface cracks as shown in Figure 3-13 and Figure 3-14, where the crack on the right hand side is connected with longitudinal crack in sample B. In addition, a small surface crack can be seen near the gauge side (Figure 3-13) which is thought to be the gauge corner cracks (fine lateral cracks) that were scattered along the rail on the gauge face as described in Section 3.1.1. Several patches of white etching layer were observed lying on the gauge side and above the major surface cracks. For sample C (denoted by sample C2), no crack was observed that can be related to the two surface cracks that were observed from longitudinal cross section (sample C). Several patches of white etching layer have been spotted mostly around gauge side as shown in Figure 3-15.

Figure 3-16 shows sample A1 and A2 in which they were placed back together after been broken by 3 point bending test. It can be seen that fracture of sample A occurred along a path that connected the void, crack mouth X, crack mouth Y, and the subsurface crack of sample A. Several crack faces that could suggest crack growth striations can be seen lying underneath the broken surface as shown in Figure 3-17. However, there are too few for them to correspond to individual wheel passes.

3.1.3 Route for further investigation

Based on the observation made from the lateral cross section, it was uncertain whether the crack on the lateral plane (sample B2) initiated from the rail surface, or subsurface since it was hard to determine the crack initiation point. Generally for surface initiated crack, the crack normally initiated from the crack mouth, located on the surface of the rail. However, these cracks have undergone quite a lot of growth for quite a long time since they initiated and that could have wiped out / destroyed the evidence of the initiation point. If the crack initiated from the surface and grew in the transverse direction into the material, therefore lateral force due to curving effort might be responsible for the growth of the crack. However, the evidence of white etching layer lying above the major surface crack of sample B2 might suggest that the crack may initiate from a subsurface layer of the rail. Thermal stress may cause the crack to propagate towards the surface which could result in spalling of the rail surface. Therefore it would be useful to consider all component of forces (longitudinal, vertical, and lateral) in the further work to fully understand the growth pattern of squat type defects under the combination of all stresses.

3.2 Evidence elsewhere

Squat type defects were not unique to Switzerland. Incidents of squat type defects were also reported elsewhere as observed in Britain and Australia. The key features of the defects observed from these two different continents will be discussed in the following section. The work reported below solely depend from reference [1] for British experience and [3], [4], [135] for Australian experience.

3.2.1 British experience

Squat type defects were reported in London Underground in which millions of pound was spent for their removal. Multiple defects with an appearance of V-shaped surface breaking crack (Figure 3-18) existed within a short length of track, with the presence of subsurface crack detected beneath the surface breaking crack. Surface depression (with the presence of crack mouth) accompanied by a widening of the running band was observed on all major defects. It was also observed that these defect formed on the rail surface approximately in the centre of the running band, in curves and also in straight track. They mostly appeared in an open area (not in tunnels) and were potentially associated with high driving traction (ie. signal).

Longitudinal cross section from one of the samples revealed the presence of a subsurface crack with a length about 23 mm tip to tip located approximately 2 mm below the surface. Patches of WEL (with different length and thickness) were also observed lying close to the main defects. The presence of undeformed pro-eutectoid ferrite (Figure 3-19) within the WEL suggested that heat input was responsible for the formation of WEL. On some of the sample, minimal plastic flow (up to a depth of 130 µm from the rail surface) was observed and below this depth, the microstructure remained undeformed.

3.2.2 Australian experience

Similar to the British experience, Australian researcher [3] reported that squat type defects were observed on heavy haul lines associated with curves and straight track in Hunter Valley. Multiple defects with an appearance of classical squat (Figure 3-20) were present in the middle of the running band within a short length of track. Subsurface cracks with a depth of approximately 4 mm below the surface were also detected from ultrasonic scans. WEL was present in some of the samples, mostly associated with smaller defects.

In a recent investigation [4], squat type defects were also observed in a different part of Australia whereby multiple defects that resulted in rail spalling (Figure 3-21) appeared in some of the lines in New South Wales. They appeared in a location approaching a signal, whether in a curve or straight track. Most of these defects occurred in the middle of the running band with the presence of multiple fine lateral cracks (gauge corner crack) observed on the gauge corner. Crack mouths were present in most of the major defects located in the middle of the defect depression. A distinct band of WEL was also observed located close to the main defect.

3.3 Summary

The defects discussed in this chapter clearly show superficial similarities with conventional RCF squats in which formation of surface breaking cracks accompanied by surface depressions was observed for all major defects. However, results from field observation and metallographical analysis strongly highlight the differences. While the conventional RCF squat normally associated with ratchetting of the rail surface [47], metallographical results show that squat type defect occurred under very minor plastic flow.

Similar observation was also reported elsewhere whereby multiple squat type defect were reported to appear in Britain and Australia. The defects investigated in this preliminary work had similarities with the British and Australian experience such as the presence of a subsurface crack, minimal surface plastic deformation, and presence of WEL. The presence of WEL observed close to the squat type defect strongly suggest that thermal input might be responsible for initiation and propagation of this type of defect. Therefore, two configurations of these defect as shown in Figure 3-8 and Figure 3-9 will be considered in the following chapter in order to provide understanding on the effect of WEL on the growth of squat type defect in rail.

3.4 Tables and figures

Table 3-1 Results from metallographical analysis

Sample	Defect type	Total length (μm)	Thickness (μm)	Remarks
A	Subsurface crack	23332		Max depth from surface = 4.32 mm
	Void			Max depth from surface = 2.03 mm Area = 2.02 mm^2 Perimeter = 7.13 mm
	WEL 1	3366	131	
	WEL 2	18558	37	
	WEL 3	421	16	
	WEL 4	1504	43	
	WEL 5	3540	97	
	WEL 6	437	21	
	WEL 7	3524	90	
	WEL 8	2572	28	
B	Subsurface crack	7141		Max depth from surface = 1.1 mm
	WEL 1	1863	49	
	WEL 2	367	25	
	WEL 3	974	24	
	WEL 4	1715	35	
	WEL 5	711	31	
	WEL 6	658	35	
	WEL 7	1345	21	
	WEL 8	744	14	
	WEL 9	1906	19	
	WEL 10	1293	27	
	WEL 11	2314	20	
C	Surface crack R	779		Inclination angle = 24.7°
	Surface crack L	928		Inclination angle = 19°
	WEL 1	780	19	
	WEL 2	11014	101	
	WEL 3	611	27	
	WEL 4	2146	82	

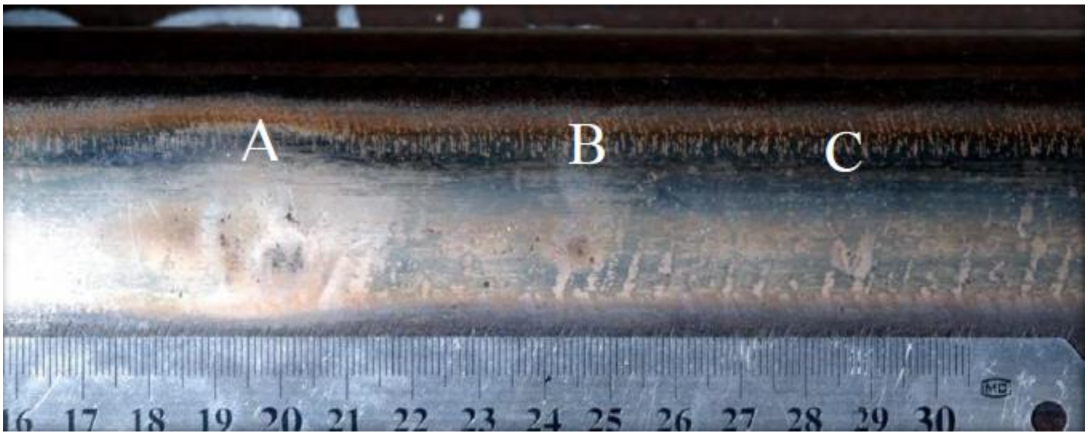

Figure 3-1 Close observation around the ultrasonically detected defect area. Gauge face at top, three defects: A (195mm), B (245mm) and C (285mm), referring to the scale in the figure.

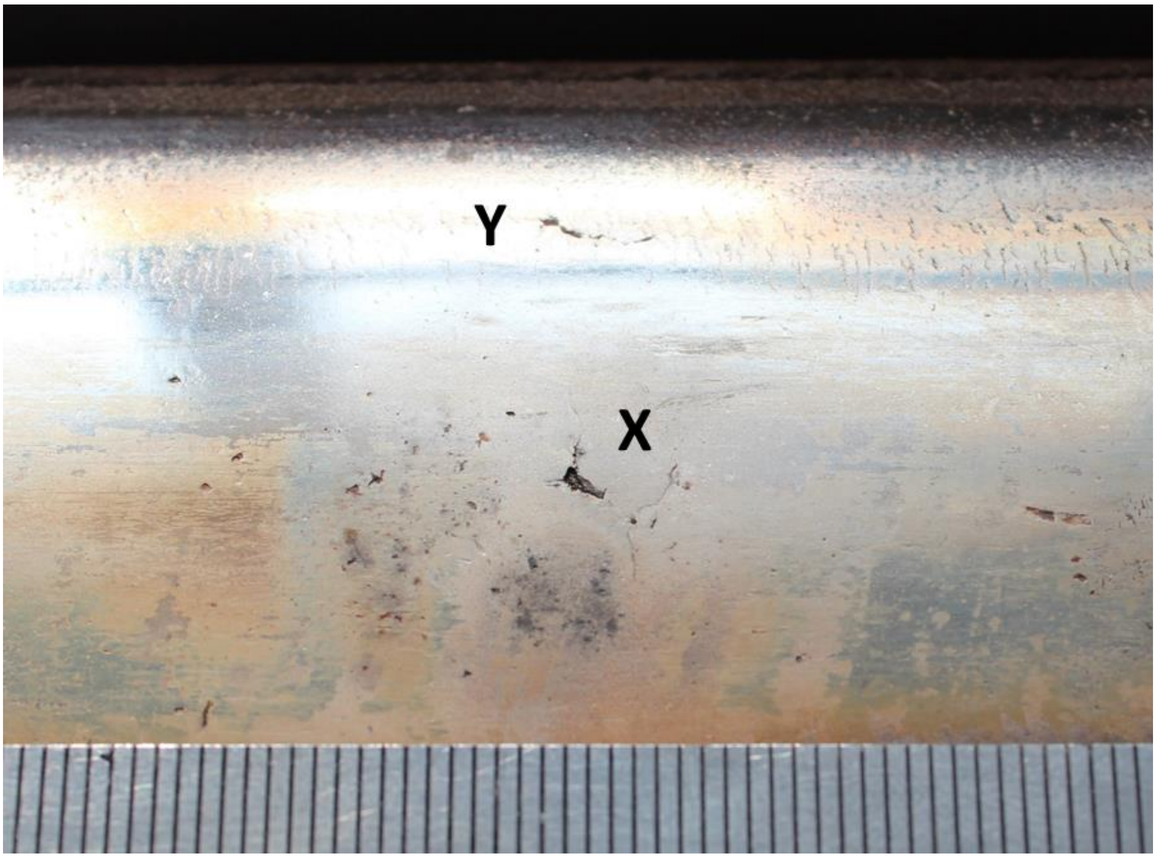

Figure 3-2 Detail observation of defect A. X and Y denotes crack mouth

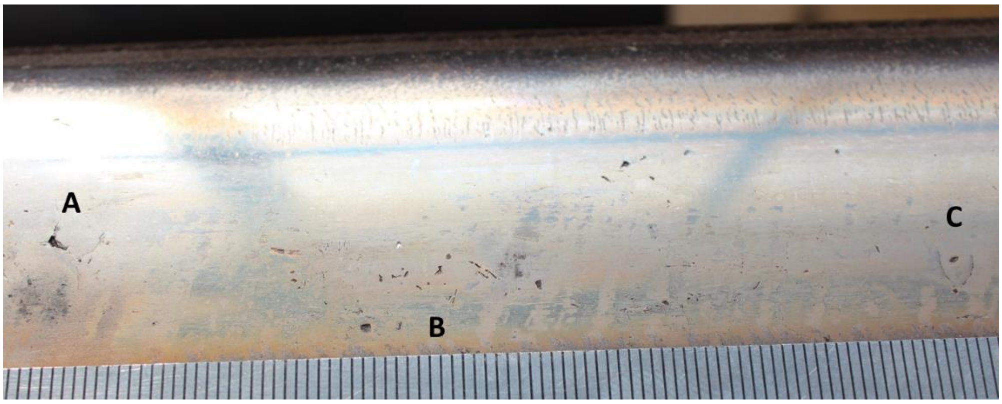

Figure 3-3 Closer observation of overall defects. Letters in the figure denote location for each defect.

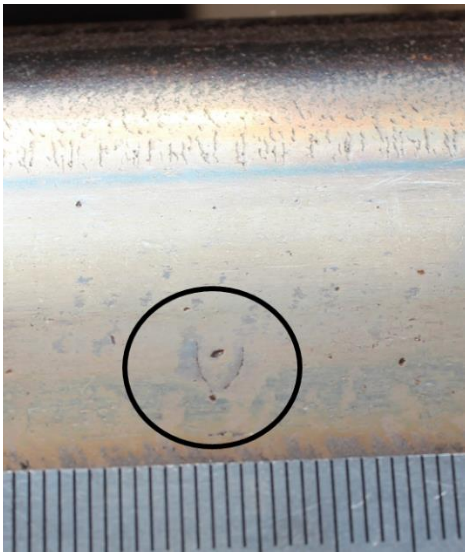

Figure 3-4 Detail observation of defect C. A small 'flap' of steel is present (circle line)

Figure 3-5 Rail surface after application of nital etch

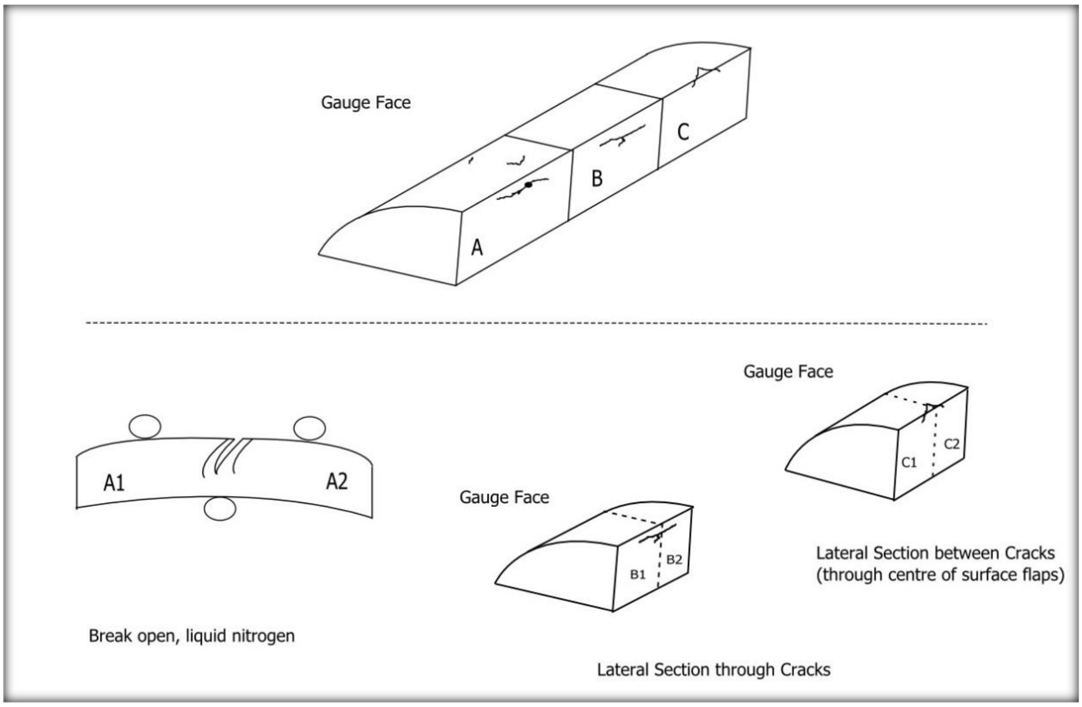

Figure 3-6 Detailed sample sectioning

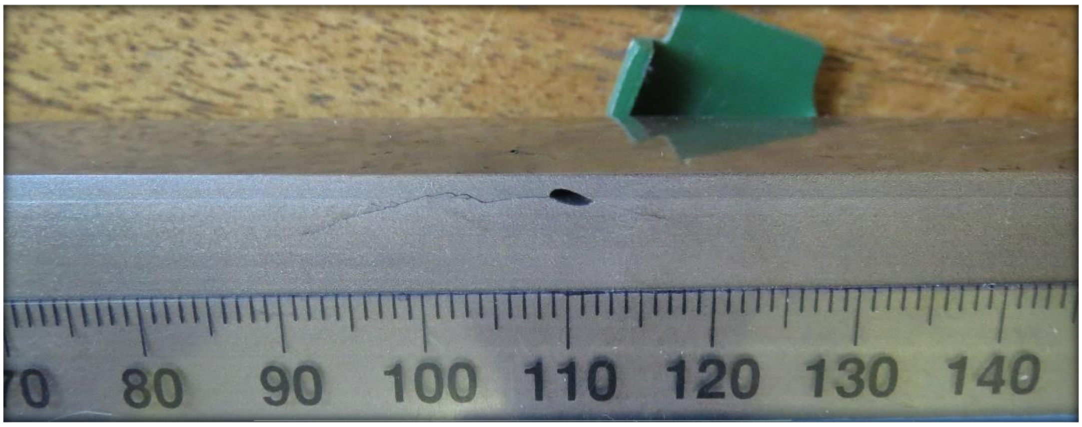

Figure 3-7 Large crack initiated from void located under main surface defect of sample A

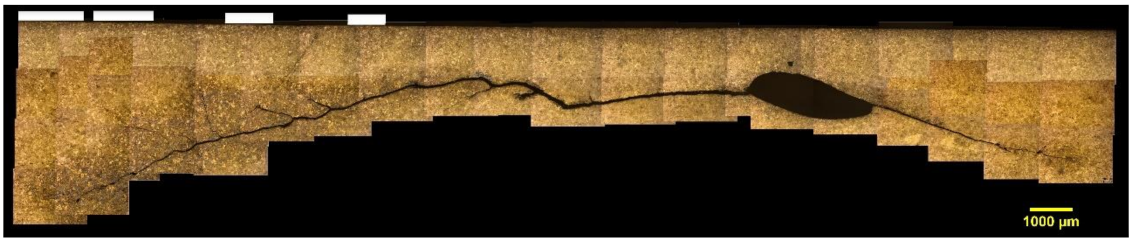

Figure 3-8 Etched longitudinal cross section for sample A. White dash near surface represent location of white etching layer

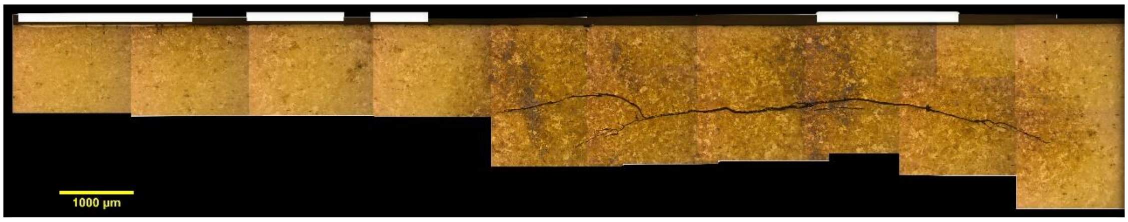

Figure 3-9 Etched longitudinal cross section for sample B. White dash near surface represent location of white etching layer

Figure 3-10 Etched longitudinal cross section for sample C. White dash near surface represent location of white etching layer

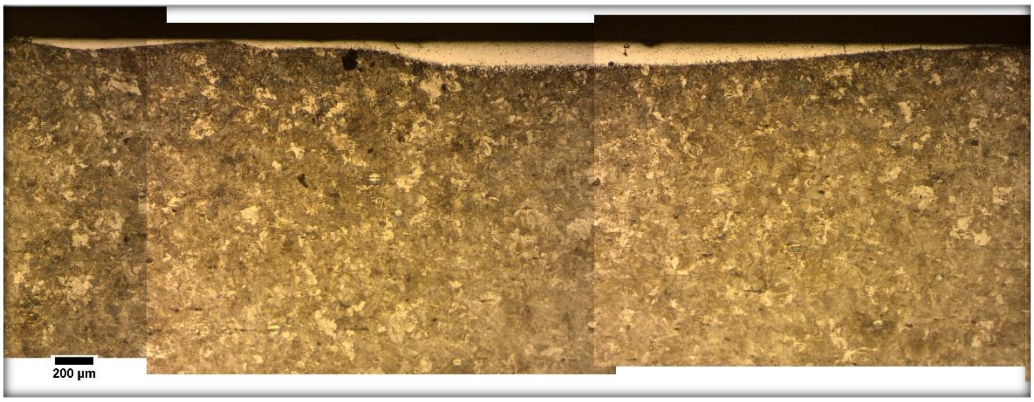

Figure 3-11 Formation of the thickest white etching layer formed on the surface of sample A.

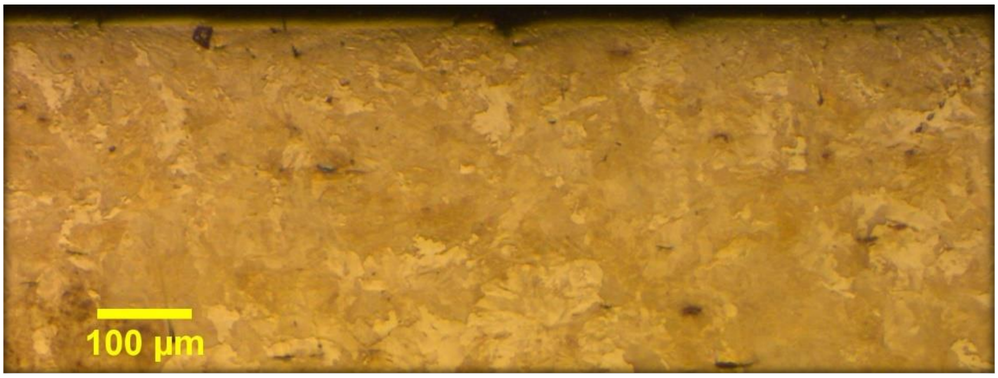

Figure 3-12 Typical observation of minor surface plastic deformation as observed on all sample. Figure show longitudinal cross section of sample B.

Figure 3-13 Lateral cross section of sample B2 White dash near surface represent the location of white etching layer. Gauge face is on the left.

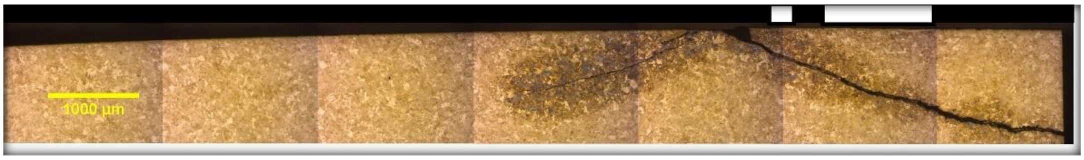

Figure 3-14 Close up on surface crack observed on sample B2. White dash near surface represents the location of white etching layer.

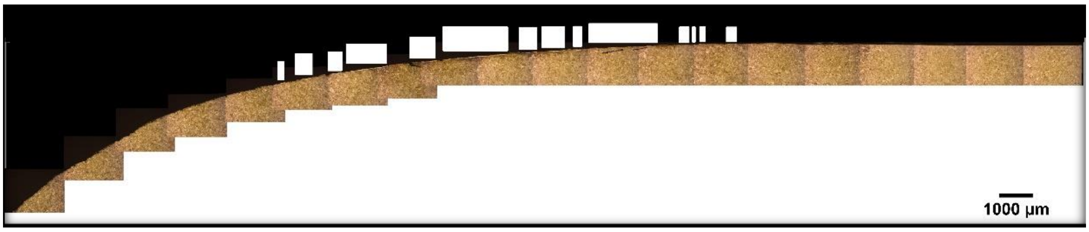

Figure 3-15 Lateral cross section of sample C2. White dash near surface represents the location of white etching layer. Gauge face is on the left.

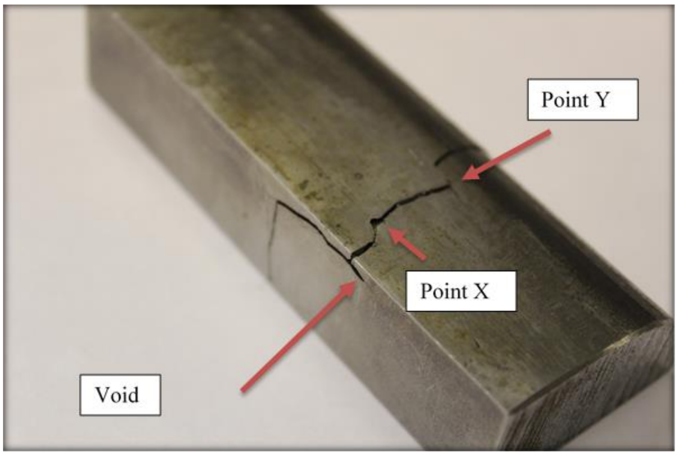

Figure 3-16 Sample A broken open by bending.

Figure 3-17 Crack faces lying underneath the surface of the broken sample A

Figure 3-18 Multiple defects appeared within a short length of track [3].

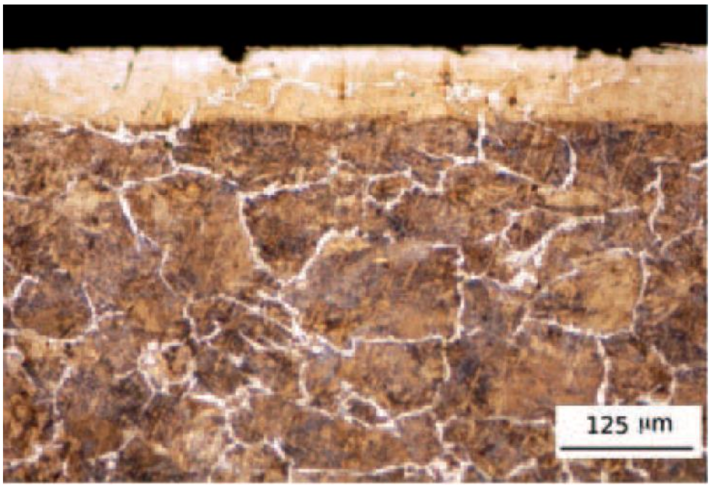

Figure 3-19 Presence of pro-eutectoid ferrite within WEL [1].

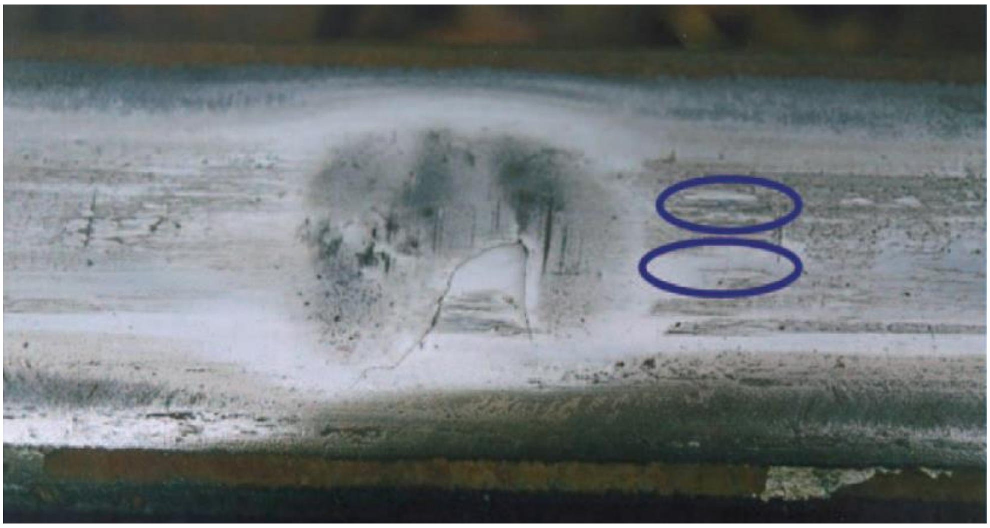

Figure 3-20 Squat type defect with an appearance of V-shaped surface breaking crack. Material such as that shown ringed appears to be WEL [3].

Figure 3-21 Squat type defect that has spalled out (delamination of rail surface) [4].

CHAPTER 4

THE POTENTIAL FOR SUPRESSING RAIL DEFECT GROWTH THROUGH TAILORING RAIL THERMO-MECHANICAL PROPERTIES

4.0 Introduction

This chapter is based on the paper with the title of "The potential for supressing rail defect growth through tailoring rail thermo-mechanical properties" [7] (see appendix) which is an extension to previous research investigating the thermal influence on crack growth in rails. The formation of white etching layer which normally associated with the presence of thermal input leads to a volume change for the steel, leaving not only a transformed microstructure, but also locked-in stress. The influence of this additional locked-in stress on the development of an initiated crack is modelled, and the work extended to consider how alternative materials which react differently to the thermal input may offer a means to suppress crack development through locking in beneficial rather than problematic stresses.

4.1 Background

In recent years, a type of rail defect named as "studs" which have superficial similarities with the squat defect have been discovered on railways and metros around the globe [84]. While the squat is normally associated with accumulation of plastic deformation on the rail surface, the stud, on the other hand, is linked to the presence of thin white etching layer (WEL) lying on the rail surface indicating evidence of severe thermal input. Study on WEL that formed on the rail surface revealed that they have martensitic structure [45] which could be formed either by repeated severe plastic deformation due to excessive mechanical work [136] or by a thermal process resulting from friction due to extreme braking and acceleration [137]. Cross sectional images from defects cut open unveil that surface plastic deformation is not present in stud defects [1], so the development of WEL due to thermal input has been investigated.

Severe thermal input has three main consequences and lasts over different durations which are:

- (i) temporary thermal expansion of the steel
- (ii) permanent metallurgical transformation of the steel to WEL
- (iii) permanent locked-in stress produced by the change of material volume associated with the metallurgical transformation.

In previous investigation [138] only additional stress due to cause (i) was considered for its effect on stress intensity factors (SIFs) describing the growth of an already initiated defect. In this chapter, the change of volume (cause iii) is brought in as additional phenomena in the modelling, opening up two routes of investigation. First, taking expansion characteristic of current rail steels undergoing transformation to WEL and examining the influence of the additional stress produced by this expansion. Second, using the same model in a design capacity to assess the most beneficial expansion (or contraction) which a heat affected area may exhibit if it is to suppress crack growth, i.e. assume that initiation of damage still occurs, how can a future rail material be created to suppress the growth of the initiated defect. Methods such as laser cladding have been proven to supress crack growth since materials that composed of better resistance properties can be coated on the railhead surface which acts as a protective barrier to combat against crack development [19], [20]. In this work, a wheel running temperature of 300 °C is considered, separate to the prior severe thermal event [139].

4.2 Modeling method and conditions

A simple two dimensional (2D) boundary element (BE) model was developed within the Beasy software package [140] to investigate the influence of the transformation of the steel to WEL on a crack that has already initiated. A single crack with different crack lengths (1 mm, 2 mm, 5 mm, 10 mm, and 15 mm) was considered where the crack is located horizontally below the contact surface at a depth of 1 mm. This configuration represents a simplified stud defect (Figure 4-1) that developed in undeformed steel. The crack sizes modelled were large relative to the microstructure dimensions, hence the model was of stress controlled crack growth, which was quantified by fracture mechanics. Microstructural anisotropy which would be important if there was extensive shear of the steel (typically affecting cracks much closer to the rail surface) was absent in the samples observed (Section 3.1.2) and therefore was not included in the model.

The 2D plane strain was assumed in the model (Figure 4-2) and a Hertzian pressure profile was used to represent the rail-wheel contact. The corresponding maximum Hertzian contact pressure of 1014 MPa with a contact half width of 5 mm was selected where the pressure and contact size correspond to a wheel of 780 mm diameter and 6.5 tonne axle load running on a UIC60 rail worn to a slightly flatter than new condition crown radius. Since the crack was embedded in the rail and would not be affected by lubrication effect, surface and crack face friction were taken as 0.3 to represent dry contact condition. Full slip case was assumed where the distribution of the shear traction, q across the contact can be described as:

$$q = fp \tag{2.28}$$

where f is the surface friction coefficient and p is the Hertzian normal load distribution. The 2D model was able to represent vertical, longitudinal, and shear stresses that characterise wheel motion in a straight track, but could not represent the lateral forces or lateral crack growth that can be significant in a curved track. This disadvantage was set against significantly lower solution times, enabling a wider range of conditions and crack sizes to be studied. Metallurgical transformation of the pearlite to martensite was simulated on a macro scale through bulk expansion or contraction of the heat affected zone, not by modelling the thermo-mechanical behaviour of the microstructure itself. The expansion depends on the specific alloy composition of the steel, with two different cases considered alongside the ‘artificial’ contraction cases used for the design study.

4.2.1 Density based calculation of volume change

The volume change of the heat affected area due to metallurgical transformation can be assesed either by density or an atomic volume based approach. To assess the change based on density, the density of pearlite was calculated by taking the density of its constituents ferrite (α iron, 7870 kg/m^3) and cementite (Fe_3C, 7700 kg/m^3) and their weight percentage, assuming a eutectoid composition steel with 0.77% carbon for which the weight fractions of ferrite to cementite are 8:1 [141]. This gives a density of pearlite with 0.77% C as 7851.1 kg/m^3, although this takes no account of the effect of other alloying elements on the density. The density of martensite is available from literature [142], although its value is sensitive to plastic deformation. This is particularly relevant to rail steel surfaces where plastic deformation of pearlite is common, although the increased hardness of martensite after transformation may protect it from further deformation. Density prior to plastic deformation [142] is 7790 kg/m^3, but may drop to 7785 kg/m^3 with 5% plastic deformation. Assuming the value for zero plastic deformation applies, the change from pearlite to martensite reduces density to 7790/7851.1 = 99.22% through an expansion of 0.78% in volume. The expansion would be greater after plastic work. A value of 0.8% is used in Table 4-1 to capture this process.

Looking at minor microstructural constituents (in addition to iron + carbon), determination of the density value for multicomponent steels was depended on the composition of the material. Miettinen has determined the density of different grade of steel with different nominal composition in weight percentage as shown in Table 4-2 [143] where it was found that different composition leads to a different value of density. For AISI 304 and AISI 316, the only difference on the composition is just a minor changes of the percentage of Chromium, Molybdenum, and Nickel (between 1% to 3%) which results in a difference density value of 52 kg/m^3. Eventhough the differences on the value of density seems small, it seems to be significant if the volume expansion of the material is considered. Considering the changes from pearlite to martensite in Table 4-2, the volume expansion for AISI 304 is 1.5% and 2.2% for AISI 316 steel. This shows that even a minor changes in the composition of the material will result in a significant effect on the volume expansion. Therefore the case of 0.8% expansion modelled in this chapter should be taken just as an example to illustrate the principles.

4.2.2 Atomic volume change approach

An alternative to the bulk density based approach is to use atomic volume data for steel microstructures in Table 4-3 [144]. Taking carbon as a weight percentage (C) and atomic volume in Angstroms cubed, values are pearlite (11.916), austenite (11.401 + 0.329C), and martensite (11.789 + 0.37C). Considering a carbon fraction of 0.77% this indicates a change of atomic volume from 11.916 Å^3 and 12.0739 Å^3 with the transformation from pearlite to martensite i.e. a volume expansion of just over 1.3%. To assess the accuracy of the results, data from Table 4-3 was used to calculate the volume changes from austenite to martensite. From the literature data, it was found that the transformation from austenite to martensite results to a volume expansion between 3%-4%. Using similar approach, the change from austenite to martensite is predicted to give an atomic volume increase of around 3.6% which is in good agreement with finding from [145]. A value of 1.3% is used in Table 4-1 to capture this approach for the pearlite to martensite volume change.

4.2.3 Implementation of volume change in modelling

The exact value of volume change with transformation will depend on the steel chemistry, and also the exact thermal path taken as the steel is heated and cooled, but the methods outlined above gave a reasonable range for which modelling could be conducted to investigate the effect on cracks in a rail. To represent the expansion and contraction through the transformation of a surface layer in the BE model, a thermal body load was applied to the whole of the transformed layer (confined from the zone definition within BEASY, regardless of contact size or position) using a temperature calculated to achieve the required volumetric expansion [146]:

$$\Delta V/Vo = 3\alpha\Delta T \tag{2.29}$$

where $\Delta V/V0$ is the volume change ratio, α is the thermal linear expansion coefficient for the material and ΔT is the temperature difference. It should be noted that this is simply a convenient way to implement expansion or contraction within an existing structure without modelling microstructural change or applying a mechanical load. It is an artificial temperature value (230 °C for 0.8% expansion and 353 °C for 1.3% expansion), distinct from the thermal boundary condition applied to represent the passing of a hot wheel over the rail with which it is combined using superposition.

For the case with a rail–wheel contact temperature rise, it was assumed that the rail surface was heated in the wheel contact area, and was elsewhere at 20 °C. This was intended to simulate ‘flash’ heating of the rail surface followed by rapid cooling as the contact moves away. The properties of the rail steel (generic value of steel and have been used throughout the model irrespective of the transformation) were Young's modulus, 210 GPa, Poisson's ratio, 0.3, and thermal linear expansion coefficient of 13 μm/mK. To identify the peak and range of stress intensity factors during the passage of a wheel, contact positions at 2.5 mm increments were examined up to 15 mm either side of the crack centre. No crack growth rate law exists specific to the loading and cracks configuration used in the current investigation. Therefore, indicative crack growth rates were calculated using the lower bound method developed for inclined surface breaking cracks in rail steel [80]:

$$\frac{da}{dN} = 0.000614\left(\Delta K_{eq}^{3.21} - 4^{3.21}\right) \text{ nm per cycle} \tag{2.30}$$

where da/dN is the crack growth rate and ΔK_{eq} is the equivalent stress intensity factor. Although the crack configuration differs, this growth law was generated using a normal grade rail steel and there is a similarity in the combination of mode I and II loading for a crack under compression. A more specific growth law for modern rail steels would be a useful area of future research.

4.3 Results and discussion

All the cases listed in Table 4-1 were investigated for a 1 mm crack length to examine a crack which has already initiated but not yet grown significantly. Modelling was also performed for a range of crack lengths from 2 to 15 mm but for the economy of modelling these cases exclude conditions 4 and 5 (1.3% expansion due to transformation) since trends are visible from the baseline case and for 0.8% expansion cases. For each condition modelled the range of stress intensity factor was assessed by considering the movement of a wheel incrementally across the crack (Figure 4-3), generating a series of SIFs. The combined action of traction and normal stress is indicated in the figure, and results in asymmetry of the results for left and right crack tips. Results are presented as stress intensity factors in Figure 4-4 to Figure 4-6, in which the origin is at the centre of the crack, hence crack tips will lie to the left or right of the origin according to crack size. Stress intensity factors are converted to indicative crack growth rates shown in Figure 4-7. As an addition to the SIF data, Table 4-4 shows stress calculated for a point 1 mm below the centre of the contact and white etching layer region, but without a crack present. This indicates that thermal expansion is particularly influential on longitudinal stress, and to a lesser extent on lateral stress, while metallurgical transformation has a strong influence on longitudinal and vertical stress on the rail. These stresses are for just a single location, and it is their combination throughout the rail during the passage of the wheel that determines the SIFs for each case considered.

4.3.1 Stress intensity factor dependence on crack size

Figure 4-4 shows the trends observed in K_I and K_{II} values for the left and right crack tips. These plots are for condition 1 (no expansion/contraction, no thermal input). For the left crack tip (Figure 4-4a), K_I shows a rise with increasing crack size, but is small even for a 15 mm crack. For comparison, a threshold stress intensity factor of 6 MPa $m^{1/2}$ for the tensile growth of cracks in carbon steel is available from Otsuka et al. [121] and has been applied in previous work on crack growth in rail steel [111], [147]. The mode II data for the left crack tip (Figure 4-4b) shows much larger stress intensity factor values, but a low sensitivity to crack size of the total SIF range during the passage of the contact. The values for shear mode growth comfortably exceed the 1.5 MPa $m^{1/2}$ shear mode threshold given by Otsuka et al. [121], so crack growth would be expected.

At the right crack tip, both mode I and II SIF ranges show rising trends with increasing crack size (Figure 4-4c and d). The mode I values are very small, but the mode II values are comfortably above the threshold. Assuming applicability of the crack growth law previously developed for inclined surface breaking cracks, Figure 4-7 and Table 4-5 show the outcome of mixed mode growth. There is a plateau in growth rate with increasing crack size for the left tip, but raising rates with increasing size at the right tip. This reflects similar trends in peak mode II SIF with increasing crack size for the left and right cracks (Figure 4-4b and d) and its strong influence over predicted crack growth rate. In crack growth for inclined surface breaking cracks, it is thought that a small mode I crack opening stress (even if itself below threshold) can “unlock” mode II growth through helping to overcome crack face friction [54]. In the current results, high values of mode II are predicted even with almost zero K_I at the right tip, although larger K_I values are predicted at the left. This may influence the tendency of the right side crack to branch (the usual mode II growth behaviour), whereas prolonged co-planar growth may be possible with the higher mode I level at the left tip. This is an aspect of the growth which requires further investigation, to better understand if and how the inclined surface breaking crack behaviour translates to these horizontally embedded cracks, and how they branch and propagate.

4.3.2 Effect of expansion and contraction of a thin surface layer

Figure 4-5 shows the effect on mode I and II stress intensity factor of expansion or contraction of a surface layer due to metallurgical transformation, focusing on the left crack tip of 1 mm crack length. These data were generated without additional thermal stress as the wheel passes. Results for the right crack tip and at other crack sizes exhibit similar behaviour. The baseline case 1 is also included. Values of K_I rise well above the baseline when the expansion of a thin surface layer is considered. Positive K_I values are present when the contact is absent, i.e. the crack becomes subject to a static mode I stress which is relieved as the compressive contact passes, producing a stress cycle. This is the case for the 1 mm crack which is short relative to the 2 mm transformed layer considered, but this effect diminishes as the crack exceeds the size of the transformed region. The values of K_I are low, in part because this is a small crack size, but they rise in proportion to the degree of expansion of the surface layer, representing possible reactions of different steel metallurgies (case 2 and 4, 0.8% and 1.3% expansion respectively). For the case of a 0.8% contraction of the surface layer (case 6) K_I is maintained at zero whatever the contact position.

For mode II under the same conditions, moderate changes take place in the peak values determining stress intensity factor range during the passage of the contact, but the overall form of the curves is similar for all cases. Inset graphs (Figure 4-5b) enable the order of the peak values to be identified. It can be seen that expansion of the surface layer increases the magnitude of both positive and negative peaks (dependent also on the level of expansion). Furthermore, contraction of the surface layer reduces the peak magnitudes, and hence the stress intensity factor range. Although the number of contact positions examined is limited, the relative size of the contact and crack mean the peak position is known in advance and can be accurately captured. The ranges can be seen numerically in Table 4-6. The changes are small, but when converted to crack growth rates (assuming applicability of the crack growth law), they raise or lower the crack growth rate relative to the baseline case across the range of the crack sizes investigated, as indicated in Figure 4-7 and Table 4-5.

4.3.3 Effect of thermal input from passing wheels

Figure 4-6 shows a selection of cases to highlight the effect of additional thermal input from warm wheels passing a site of previous thermal damage with metallurgical transformation. Expansion and contraction by 0.8% are considered, but the 1.3% cases are excluded from the plot for clarity. From Figure 4-6a for mode I, it can be seen that the thermal input considered (dashed lines) makes insignificant changes to the stress intensity factor. The behaviour is dominated by the effect of metallurgical expansion relative to the base case (producing a rise in K_I values), or contraction (for which K_I is maintained at zero). As discussed above, the values of K_I are all very small, but it is the trends that are of significance.

For K_{II} (Figure 4-6b) the overall form of the curves for variation of stress intensity factor during the passage of the contact is insensitive to the differences between cases with and without additional thermal input. Dashed lines in the plot represent the cases with additional thermal input. At negative contact positions, there is some sensitivity of K_{II} to thermal input. At positive contact positions, there is almost no effect from the thermal input, with K_{II} for metallurgical expansion or contraction cases being above or below baseline values irrespective of the additional thermal input.

The effect of thermal input on SIF range is shown numerically in Table 4-6. For both metallurgical expansion (cases 2, 3) and contraction (cases 6, 7) the trend emerges that thermal input produces (i) minor or no change in ΔK_I, and (ii) an increase in ΔK_{II}. The crack growth predictions (Figure 4-7) show that a contracting microstructure is beneficial in suppressing crack growth (growth rate in case 6 is close to or reduced below the baseline case). However, this benefit is negated by surface heating from a warm wheel (case 7) for all but very small cracks which are wholly below the 2 mm wide transformed expansion/contraction region. For an expanding microstructure (case 2) the crack growth rate is always above the baseline case, and is made even higher when a warm wheel is considered (case 3).

4.3.4 Microstructure design

The work here has considered a range of crack sizes at 1 mm below the surface, and indicates suppression of crack growth is possible if metallurgical transformation through thermal input produces contraction rather than expansion of the microstructure (considering this separately from temporary thermal expansion). This indicates it would be beneficial to study steel chemistry that can achieve this behaviour, or to undertake tests on a range of existing rail steels to see if some types already have this beneficial property. Beyond comparison of crack growth predictions with the physical evidence for existing rail defects (Figure 4-1), validation depends on identifying such a material, and developing a crack growth law specific to mixed mode non inclined subsurface cracks. When considering new rail coating technologies [20] there is also the possibility of choosing a coating with this crack suppressing property. Even if contraction cannot be achieved, there would be benefit in selecting steel metallurgy able to reduce levels of expansion when the metallurgical transformation takes place following thermal input. In further work a crack closer to the surface should be considered to understand the very earliest stage in the growth of a defect near thermal damage, and whether there is a prospect of “designing out” growth of cracks from this damage type.

4.4 Summary

Evidence of severe thermal loading (white etching layer, WEL) is often associated with rail defects. Severe thermal input has three main consequences, which last over different durations: (i) temporary thermal expansion of the steel, (ii) permanent metallurgical transformation of the steel to WEL, and (iii) permanent locked-in stress produced by the change of material volume associated with the metallurgical transformation. The modelling focuses on area (iii) and predicts that WEL can accelerate the growth of cracks below it through locked in stress due to the metallurgical transformation from pearlite to martensite which causes a local increase in the volume of the rail steel. Conversely, taking a hypothetical case in which thermal damage leads to a permanent contraction of the steel microstructure it is predicted that crack growth rate can be reduced. The changes predicted in crack growth rate are small, but point to the interesting possibility that if a material (new steel chemistry or a clad layer of a non-steel material) were to contract locally in response to thermal damage it could suppress any subsequent crack growth close to this damage, or at the interface between the clad layer/ repair and the underlying rail which is a crucial position prone to defects. Validation against physical samples depends on the creation of a suitable rail surface material offering contraction in response to thermal transformation. This, along with investigation to better understand if and how existing understanding of inclined surface breaking crack behaviour translates to horizontally embedded cracks, is recommended as the subject of future research.

4.5 Tables and figures

Table 4-1 Conditions modelled

Case	Expansion due to transformation (%)	Rail-wheel contact temperature rise (°C)
1	0	0
2	0.8	0
3	0.8	300
4	1.3	0
5	1.3	300
6	-0.8	0
7	-0.8	300

Table 4-2 Density value of different steel grade

Steel Grade	Nominal Compositions (in weight percent)							Density at 25°C (kg/m3)
	C	Si	Mn	Cr	Mo	Ni	N	
AISI 1016	0.16	0.3	0.8	-	-	-	-	7846
AISI 304	0.04	0.5	1.5	18	0.3	9.2	0.04	7912
AISI 316	0.04	0.5	1.5	17	2.6	12	0.04	7964

Table 4-3 Atomic volume of different microstructure constituents of ferrous alloys [144]

Phase	Apparent atomic volume, Å3
Ferrite	11.789
Cementite	12.769
Ferrite + carbides	11.786 + 0.163C
Pearlite	11.916
Austenite	11.401 + 0.329C
Martensite	11.789 + 0.37C

Table 4-4 Stress (MPa) at 1mm from the rail surface, centrally below the contact and transformed layer.

Case	Longitudinal	Vertical	Lateral	Shear
1	-661.2	-995.6	-497.0	-209.1
2	-632.8	-968.7	-480.5	-212.5
3	-604.4	-965.1	-470.8	-213.2
6	-688.9	-1022.0	-513.2	-205.7
7	-660.4	-1018.0	-503.6	-206.5

Table 4-5 Crack growth rates (nm/cycle) for all the cases and sizes of crack modelled

Case	**1 mm**		**2 mm**		**5 mm**		**10 mm**		**15 mm**	
	L	**R**	**L**	**R**	**L**	**R**	**L**	**R**	**L**	**R**
1	3.0	3.4	4.1	3.2	5.9	4.7	5.6	7.4	5.1	8.0
2	3.8	4.2	5.6	3.7	8.3	4.8	9.6	8.3	9.9	9.0
3	4.1	4.7	7.4	5.2	10.7	6.7	10.8	10.1	11.6	11.0
4	4.5	4.8	-	-	-	-	-	-	-	-
5	4.5	5.0	-	-	-	-	-	-	-	-
6	2.4	2.8	3.4	2.7	5.7	4.7	5.3	7.4	4.9	7.9
7	2.6	3.3	5.0	3.8	8.2	6.5	7.7	9.2	7.3	9.9

Table 4-6 Mode I and II stress intensity factor range for all cases modelled.

Case	**1 mm**				**2 mm**				**5 mm**				**10 mm**				**15 mm**			
	L		**R**		**L**		**R**		**L**		**R**		**L**		**R**		**L**		**R**	
	ΔK_I	**ΔK_{II}**	**ΔK_I**	**ΔK_{II}**	**ΔK_I**	**ΔK_{II}**	**ΔK_I**	**ΔK_{II}**	**ΔK_I**	**ΔK_{II}**	**ΔK_I**	**ΔK_{II}**	**ΔK_I**	**ΔK_{II}**	**ΔK_I**	**ΔK_{II}**	**ΔK_I**	**ΔK_{II}**	**ΔK_I**	**ΔK_{II}**
1	0.1	14.2	0.1	14.8	0.2	15.6	0.0	14.4	2.6	17.3	0.3	16.3	4.2	16.7	0.3	18.7	4.4	16.1	0.3	19.2
2	1.4	15.1	1.2	15.6	2.2	17.0	1.7	15.0	3.4	19.1	1.5	16.3	5.5	19.5	2.2	19.3	6.2	19.5	2.9	19.7
3	1.3	15.5	1.2	16.3	2.1	18.6	1.7	16.7	3.4	20.7	1.5	18.1	5.6	20.3	2.1	20.5	6.3	20.6	2.8	21.0
4	2.1	15.7	1.9	16.1	-	-	-	-	-	-	-	-	-	-	-	-	-	-	-	-
5	2.1	15.8	1.9	16.3	-	-	-	-	-	-	-	-	-	-	-	-	-	-	-	-
6	0.0	13.3	0.0	13.9	0.0	0.0	0.0	13.7	2.4	17.1	0.8	16.3	4.1	16.4	0.7	18.7	4.4	15.9	0.5	19.1
7	0.0	13.6	0.0	14.6	0.0	0.0	0.0	15.3	2.2	19.2	0.6	18.0	4.2	18.5	0.5	20.0	4.6	18.1	0.3	20.5

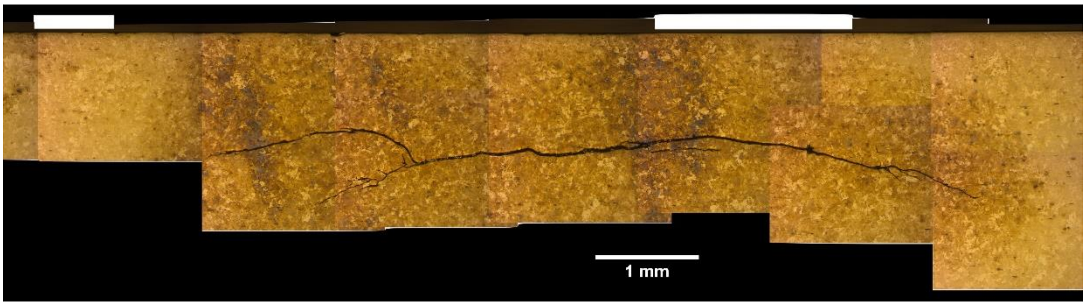

Figure 4-1 Example of "stud" defect morphology below the running band in a longitudinal cross section from a high speed mixed traffic line. The central portion of the crack is close to horizontal and lies at approximately 1 mm below the rail surface in an undeformed microstructure. The white marker above the rail surface indicates the location of a patch of white etching layer on the rail surface with a thickness around 100 µm. The surface depression and plastic deformation characteristic of a "squat" defect are absent.

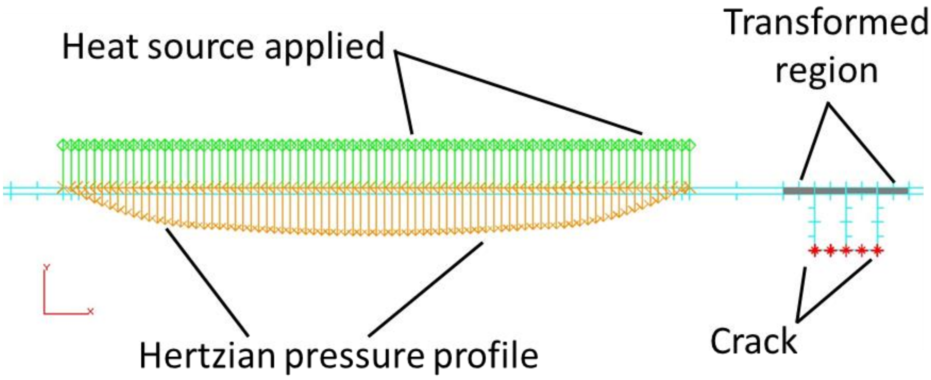

Figure 4-2 BE model of rail–wheel contact with horizontal crack of 1 mm located 1 mm below the rail surface. 2 mm length of metallurgically transformed layer with 100 µm thickness from a previous thermal event is shown grey. The heat source moves together with the contact load traversing the rail surface.

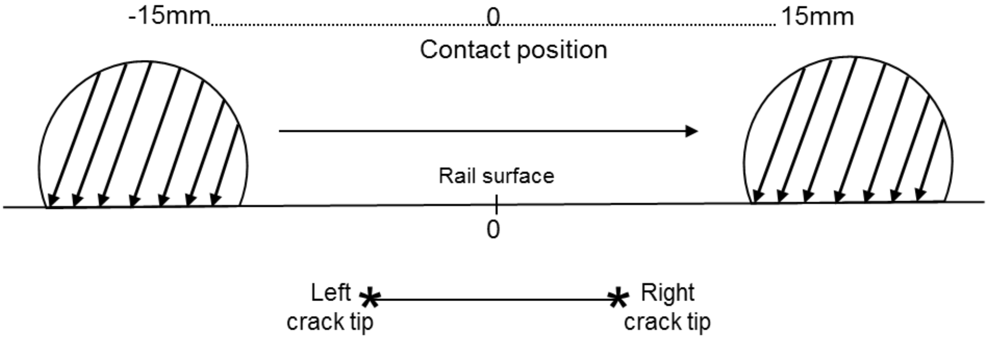

Figure 4-3 A series of analyses are performed with the incremental movement of the contact across the crack. The origin of the position is measured from the crack centre.

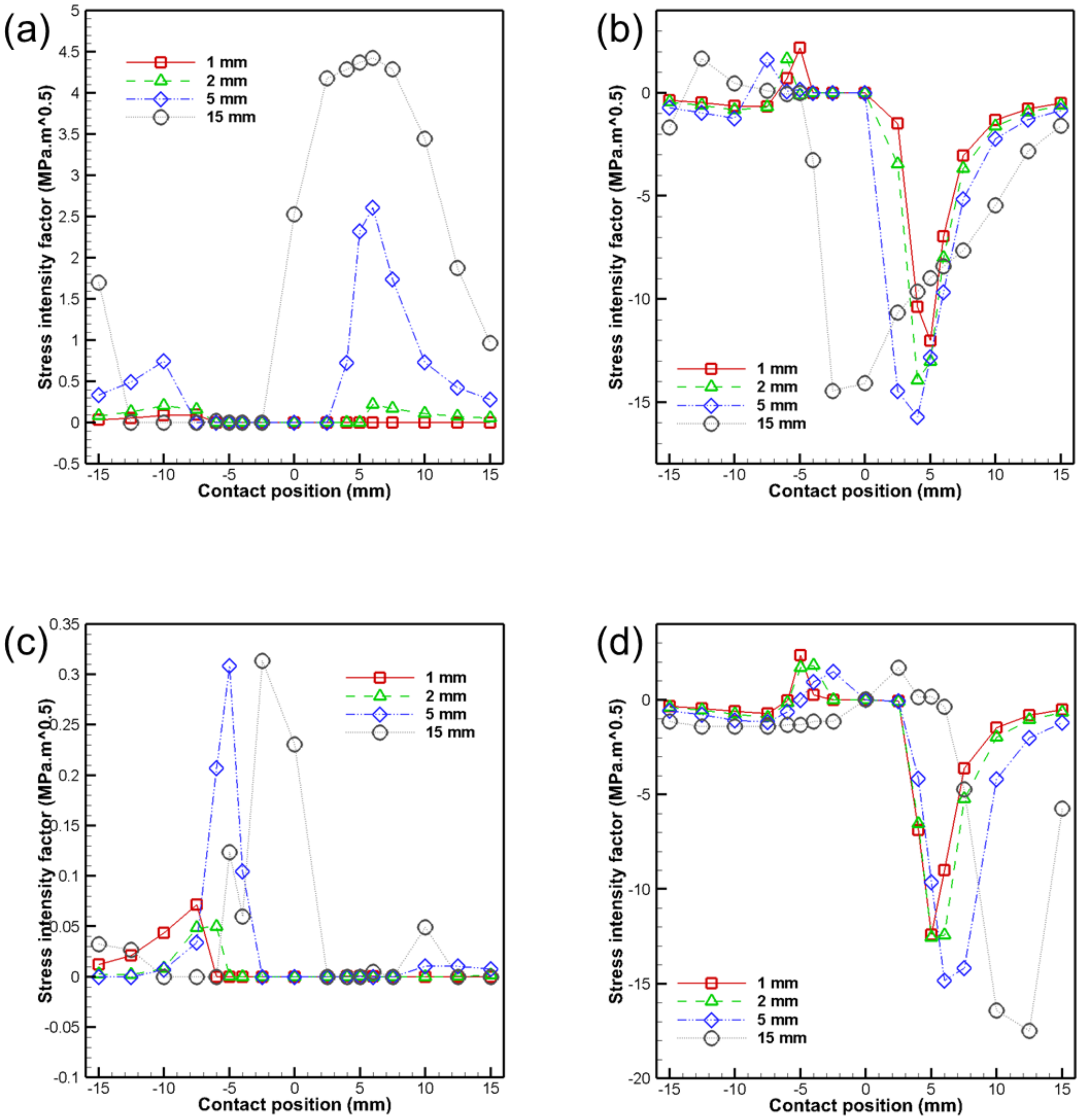

Figure 4-4 Stress intensity factor dependence on contact position. (a) left tip mode I, (b) left tip mode II, (c) right tip mode I, and (d) right tip mode II

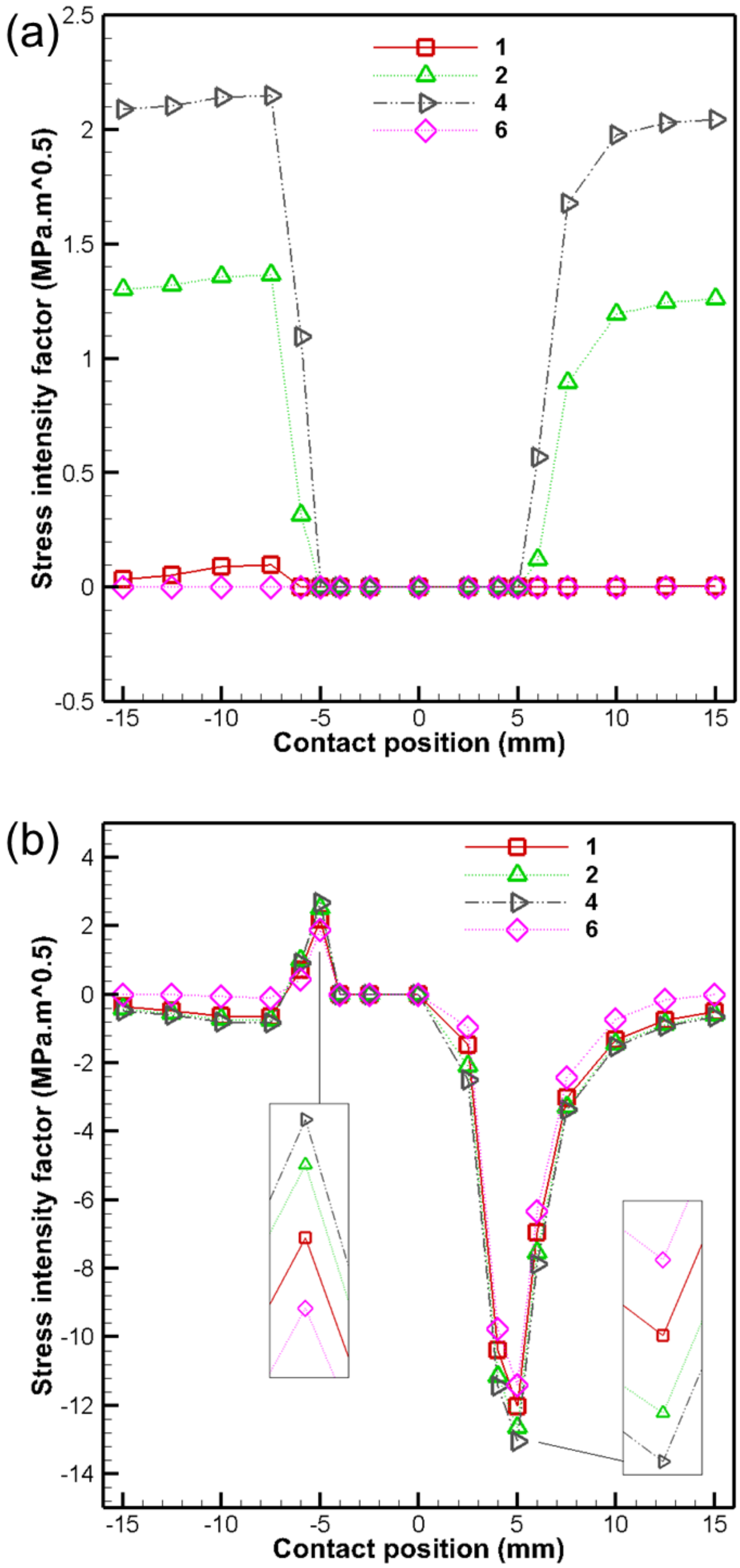

Figure 4-5 Effect of metallurgical expansion and contraction (represented as density change) on stress intensity factor for 1 mm crack, left crack tip. (a) Mode I, and (b) mode II. Legend entries refer to cases in Table 4-1

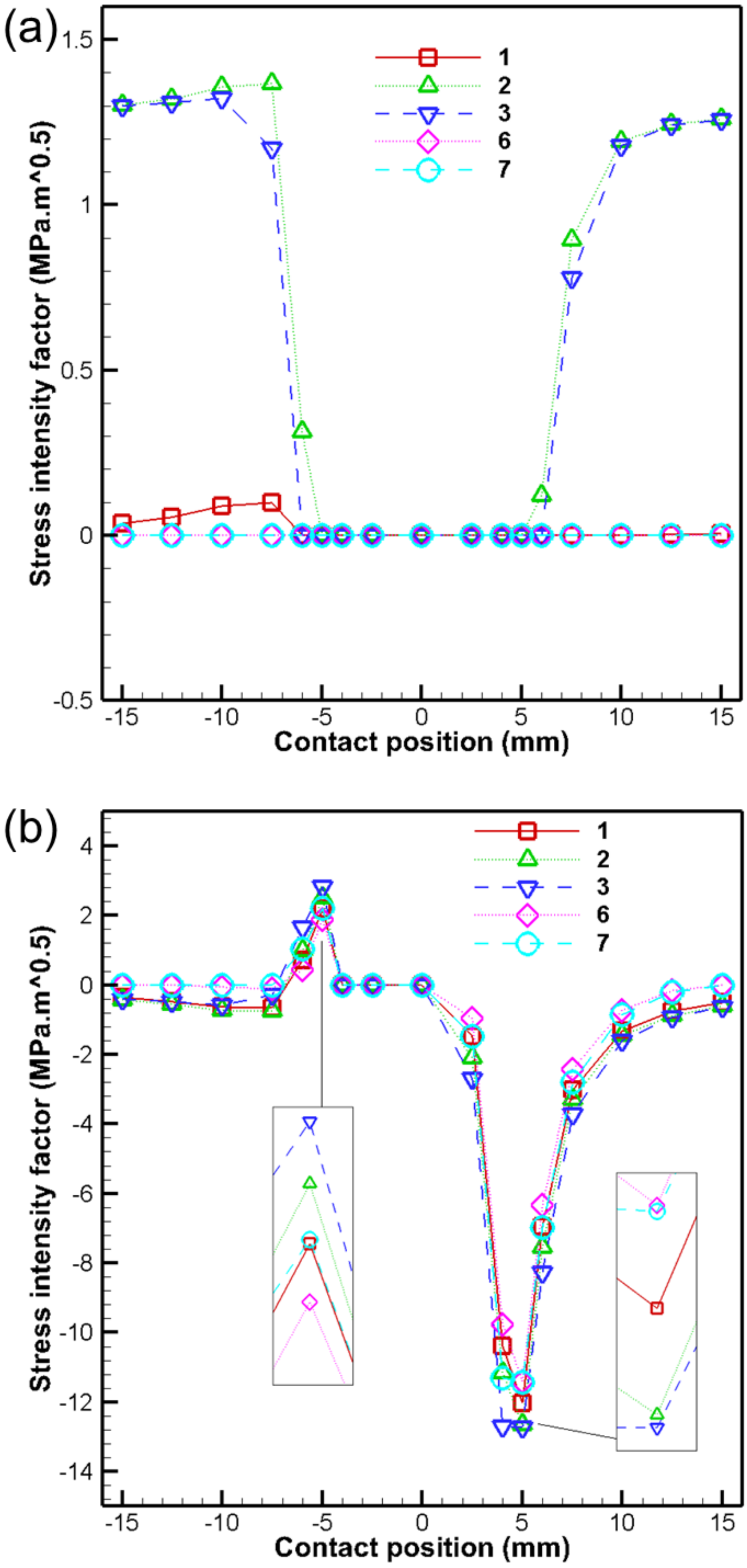

Figure 4-6 Effect of additional thermal stress (warm wheels) on stress intensity factor for 1 mm crack, left crack tip. (a) Mode I, and (b) mode II. Legend gives case number from Table 4-1.

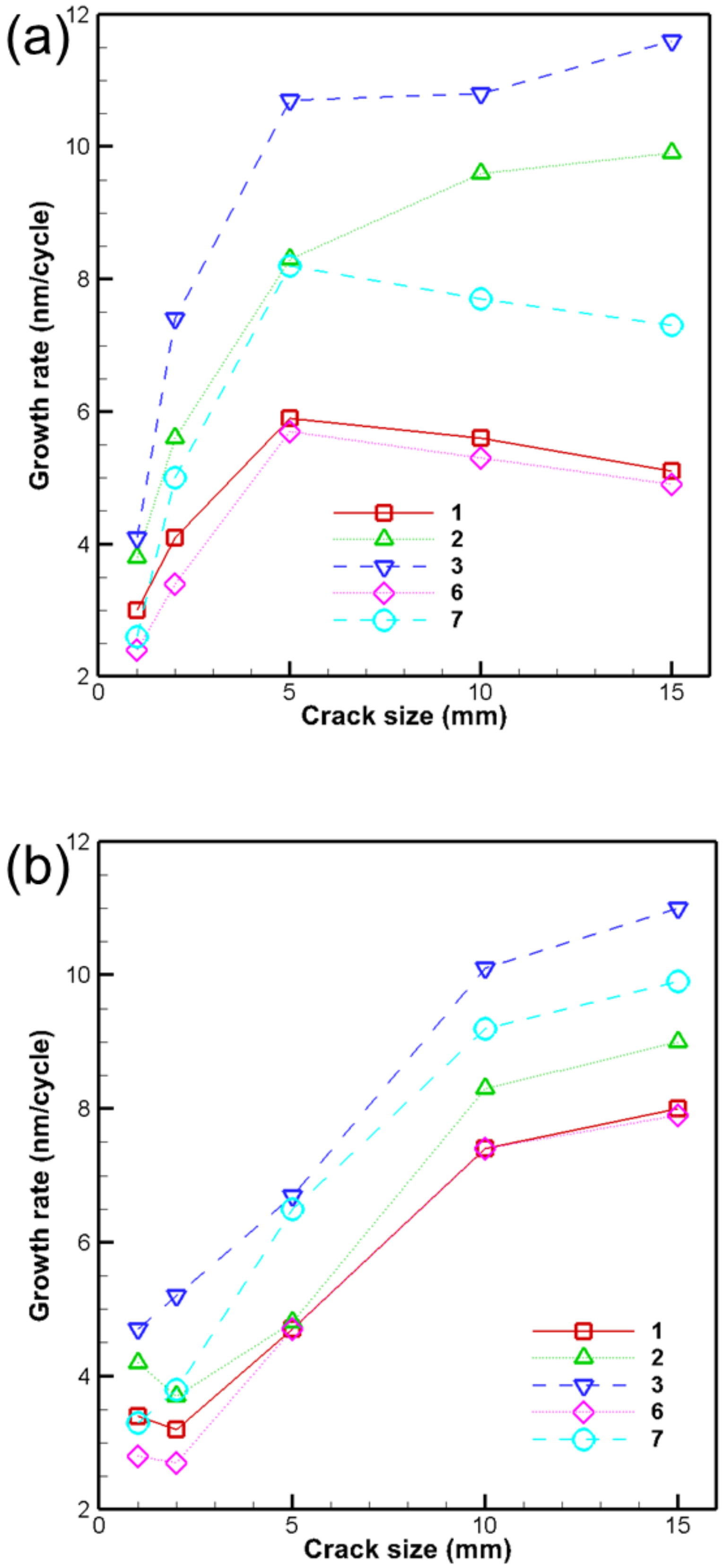

Figure 4-7 Crack growth rate dependence on crack size for cases 1, 2, 3, 6, and 7. (a) Left crack tip, and (b) right crack tip. Case 6 is equal to the baseline case 1 for cracks of 5 mm length an over.

CHAPTER 5

THE EFFECT OF WHITE ETCHING LAYER CONFIGURATION ON A LARGER RAIL DEFECT

5.0 Introduction

The formation of defects in rail is one of the main issues that affects the integrity of a rail life. Defects such as void/porosity could be formed in the rail due to improper manufacturing process, imprudent handling process, and as a result from wheel-rail contact. If they remain in the rail, potential damage process might develop which could result in catastrophic failure. In the previous chapter, it was found that the formation of the metallurgical tranformed layer above a defect can enhance the growth of a crack significantly. However, only a single configuration of the transform region was considered whereby observation from Section 3.1.2 suggest that the transformed region appeared in a different type of form (patches with different length and thickness). In this chapter, a crack that initiated from a large void was modelled to investigate the repercussion of white etching layer configuration on larger defects in rail. Different length, thickness, and arrangement of this transformed region were considered to identify how does the combination of a larger defect with a different configuration of this transformed region will affect the growth of a crack.

5.1 Background

Porosity, voids, and inclusions are undesirable imperfections that developed in a metal casting process. The term porosity is widely used to describe any hole or void formed in a cast product [148]. In the rail manufacturing process, porosity could be formed in rails due to improper control during the vacuum degassing process. As the molten steel changes state from liquid to solid during the manufacturing process, trapped gas that is dissolved in the molten steel would remain in bubble form as the steel solidifies [149] which could result in sudden rail fracture.

Due to a greater demand in the rail transport industry, the increase in train capacity, larger axle loads, and higher speed have resulted in a greater variety and frequency on the formation of rail defects across the rail network [150]. Smaller defects may remain in track until evidence of their growth led to rail removal, but for larger defects, immediate rail replacement is required [69]. During a rail removal process, the rail containing defects is removed and replaced with a new rail that is joined together by a welding process. Thermite welding or exothermic welding is one of the methods that is widely used to weld railway rails [151] due to its portability, low cost, and relatively short completion time [152]. This method involves solidification of molten steel which is similar to a casting process. Casting defects such as porosity are often found in thermite welds as reported in [151]–[159] since welding can be considered as a casting process.

According to [160], voids could also form in a small region below the sliding contact assuming they nucleate from the separation of a harder particle such as inclusion. An experimental study by [161]–[163] suggests that voids could nucleate from hard particles either by particle fracture or by separation of the particle matrix. These findings are relevant to rail applications where inclusions are often present in the rail since the rail is composed of some alloying elements. Therefore, even if a rail is fabricated free from defects such as casting defects or weld defects, voids could still form in a rail due to inclusions.

Fruitful research has been done in the past to study the effect of inclusions in rails [164]–[169]. If inclusions remain in the rail, they may establish a favoured region of stress concentration. Potential damage process might develop (depending on the level of stress and wear rate) which could result in catastrophic failure. In a recent investigation [170], the researcher concludes that a larger defect could increase the stress intensity factor (of a crack that initiated from the larger defect) which proportionally affects the crack growth rate by 19 times. However, the study does not include the effect of metallurgical transformed region / white etching layer present above the larger defect. In the previous chapter, only a single thin metallurgical transformed layer with a fixed length was considered to identify the effect of metallurgical transform region on the growth of a crack. Observation from recent work [2] suggests that the metallurgical transformed regions sometimes form as patches (not continuous) with various length and thickness. Therefore it would be interesting to study the effect of a different configuration of transformed region on cracks that initiated from larger defect in rail. To demonstrate these issues, a simple two dimensional (2D) boundary element (BE) model was developed within the Beasy software package [140] to investigate the influence of contradistinct white etching layer configuration (Figure 5-1) on a larger defect in rail.

5.2 Modeling method and conditions

The modelling method was almost identical with the previous chapter (described in Section 4.2) except for the type of defect and configuration of the transform region considered. The model variables and conditions were decided to match the operating condition of a high speed traffic provided by the SBB [2].In this chapter, a specific defect (Figure 5-2) described in the morphological study (Section 3.1.2) is considered in the modelling. An in-depth case study is made of a large void (maximum length of 2.9 mm and a maximum height of 0.9 mm) that was modelled to investigate the repercussion of white etching layer configuration on a larger defect in rail. The defect was located approximately 2 mm below the rail surface with two inclined cracks (referred as left and right crack) initiated from the left and right side of the void. This configuration represents a large defect in the rail that developed in undeformed steel. The left crack has an inclination angle of 4.65° while the right crack has an inclination angle of 15.68°. Different crack lengths (0.5 mm, 1 mm, 2 mm, and 4 mm) were considered to examine the effect of white etching layer conguration on the crack growth rate. Instead of modelling the void as an elliptical shape [170], the real geometry of the defect was modelled by extracting the defect perimeter coordinates from the metallographic image using an open source data extractor package known as the G3data [171]. Initial modelling work has been performed prior to this study to identify whether it would be convenient to simplify the void as an elliptical shape. It was found that by simpifying the void as an elliptical shape, the crack initiation point (determined based on Tresca effective stress value as the contact move across the defect) of the left crack would be at incorrect position and higher magnitude of stress was generated at the crack initiation point for the elliptical shape compared to the real geometry (Figure 5-3). Therefore it was decided not to simplify the geometry of the defect and the exact geometry was used throughout this study since the above mentioned effect might cause inaccurate results on the determination of stress intensity factor value.

Five cases have been considered throughout this study as indicated in Table 5-1. For case 1, no metallurgical expansion layer has been considered and case 1 has been chosen as the baseline case to identify the effect when a metallurgical transformed layer with a different configuration exist above the larger defect. The configuration of the model for case 1 is shown in Figure 5-4a. Case 2 to case 4 are similar in terms of the transform region thickness except for the length and configuration of additional transform region. For case 2, a thin metallurgical transform layer with a thickness of 250 µm lying above the defect was considered where the total length of the transform region was set to be 4 mm covering the whole length of the void (Figure 5-4b). Case 3 is almost identical with case 2 whereby both of these two cases posses similar thickness of transform region. However, an additional 1 mm length of transform region was added on both left and right side of the main transform region (Figure 5-4c) to represent a longer metallurgical transform region. Case 4 represents patches of metallurgically transformed region where two additional transform regions with a length of 1 mm were placed on the left and right side of the main transform region with a spacing of 1 mm between the additional transform region and the main transform region (Figure 5-4d). Case 5 has a similarity with case 2 whereby both of the transform regions shared a similar length of 4 mm. However the thickness of the metallurgically transformed region for case 5 is four times the thickness of case 2 resulting in a total thickness of 1 mm which represents a case of a thicker metallurgical transform region. To investigate the repercussion of white etching layer configuration on larger defects in rail, the white etching layer was represented in the model by applying a thermal body load to the whole region of transformed layer which symbolizes an expansion of a surface layer due to volume change. The value of expansion due to transformation was taken as 0.8% which was calculated based on the changes in density from pearlite to martensite as previously described in Section 4.2.1 and [7].

5.3 Results and discussion

All the cases listed in Table 5-1 were investigated for a 0.5 mm crack length to examine a crack that has initiated from a void but not yet grown significantly. Modelling was also performed for a range of crack lengths of 1 to 4 mm to investigate the effect of a different configuration of the metallurical transformed layer on propagated cracks. For each condition modelled, the range of stress intensity factor was assessed by considering the movement of a wheel incrementally across the defect (Figure 5-5), generating a series of

SIFs. The combined action of traction and normal stress is indicated in the figure, and results in asymmetry of the results for left and right crack tips. Results are presented as stress intensity factors in Figure 5-6 to Figure 5-12, in which the origin is at the void centre. Figure 5-7 and Figure 5-8 show the effect of metallurgical expansion layer on stress intensity factor for 1 mm crack for all the cases considered. Stress intensity factors are converted to indicative crack growth rates as display in Figure 5-13.

5.3.1 Stress intensity factor dependence on crack size

The trends in mode I and mode II SIF for the left and right crack tips that initiated from a larger defect is shown in Figure 5-6 where consideration was made for case 1. This case only considered mechanical load (without considering any metallurgical transformed layer above the void). The mode I SIF shows a rise with increasing crack size for the left crack tip (Figure 5-6a), but the values are small even for larger cracks (4mm) where the peak K_I is still below the threshold SIF (6 MPa.m$^{1/2}$ for tensile growth of cracks in carbon steel [121]). Data for the mode II SIF (Figure 5-6b) shows higher stress intensity factor values even for smallest crack where the range exceeded the shear mode threshold of 1.5 MPa.m$^{1/2}$ proposed by Otsuka et al. [121]. Even though the value of mode I SIF does not exceed the opening mode threshold, crack growth would still be expected since the range of mode II SIF exceeded the shear mode threshold value.

For the right crack tip, the range of K_I and K_{II} show rising trends with increasing crack size (Figure 5-6c and d). However, there was some reduction in the range of K_{II} once the crack reaches a size of 4 mm for the left and right crack tip. This reflects the trend in the outcome of crack growth under mixed mode developed for inclined surface breaking cracks (Figure 5-13 and Table 5-2) where there is an increase in the growth with an increase of crack size, but decreased once both cracks exceeded a size of 2 mm.

As the crack size increase, the tip moves deeper into the material where the stress region become lesser with an increasing depth. A similar observation can be seen from the shear stress plot (Figure 5-14) where the magnitude of the shear stress starts to decrease with an increasing depth. As the crack reach some critical crack length and depth, this results in a reduction in stress intensity value hence resulting in a drop in the growth rate [172]. Therefore, the propagation of the crack may tend to slow even though the crack elongate.

Looking at the trend of the growth rate, it was noticed that the left crack tip experience higher growth rates compared to the right crack tip. A similar observation can be seen from the defect metallography (Figure 5-2) where the left crack tip is longer than the right crack tip. As stated in Section 5.2, the right crack tip has higher inclination angle compared to the left crack tip. Therefore with an increasing crack size, the right crack tip will always be deeper into the material compared to the left crack tip hence will always experience lesser stress magnitude.

5.3.2 Expansion effect of a thin surface layer on cracks initiated from void

The effect of the thin expansion layer on mode I and II SIF for the left crack tip is shown in Figure 5-9 and the baseline (case 1) is included for comparison. The trend (Figure 5-9a) shows that the presence of the metallurgical transformed layer has a significant effect on the mode I SIF where its value will always be above the baseline case if the contact is far from the crack tip. However, this effect is only valid for short crack size (0.5 – 2 mm) whereby for the largest crack (4 mm), the expansion of the transformed layer gives very minor effect on the K_I value. This phenomenon is similar to the case for horizontal crack described in Section 4.3.2 where the effect will diminish as the crack lengthens. Even though the expasion of the transformed layer give a rise on the K_I value, the range is still below the opening tensile threshold even for the largest crack size. For mode II data (Figure 5-9b), the trend shows that the expansion of the transformed layer increases the magnitude of the negative and positive peak but the effect is small. These differences can be seen numerically in Table 5-3. The changes are small and reduce as the crack extends. Results for the right crack tip exhibit similar behaviour where expansion of the transformed layer only affects the range of K_I value for shorter crack and gives very little effect on the range of mode II SIF.

The expansion of the metallurgical transform layer lying above the defect will introduce an opening stress region below its whole length until a certain depth as shown in Figure 5-15. It can be seen that the region of the maximum opening stress occured at the side of the defect where crack initiation point is located. For the shortest crack (0.5 mm), the whole length of the crack is situated at the region where maximum opening stress occured (e.g. y-direction direct stress). As the crack lengthens, the crack tip had exceeded these maximum stress regions where only some part of the crack length is affected by the opening stress and this will result in a very minor reduction in the K_I value as the crack lengthens.

Since the defect is located further away from the transformed region (eight times the thickness of the transformed region), therefore the effect of the thin transformed region gives a small effect on the range of mode I and mode II SIF. Unlike the case in the previous chapter where the horizontal crack is located closer to the transformed region and therefore impacts both mode I and mode II SIF significantly, the tip for an inclined crack is located further away from the highest stress region as the crack lengthens hence resulting in a lesser effect on the range of K_I and K_{II} value. It can be concluded that the expansion of the thin transformed layer will only give significant affect on the range of K_I and K_{II} value if the defect (crack tip) is located closer to the transform region.

5.3.3 Effect of longer expansion layer

Figure 5-10 display a selection of cases to highlight the effect of an increasing length of the transformed region from 4 mm to 6 mm (focusing on the left crack tip for 1 mm crack size). The baseline case (case 1) is also included for comparison. The trend in mode I (Figure 5-10a) shows that an increase in the length of the transformed region (case 3) will raise the K_I value above the case when a shorter transform region is considered (case 2) but the effect is small. Maximum effect occurs when the crack grows to a size of 2 mm as can be seen numerically from Table 5-3. However, the longer transform region makes insignificant changes as the crack lengthens to a size of 4 mm.

For mode II data (Figure 5-10b) the variation of SIF during the motion of the contact is insensitive to the differences between cases with the longer transformed region or with the shorter transform region. Even for a larger crack, the trend exhibit similar behaviour. At negative contact position there is almost no effect between shorter expansion region (case 2) compared with longer expansion region (case 3) while for positive contact position, there is some sensitivity of the peak K_{II} value from an increasing length of the transform region.

As mentioned earlier, the effect of a longer transform region (case 3) on a crack initiated from void will increase the K_I value with an increase of the crack size (for 1 mm and 2 mm) but with a minimum effect compared to the case when a shorter transform region is considered (case 2). However, these effects will diminish once the crack grows to a size of 4 mm. As mentioned earlier in Section 5.3.2, the presence of the transform region will introduce an opening stress region below its whole length of the transformed material. When a longer expansion layer is considered, the opening stress region became wider (Figure 5-16) and any crack length that is located within this region will experience higher opening stress which attributes to higher K_I value. For a 1 mm crack, the whole crack length is located below the transform region when case 3 is considered. The whole crack length (in case 3) will experience higher opening stress due to the expansion of the transformed region compared to case 2 where only some part of the crack face experienced the opening stress that affects the K_I value. However, as the crack lengthens to a size of 4 mm, the tip of the crack has exceeded the length of the transform region (where only some part of the crack is affected by the expansion of the transform region) hence resulting in insignificant changes on the mode I value. This reflects the trend in the crack growth predictions (Figure 5-13) whereby a longer transformed layer (case 3) will raise the growth rate of the crack above the case of a shorter transform region (case 2), but with a very minimum effect.

5.3.4 Effect of patchy transform region

As mentioned in Section 5.2, the configuration of the transform layer for case 4 is quite similar to case 2. However, there is an additional 1 mm long transform layer on each side of the main transform layer, with a spacing of 1 mm as shown in Figure 5-4. An example of white etching layer patches that formed on the rail surface is shown in Figure 5-1.

The effect of a patchy transformed region on mode I and mode II SIF for 1 mm crack focusing on the left crack tip can be seen from Figure 5-11. The trend in Figure 5-11a shows that the value of K_I rises above baseline (case 1) but fall below case 2 throughout all positions of the contact. Looking at the numerical changes in Table 5-3, the trend change where the range of mode I SIF for case 4 raise above ΔK_I for case 2 as the crack lengthens from 2 mm to 4 mm. Although the SIF changes are small, they do influence the trend of the crack growth (Figure 5-13) where patches of white etching layer will drive to a higher crack growth in case 4 compared to case 2 as the crack lengthens, however, the effect is still lower compared to the case when longer transform region is considered (case 3). For the mode II data (Figure 5-11b), the patches of the transform region give minimal but variable effect on the range of mode II SIF. For all sizes of crack modelled, it was found that patchy white etching layer has an insignificant effect on the ΔK_{II} value compared to case 2.

Looking at the results overall, when patches of transform region formed on the surface, they will introduce an opening stress region below the transformed region (similar to case 2 and 3) due to volume expansion. However, the presence of gap/spacing between the transform region will introduce an additional compressive stress region below the gap (Figure 5-17). Since the transform region expands due to volume expansion particularly noticeably when the contact is not present, the non-transformed region of the gap will compress due to the reaction movement (Newton 3rd law) and this will result in the formation of the compressive stress region under the gap. Therefore any crack tip that lies in this region will experience compressive stress that will reduce its K_I value. Focusing on the left crack tip, Figure 5-19 show the deformed plot for case 4 when the contact is not present. For the 1 mm crack size, some part of the crack is located at the tensile stress region while some part especially the crack tip is located at the compressive stress region (Figure 5-19a). This results in a small reduction in the ΔK_I value compared to case 2 for similar crack size. However, as the crack lengthens to a size of 2 mm, some part of the crack especially near the crack tip is located at the opening stress region (Figure 5-19b) and this attribute to higher ΔK_I value compared to case 2. Hence although minor, the variation in SIF observed can be seen to be caused by the physical region modelled and not by artifacts of the modelling process.

5.3.5 Effect of thicker transform region

The effect of thicker transform region on the mode I and mode II SIF for the 1 mm crack size (focusing on the left crack tip) is shown in Figure 5-12. The length of the transform region for this case (case 5) is similar to case 2, however, it is 4 times thicker compared to the thickness of the transform region for case 2. Looking at the effect in mode I (Figure 5-12a), the values of K_I for thicker transform region (case 5) rise well above case 2 when the contact is absent. Under the same condition, thicker transform region also has a significant effect on the range of K_{II} (Figure 5-12b) where the peak of the K_{II} value falls below the baseline case at negative contact positions and rises significantly in magnitude at positive contact positions.

The effect of thicker transform region on stress intensity factor range can be seen numerically in Table 5-3 where the trend emerges that thicker transform region produces a major change in both ΔK_I and ΔK_{II} (for example the differences on ΔK_I value is about 53% for 2 mm left crack). This reflected in the trend in the crack growth rate (Figure 5-13) where a thicker transform region results in higher growth rate compared to all other cases considered. The trend in the crack growth rate for case 5 is similar to all the other cases where the growth rate increase with an increasing crack size, but decreased as the crack exceeded the size of 2 mm.

Similar to case 2, the formation of thicker transform region will generate opening tensile stress region under the deformed layer most noticeably when the contact is not present as shown in Figure 5-18, but with a higher magnitude of stress than case 2 due to the impact of the thicker transformed layer. With a thicker transform region, the defect and the crack tip will be located nearer to the transform region and they will experience a higher level of stresses which affect both K_I and K_{II} value. For a shorter cracks size, they will always locate in this high stress region. However as the crack lengthens, the crack tip will be located further away from the high stress region which will give a drop to both ΔK_I and ΔK_{II} value. This indicates that thicker transform region will results to a higher Mode I and mode II SIF which will also enhance the crack growth rate. Even for a thin transform region, a higher crack growth rate would be possible if the defect is located closer to the transform region.

5.3.6 Real world consideration

In this chapter, since the defect is located 2 mm away from the transform region, the effect of a different configuration of the metallurgical transformed layer does not show significant effect between most cases considered (apart from the case of thicker transform region). However, looking at the trend where thicker transform region is considered, it is expected that different configuration of these transform region will have a more significant effect if the defect is located closer / nearer to the transform region. These effects will be greater if a horizontal crack instead of an inclined crack is considered (Figure 5-20).

It is known that there is an interaction between wear and fatigue crack whereby some rail steel grades wear more rapidly, and small cracks are always removed when wear process dominates. Typical rail wear rate maeasured from twin disc test under a dry condition with a maximum pressure of 1500 MPa is around 1.05 nm/cycle [173] where the value would rise up to 2.5 nm/cycle when decarburised layer are present on the rail surface [174]. However the crack growth predicted in this study for a small crack size is at least 6 times higher than the wear rate mentioned in the literature, and its growth rate will rise if the expansion of a transformed layer is considered.

5.4 Summary

Severe thermal loading for example caused by poor traction control has resulted in a formation of a thick metallurgical transformed layer on the rail surface which is known as the white etching layer. Similar but much thinner layer are also produced during normal running. The presence of white etching layer on a rail remove from service (normally associated with squat type defect) comes in various type of form where sometimes the layer is not continuous and appear in the form of patches with various thickness and sizes. The effect of different WEL configurations on an inclined crack initiated from larger defect have been studied leading to the following conclusions:

a) The presence of thin (0.25 mm) metallurgical transformed layer / white etching layer lying above the defect will give an increase in the growth rate for an inclined crack. However, the effect reduces with an increasing crack size as the crack tip moves away from the region of maximum stress.
b) A longer (6 mm) metallurgical transformed layer will increase growth rate for an inclined crack compared to a shorter (4 mm) transformed layer with a similar thickness. However, in this study, the effect is small with a maximum difference of 4% in crack growth rate.
c) Patches of white etching layer will have lower crack growth compared to a continuously transformed layer while the crack tip is below region which is not transformed. However, the rate will increase once the crack tip enters the next region of a following metallurgical transform layer.
d) Thicker (1 mm) transform region will increase the crack growth rate by at least 1.3 times compared to thinner (0.25 mm) transform region with a similar length.

Even for larger crack size, the growth rate rises well above other cases considered while the crack lies below the transformed region.

Since the crack considered in the model is subsurface, therefore there is no interaction of the crack and the wear. But to give some context to its growth rate, it was found that the growth rate is at least 6 times higher than the wear rate mentioned in the literature, and its growth rate will rise if the expansion of a transformed layer is considered. Looking at the overall behaviour of the crack (Figure 5-2), there is a tendency for this crack to grow transversely potentially leading to rail fracture under bending stress. Therefore, immediate rail replacement is required once the crack grows to its critical crack length [61].

Detection of this kind of defect is the key in order to monitor its growth behaviour before it leads to catastrophic failure. However, the presence of smaller defects lying above this larger and deeper defect could mask the ultrasonic signal during the inspection, preventing the detection of this larger defect. In addition, some defects could not be detected by ultrasonic scan if the crack is located just below the surface. Therefore, a new method of detection is needed to overcome this issue and this will be discussed in the following chapter.

5.5 Tables and figures

Table 5-1 Conditions modelled

Case	Consideration
1	No metallurgical transformed layer
2	Thin (0.25 mm) metallurgical transformed layer (length: 4 mm)
3	Extension of thin (0.25 mm) metallurgical transformed layer (length: 6 mm)
4	Patches of thin (0.25 mm) metallurgical transformed layer (length: 6 mm)
5	Thick (1 mm) metallurgical transformed layer (length: 4 mm)

Table 5-2 Crack growth rates (nm/cycle) for all the cases and sizes of crack modelled

Case	0.5 mm		1 mm		2 mm		4 mm	
	L	R	L	R	L	R	L	R
1	12.0	16.0	34.1	32.3	48.0	41.5	35.4	34.1
2	13.7	18.7	37.3	36.0	50.4	44.2	37.3	36.1
3	13.3	18.4	38.4	36.6	52.5	45.6	38.3	36.8
4	13.2	17.8	35.7	34.9	51.4	44.5	37.7	36.3
5	17.3	28.2	47.3	50.1	60.1	56.8	47.7	47.0

Table 5-3 Mode I and Mode II SiF range for all case modelled

Case	0.5 mm				1 mm				2 mm				4 mm			
	L		R		L		R		L		R		L		R	
	ΔK_I	ΔK_{II}	ΔK_I	ΔK_{II}	ΔK_I	ΔK_{II}	ΔK_I	ΔK_{II}	ΔK_I	ΔK_{II}	ΔK_I	ΔK_{II}	ΔK_I	ΔK_{II}	ΔK_I	ΔK_{II}
1	3.3	21.5	0.0	23.8	3.3	29.9	0.0	29.6	4.0	33.2	0.3	32.0	4.9	30.0	2.3	30.0
2	4.8	22.2	1.6	24.9	4.5	30.6	1.5	30.6	4.5	33.7	1.2	32.6	4.6	30.6	2.1	30.6
3	4.5	22.0	1.4	24.8	4.9	30.8	1.7	30.7	5.2	34.0	1.7	32.9	4.6	30.8	2.2	30.7
4	4.1	22.0	1.0	24.6	3.9	30.3	1.1	30.3	4.8	33.8	1.4	32.6	4.9	30.7	2.3	30.6
5	6.8	23.4	6.1	27.7	7.2	32.5	6.2	33.3	6.9	35.2	5.4	34.8	6.1	32.8	4.0	33.0

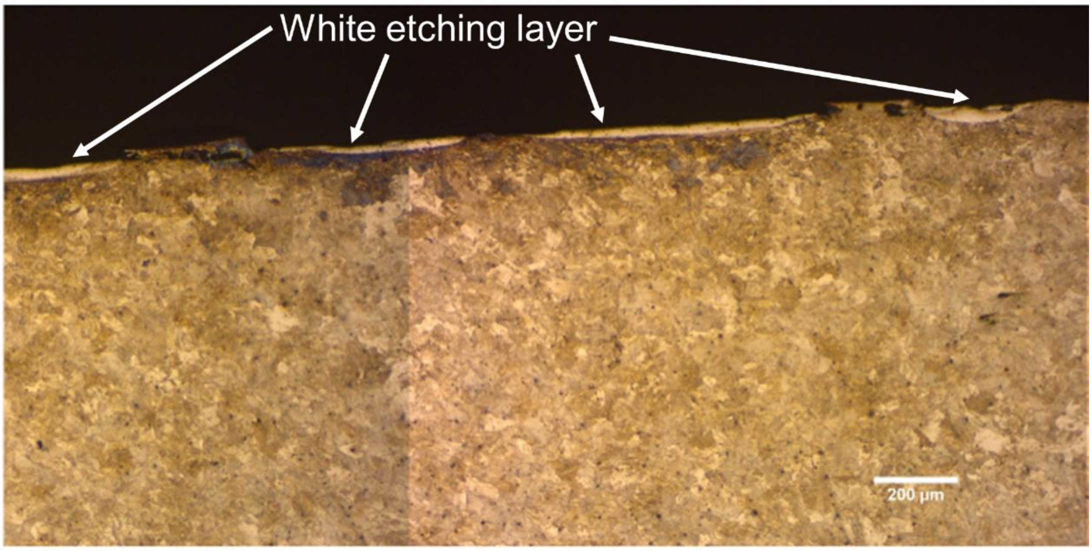

Figure 5-1 Patches of white etching layer lying on the rail surface

Figure 5-2 Example of massive void morphologhy below the running band in a longitudinal cross section from a high speed mixed traffic line. The central portion of the defect lies approximately 2 mm below the rail surface. Incline crack initiated from the left and right side of the void.The white marker above the rail surface indicates the location of a patch of white etching layer with a thickness ranging between 20 to 250 µm.

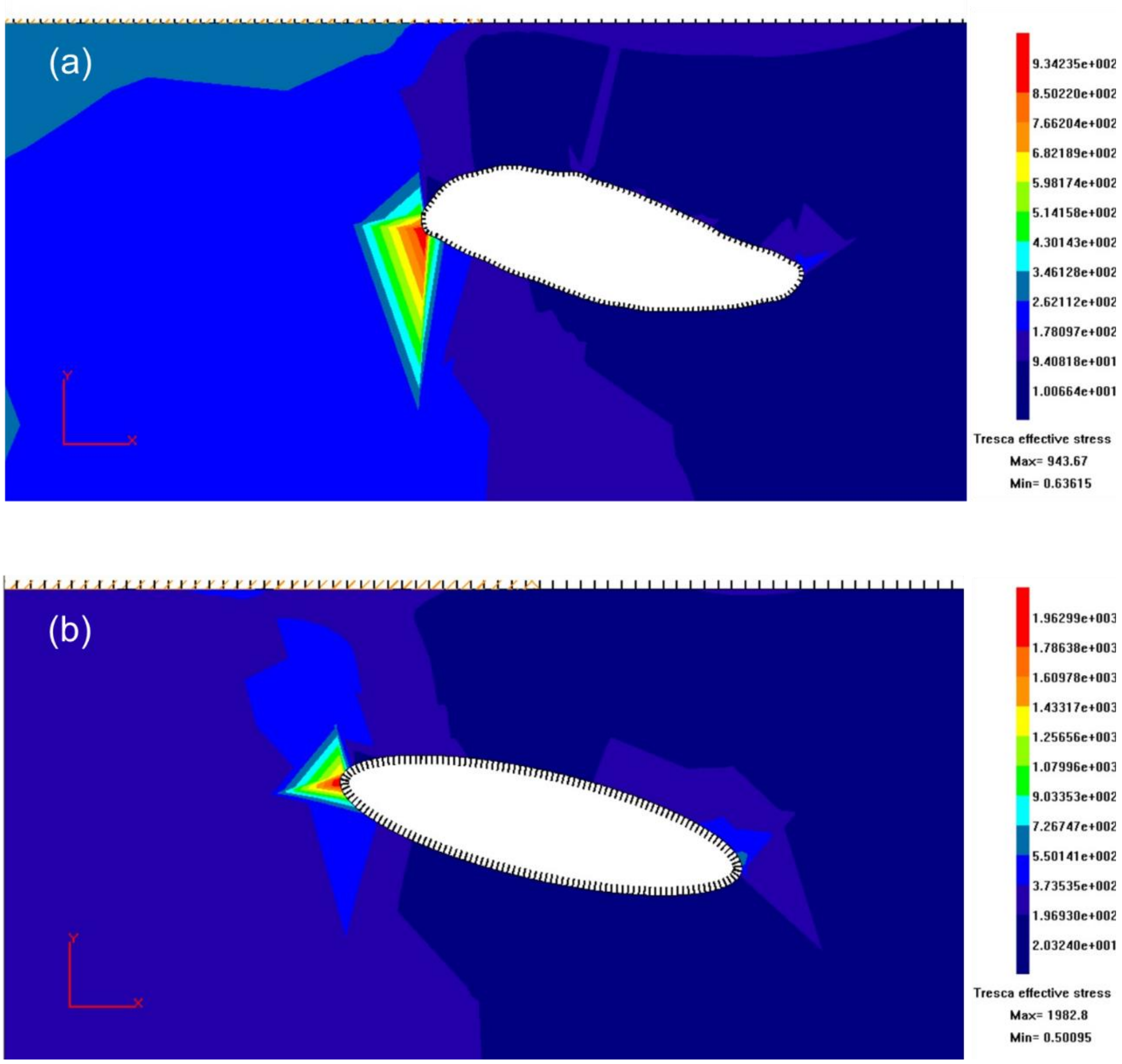

Figure 5-3 Comparison of crack initiation point between two different geometry under similar condition. (a) real geometry. (b) simplified elliptical geometry.

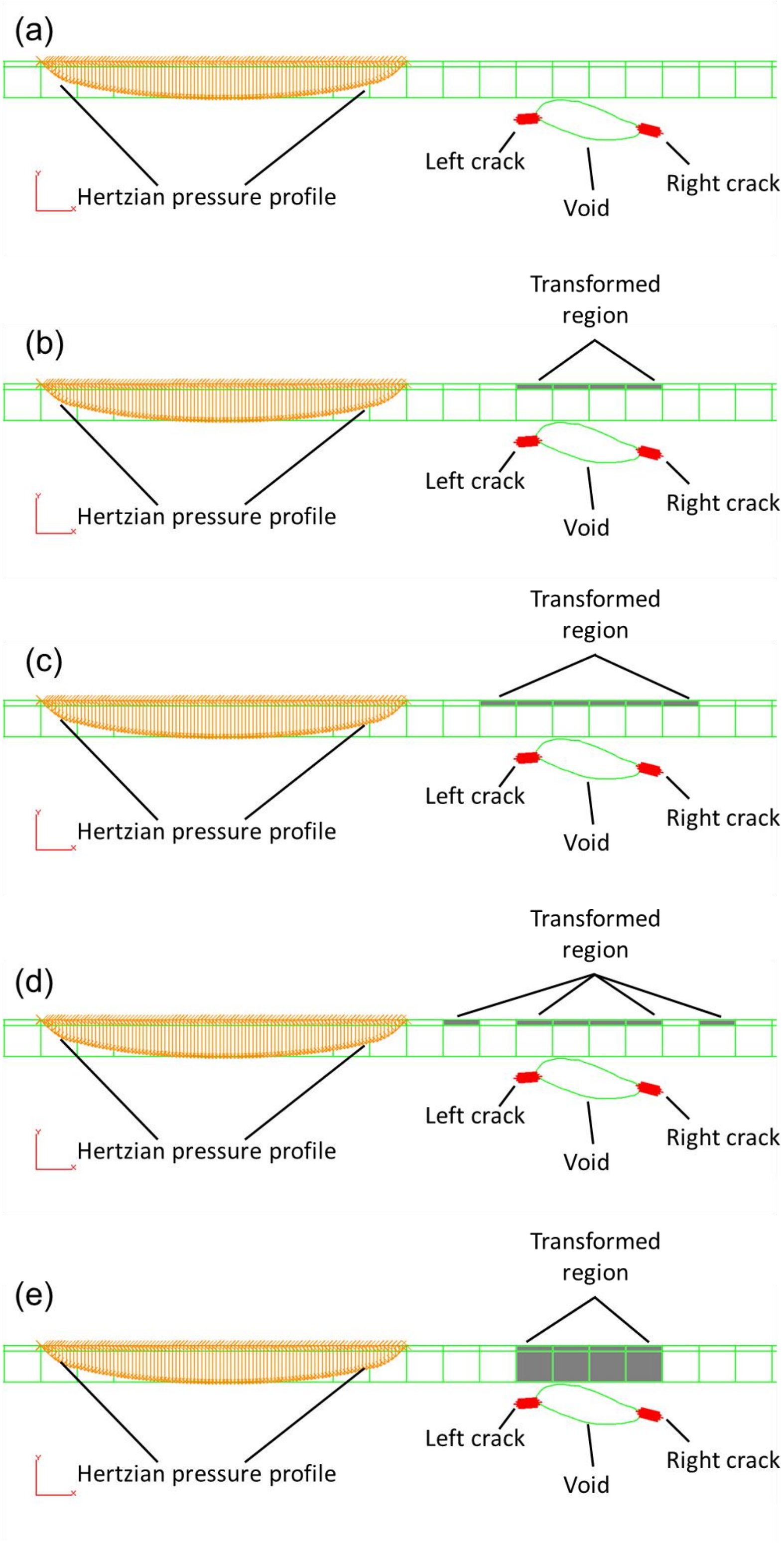

Figure 5-4 Representation of BE model of rail–wheel contact for 2 incline cracks initiated from the left and right side of a larger defect (named as left and right crack). (a) case 1 - no metallurgical transform region considered. (b) case 2 – thin metallurgical transform region lying above the void with a continuous length of 4 mm and a thickness of 250 µm. (c) case 3 – longer thin metallurgical transform region lying above the void with a continuous length of 6 mm and a thickness of 250 µm. (d) case 4 – similar with case 2 where thin metallurgical transform region lying above the void with a continuous length of 4 mm and a thickness of 250 µm. Two additional transform region with similar thickness and a length of 1 mm was placed on the left and right side of the main transformed region with a spacing of 1 mm to represent patches of transformed region. (e) case 5 – thick metallurgical transform region lying above the void with a continuous length of 4 mm and a thickness of 1 mm.

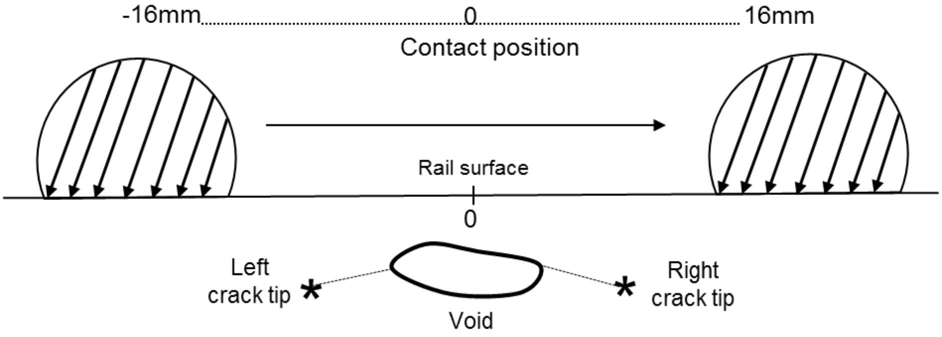

Figure 5-5 A series of analyses are performed with incremental movement of the contact across the defect. The origin of the position is measured from the centre of the void.

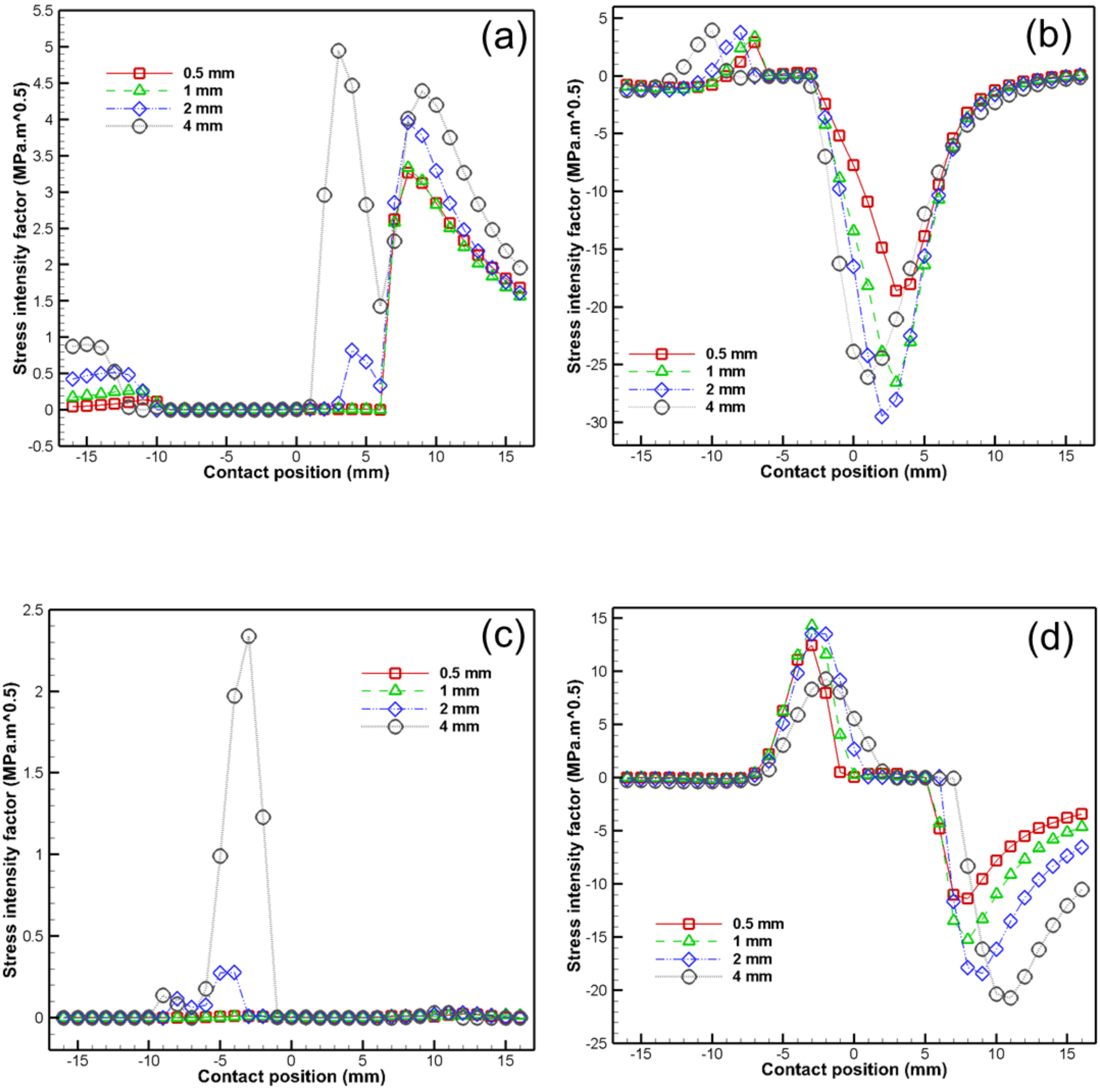

Figure 5-6 Stress intensity factor dependence on contact position. (a) left tip mode I, (b) left tip mode II, (c) right tip mode I, and (d) right tip mode II

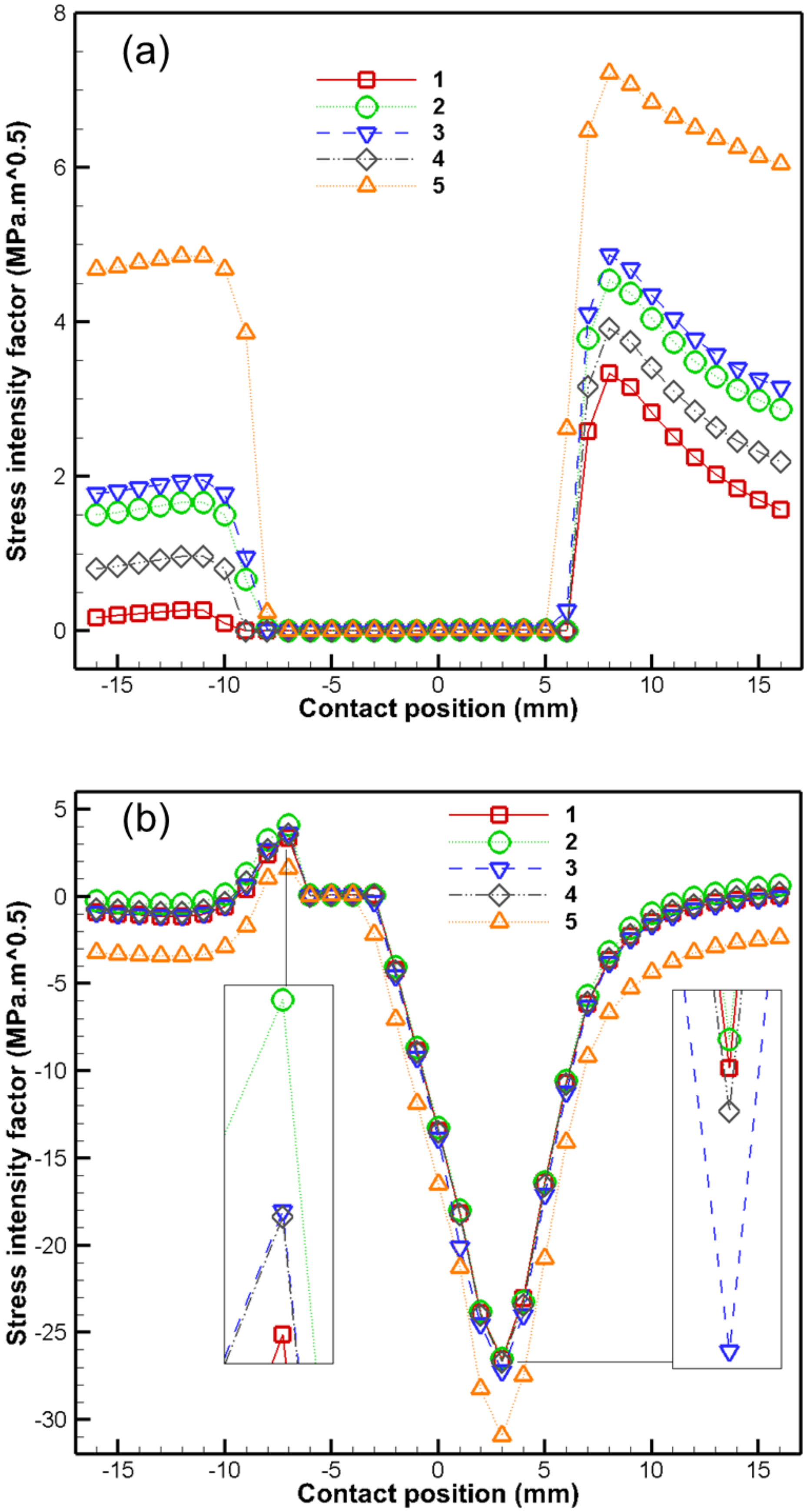

Figure 5-7 Effect of metallurgical expansion layer (represented as density change) on stress intensity factor for 1 mm crack, left crack tip. (a) Mode I, and (b) mode II. Legend entries refer to cases in Table 5-1

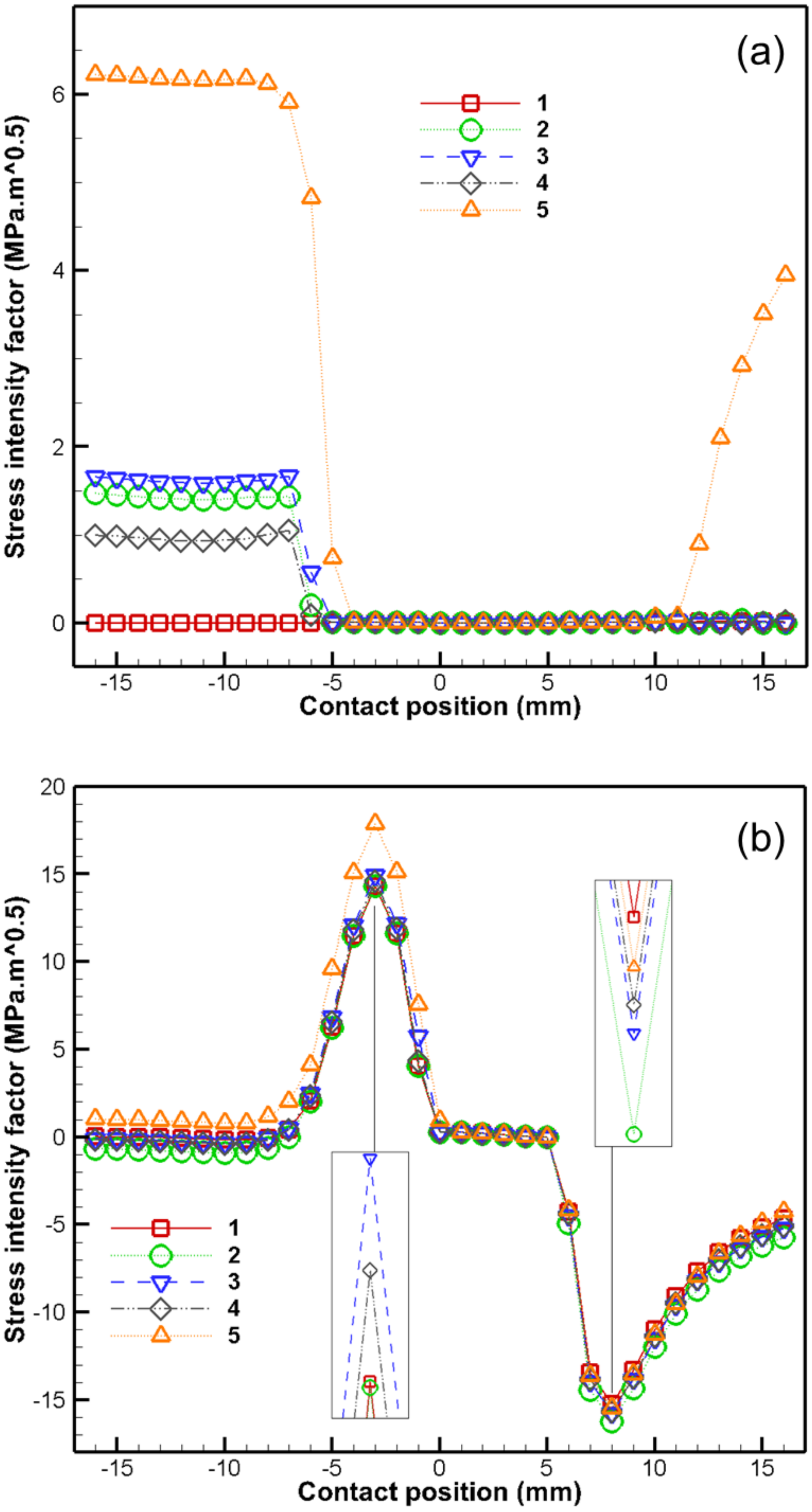

Figure 5-8 Effect of metallurgical expansion layer (represented as density change) on stress intensity factor for 1 mm crack, right crack tip. (a) Mode I, and (b) mode II. Legend entries refer to cases in Table 5-1

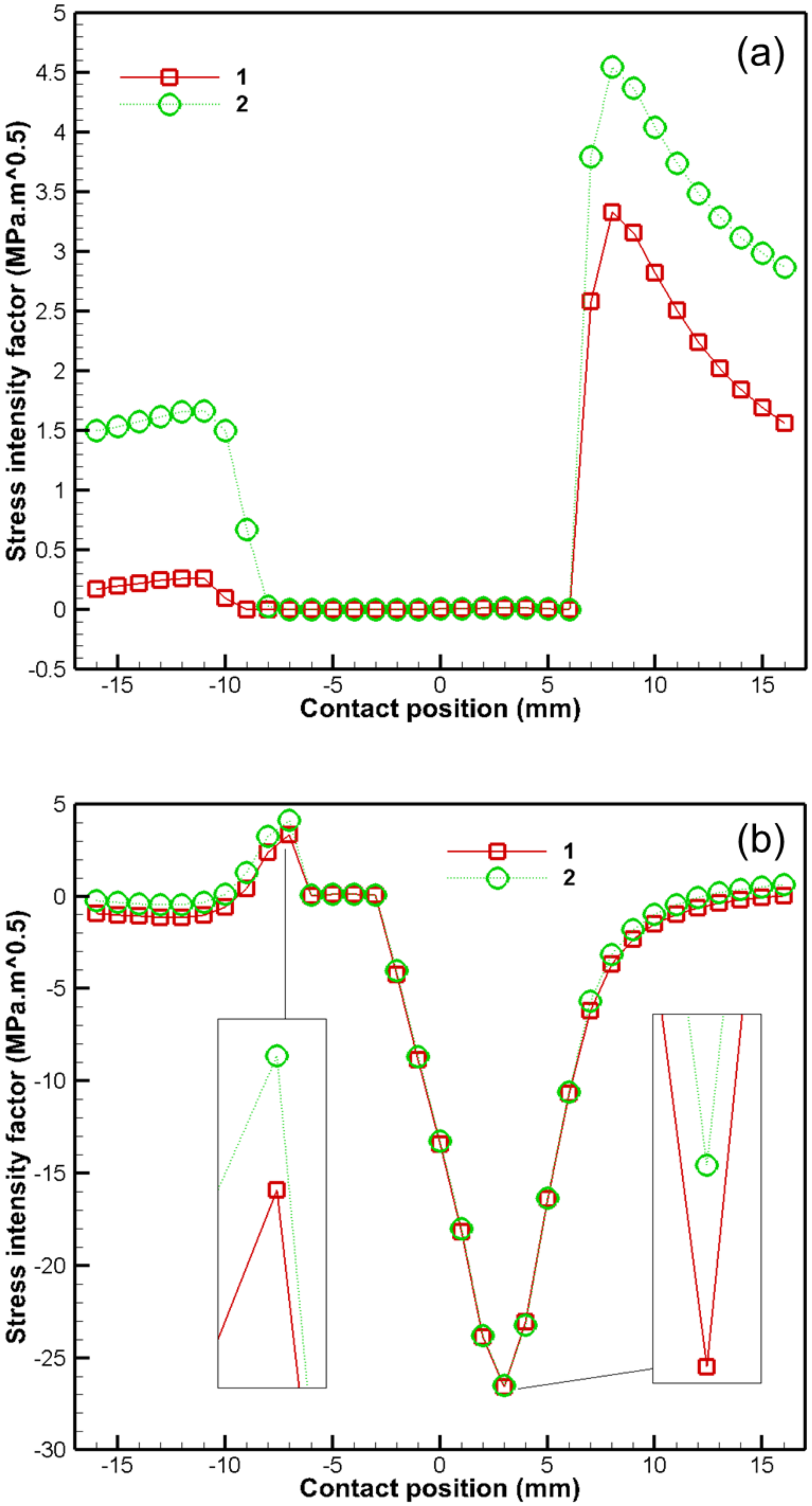

Figure 5-9 Effect of a thin metallurgical expansion layer (represented as density change) on stress intensity factor for 1 mm crack, left crack tip. (a) Mode I, and (b) mode II. Legend entries refer to cases in Table 5-1

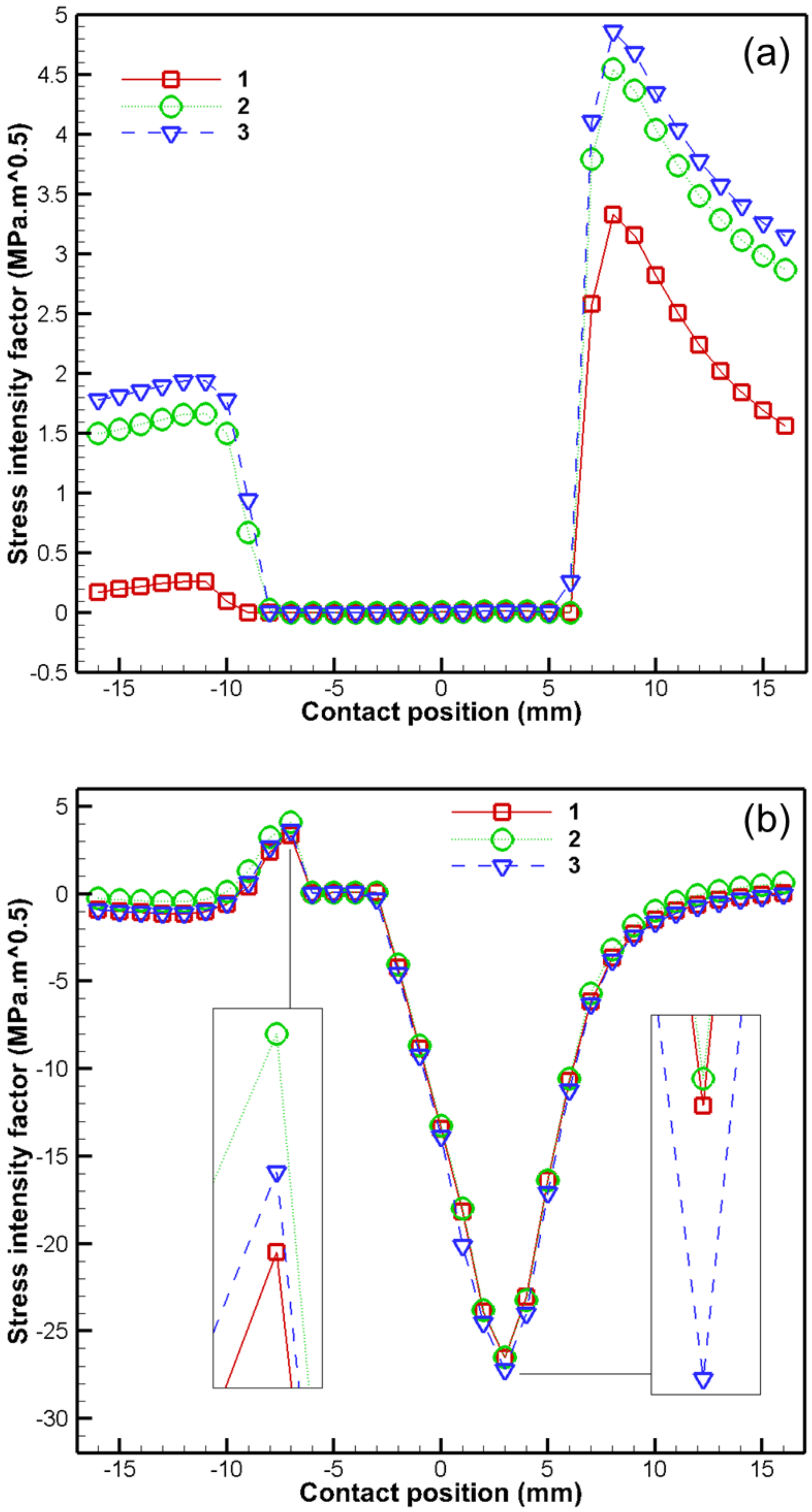

Figure 5-10 Effect of a longer thin metallurgical expansion layer (represented as density change) on stress intensity factor for 1 mm crack, left crack tip. (a) Mode I, and (b) mode II. Legend entries refer to cases in Table 5-1

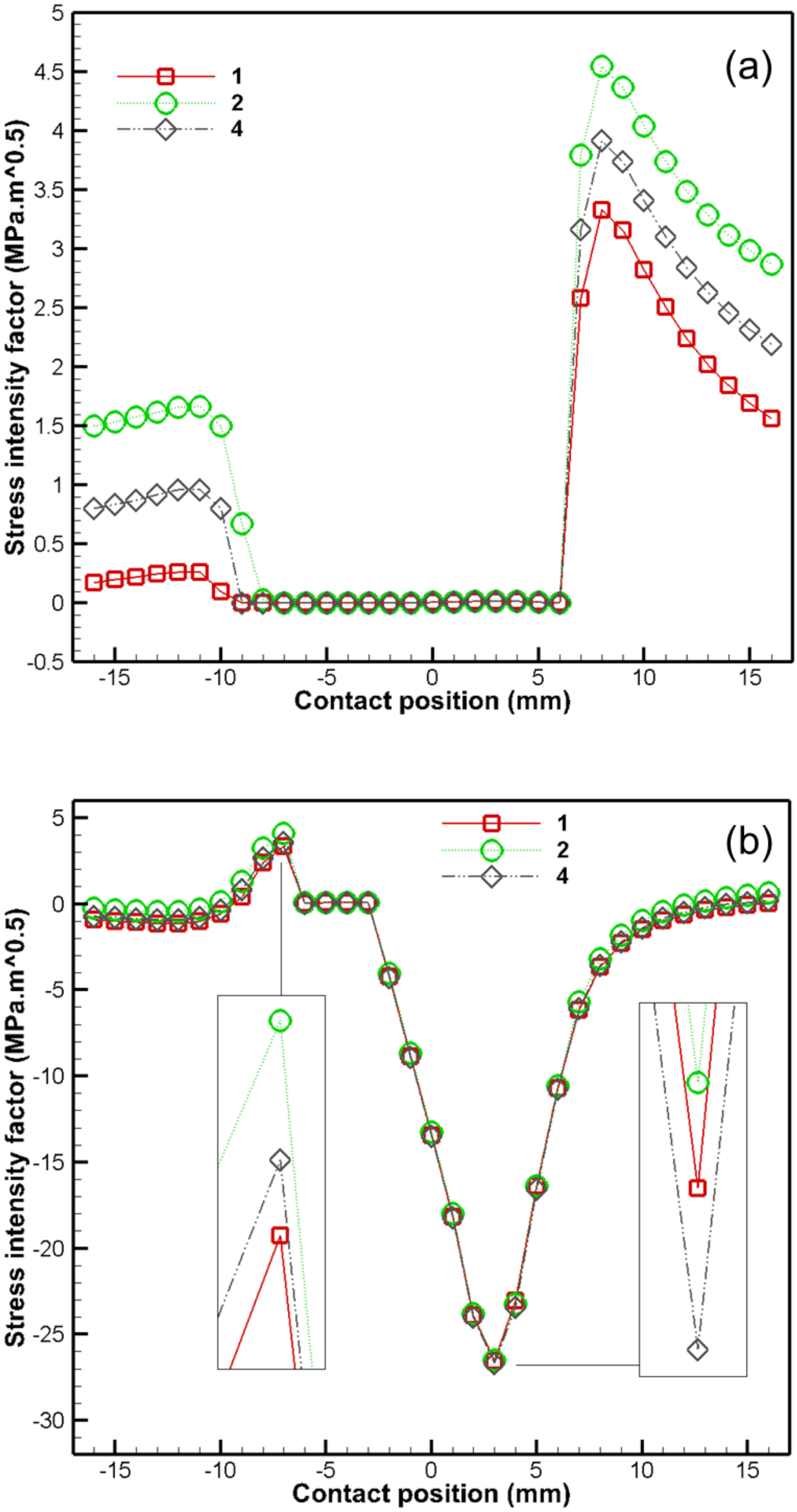

Figure 5-11 Effect of thin metallurgical expansion layer patches (represented as density change) on stress intensity factor for 1 mm crack, left crack tip. (a) Mode I, and (b) mode II. Legend entries refer to cases in Table 5-1

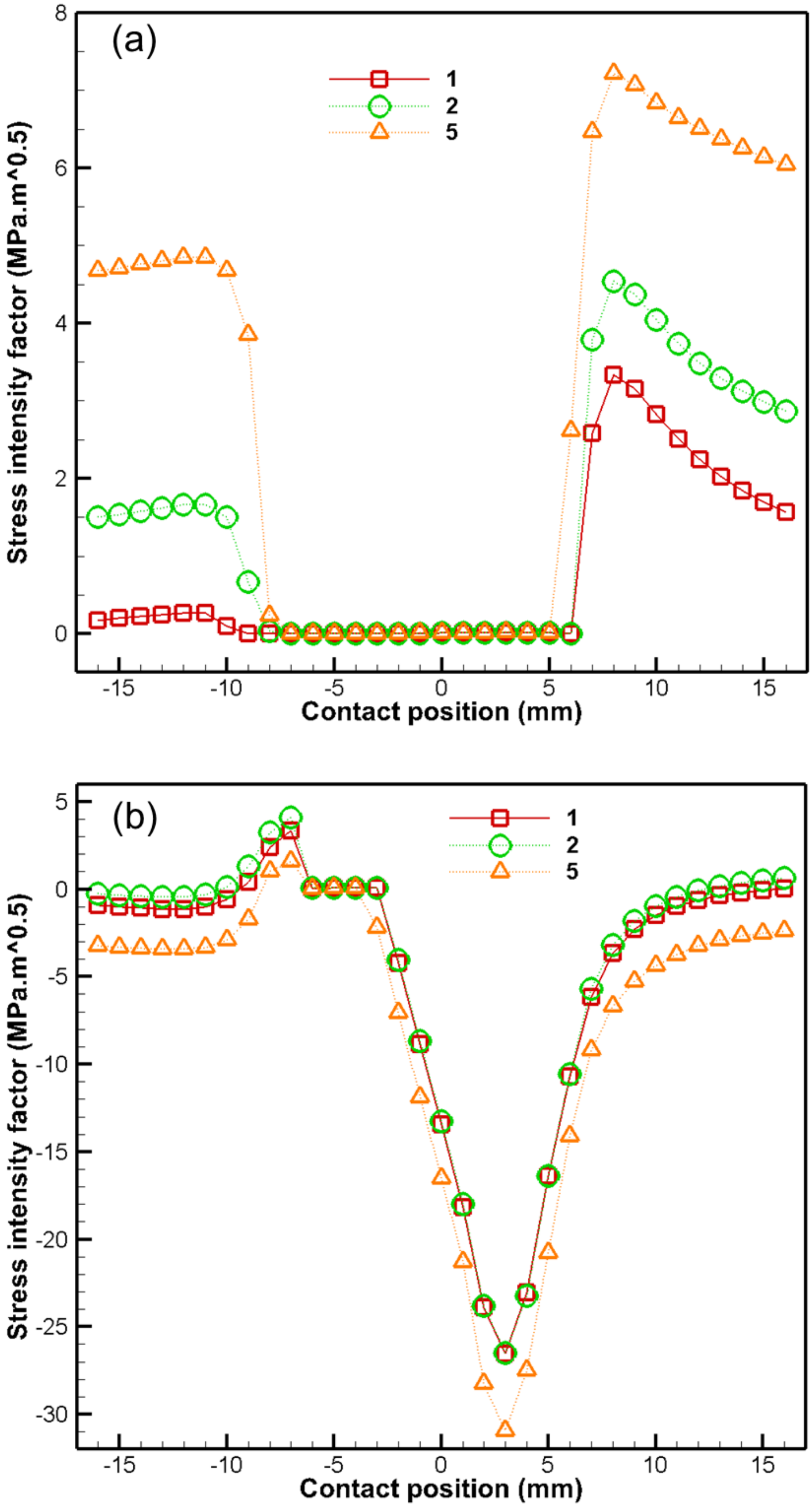

Figure 5-12 Effect of thick metallurgical expansion layer (represented as density change) on stress intensity factor for 1 mm crack, left crack tip. (a) Mode I, and (b) mode II. Legend entries refer to cases in Table 5-1

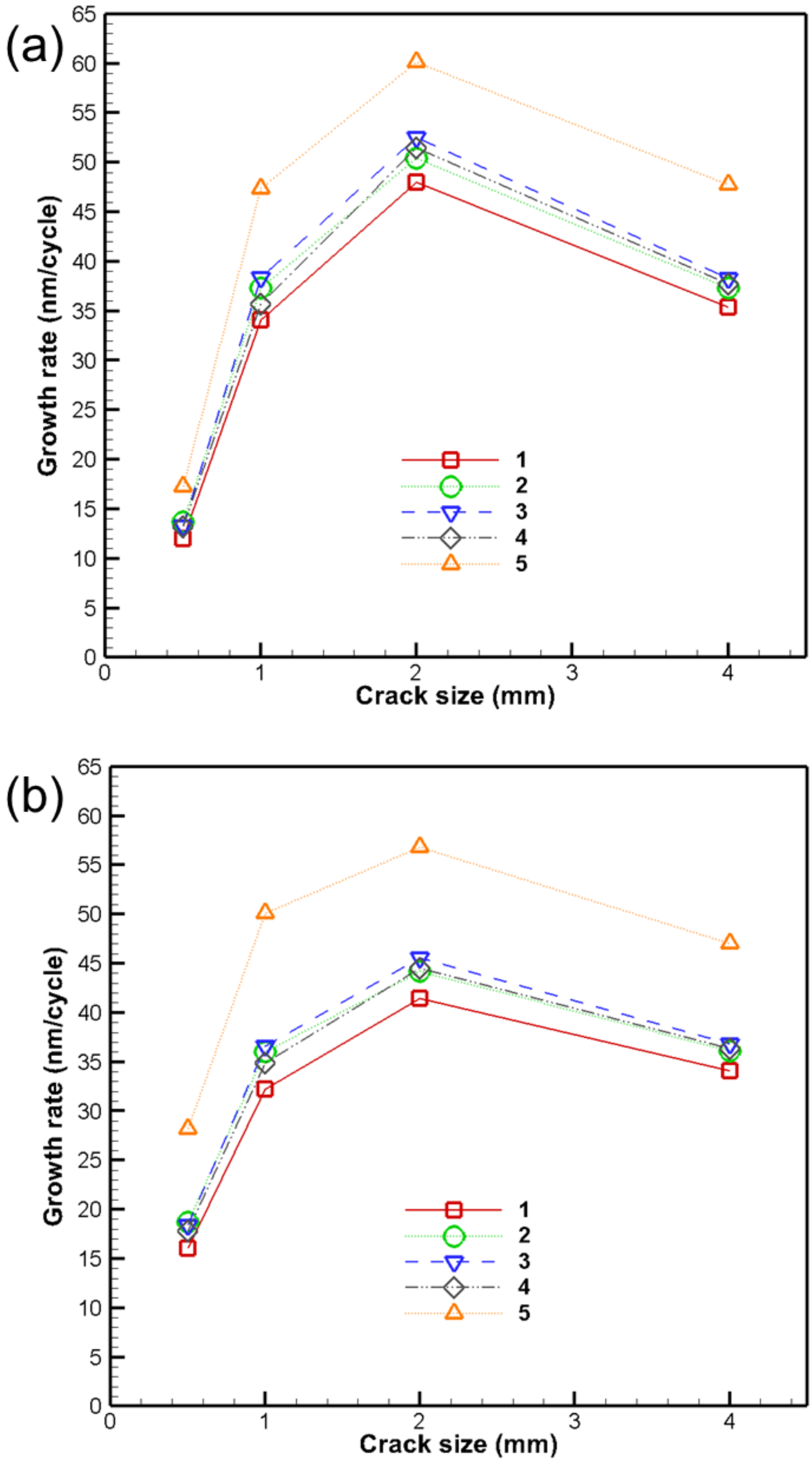

Figure 5-13 Crack growth rate dependence on crack size for all cases considered. (a) Left crack tip, and (b) right crack tip.

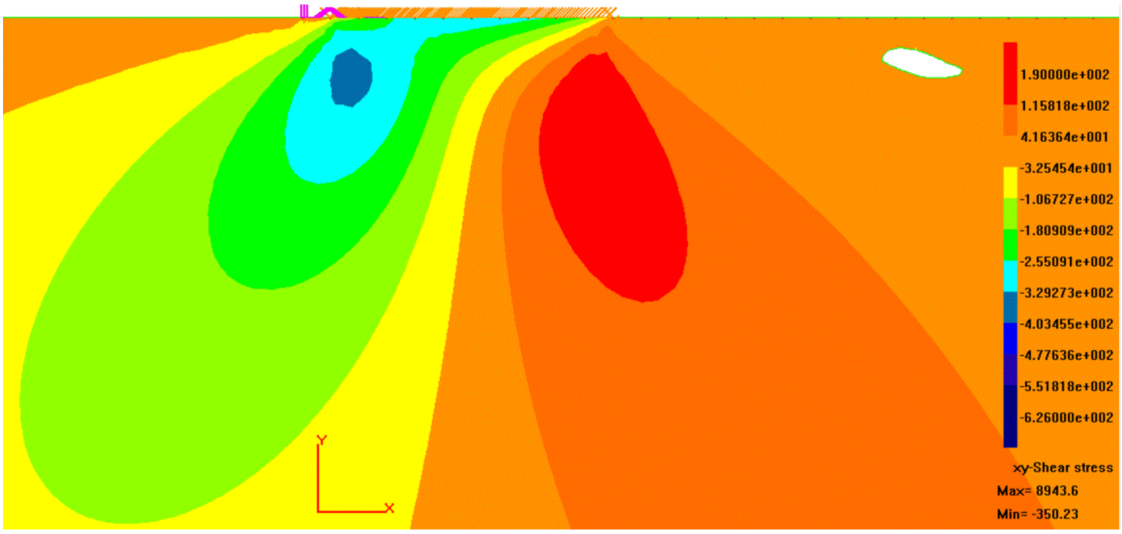

Figure 5-14 Shear stress plot at -16mm contact (far away from the defect) for case 1. Units in MPa.

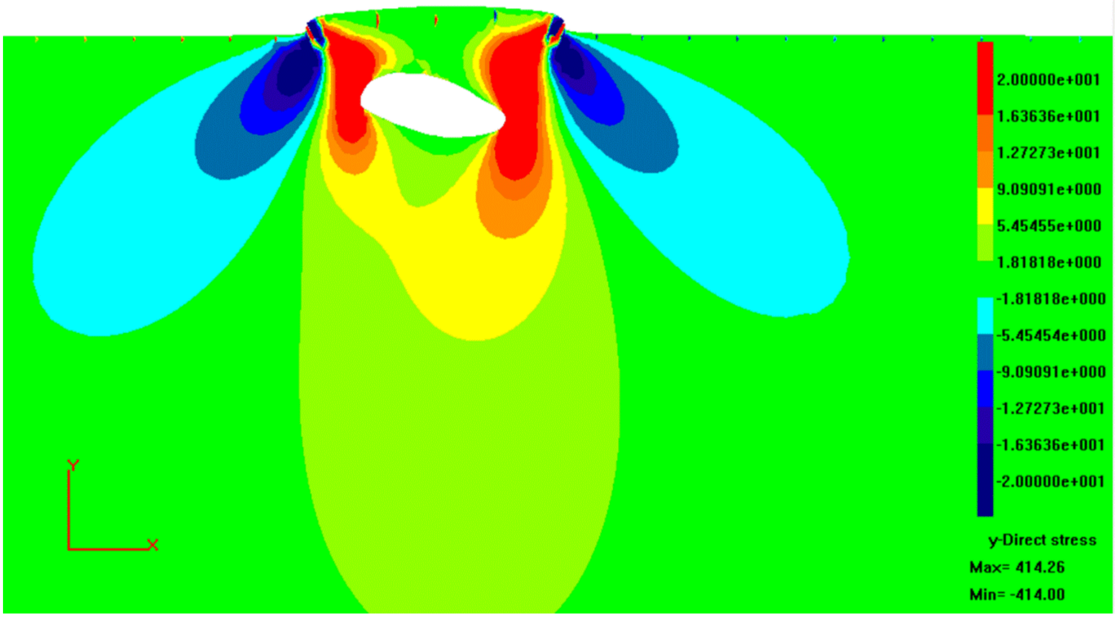

Figure 5-15 Deform vertical stress plot for the case where thin expansion layer is present above the defect (case 2). Mechanical load (contact) and crack were absent. The deformation plot scale factor was set to 100 for clarity. Units in MPa.

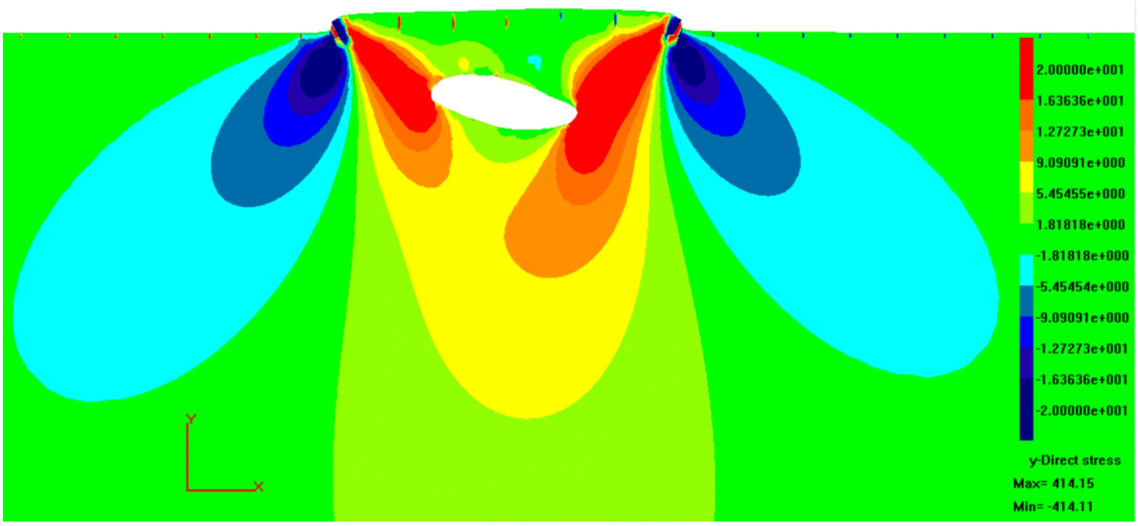

Figure 5-16 Deform vertical stress plot for the case where longer thin expansion layer is present above the defect (case 3). Mechanical load (contact) and crack were absent. The deformation plot scale factor was set to 100 for clarity. Units in MPa.

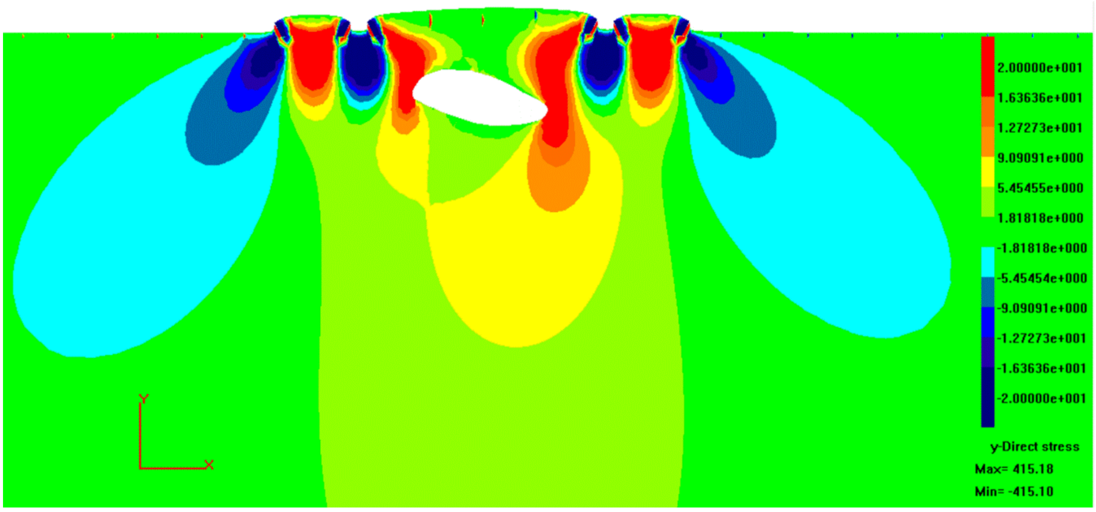

Figure 5-17 Deform vertical stress plot for the case where patches of thin expansion layer are present above the defect (case 4). Mechanical load (contact) and crack were absent. The deformation plot scale factor was set to 100 for clarity. Units in MPa.

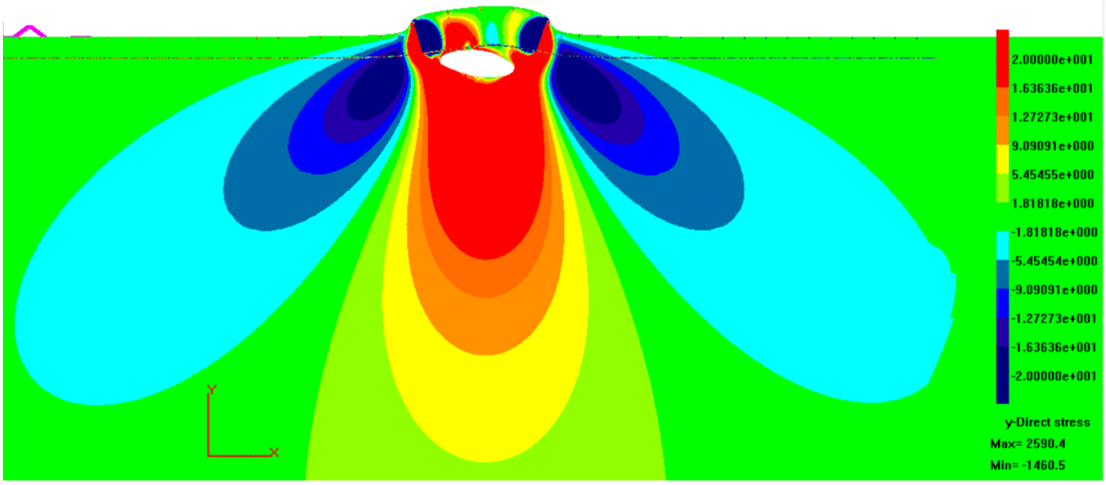

Figure 5-18 Deform vertical stress plot for the case where thicker expansion layer is present above the defect (case 5). Mechanical load (contact) and crack were absent. The deformation plot scale factor was set to 100 for clarity. Units in MPa.

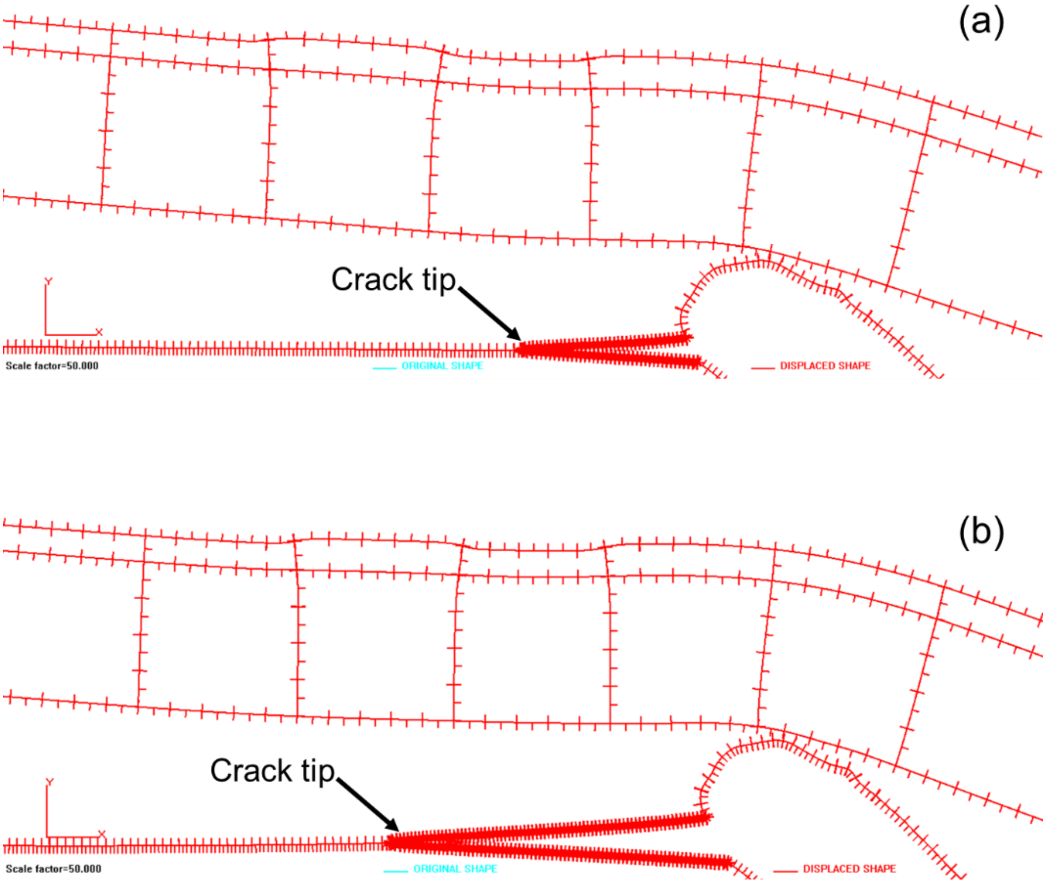

Figure 5-19 Deformed plot for the case where patches of thin expansion layer are present above the defect (case 4) focusing on the left crack tip. Mechanical loads (contact) were absent. The deformation plot scale factor was set to 50 for clarity. (a) 1 mm crack size. (b) 2 mm crack size.

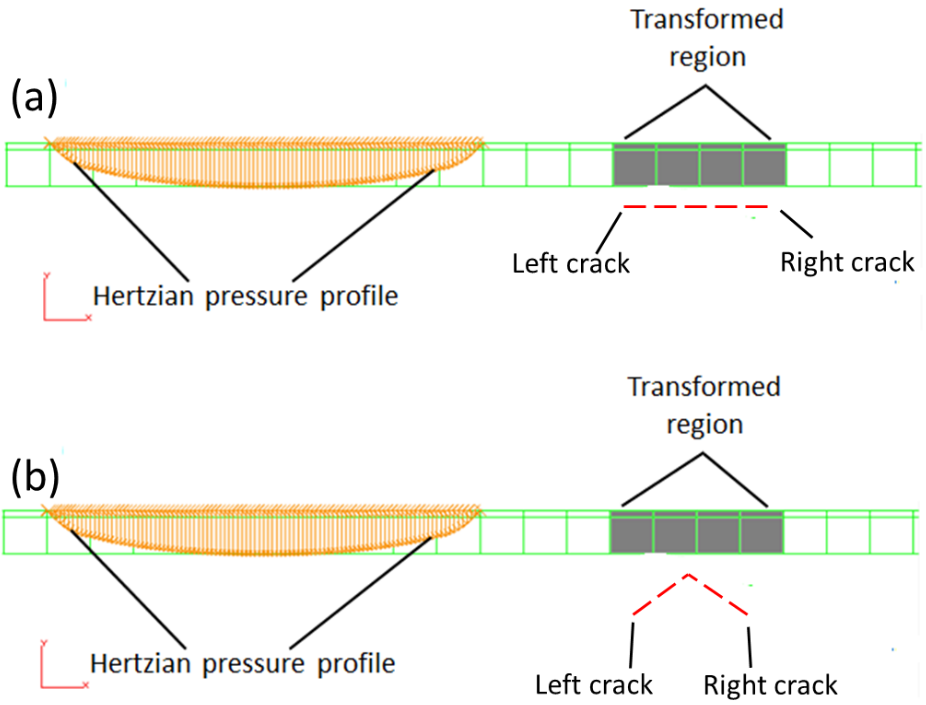

Figure 5-20 Comparison between different modelling defect configuration. (a) horizontal crack. (b) incline crack.

CHAPTER 6

DEFECT DETECTION IN RAIL WITH THE APPLICATION OF DIGITAL IMAGE CORRELATION

6.0 Introduction

Regular track inspection is one of the processes to ensure continuous safety and reliability in train operation. The current practices to perform track inspection are normally by visual inspection to check the general condition of the track and its components, measurement of rail profile to check the rail profile remains within acceptable limit, assessment of track geometry to ensure the correct spacing between the rail, and detection of flaws and cracks in the rail to ensure the rails are free from defects such as rolling contact fatigue cracks.

In order to ensure the rails are free from defects, a method that could detect the presence of defects (surface and internal defects) will be discussed in this chapter. By incorporating digital image correlation (DIC) technique, this method was found to be reliable and effective to detect damage in rails. Type of defects that have been considered is common defects that are found in rail such as pitting, gauge corner crack, surface crack, and also squat type defect.

6.1 Background

Since the derailment incident in Hatfield that cause fatalities to four innocent lives due to improper maintenance actions [175], the focus of rail research has changed tremendously to avoid this tragic incident from happening again. An investigation that was conducted following the incident led to a discovery that more than 2000 sites of United Kingdom network possess cracks that could result in the development of catastrophic fracture and subsequent fragmentation of a rail [176]. Since then, numerous research has been carry out which focused on defect study such as the effect of multiple crack interaction that could leads to RCF [62], the effect of fricion modifier on RCF and wear on the rail [63], crack growth study focussing on RCF cracks [177]–[184], and also on rail flaw detection with the application of Ultrasonic Testing, Eddy Current Test, and Phase Array Inspection [185]–[188].

Non destructive technique (NDT) is the most common technique that is widely used to detect damage in rails which comprise of either contact method (ultrasonic tranducers) or non contact method (magnetic induction, pulse eddy current, and visual cameras) [189]. Even though the methods mentioned were found reliable to detect the presence of defects particularly cracks, only visual imaging method gives add on value where the type of defects can be known through image acquired and remedial action can be taken without a need of further investigation. However, the imaging system has some drawback where it can only detect surface defect and does not provide any data on the existence of flaws within the material. Therefore it will be interesting to develop a method that not only could detect the presence of defects (surface or subsurface), but also would provide additional information that could be used for further analysis. It is also essential to ensure that the method could be incorporated with the automated track inspection system so that disruptions and delay that could cause an increase in overhead cost can be avoided.

In this study, a method that utilizes Digital Image Correlation (DIC) has been developed for defect detection in the rail. DIC operates by comparing digital images of a material at different level of deformation. It is well known that DIC have been used widely for asessment of in-plane (2 Dimensional) or out of plane (3 Dimensional) deformation [190]. Recent advancement in cracks studies has also utilized DIC techniques as being reported in [191]–[198]. However, there was limited use of DIC in the rail application where the DIC techniques were only applied to monitor and measure vertical displacement in rails and bridges [199]–[201]. By considering the scenario where crack would open in the tensile region under bending load during the passage of the train (Figure 6-1) [202], samples containing surface and internal defects was loaded under 4 point bend test where DIC technique have been integrated during the bending test to provide images of deformation at different stages of loading. Further analysis of the DIC results was carried out to identify the difference in the outcome between the sample containing internal defects as compared to sample that only contained surface defects. A Boundary Element (BE) model that contained a different type of defect that does not present in the testing sample was also developed to identify the potential of the method to detect the presence of different type of defects.

6.2 Specimen preparation and test method

6.2.1 Internal defect identification

Two R260 grade rails with a profile of 60E1 that contained defects have been removed from service and were selected as the samples for the initial UT investigation. The first rail had a length of 1.24 m while the other was 1.378 m. Initially, the rails were brought to TATA steel Swinden Technology Centre to identify whether the rail contained internal defects and also to record the information of the defects. The test was performed using Krautkramer USM36L flaw detector and two type of transducers were used which were the 0° angle to detect horizontal cracks and also the 70° angle transducer to detect the transverse crack. The estimated location of any crack identified from the initial test was marked on the gauge side of the rail as shown in Figure 6-2.

6.2.2 Detail Ultrasonic Testing investigation

Since the main objective of the initial UT investigation was only to identify whether the sample contained internal defect or not, a more detailed UT investigation was performed on the sample using GM100 ultrasonic thickness gauge (Figure 6-3) to identify the exact position of the internal defects, map its position, measure its depth and length, and also to estimate where to section the rail for sample preparation for DIC test. A gridding technique that was introduced by Kaewunruen and Ishida was adopted where a 10 x 10 mm grid was drawn on the rail surface to ease the mapping process of the internal defects on the rail surface [203]. Instead of using 10 x 10 mm grid, a finer grid of 5 x 5 mm was implemented in order to map a finer detail of any internal defects found (Figure 6-4). The transducer was moved on each grid box and any internal defect found was mapped and its depth from the surface was recorded (Figure 6-5). From the results, four samples were selected to be used for bending test. The criteria for the selection were based on the sample with largest (Sample A), medium (Sample B), and smallest (Sample C) internal defect size. A sample without any internal defect (Sample D) was also selected to be used for comparison. All of the 4 samples were machined 30 mm from the railhead surface to remove the rail foot and were sectioned to a length of 500 mm as shown in Figure 6-6. This gives a final dimension of each sample to be 500 x 72 x 30 mm.

6.2.3 Four point bending test with application of Digital Image Correlation

Prior to the bending test, all of the samples (Sample A, B, C, and D) were painted with white acrylic-based aerosol spray on the railhead surface as an undercoat to avoid any reflection during the test. Random speckles were then created on the sample surface using matt black acrylic-based aerosol spray. Figure 6-7 shows the example of random speckles pattern created on one of the samples.

A four point bend test was performed on the sample so that the maximum flexural stress is uniform over the section of the rail between loading points covering the area where the defect is located. Figure 6-8 shows the schematic diagram of the four point bending test used in the experiment. Schenk 250kN top down machine was used to bend the sample vertically while 3D DIC techniques were incorporated during the bending test to identify any deformation that happened on the rail head surface during the test (Figure 6-9).

Each sample was loaded vertically from 0 kN to a maximum loading of 150 kN. Once the loading reached 150 kN, the sample was unloaded back to 0 kN. However, for Sample B and C, two different test were performed for each sample. For the first test, the region of interest (ROI) were focused on the area containing internal defect while for the second test, the ROI focused on the area without any internal defects as shown in Figure 6-10 and Figure 6-11. The loading and unloading rate for each sample was set to be 0.5 kN/s. Consecutive images of the ROI for each loading/unloading cycle were captured by two digital cameras, DCP 5.0 LIMESS Messtechnik & Software GmbH coupled with Schneider Kreuznach Xenoplan 2.8/50 macro lens. The stereo angle was set to be 30° which produce an ROI test size of 28 x 24 mm. Prior to the bending test, the camera system was calibrated using an 11 x 10 uniformly spaced dot pattern with a spacing of 1.5 mm between the dots. This configuration gives a calibration score (average distance between actual dot location and theoretical dot location) of 0.0786 pixels. The experimental data obtained in this test were processed with VIC-3D software from

Correlated Solutions, Inc [204]. Sixty one correlation subset size was chosen to ensure that there was a sufficiently distinctive pattern contained in the area used for correlation.

6.3 Modelling

6.3.1 Three dimensional Boundary Element Modelling

A simple 3D BE model containing defects similar to the defects found in the testing sample was developed using BEASY software package [140] where two major modelling works were conducted (i): initial modelling for validation purpose, and (ii): modelling transverse defect in rail. Instead of modelling the real geometry of the rail head, a rectangular beam with a similar dimension (maximum length, width, and height) with the testing sample was modelled for simplification as the principle still remain the same. Figure 6-12 to Figure 6-14 show the modelling condition where the model was fully constrained on a small part of the rail surface in the vertical direction (Y axis) denoted by a green triangle. Spring boundary condition (pink kink line) with a stiffness of 0.1 kN were placed in the same location of the vertical support to allow free movement on longitudinal (Z axis) and lateral (X axis) direction. Two line forces (denoted by yellow arrow) with a summation of 150 kN vertical loading covered the whole width (lateral direction) of the beam were placed on the bottom of the rail surface. This configuration matched the bending test condition as shown in Figure 6-8. Table 6-1 listed the modelling properties used in this study.

6.3.2 Initial modelling for validation purpose

To assess the acuracy of the modelling results, the results from the experimental work was compared with the results from the BE model. Two cases were considered (a): a V shape shallow angle surface breaking crack (Figure 6-12) which was similar to the defect found on Sample A, and case (b): two vertical shallow surface breaking cracks (Figure 6-13) which were quite similar to the cases where the sample only contained surface defects without any subsurface defects beneath them (Sample B1). Semi elliptical shape was used to model the crack for case (a) since it is widely used to represent surface breaking cracks in modelling studies and this kind of crack face shape often appears when a rail containing squat defect is broken open [80], [205], [206]. Two semi elliptical crack connected to each other on their crack mouth forming a V shape crack (when looking from the top) was modelled where its dimension was based on the data from the detail ultrasonic test. The major semi axis length of the larger crack was set to be 15 mm and 5 mm length for the smaller crack based on the measurement made on the defect found in Sample A. Both cracks were positioned into the material with a shallow angle of 8°. For case (b), the cracks existed vertically into the material where the subsurface crack tip was at a depth of 0.5 mm from the surface. This represents shallow depth surface breaking cracks.

6.3.3 Modelling 45° tranverse defect in rail

Further modeling work was conducted to model a transverse crack which was not present in the testing sample. The purpose of this modelling work was to identify the potential for the DIC method to detect the presence of transverse crack in rail. The model was otherwise the same as the initial model as described in Section 6.3.2. To represent a transverse crack that initiates from the surface, a semi elliptical crack with its tip growing vertically into the material was modelled where the subsurface tip was located at a depth of 15 mm from the surface. Figure 6-14 show the modelling condition for the transverse crack modelled.

6.4 Results and discussion

6.4.1 Initial Ultrasonic Testing investigation

Figure 6-15 and Figure 6-16 shows the physical appearances of the surface defect on the rail surface of Sample 1 and 2. Both samples contained 7 different areas of surface defects with internal defects underneath them. The internal defects that were detected by the initial ultrasonic test lie between 2-5 mm from the rail surface. No transverse crack was found during the initial ultrasonic investigation. Looking at the appearances of the defects on both figures, various type of defects appeared on the rail surface of both samples such as surface breaking crack, squat type defect, depression, pitting, and gauge corner crack which was normally found on the in service rail head surface. Table 6-2 and Table 6-3 summarize the details of the defects found on Sample 1 and Sample 2 from the initial ultrasonic test.

6.4.2 Detail Ultrasonic Testing investigation

Some of the results from the internal defects mapping for Sample 1 and 2 can be found from Figure 6-17 to Figure 6-19. For Sample 1, the shallowest and the deepest internal defect was found to be 1.5 mm and 3.5 mm while for Sample 2, 1.6 mm and 3.9 mm from the surface respectively. The average depth of the internal defect for both samples was between 2-3 mm from the railhead surface which is in the same range with the results of the initial ultrasonic test, but with higher precision. Based on the internal defect mapping results of Sample 1 and 2, four number of samples were selected to be used for the bending test where each sample contained different type of surface defect with different size of internal defects underneath them.

Figure 6-20 shows the defect of Sample A where it has a characteristic of the squat type defect based on the appearance of V shape surface breaking crack. The internal defects size on Sample A was found to be the largest compared to the other 3 samples. Figure 6-21 to Figure 6-23 show the defect of Sample B, C, and D respectively where Sample B has medium internal defect size while Sample C has the smallest defect size, and Sample D was free from any internal defect.

6.4.3 Four point bending test with application of Digital Image Correlation

Physical changes that happened on each sample’s surface under loading were examined. Similar results were obtained and therefore, only changes that happened on Sample A is reported in detail since it has the largest defect size (on the surface and subsurface) compared with all of the other samples. It also has superficial similarities with squat defects in rails which are a common threat to rail life. Comparison on the DIC displacement (longitudinal, lateral, and vertical) and strain plot for the surface of the other sample is made for the case where each sample was under maximum loading of 150 kN (*note: all of the images for displacement and strain plot are rotated. Rails run from top to bottom of the figures)

6.4.4 Physical changes on Sample A surface

Figure 6-24b shows the longitudinal contour plot from the bending test under initial conditions before any vertical load is applied to the sample. The V shape crack and surface pitting can be seen clearly on the contour plot, similar to what can be seen from Figure 6-24a even though the sample in Figure 6-24b was covered with paint and speckles. All these data was derived from Digital Image Correlation which looks at the movement of the speckles as the load is applied. Some white region area representing the area where correlation could not be made can be seen on the V shape crack mouth and on the largest surface pitting. Although this region is out of measuring range, their size and shape still give some useful information. As the sample was loaded under a vertical loading of 39 kN, a small white region area started to appear at the apex of the V shape crack (marked with red dashed circle in Figure 6-24c). As the load increased to 78 kN, another white region area appeared at the tip of the V shape crack mouth as shown in Figure 6-24d marked with yellow line circle. The existing white region area (red dashed circle) was found to enlarge at this point. As the sample was loaded to its maximum loading of 150 kN, both white region area (red dashed circle and yellow line circle in Figure 6-24e) was found to expand in size compared to its original size in Figure 6-24d. However, once the sample is unloaded to its final state of 0 kN loading, the white region area at the tip of the crack mouth (yellow line circle in Figure 6-24f), disappeared completely even though the white region area at the apex of the V shape crack remains (red dashed circle).

Due to an uneven surface profile of the rail (significant depth difference due to steep changes in profile) such as deep surface pitting, the speckles could not penetrate in the mouth of the pitting thus resulting in the presence of some white region area in the sample even though the sample is not yet loaded with any vertical load. As the sample was loaded to 39 kN, the area around the apex of the V shape crack (red dashed circle) experienced high deformation and initiated the opening of the crack mouth which results in the formation of the white region area (due to loss of correlation). With an increasing load, the existing white region area (red dashed circle) expands in size and more region of the crack mouth experienced high deformation which introduces a second white region area to be formed (yellow line circle). As the sample was loaded under 150 kN, the stress on the surface exceeded the material yield strength (where simple bending calculation shows that the surface experienced bending stress of 694.4 MPa while σ_{yield} = 528 MPa) which results in a wider opening of crack mouth that cause the white region areas to expand. As the sample is unloaded, the crack mouth begins to shut and once the sample reached its final condition (0kN vertical load), the crack mouth shuts completely and the speckles that have displaced earlier, return to their original position resulting in the disappearance of the white region area (yellow line circle). However, the white region area that appeared on the apex of the V shape crack (red dashed circle) still remain but with a reduction in size once the sample reached its final condition. This suggests that the area around the apex of the V shape crack (red dashed circle) experienced higher deformation compared to the other white region area (yellow dashed circle) which disable the speckles around that region to return to their initial position under final condition. By comparing the strain experienced in both region (Figure 6-25), it was found that the area around the apex of the V shape crack (red dashed circle) experienced higher deformation compared to the other white region area (yellow line circle) under loading and unloading.

6.4.5 Comparison on longitudinal displacement plot

Figure 6-26 and Figure 6-27 show the DIC longitudinal displacement plot for each sample as they were loaded to a level exceeding their Yield Strength under 150 kN vertical load. For Sample A, the displacement plot (Figure 6-26a_2) display intense contour lines concentrated around the crack faces which highlight the features of the V shape crack making it more visible similar to the features of the crack faces in the DIC ROI (Figure 6-26a_1). A similar trend was found for all of the other samples where the longitudinal displacement plot highlights the shape of any surface breaking crack. It was also noted that longitudinal contour lines were found to converge on the crack tip forming a curved line contour. This trend was also found in [207] where the curved contour formed and converged on the crack tip when the specimen is under uniaxial tensile loading. The trend also shows that for most of the samples, the magnitude of the longitudinal displacement value decrease with position along the rail from top to bottom of the figure. Only Sample B2 and Sample C2 that contained internal defect (Figure 6-26c_2 and Figure 6-27c_2) show opposite trend. The longitudinal displacement plot also enables the quantification of the number of the surface breaking cracks within the DIC ROI. The major size crack is highlighted with red dash box while smaller crack is highlighted with blue dash box in each figure of displacement plot.

The contour lines of the longitudinal displacement plot were distributed evenly parallel to each other in horizontal direction. However, due to the existence of the surface defects such as surface breaking cracks cause disturbance to the distribution of the contour lines which results in the formation of curved line contour on the crack tip. The contour line also formed around the crack faces which in the end highlighted the shape of the surface crack. The intensity of the concentrated contour line around the crack face depends on the separation of the crack face. A wider open crack face will result in the formation of more intense contour lines around the crack face. On the other hand, the displacement magnitude depends on the position of the DIC ROI in the longitudinal direction. As the ROI is located closer to the centre in the longitudinal direction, the lower the value of displacement magnitude would be.

6.4.6 Comparison on lateral displacement plot

The lateral displacement plot (Figure 6-28 and Figure 6-29) shows different trends compared to the longitudinal displacement plot. There were fewer contour lines concentrated around the crack faces that highlight the shape of the crack for most of the other sample. Only Sample A show significant contour lines concentrated around the crack faces but not as intense compared to what can be seen in the longitudinal displacement plot (Figure 6-26 and Figure 6-27). For Sample A, widely distributed curved contour (highlighted by red dash box) was formed around the V shape crack and coincide with the location of the internal defect detected earlier from the UT test (Figure 6-28a$_1$); forming a kidney shape that was normally found on a typical squat type defect (Figure 6-30a). The kidney shape still remains visible even though the sample is unloaded to its final condition (0 kN vertical load), but with a reduction in size and magnitude of the displacement. For the other samples, a similar trend of the widely distributed curved contour was found only when the DIC ROI is located within the area where the surface crack was associated with an internal defect (Figure 6-28c$_2$ and Figure 6-29b$_2$). The contour lines of the lateral displacement plot were predominantly distributed evenly parallel to each other in the vertical direction when the sample only contained surface crack which is not associated with internal defects (Figure 6-28b$_2$, Figure 6-29a$_2$, and Figure 6-29c$_2$).

The existence of the internal defects on some of the samples (Sample A, B2, and C2) results in the phenomena of the widely distributed curved contour forming around the associated surface crack. Since the surface crack has grown into the material to a certain depth, some region of material adjacent to the free surfaces remains almost unloaded as the sample bulk was loaded exceeding its yield strength during which the crack mouth opens. Such opening causes disturbance to the uniformity of lateral displacement where the distribution will follow the shape of the crack mouth opening which forms the widely distributed curved contour. As for the sample where the surface crack is not associated with any internal defect (Sample B1, C1, and D), the size of the crack mouth opening is very small since the surface breaking crack grew very shallow into the material with shorter crack length and there is little unloaded material. Results from modelling work show that the opening of the crack mouth depends on the ratio between the crack length and its depth. The deeper the crack grows into the material, the wider the crack mouth opening.

6.4.7 Comparison on vertical displacement plot

The plot of vertical displacement contour (Figure 6-31 and Figure 6-32) shows almost identical trend between each sample. The only difference is that, for Sample A, B2, and C2, widely distributed curved contour was formed on the tip of the surface crack as shown in Figure 6-31a$_2$, Figure 6-31c$_2$, and Figure 6-32b$_2$ (highlighted by red dash box) while for Sample B1, C1, and D, the trend looks identical to each other (Figure 6-31b$_2$, Figure 6-32a$_2$, and Figure 6-32c$_2$). The magnitude of the vertical displacement was found to decrease from left to right of the vertical displacement plot. The range of maximum vertical displacement for each sample under 150 kN vertical loading was between 3.6 - 4.4 mm. As each sample was loaded to 150 kN and unloaded back to their final condition (0 kN vertical load), there was some variation on the final vertical displacement value ranging between 0.7-0.9 mm. Figure 6-33 show the comparison on the vertical displacement plot for Sample B1 during initial condition and its final state condition.

The variation in the final vertical displacement value for each sample indicates that each sample was loaded exceeding their Yield strength and cause the material to be permanently deformed vertically (bent) between 0.7 - 0.9 mm. Due to the high load applied on the sample especially when the stress around the crack exceeded yield stress of the material, this has resulted in the formation of curved contour at the crack tip for the sample containing an internal defect. This suggests that the stress around the crack tip has exceeded the yield strength and caused the mouth to stretch open. The formation of the elliptical contour is load related where it started to appear as the sample is loaded exceeding its yield strength and becoming larger in size and magnitude with an increasing load. However, the elliptical contour totally dissapeared as the sample is unloaded to 0 kN which indicate that the crack mouth has completely shut.

6.4.8 Comparison on major principal strain plot

The overall trend for each strain plot looks alike whereby highest strain value (red fill) was found filling up the crack face on each strain plot in Figure 6-34 and Figure 6-35 which significantly highlighted the shape of the crack. Based on the strain plot, it is easier to quantify the number of the defects since the features of each defect are clearer compared to the longitudinal displacement plot. There were also some significant differences from the expectation for a sample containing an internal defect, a contour of a fish tail shape was formed at the surface crack tip (highlighted with red dash box) as shown in Figure 6-34a_2, Figure 6-34c_2 and Figure 6-35b_2. The same phenomena do not exist for the sample which does not contain internal defect (Sample B1, C1, and D) eventhough the sample was loaded to a maximum load of 150 kN.

Principal strain plot combines all the axes of deformation where all the ‘clues’ are captured here making the finding clearer. Sample A experience highest range of strain compared to the other sample because the size of the defect in Sample A was significantly larger compared to the defects in the other samples. This will results in more deformation happened on the material within the defect, and it will be expected that high strain will accumulate under cylic loading (from repetetive train passed). Any crack face will experience the highest strain compared to the neighbouring material under loading. When a defect such as crack is under stress, the particular area will experience higher stress concentration due to high stress localization, making the material around displace more compared to the other area where defect does not exist. The material avove the defect also becomes unloaded in bending configuration. The phenomena of fish tail contour that only occured for samples containing internal defect shows that the particular area is unsupported and would be the best path for the crack to grow (depending on the microstructure around the crack tip). Any internal defect will give a rise on the stress localization at the surface crack tip thus producing the fish tail contour ahead of the surface crack tip. According to Pattaky, the contour that formed ahead of the crack tip in strain distribution represent the plastic zone area [208]. The plastic strains that accrued during a loading cycle with an existence of crack will results in the development of plastic zone ahead of the crack tip [106]. The symmetrical shape of the plastic zone (fish tail contour) found on the strain plot suggest that the material is under mode I pure loading. It is expected that if the sample remains in service, the surface crack tip will propagate according to the direction of the plastic zone shape. At this point, it is conclusive that the strain plot gives an essential information on the number of surface defects, physical appearances, internal defects indication, and also grow path of the defects.

6.4.9 Three dimensional boundary element modelling

6.4.9.1 Initial modelling for validation purpose

Figure 6-36 and Figure 6-37 were generated to show a comparison of the displacement plots between modelling and experimental results for Sample A and B1. The internal crack was represented in the BEASY model as described in Section 6.3.2. Looking at the results, there is good agreement between the modelling work and experimental work. For Sample A, the formation of the curved contour that converges on the crack tip is well predicted by the model in the longitudinal displacement plot (Figure 6-36a_1). The formation of the wide curved contour on the lateral displacement plot (Figure 6-36b_1) due to the opening of the crack face was also predicted by the model similar to what can be seen from the experimental displacement plot (Figure 6-36b_2). In addition, the model also manages to display the opening of the crack tip where the formation of the widely distributed curved contour can be seen at the crack tip in both modelling and experimental vertical displacement plot (Figure 6-36c_1 and Figure 6-36c_2). The crack mouth opening phenomena was observed from the deformed image (Figure 6-38) in modelling work of Sample A. It can be seen that under loading of 150 kN, only a small part of the crack experienced the opening of the crack mouth (pointed by black arrows in Figure 6-38).

The longitudinal displacement plot from the modelling work for Sample B1 (Figure 6-37a_1) also show a similar trend with Sample A modelling results. No intense contour line that could highlight the features of the crack were concentrated on the two shallow surface crack that has been modelled. However, there was some disturbance on the distribution of the contour lines which located around the surface crack indicating an existence of a surface defect. On the other hand, similarities can be seen between the lateral displacement plot for modelling and the experimental whereby the formation of arrow contour on the crack tip where the apex is pointing to the left of the page can be seen on both the model and experimental plots (Figure 6-37). Although principal strain plot is valuable where it gives essential information such as the number of defects, appearances, etc, it was not available directly from the modelling software. Therefore displacement plot is used to make a comparison between the model and experimental results.

6.4.9.2 Modelling 45° transverse defect in rail

The comparison of the modelling output for longitudinal and lateral displacement plot between transverse crack, shallow surface crack (similar to sample B1), and the V shape surface breaking crack (representing sample A) is shown in Figure 6-39. The longitudinal displacement plot show similar trend for all of the case modelled where curved contours were found to converge on the crack tip. On the other hand, some significant difference can be found from the trend of the lateral displacement plot. The formation of the wide curved contour due to the opening of the crack face for the transverse defect (Figure 6-39b_1) shows a symmetrical contour formation compared to models of Sample B1 (Figure 6-39b_2) and Sample A (Figure 6-39b_3).

45° transverse defect will have a symmetrical crack face opening due to its orientation where it grows deep vertically into the material without any angle. Since the crack on Sample A grew into the material with a shallow angle, the opening of the crack face will be asymmetrical where one side of the crack face will open on the surface while the other side opens into the material as shown in Figure 6-40. This will affect the distribution of the contour line and results to a different formation of the wide curved contour on the lateral displacement plot. The difference on the crack face opening phenomena gives a very good indication to distinguish between transverse defect with another type of defect.

6.5 Summary

The limitations (high cost, inaccurate output, delays) of some current practice on crack detection in rail has provided a need to develop a non contact method that could detect the presence of defects along with additional information that could be used for further analysis. The results show that DIC technique was found to be useful not only for defect detection in rail, but also provide additional information such as defect visualization, defect population, and maximum strain field location. On top of that, defect with a smaller size which could not be observed by naked eye can be visualized easily using this technique. The results in this chapter represent a proof of concept, but much further work is needed to move towards a robust technique for application in the field.

The BE modelling technique was found to be reliable for modelling different type of defect since the modelling results show good agreement with the experimental results. Modelling results show that there is a clear indication to distinguish between transvere defect with another type of defect based on the opening of the crack face. Therefore there is a high potential for this method to detect the presence of transverse defect to overcome the limitation of the current defect detection practice. If this method can be combined with the ultrasonic method, further analysis can be made using the modelling technique to estimate the life of the rail containing a different type of defect. Testing on a full scale rail along with modelling different type of defect such as defects that initiated from the subsurface is the subject of future research to extend this proof of concept.

6.6 Tables and figures

Table 6-1 R260 grade rail properties used in the modelling section, taken from [209]

Properties	Value
Ultimate tensile strength	923MPa
Yield strength	528MPa
Young Modulus (E)	210 GPa
Poisson ratio	0.25

Table 6-2 Details of the defects found on Sample 1. Sample length 1240mm. Location of the surface defect and subsurface defect (mark on the gauge corner of the rail) was determined from left to right of Figure 6-15.

Image number	Description	Location of surface defect (cm)	Location of subsurface defect (cm)
1	V surface crack	24.5-25.5	22-26.5
2	V surface crack	31-32 , 33.5-34.5	29.5-34.5
3	Surface crack	39-40	39-39.5
4	Depression (dark marking)	45-46	45.5-46
5	Squat	86.5-87.5	85-89
6	Surface crack	92-93	91-94
7	Surface crack	108-108.5	107.5-108.5

Table 6-3 Details of the defects found on Sample 2. Sample length 1378mm. Location of surface defect and subsurface defect (mark on the gauge corner of the rail) was determined from left to right of Figure 6-16

Image number	Description	Location of surface defect (cm)	Location of subsurface defect (cm)
1	Squat	17-20.5	17-19.5
2	Squat	28.5-30.5 , 32-33.5	28-33
3	Depression (dark marking)	39.5-40.5	40-42
4	Baby squat (very small squat)	69-69.5	69-70
5	Baby squat (very small squat)	75.5-77	75-78
6	Surface crack	91.5-95	91-96
7	Surface crack	102	101.5-102.5

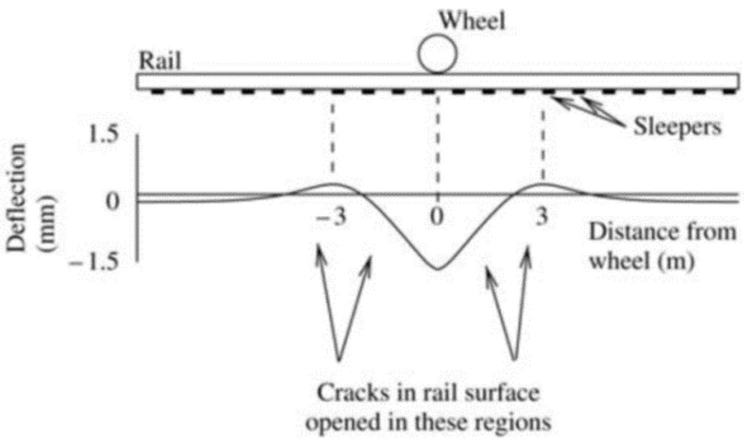

Figure 6-1 Vertical deflection of a rail due to bending load from a single wheel [202]

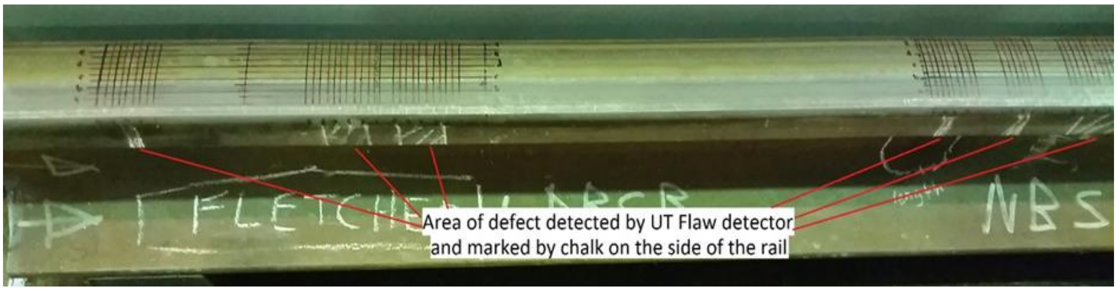

Figure 6-2 Sample 1 has been marked on its side showing an estimated location of the defect.

Figure 6-3 GM100 ultrasonic thickness gauge couple with 10mm diameter transducer. Working frequency 5MHz, accuracy ±1%, and thickness measuring range of 1.2-225mm (steel).

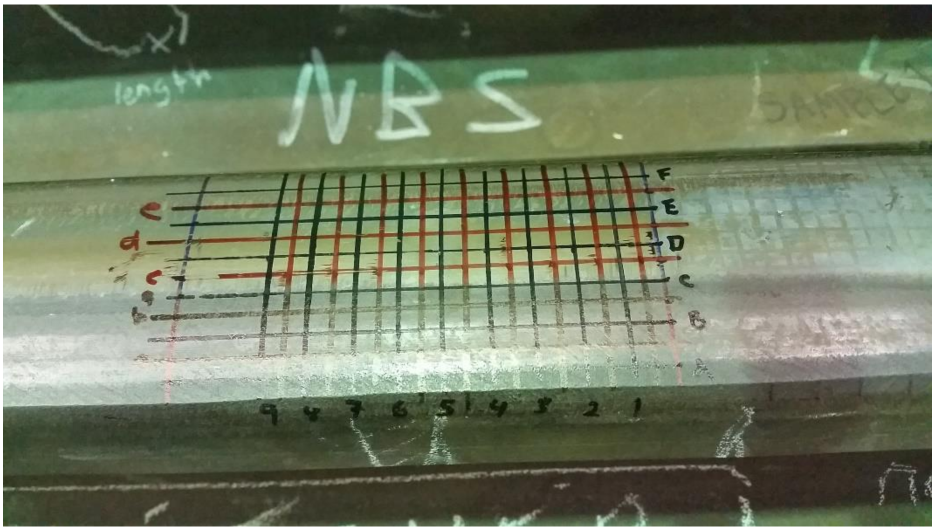

Figure 6-4 A 5x5mm grid drawn on the rail surface to map the location of subsurface defects

Figure 6-5 Internal defect was identified on Sample 1 with a depth of 2.2mm from the rail surface.

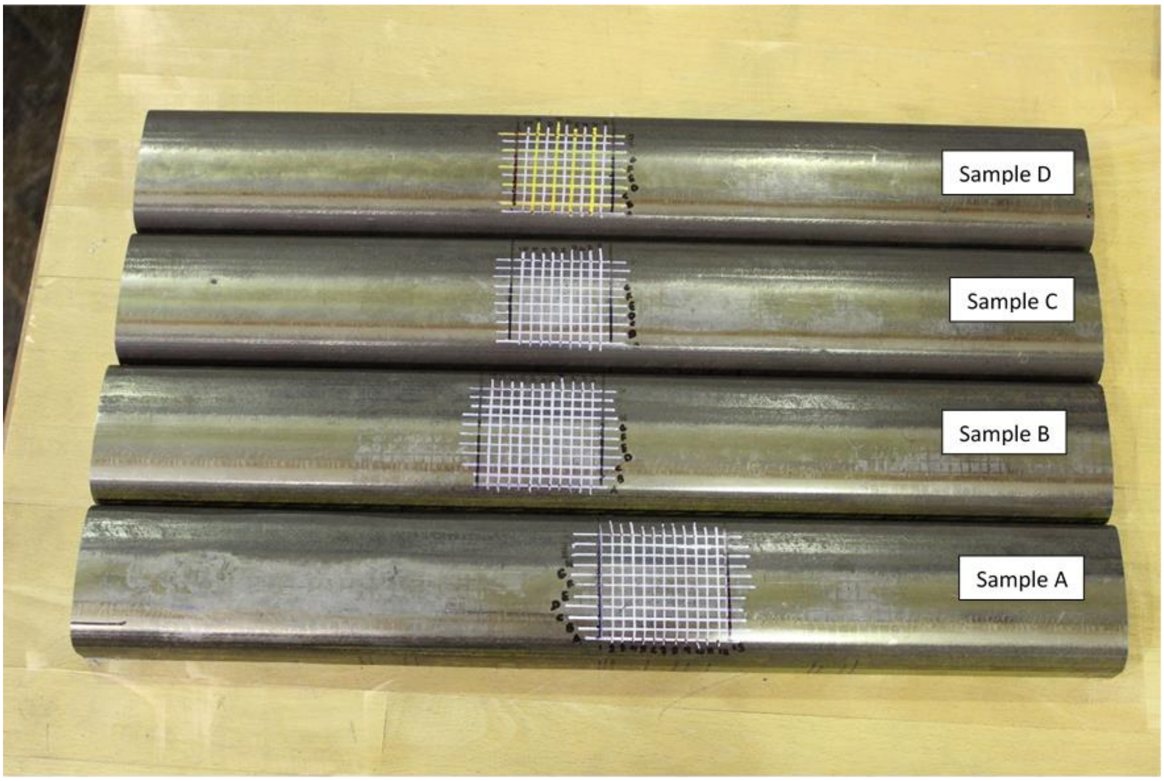

Figure 6-6 Four samples have been selected and machined 30mm from the railhead surface and section to a length of 500mm for bending test.

Figure 6-7 Random speckles pattern created on Sample A

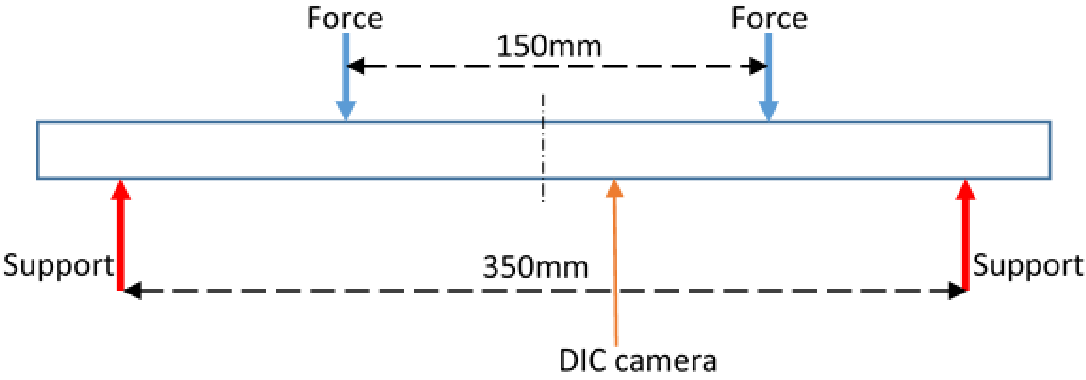

Figure 6-8 Schematic diagram of the four point bending test which incorporates 3D DIC technique

Figure 6-9 Four point bending test with application of DIC

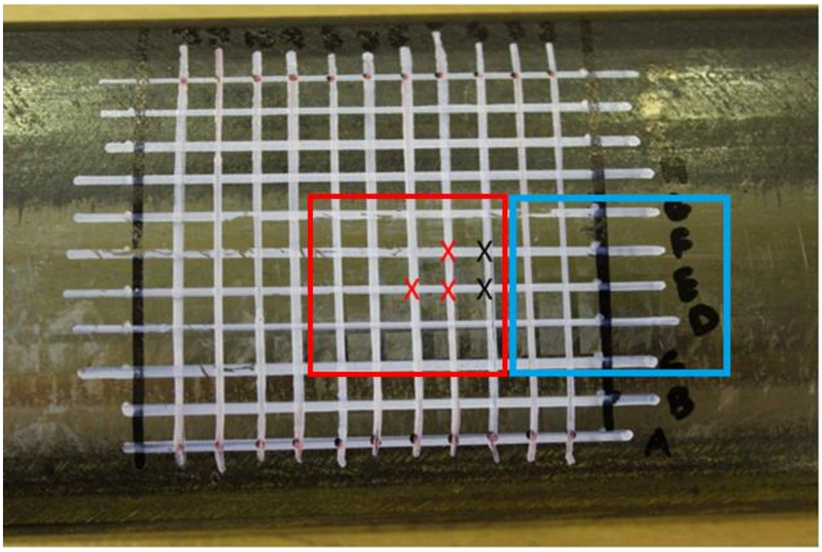

Figure 6-10 Two different regions of interest (ROI) considered for Sample B. Red square denotes the area containing internal defect (first test) while the blue box is free from internal defects (second test). 'X' marked the location of internal defect

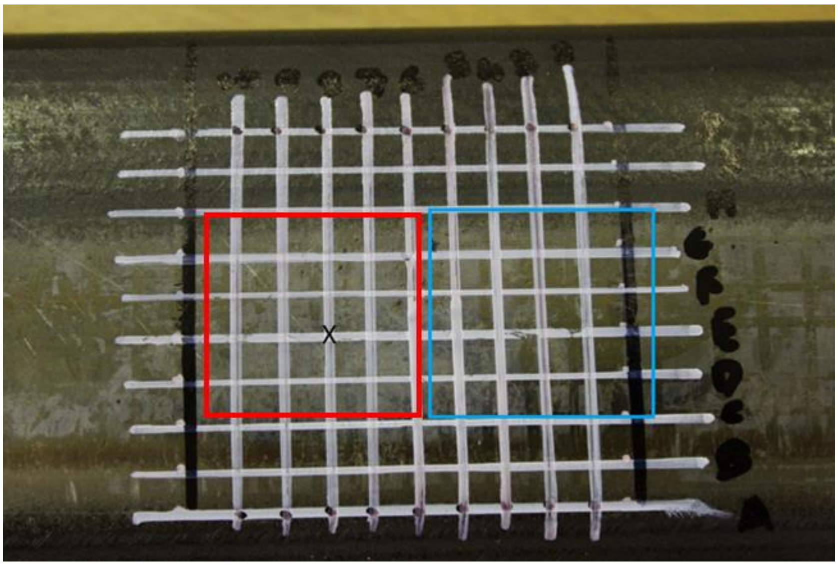

Figure 6-11 Two different regions of interest (ROI) considered for Sample C. Red square denotes the area containing internal defect (first test) while the blue box is free from internal defects (second test). 'X' marked the location of internal defect

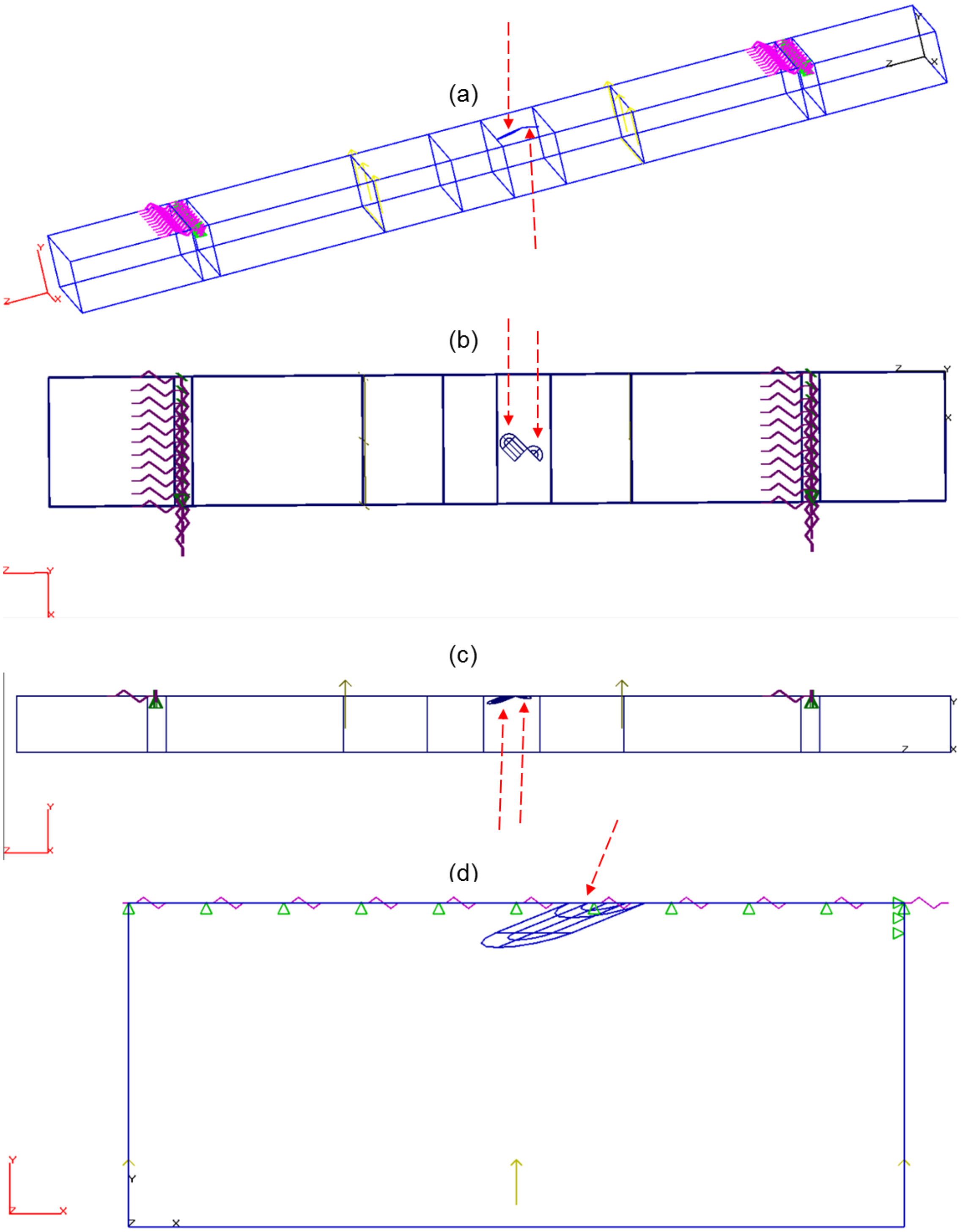

Figure 6-12 BEM model for V shape shallow angle surface breaking crack (similar to Sample A). Green triangle represents full constraint in the vertical direction (Y axis), pink kink line depicts spring boundary condition with a stiffness of 0.1kN in longitudinal (Z axis) and lateral (X axis) direction, yellow arrow potray line force contact and red dashed arrow showing the location of the semi eliptical crack. (a) isometric view. (b) top view. (c) front view. (d) side view.

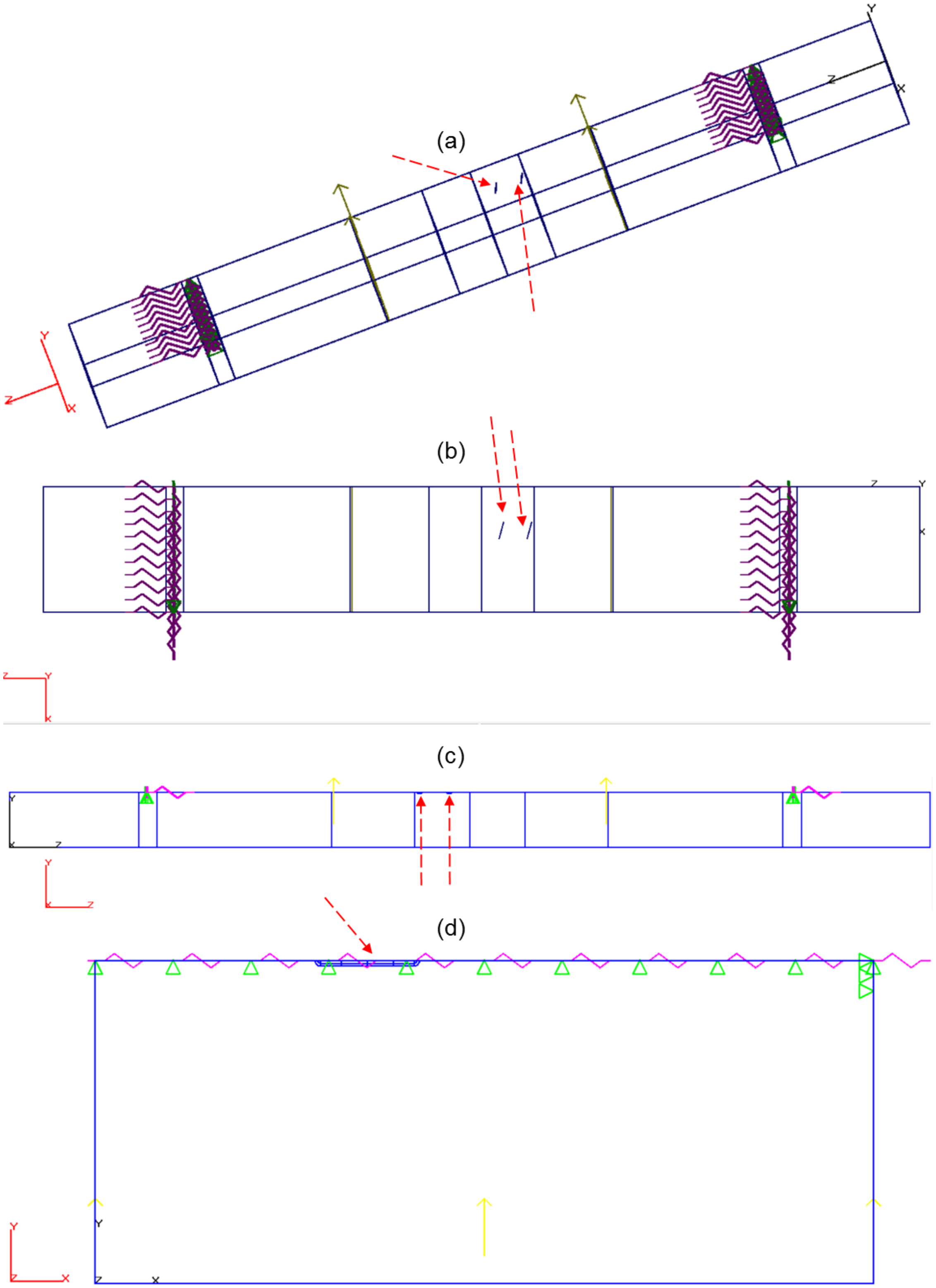

Figure 6-13 BEM model for vertical shallow surface breaking crack (similar to Sample B1). Two cracks were modelled instead of three (Sample B1). Green triangle represents full constraint in the vertical direction (Y axis), pink kink line depicts spring boundary condition with a stiffness of 0.1kN in longitudinal (Z axis) and lateral (X axis) direction, yellow arrow potray line force contact and red dashed arrow showing the location of the semi eliptical crack. (a) isometric view. (b) top view. (c) front view. (d) side view.

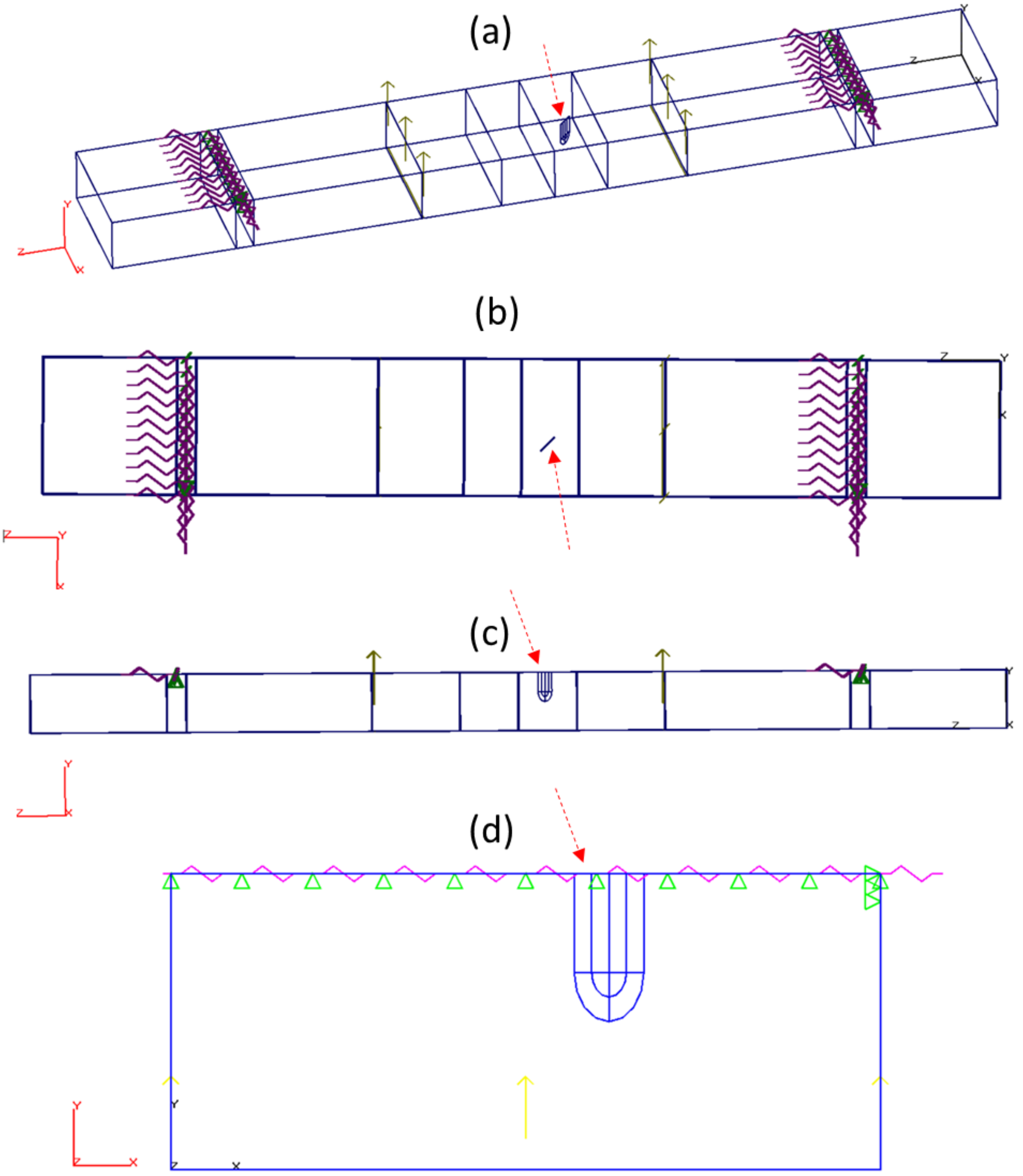

Figure 6-14 BEM model for transverse crack. Green triangle represents full constraint in the vertical direction (Y axis), pink kink line depicts spring boundary condition with a stiffness of 0.1kN in longitudinal (Z axis) and lateral (X axis) direction, yellow arrow potray line force contact and red dashed arrow showing the location of the semi eliptical crack. (a) isometric view. (b) top view. (c) front view. (d) side view

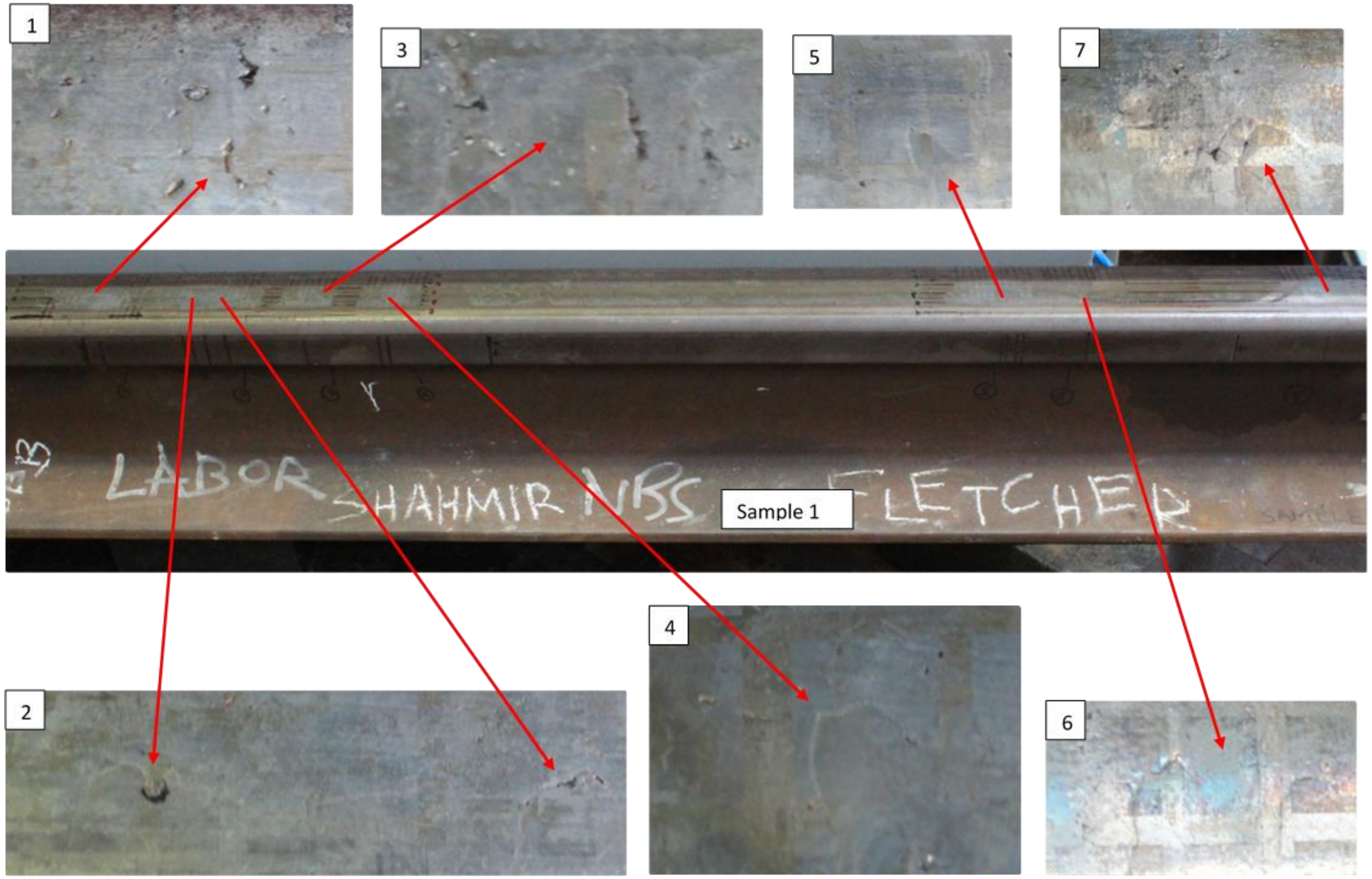

Figure 6-15 Defect appearance on the rail surface of Sample 1 which contained internal defect underneath them. The red arrow shows the location of each defect on the rail surface.

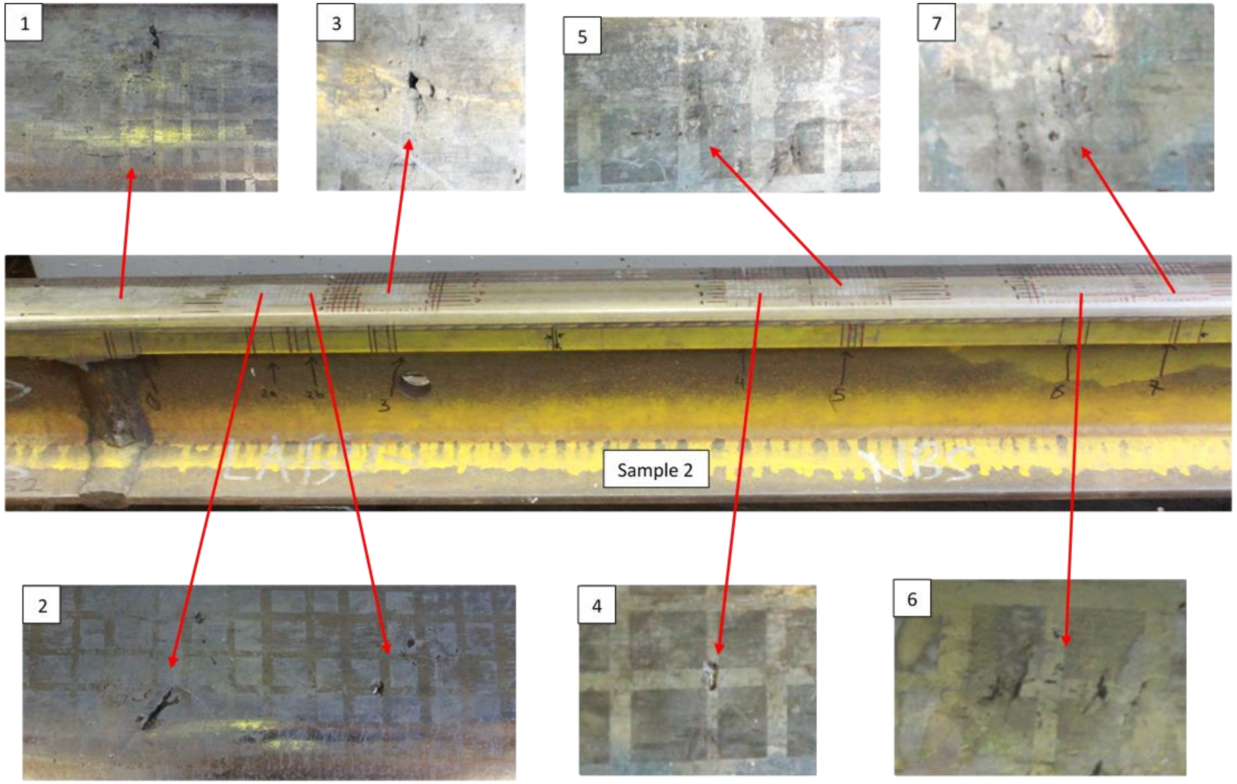

Figure 6-16 Defect appearance on the rail surface of Sample 2 which contained internal defect underneath them. The red arrow shows the location of each defect on the rail surface.

	1	2	3	4	5	6	7	8	9	10	11	12	13	14	15
A															
a															
B															
b															
C							2.2								
c						2.6		2.4							
D					3.5										
d						2.1									
E															
e															
F															

Figure 6-17 Internal defect mapping and its depth from the surface for Sample 1, defect 5. Colours represent the depth of defect from the surface. Black: 1.0 – 1.9 mm, blue: 2.0 – 2.9 mm, and red: 3.0 – 3.9 mm.

	1	2	3	4	5	6	7	8	9	10	11	12	13	14	15
A															
a															
B															
b						3.3									
C							3.5								
c						1.6		2.4		3.2					
D							3.3		2.3		3.5				
d						2.6		1.7		3.3					
E									1.8		1.6				
e															
F															

Figure 6-18 Internal defect mapping and its depth from the surface for Sample 2, defect 1. Colours represent the depth of defect from the surface. Black: 1.0 – 1.9 mm, blue: 2.0 – 2.9 mm, and red: 3.0 – 3.9 mm.

	1	2	3	4	5	6	7	8	9	10	11	12	13	14	15
A															
a															
B					1.8		2.1								
b				2.5		2.1				2.2					
C			3.2		2.6		2.3				2.3		3.8		
c				2.7		3.2		3.3							
D															
d															
E															
e															
F															

Figure 6-19 Internal defect mapping and its depth from the surface for Sample 2, defect 2. Colours represent the depth of defect from the surface. Black: 1.0 – 1.9 mm, blue: 2.0 – 2.9 mm, and red: 3.0 – 3.9 mm.

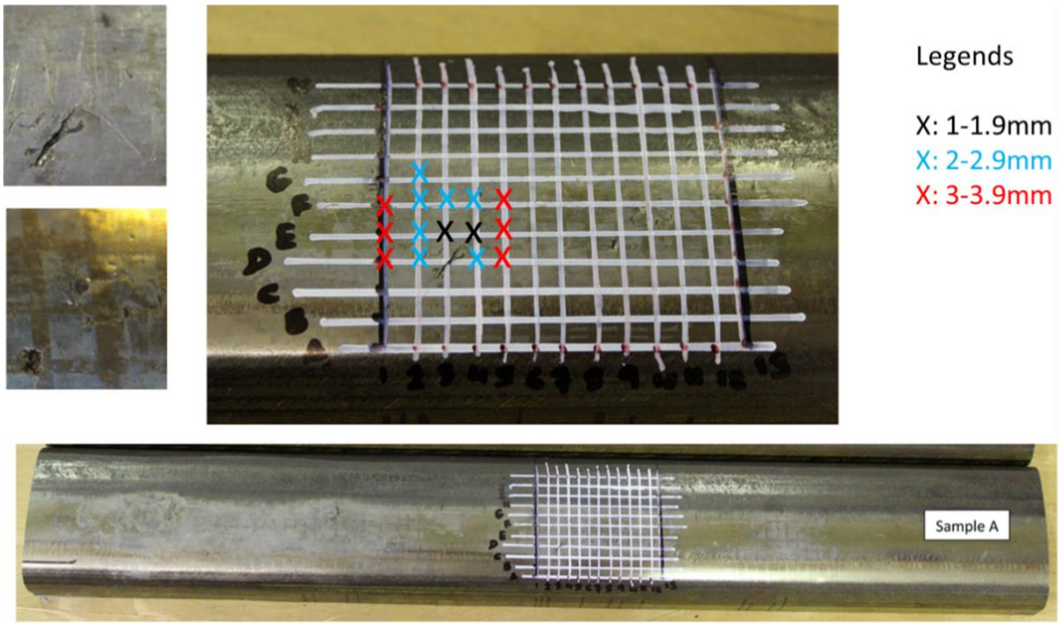

Figure 6-20 Sample A - Squat type defect with largest internal defect size. 'X' marked the location of the internal defect.

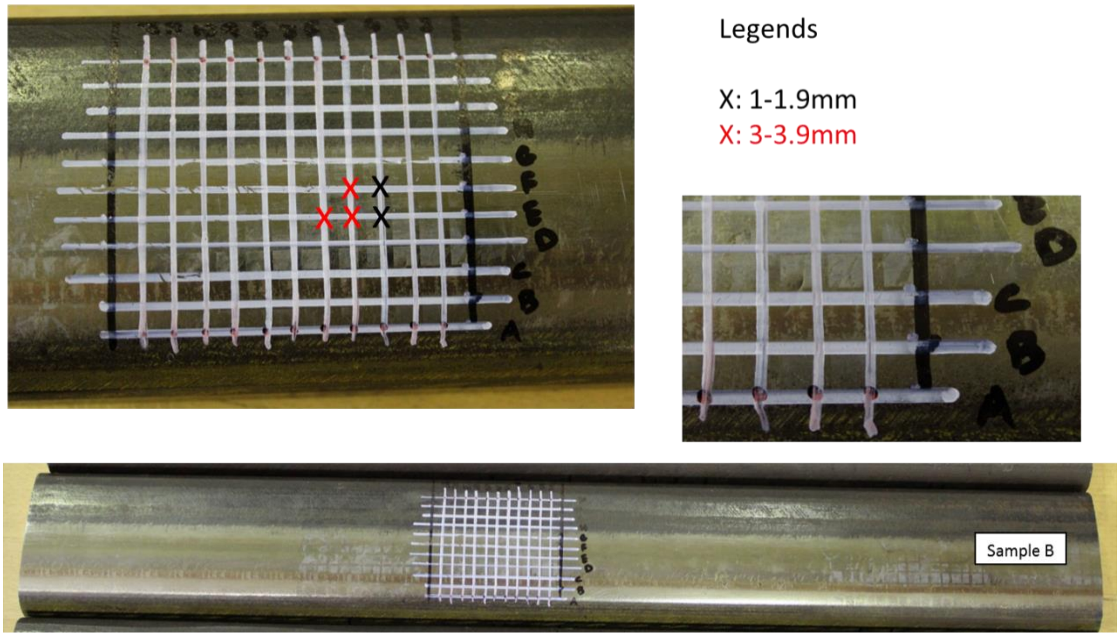

Figure 6-21 Sample B – Baby squat defect with medium internal defect size. 'X' marked the location of the internal defect.

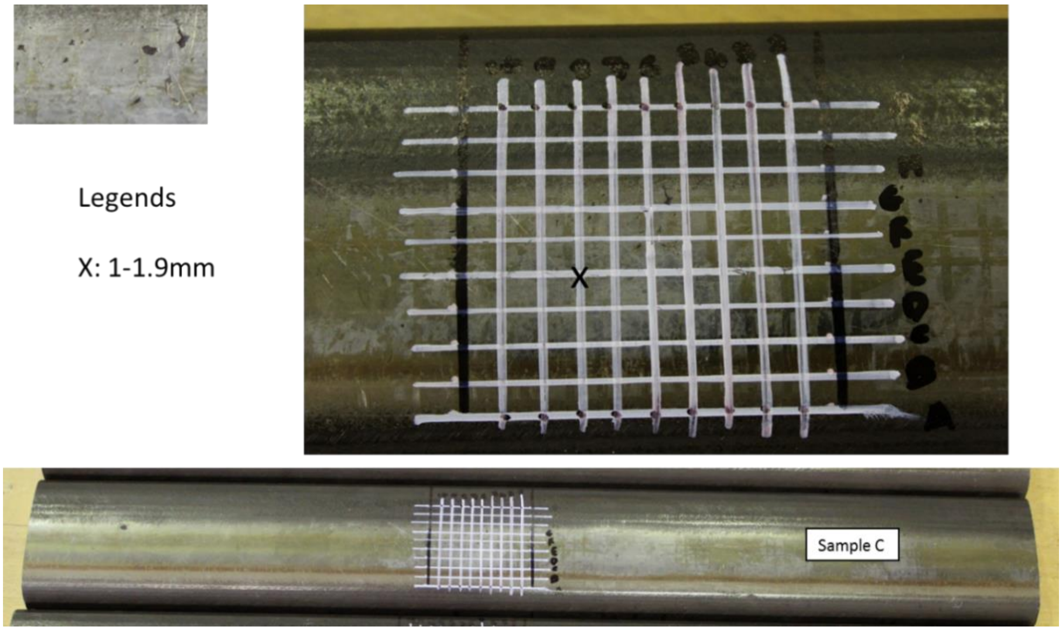

Figure 6-22 Sample C – Pitting and surface breaking crack with smallest internal defect size. 'X' marked the location of the internal defect.

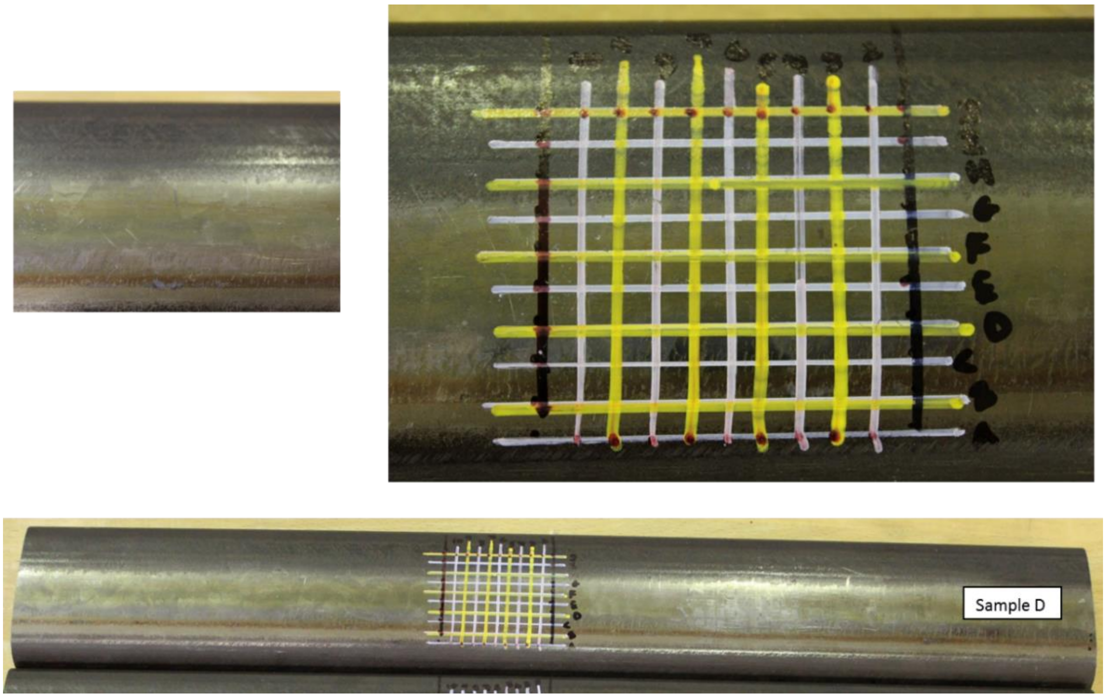

Figure 6-23 Sample D – Surface crack without any internal defects

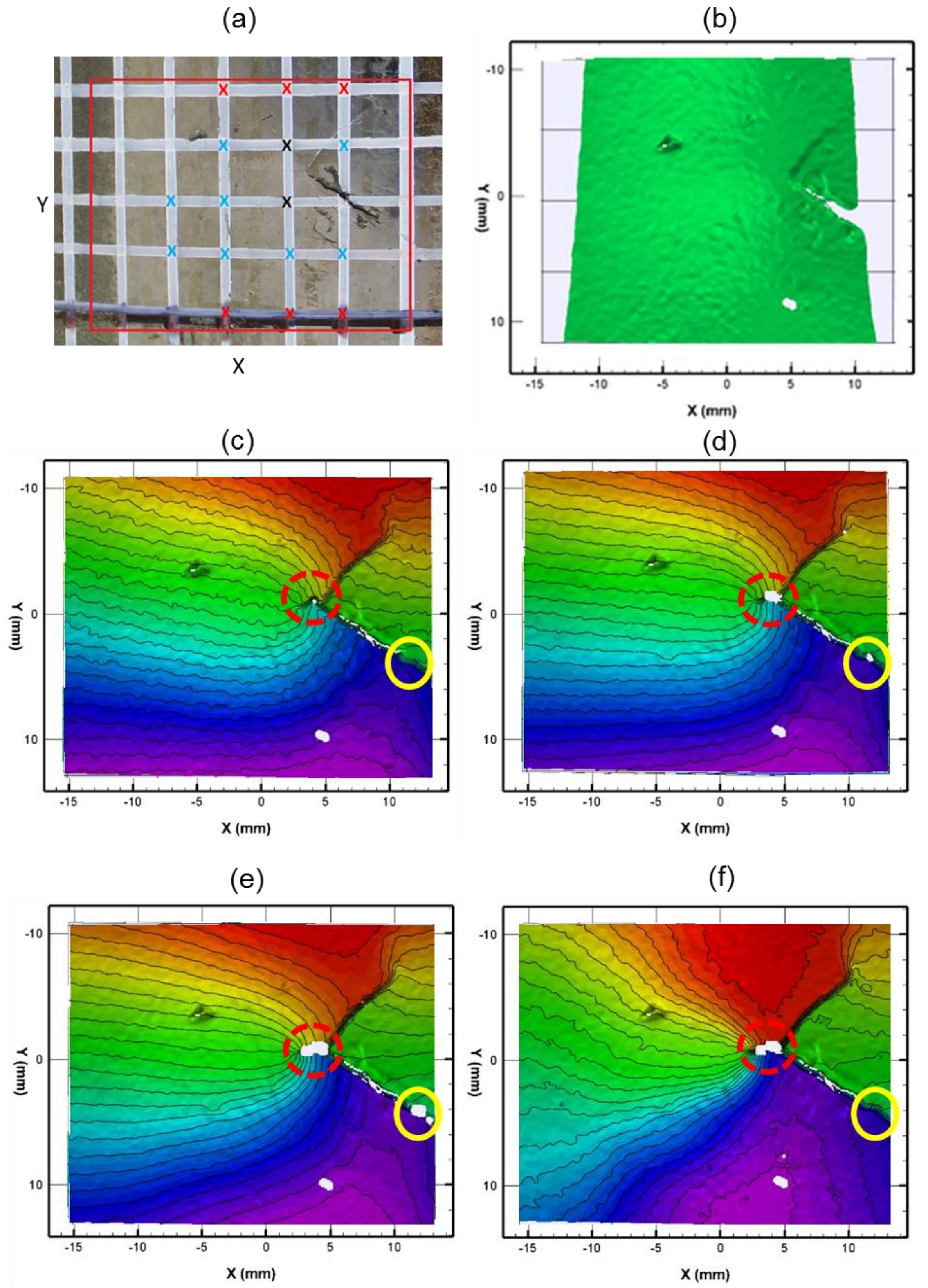

Figure 6-24 DIC ROI and longitudinal displacement plot for Sample A in the XY plane. (a) Image of the defect taken with a normal digital camera before bending test, red box represent the area for DIC ROI and X marked the location of the internal defect. (b) Longitudinal displacement plot from the DIC before the load is applied- initial condition. (c) Longitudinal displacement plot under vertical loading of 39 kN. (d) Longitudinal displacement plot under vertical loading of 78 kN. (e) Longitudinal displacement plot under vertical loading of 150 kN. (f) Longitudinal displacement plot once the test ended, final state.

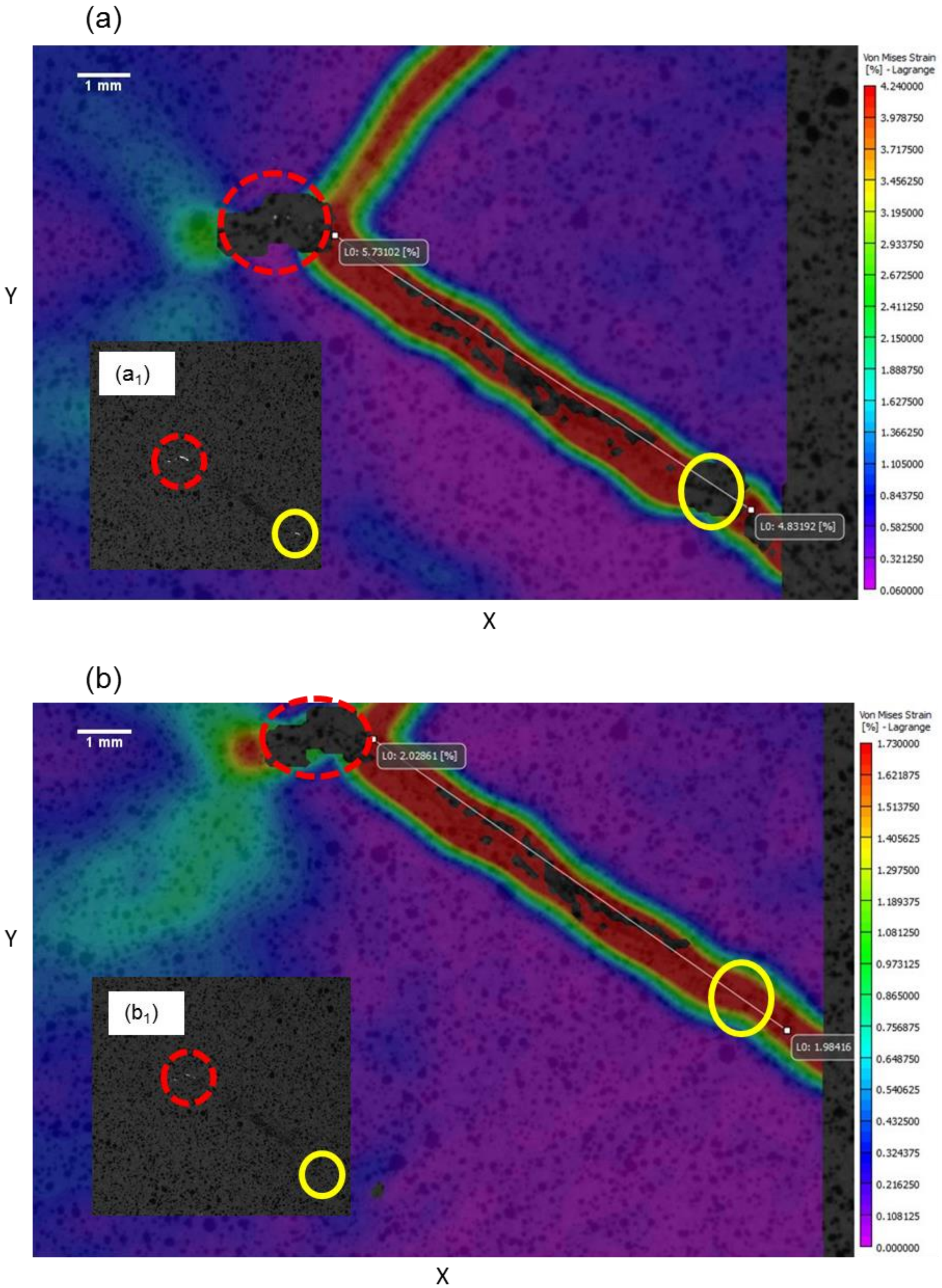

Figure 6-25 Von Mises Strain percentage for V shape crack on Sample A under: (a) maximum loading of 150 kN, (b) unloaded to final condition of 0 kN. (a1) and (b1) focused on the V shape crack with speckle pattern covering the sample surface.

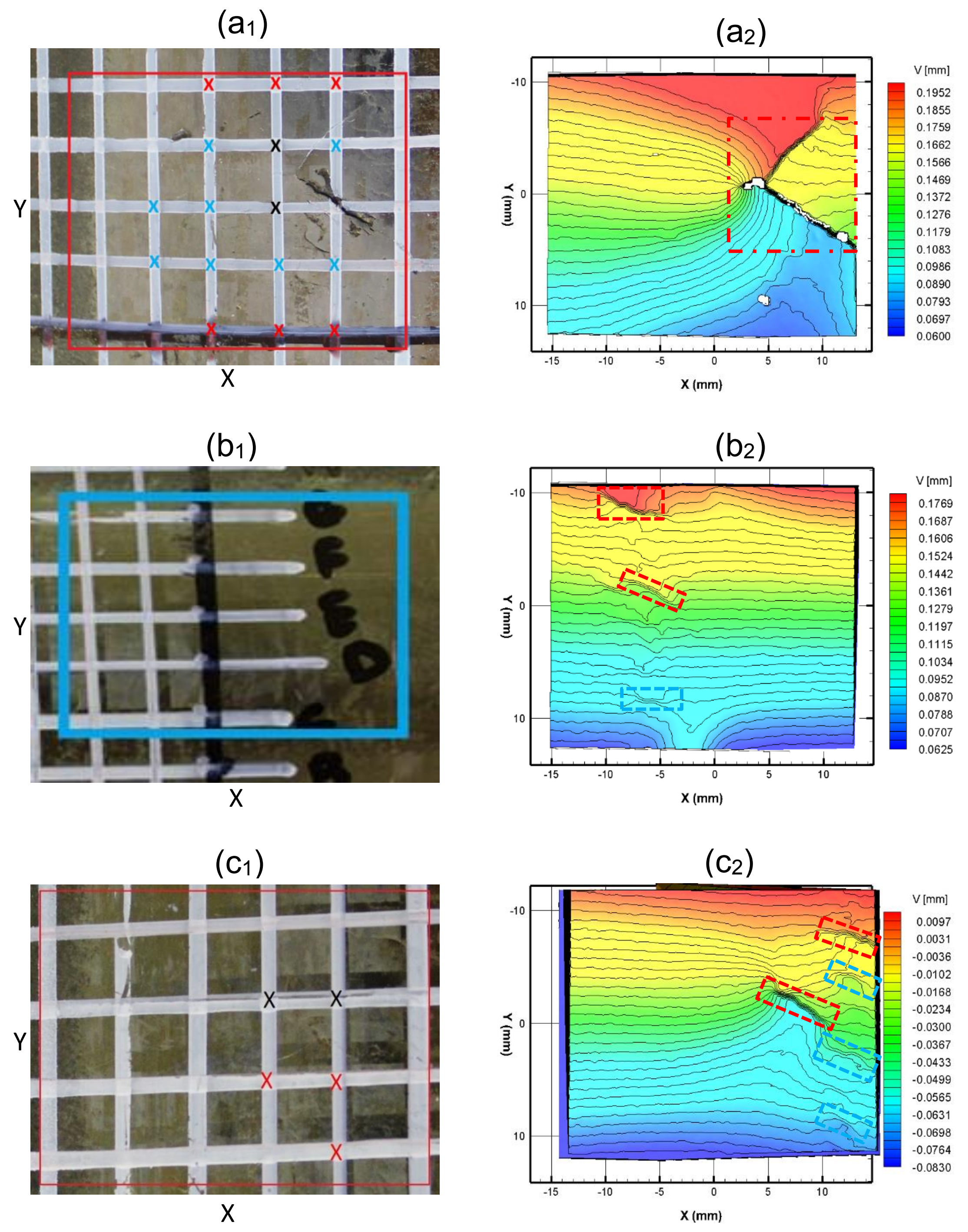

Figure 6-26 DIC ROI (left) and longitudinal displacement plot (right) under 150 kN vertical loading. Red and blue box represent DIC ROI. Internal defect location marked with "X". (a_1-a_2) Sample A, containing internal defects within DIC ROI. (b_1-b_2) Sample B1, does not contain internal defects within DIC ROI. (c_1-c_2) Sample B2, containing internal defects within DIC ROI.

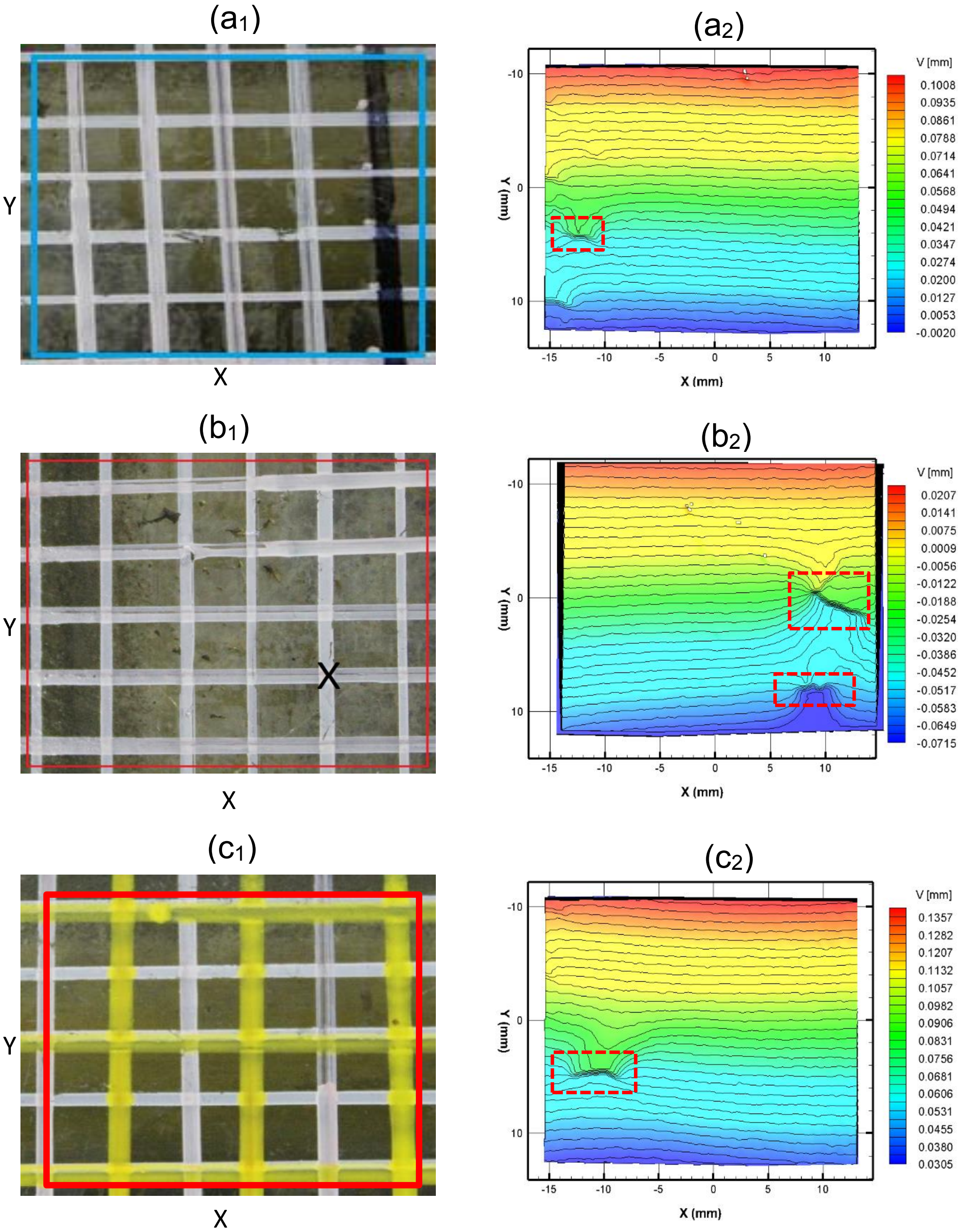

Figure 6-27 DIC ROI (left) and longitudinal displacement plot (right) under 150 kN vertical loading. Red and blue box represent DIC ROI. Internal defect location marked with "X". (a_1-a_2) Sample C1, does not contain internal defects within DIC ROI. (b_1-b_2) Sample C2, containing internal defects within DIC ROI. (c_1-c_2) Sample D, does not contain internal defects within DIC ROI.

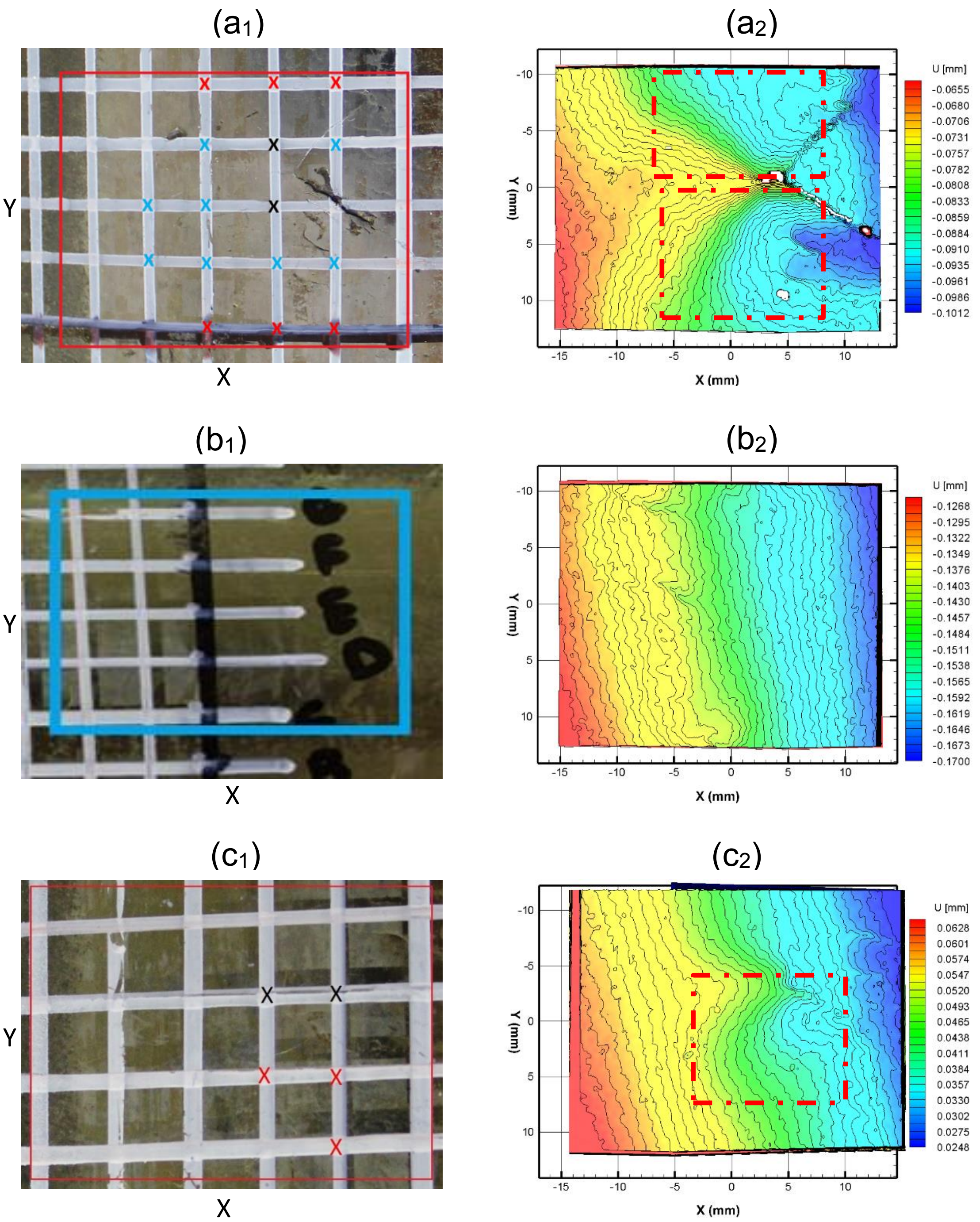

Figure 6-28 DIC ROI (left) and lateral displacement plot (right) under 150 kN vertical loading. Red and blue box represent DIC ROI. Internal defect location marked with "X". (a_1-a_2) Sample A, containing internal defects within DIC ROI. (b_1-b_2) Sample B1, does not contain internal defects within DIC ROI. (c_1-c_2) Sample B2, containing internal defects within DIC ROI.

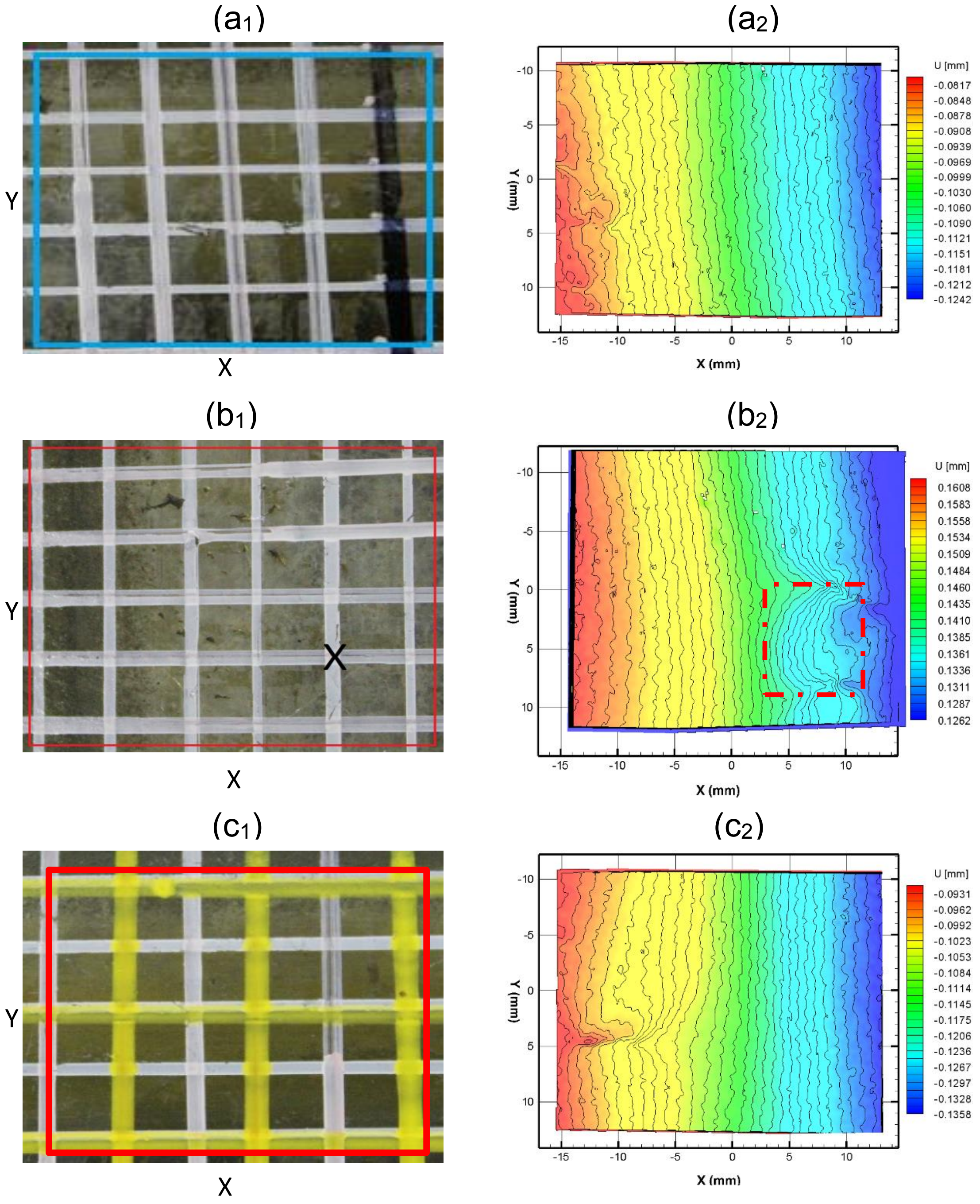

Figure 6-29 DIC ROI (left) and lateral displacement plot (right) under 150 kN vertical loading. Red and blue box represent DIC ROI. Internal defect location marked with "X". (a$_1$-a$_2$) Sample C1, does not contain internal defects within DIC ROI. (b$_1$-b$_2$) Sample C2, containing internal defects within DIC ROI. (c$_1$-c$_2$) Sample D, does not contain internal defects within DIC ROI.

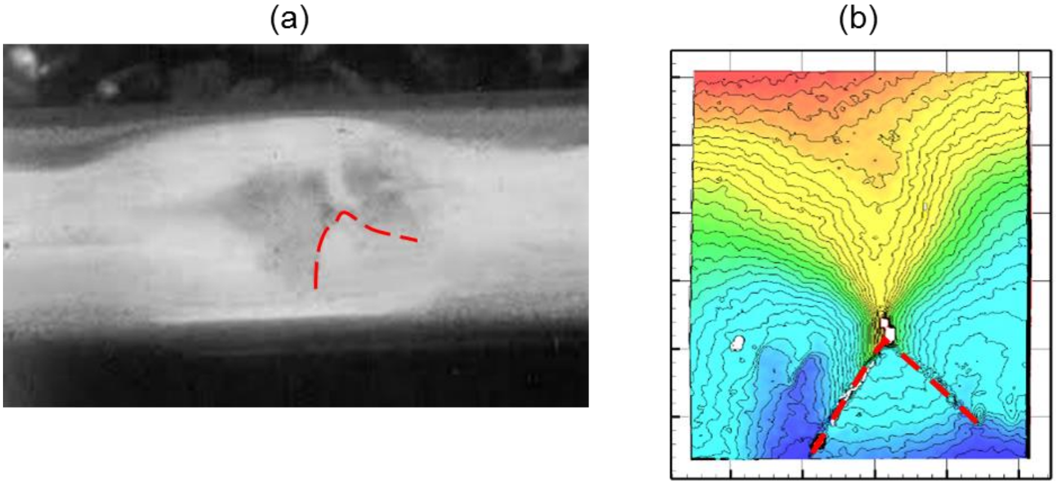

Figure 6-30 (a) Squat type in rail consisting of a V shape surface crack (marked with red dash line) and dark spots with an appearance of kidney shape [210]. *(b) Lateral displacement plot for Sample A with a curve contour (turquoise fill) under loading of 150 kN forming kidney shape similar to typical squat defect. Red dash line represents shape of surface crack.*

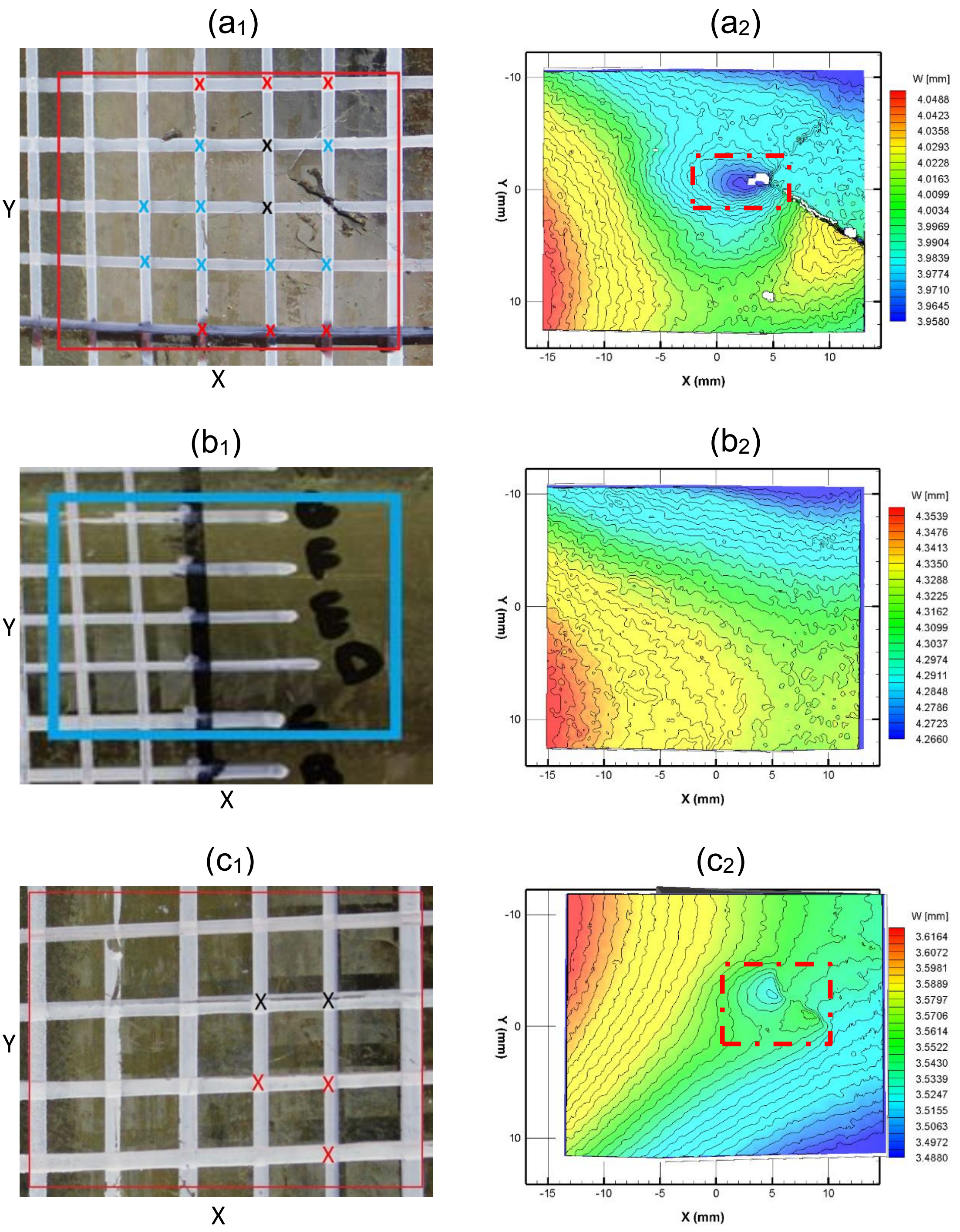

Figure 6-31 DIC ROI (left) and vertical displacement plot (right) under 150 kN vertical loading. Red and blue box represent DIC ROI. Internal defect location marked with "X". (a_1-a_2) Sample A, containing internal defects within DIC ROI. (b_1-b_2) Sample B1, does not contain internal defects within DIC ROI. (c_1-c_2) Sample B2, containing internal defects within DIC ROI.

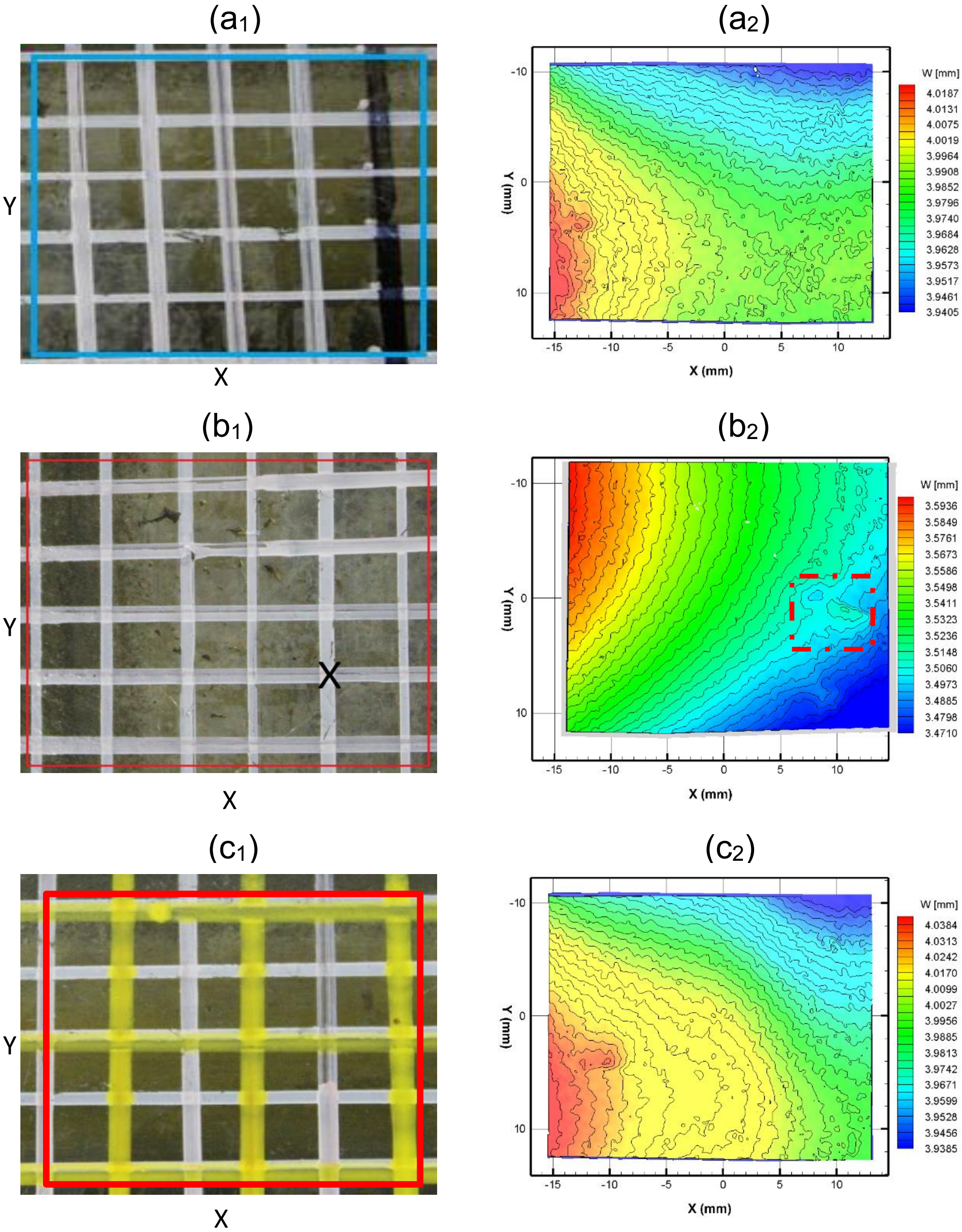

Figure 6-32 DIC ROI (left) and vertical displacement plot (right) under 150 kN vertical loading. Red and blue box represent DIC ROI. Internal defect location marked with "X". (a_1-a_2) Sample C1, does not contain internal defects within DIC ROI. (b_1-b_2) Sample C2, containing internal defects within DIC ROI. (c_1-c_2) Sample D, does not contain internal defects within DIC ROI.

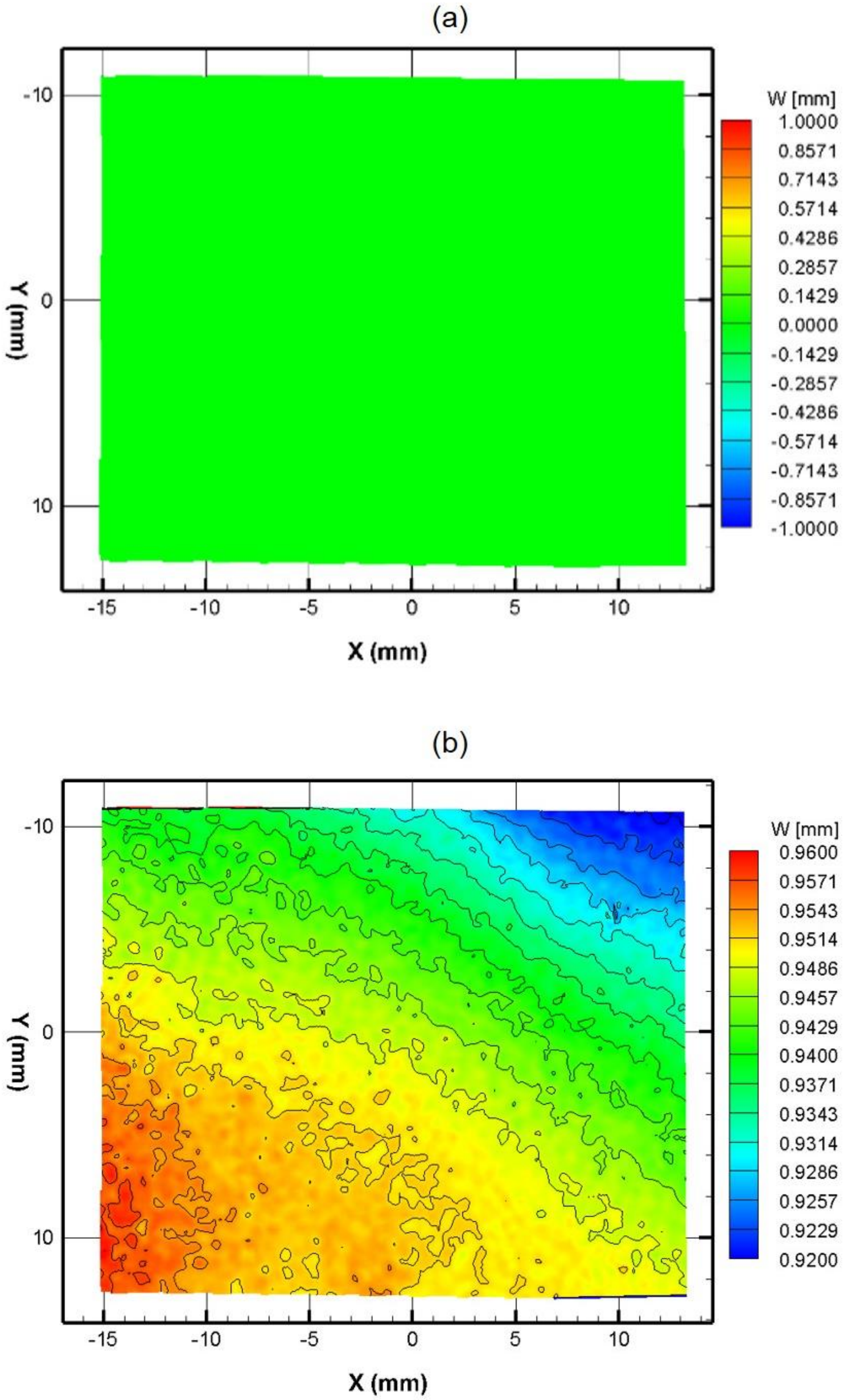

Figure 6-33 Vertical displacement plot for Sample B1: (a) initial condition, before any vertical loading is applied. (b) final state, loaded to 150 kN and unloaded to 0 kN vertical loading.

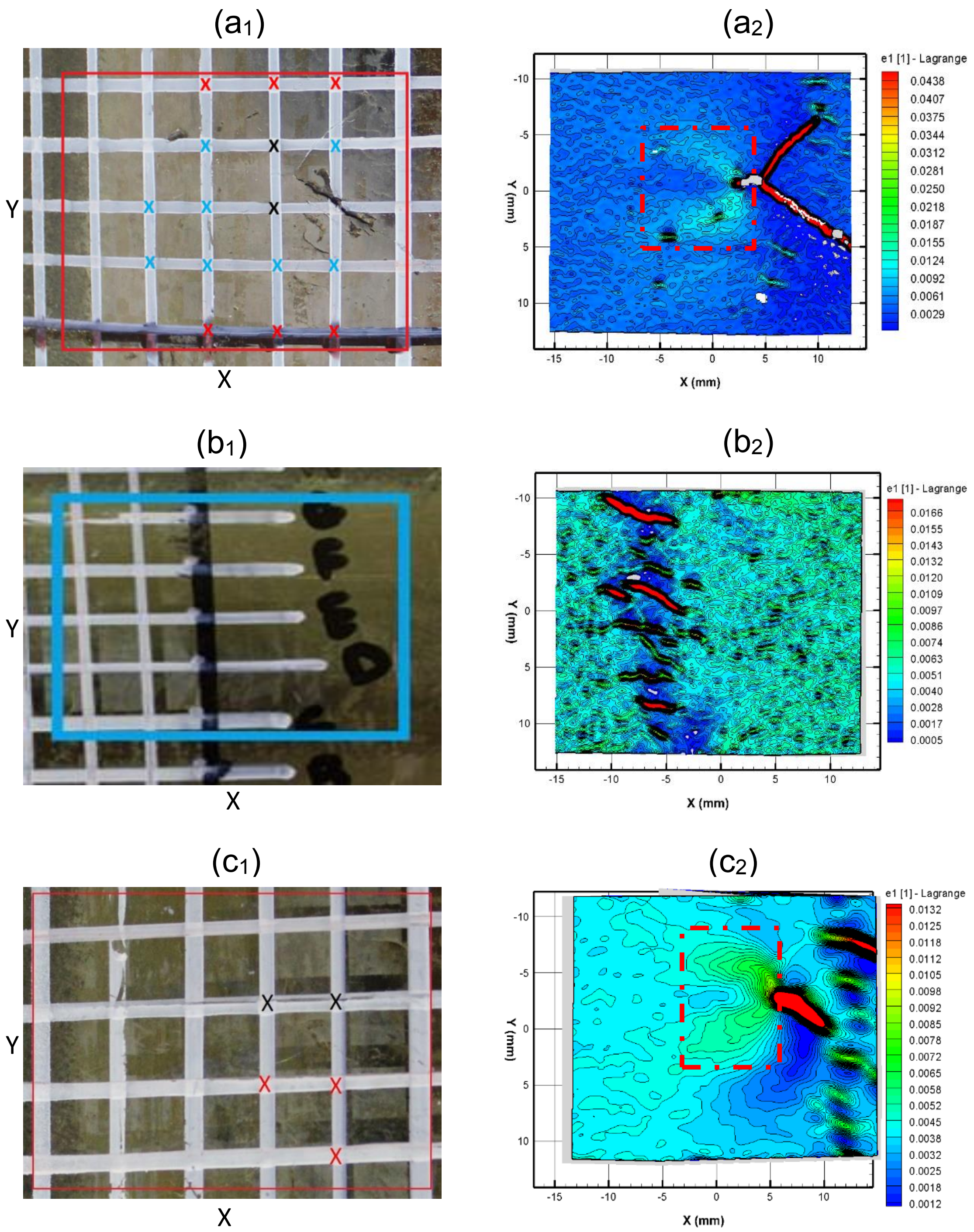

Figure 6-34 DIC ROI (left) and principal major strain plot (right) under 150 kN vertical loading. Red and blue box represent DIC ROI. Internal defect location marked with "X". (a_1-a_2) Sample A, containing internal defects within DIC ROI. (b_1-b_2) Sample B1, does not contain internal defects within DIC ROI. (c_1-c_2) Sample B2, containing internal defects within DIC ROI.

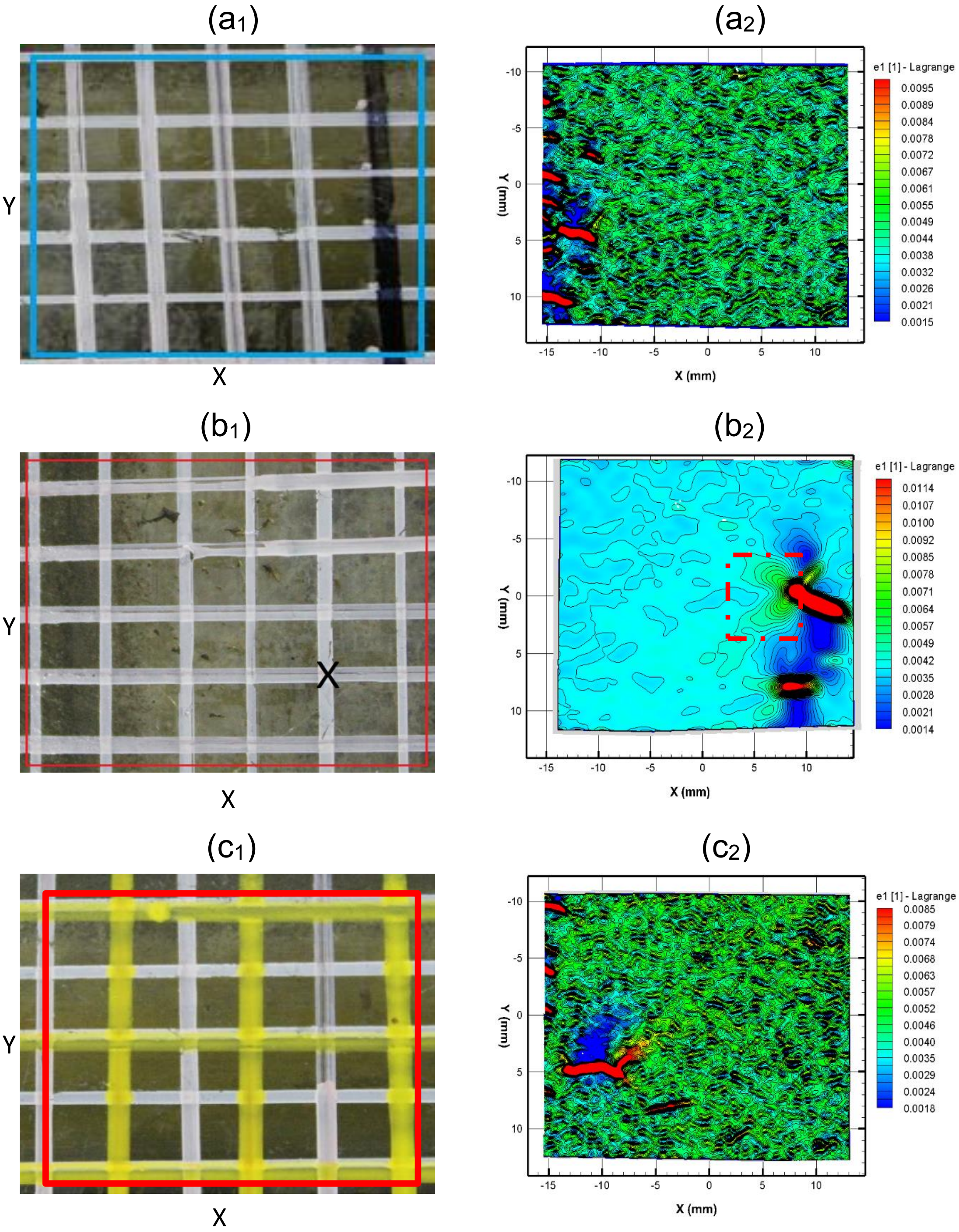

Figure 6-35 DIC ROI (left) and principal major strain plot (right) under 150 kN vertical loading. Red and blue box represent DIC ROI. Internal defect location marked with "X". (a_1-a_2) Sample C1, does not contain internal defects within DIC ROI. (b_1-b_2) Sample C2, containing internal defects within DIC ROI. (c_1-c_2) Sample D, does not contain internal defects within DIC ROI.

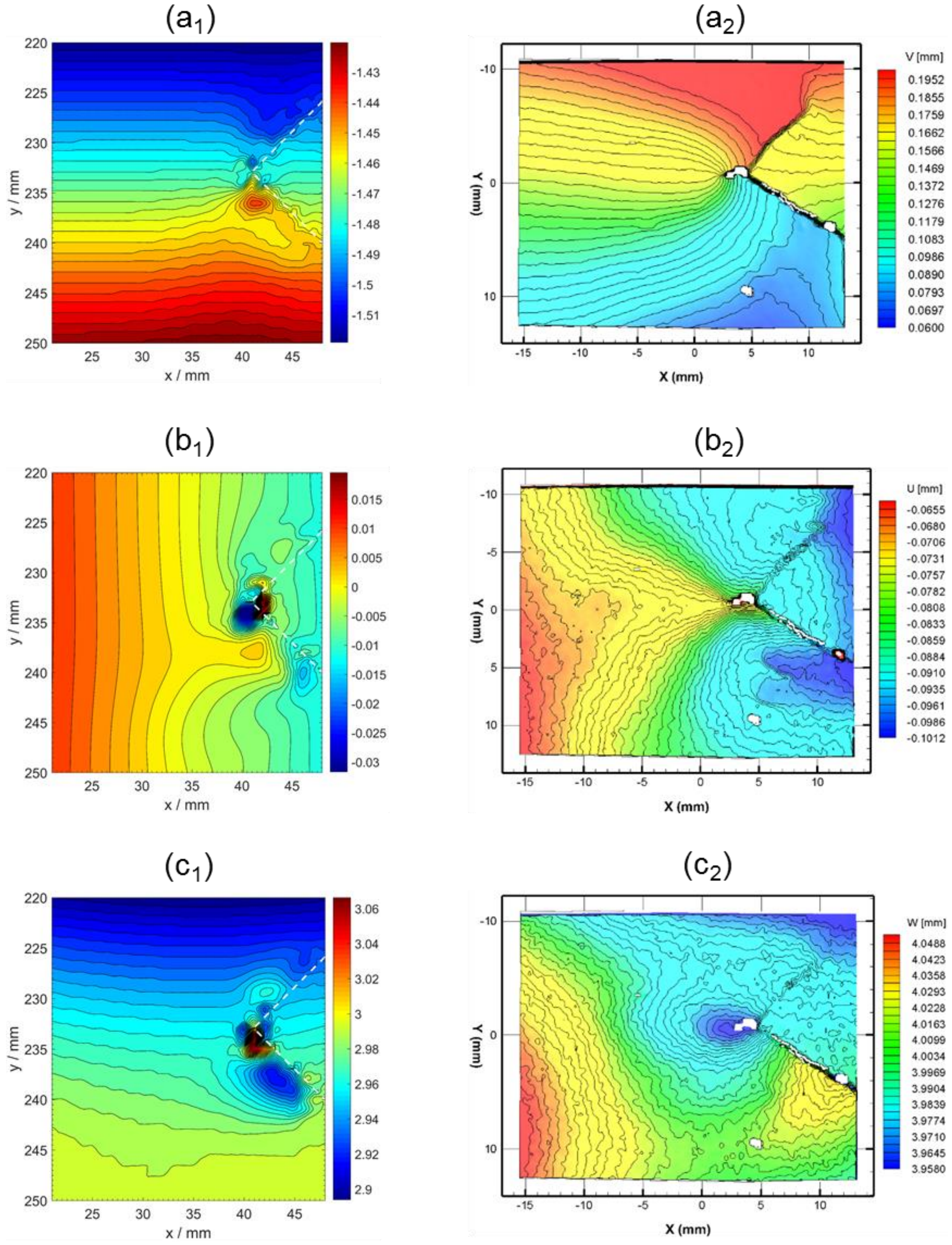

Figure 6-36 Comparison on displacement plot between modelling (left) and experimental results (right) for Sample A. (a) longitudinal displacement plot. (b) lateral displacement plot. (c) vertical displacement plot. White dash line was superposed in the image to represent the crack modelled.

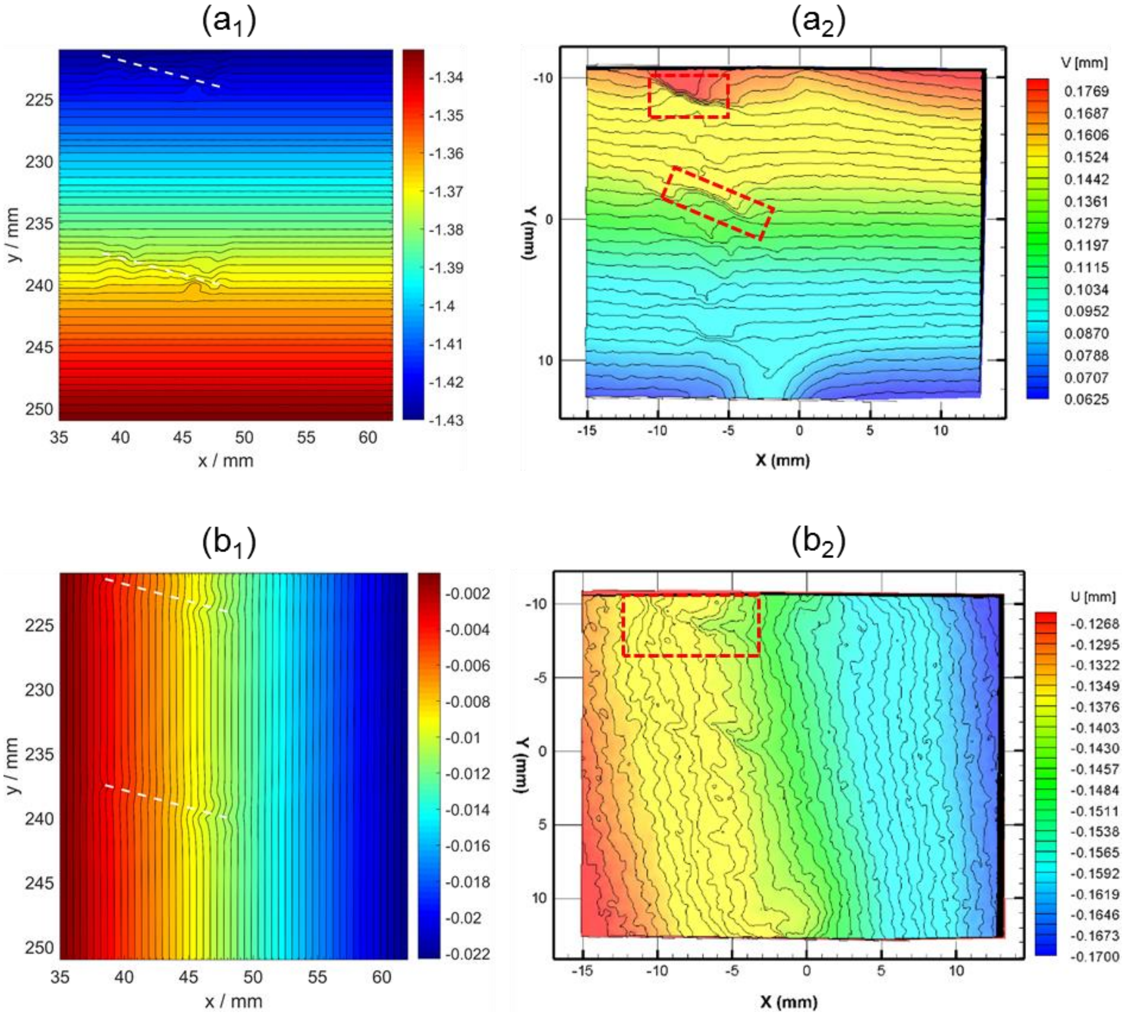

Figure 6-37 Comparison on displacement plot between modelling (left) and experimental results (right) for Sample B1. (a) longitudinal displacement plot. (b) lateral displacement plot. White dash line was superposed in the image to represent the crack modelled.

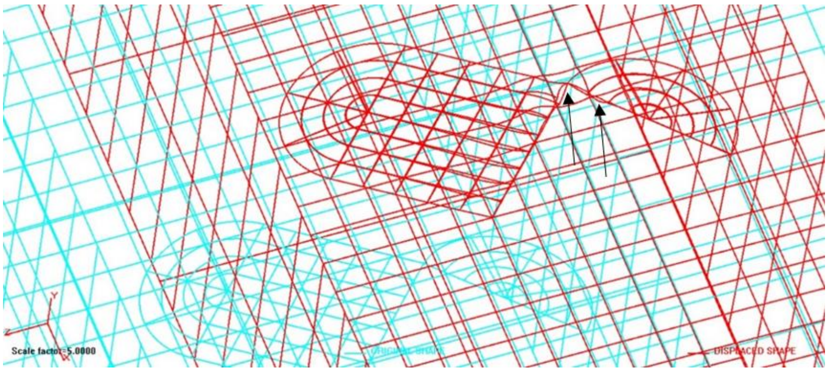

Figure 6-38 Opening of the crack tip that caused the formation of elliptical contour on the crack tip in the vertical displacement plot for Sample A. Two blacks arrows are pointing to the location of the crack tip. Red sketch represents deformed shape while turqoise represent the original shape. The image was scaled up to a factor of 5 for clarity.

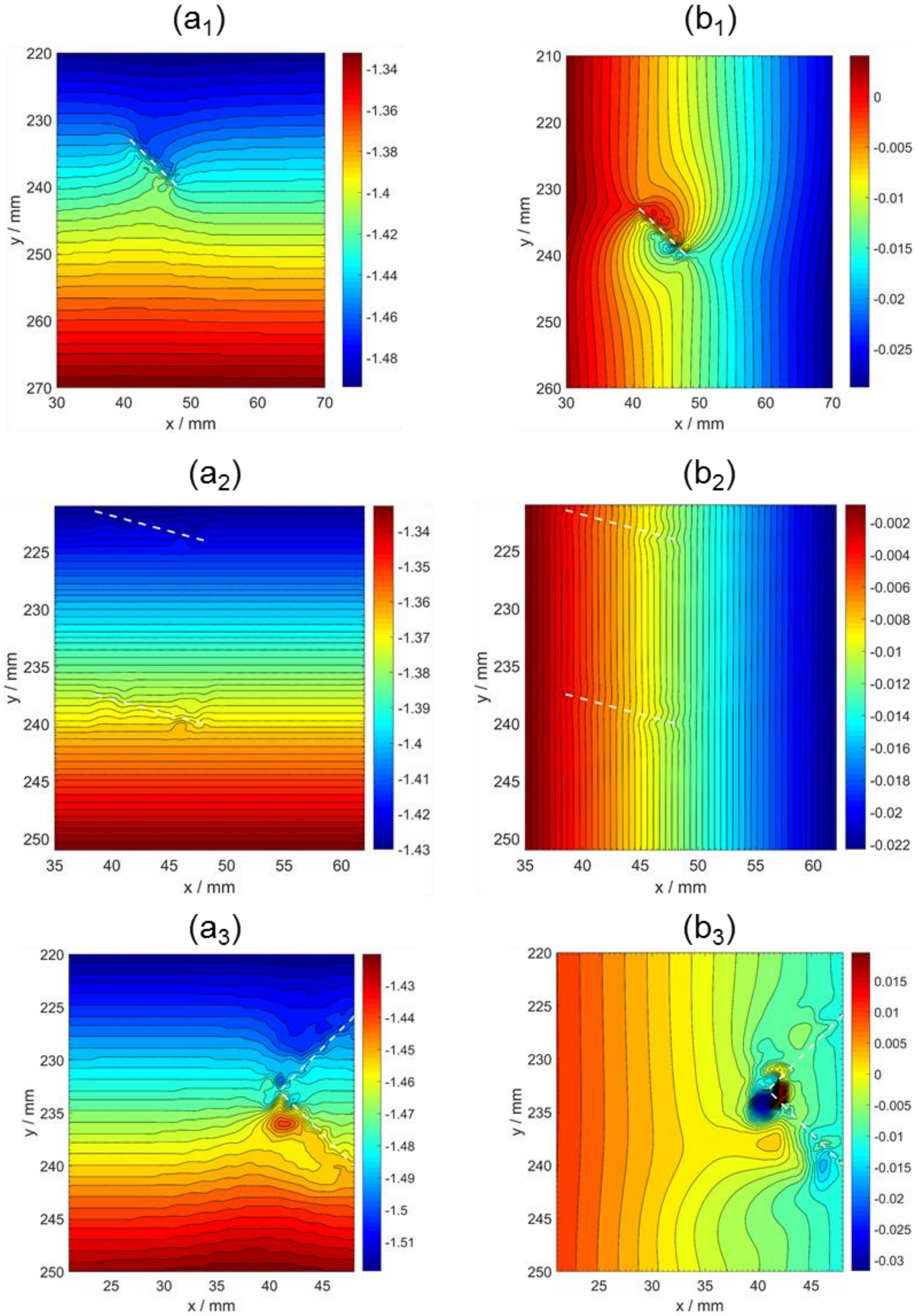

Figure 6-39 Comparison on the longitudinal displacement plot (a – left) and lateral displacement plot (b – right) between transverse crack defect (a_1 and b_1), representing Sample B1 (a_2 and b_2), and representation of Sample A (a_3 and b_3) from the modelling results. White dash line was superposed in the image to represent the crack modelled for each case.

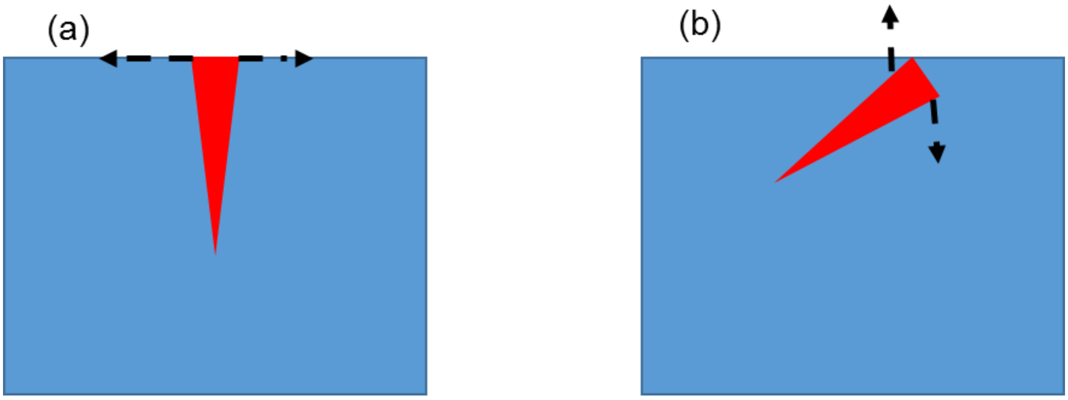

Figure 6-40 Opening of the crack face for (a) transverse crack and (b) shallow angle surface breaking crack. Red triangle represents crack in a material. Black dash arrow represents the opening direction of the crack face.

CHAPTER 7

CONCLUSIONS

7.0 Conclusions

The key contribution of this work are:

- Provide better understanding of squat type defects and classical squats
- Provide understanding of the growth pattern of cracks under the effect of thermal input and metallurgical transformed layer which could serve as a basis for maintenance schedules (grinding)
- Introduce a possible control measure that could suppress crack development in rail
- Introduce a proof of concept to detect and classify defect in rails without resulting in delays and disruptions to the train operation.

The research presented in this thesis is concerned with squat type defects in rail, which were reported to appear in several locations across the globe where the cost incurred for their removal leads to a major increase of track maintenance cost. These defects have superficial similarities with the classical RCF squat, however, it was suggested in the literature that the squat type defects are associated with thermal input rather than a ratchetting phenomenon that is responsible for the formation of classical RCF squats. Limited research has been undertaken since their discovery leaving them poorly understood especially on their initiation and propagation mechanism.

The investigation of squat type defects in rail through a series of visual observations and morphological analysis on a rail that has been removed from service was undertaken at the preliminary stage of the research as described in chapter 3. These investigations provide very useful data to be used for further analysis in order to better understand these defects. The results clearly suggest that fluid entry as observed with RCF classical squats was not responsible for the growth of squat type defects since no sign of corrosion on the crack faces can be seen on any of the samples investigated. The presence of WEL with minimal plastic flow strongly suggests that thermal input is responsible for the initiation and propagation of squat type defects. However, it was not possible to measure the effect of WEL on the growth of squat type defect directly from this preliminary investigation. Therefore, two configurations of subsurface crack as observed from morphological analysis were selected and considered in chapter 4 and 5 to understand the influence of WEL on the initiation and propagation of subsurface cracks as observed in chapter 3.

The influence of steel transformation to WEL on a crack that has already initiated was investigated in chapter 4. For this purpose, the configuration of crack as observed in chapter 3 was modelled where the configuration represents a simplified horizontal subsurface crack that developed in undeformed steel with WEL above the crack. The results highlight that WEL can accelerate the growth of cracks below it through locked in stress due to the metallurgical transformation from pearlite to martensite which causes a local increase in the volume of the rail steel. Additional thermal stress that occurred due to the high temperature of the wheel under operation would also enhance the development of the crack through an increase in mode II stress intensity factor. A possible control measure that could suppress crack development is introduced once the effect of WEL and the growth pattern is well understood. While promising, this modelling work only considers a single configuration of WEL with a single thickness and length but results from track sample in the previous chapter show that WEL appears in different dimensions (patches with different length and thickness). Therefore, the configuration of a different form of WEL was considered in chapter 5 to provide more understanding of how a combination of larger defects with a different configuration of this WEL transformed region will affect the growth of a crack.

In chapter 5, a crack that initiated from a large void was modelled using boundary element model to investigate the repercussion of white etching layer configuration on larger defects in rail. The configuration studied represents a large defect in the rail that was observed during the preliminary investigation as described in chapter 3. Several different cases were considered which include thin, thick, longer, and patches of WEL. These investigation has provided a better understanding of how a crack initiated from a larger defect grows under the effect of WEL. The results highlight that different configuration of WEL will accelerate the growth of the crack at different rates in which a thicker transform region dominates the growth of the crack since the crack tip experienced a higher level of stresses which affect both mode I and mode II stress intensity factor. The crack growth predicted in this study for a small crack size is at least 6 times higher than the wear rate mentioned in the literature and will increase further if the expansion of a transformed layer is considered making it impossible to be removed by natural wear. This suggests that detection of this kind of defect is the key in order to monitor its growth behaviour before it leads to catastrophic failure. However, if smaller defects are presence above these larger defect, this could mask the ultrasonic signal during inspection that prevents its detection. Therefore, a new method of detection is needed to overcome these issue and were discussed in chapter 6.

A non-contact method that could detect the presence of defects (surface and internal defects) has been explored in chapter 6 by applying a digital image correlation (DIC) technique. The results highlight that this method is reliable and effective at detecting damage in rails. The results suggest that DIC technique is useful not only for defect detection in rail, but can also provide additional information such as defect visualization and defect population. In addition, any defect with a smaller size which could not be observed by naked eye can be visualized easily using this technique. However, the work discussed in chapter 6 only represents a proof of concept where much further work is needed to move towards a robust technique for application in the field.

With the understanding acquired from this study, it was found that the formation WEL especially near/above squat type defect would accelerate the development of these defects. Therefore, removing the layer in these problematic regions through scheduled grinding would be useful as a practical measure to suppress the growth of these defects. As understanding of the growth pattern of the defects under different conditions improves, the growth rate prediction could be used as a guideline to predict the right frequency of grinding in order to ensure system safety and reduce system infrastructure maintenance cost at the same time.

CHAPTER 8

FUTURE WORK

8.0 Recommended further investigations

The work presented in this thesis has provided a better understanding on the role of thermal input (in the context of metallugically transformed layer) in squat type defects in rail. However, the work has not been completely exhaustive where further investigation can be undertaken to understood additional aspects of the squat type defect.

Although the work presented in chapter 4 suggests that the formation of WEL above a defect can enhance the growth of the crack significantly, the growth rate predicted for the defect was calculated based on incline crack growth law for BS11 rail steel. However, the squat type defect was observed to form as a horizontal subsurface crack in R260 grade rail steel. A more specific crack growth law for modern rail steels would be a useful area for future research to provide an accurate prediction of crack growth under different material and different configuration. This could be achieved using a similar method as described in the literature [120] by considering different crack configurations on a different type of cruciform material.

The work considered in chapter 4 also indicates that suppression of crack growth is possible if metallurgical transformation through thermal input produces contraction rather than expansion of the microstructure. This indicates that it would be beneficial to study steel chemistry that can achieve this behaviour. This may involve performing some tests on a range of existing rail steels to identify whether any existing material already has this beneficial property. If such behaviour does not exist, selecting steel metallurgy that are able to reduce the level of expansion when the metallurgical transformation takes place following thermal input would be beneficial in order to be used as a coating material or as whole rails to supress any subsequent crack growth.

The results obtained from chapter 4 show that contraction of the metallurgical transformed region might be beneficial to suppress the subsequent growth of horizontal near surface crack. With respect to the in-depth case study on the repercussion of white etching layer configuration on larger defect / void as presented in chapter 5, the results indicates that no matter what the configuration of WEL are (patches, different length and thickness), the presence of WEL will still accelerate the growth of the crack especially when the crack has initiated from a larger defect such as void. Therefore it would be useful to consider the contraction layer cases in the model to investigate whether the contraction layer would be beneficial to supress the effect of the larger defect/void that acts as stress concentrator which leads to faster crack growth.

It should be noted that the work undertaken in both chapter 4 and 5 assumed that the crack extends along its original plane since the predicted mode II stress intensity factor exceed the shear mode threshold given by Otsuka [121]. However, in general, the crack would branch in a different direction due to the effect of mode I stress intensity factor. Therefore, it would be useful to include the crack branching prediction [211] in these models to investigate whether the effect of thermal input would lead to spalling effect or transverse defect. Furthermore, the model developed in both chapter 4 and 5 were performed based on two dimensional model in which the effect of lateral stresses was not considered. Lateral stresses could be generated either by steering forces or as a result from metallurgical transform layer. Therefore, extending this work in three dimensional model would provide full understanding on the growth pattern of squat type defects under a combination of all stresses.

The results presented in chapter 6 represent a proof of concept as the first stage toward a robust technique for application in the field. Since the specimen considered in chapter 6 only involved a railhead containing defects (not the full geometry), testing on a full scale rail would be beneficial to extend this proof of concept. Furthermore, only samples containing surface and internal defects were investigated, and validation between modelling work and experimental work could not be made for defects that solely occurred in the subsurface region. Thus, it would be interesting to perform similar tests on a variety of rails containing defects, in order to validate the capability of this technique in predicting failure caused by all different types of defect.

References

[1] S. L. Grassie, D. I. Fletcher, E. a. Gallardo Hernandez, and P. Summers, “Studs: a squat-type defect in rails,” *Proc. Inst. Mech. Eng. Part F J. Rail Rapid Transit*, vol. 226, no. 3, pp. 243–256, Oct. 2011.

[2] D. I. Fletcher and S. H. Sanusi, “SBB Rail Analysis,” Sheffield, 2013.

[3] S. L. Grassie, “Squats and squat-type defects in rails: the understanding to date,” *Proc. Inst. Mech. Eng. Part F J. Rail Rapid Transit*, vol. 226, no. 3, pp. 235–242, Oct. 2011.

[4] S. L. Grassie, “Studs and squats: The evolving story,” *Wear*, vol. 366–367, no. Contact Mechanics and Wear of Rail / Wheel Systems, CM2015, pp. 194–199, 2016.

[5] S. L. Grassie, D. Fletcher, E. A. Gallardo-hernandez, and P. Summers, “Squats and studs imilarities and differences,” no. June 2011.

[6] C. Bernsteiner, G. Muller, A. Meierhofer, K. Six, D. Kunstner, and P. Dietmaier, “Development of white etching layers on rails: Simulations and experiments,” *Wear*, vol. 366–367, pp. 1–7, 2016.

[7] D. I. Fletcher and S. H. Sanusi, “The potential for suppressing rail defect growth through tailoring rail thermo-mechanical properties,” *Wear*, 2015.

[8] R. Ritchie, *Railways; their rise, progress, and construction*. London: Longman, Brown, Green, and Longmans, 1846.

[9] R. M. Martin, *Railways - past, present, & prospective*. London: W.H. Smith and Son, 1849.

[10] R. MacFadyen, “A short history of Britain’s railways,” *The Museum of Scottish Railways*, 2013. [Online]. Available: http://www.bkrailway.co.uk/wp-content/uploads/2013/11/EDUCATION-PACK-SECTION-3-Railway-History-Col.pdf. [Accessed: 26-Oct-2016].

[11] M. Bailey, "The history of tracks and trains : a lesson in joined-up thinking," in *Proceedings of ICE*, 2005, no. August, pp. 134–142.

[12] R. a Smith, "Hatfield Memorial Lecture 2007
Railways and materials: synergetic progress," *Ironmak. Steelmak.*, vol. 35, no. 7, pp. 505–513, 2008.

[13] P. J. Webster, G. Mills, X. Wang, and W. P. Kang, "Residual Stress Measurements in Rails by Neutron Diffraction," in *Rail Quality and Maintenance for Modern Railway Operation: International Conference on Rail Quality and Maintenance for Modern Railway Operation Delft June 1992*, J. J. Kalker, D. F. Cannon, and O. Orringer, Eds. Dordrecht: Springer Netherlands, 1993, pp. 307–314.

[14] T. Sasaki, S. Takahashi, Y. Kanematsu, Y. Satoh, K. Iwafuchi, M. Ishida, and Y. Morii, "Measurement of residual stresses in rails by neutron diffraction," *Wear*, vol. 265, no. 9–10, pp. 1402–1407, 2008.

[15] TATA Steel, "Rail technical guide," 2013.

[16] C. Esveld, *Modern Railway track*, Second Edi. MRT Productions, 2001.

[17] "History," *Voestalpine Schienen GmbH*. [Online]. Available: https://www.voestalpine.com/schienen/en/Company/History/. [Accessed: 21-Nov-2016].

[18] D. G. Girsch, D. N. Kumpfmüller, and R. Belz, "Comparing the life-cycle costs of standard and head-hardened rail," *Railway Gazette International*, Sep-2005.

[19] F. J. Franklin, G. J. Weeda, A. Kapoor, and E. J. M. Hiensch, "Rolling contact fatigue and wear behaviour of the infrastar two-material rail," *Wear*, vol. 258, no. 7–8, pp. 1048–1054, 2005.

[20] S. R. Lewis, R. Lewis, and D. I. Fletcher, "Assessment of laser cladding as an option for repairing/enhancing rails," *Wear*, vol. 330–331, pp. 581–591, 2015.

[21] H. Tournay, "Rail and Wheel Profile Design," in *Guidelines to best practices for heavy haul railway operations: Wheel and rail interface issues*, First edit., Virginia, U.S.A: International Heavy Haul Association, 2001, p. 484.

[22] M. Pau and B. Leban, “Experimental detection of wheel-rail contact irregularities,” in *Proceedings of the 7th World Congress on Railway Research (WCRR)*, 2006, pp. 4–8.

[23] H. I. Andrews, “The contact between a locomotive driving wheel and the rail,” *Wear*, vol. 2, pp. 468–484, 1958.

[24] M. B. Marshall, R. Lewis, R. S. Dwyer-Joyce, U. Olofsson, and S. Björklund, “Ultrasonic characterisation of a wheel/rail contact,” *Tribol. Ser.*, vol. 43, pp. 151–158, 2003.

[25] J. J. Kalker, *Wheel-rail wear calculations with the program CONTACT*. Faculty of Mathematics and Informatics, 1987.

[26] T. Telliskivi and U. Olofsson, “Contact mechanics analysis of measured wheel – rail profiles using the finite element method,” *Proc. Inst. Mech. Eng. Part F J. Rail Rapid Transit*, vol. 215, no. 2, pp. 65–72, 2001.

[27] M. S. Sichani, “On efficient modelling of wheel-rail contact in vehicle dynamic simulation,” KTH Royal Institute of Technology, Stockholm, 2013.

[28] H. Hertz, “Über die Berührung fester elastische Körper,” *J. Für Die Reine U. Angew. Math.*, vol. 92, no. 110, pp. 156–171, 1881.

[29] F. W. Carter, “On the action of a locomotive driving wheel,” in *Proceedings of the Royal Society of London A: Mathematical, Physical and Engineering Sciences*, 1926, pp. 151–157.

[30] K. L. Johnson, “The Effect of Tangential Contact Force Upon the Rolling Motion of an Elastic,” *Trans ASME*, vol. 80, pp. 339–346, 1958.

[31] Z. Ren, S. Glodez, G. Fajdiga, and M. Ulbin, “Surface initiated crack growth simulation in moving lubricated contact,” *Theor. Appl. Fract. Mech.*, vol. 38, no. 2, pp. 141–149, 2002.

[32] John Williams, “Contact Between Surfaces,” in *Engineering Tribology*, Cambridge University Press, 1994, pp. 73–132.

[33] J. Kalousek and E. Magel, “Modifying and managing friction,” *Railw. Track Struct.*, vol. 5, pp. 5–6, 1997.

[34] D. F. Moore, *Principles and Applications of Tribology: Pergamon International Library of Science, Technology, Engineering and Social Studies: International Series in Materials Science and Technology*, vol. 14. Elsevier, 2013.

[35] U. Olofsson, Y. Zhu, S. Abbasi, and R. Lewis, “Tribology of the wheel–rail contact – aspects of wear, particle emission and adhesion,” *Veh. Syst. Dyn.*, vol. 51, no. 7, pp. 1091–1120, 2013.

[36] J. W. Stead, “Iron Into Steel,” *J WEST Scotl. IRON STEEL INST*, vol. 19, p. 169, 1911.

[37] H. Uetz and K. Sommer, “Investigations of the effect of surface temperatures in sliding contact,” *Wear*, vol. 43, no. 3, pp. 375–388, 1977.

[38] J. F. Archard and R. A. Rowntree, “Metallurgical phase transformations in the rubbing of steels,” in *Proceedings of the Royal Society of London A: Mathematical, Physical and Engineering Sciences*, 1988, pp. 405–424.

[39] W. D. Callister and D. G. Rethwisch, *Materials science and engineering: an introduction*, vol. 7. Wiley New York, 2007.

[40] T. S. Eyre and A. Baxter, “The formation of white layers at rubbing surfaces,” *Tribology*, vol. 5, no. 6, pp. 256–261, 1972.

[41] E. A. Shur and I. I. Kleshcheva, “Structure and properties of white layers formed at high velocities of friction,” *Sov. Mater. Sci.*, vol. 14, no. 3, pp. 280–284, 1978.

[42] W. Lojkowski, M. Djahanbakhsh, G. Bürkle, S. Gierlotka, W. Zielinski, and H. J. Fecht, “Nanostructure formation on the surface of railway tracks,” *Mater. Sci. Eng.*, vol. 303, no. 1–2, pp. 197–208, 2001.

[43] G. Baumann, H. J. Fecht, and S. Liebelt, “Formation of white-etching layers on rail treads,” *Wear*, vol. 191, no. 1–2, pp. 133–140, 1996.

[44] S. B. Newcomb and W. M. Stobbs, “A transmission electron microscopy study of the white-etching layer on a rail head,” *Mater. Sci. Eng.*, vol. 66, no. 2, pp. 195–204, Sep. 1984.

[45] W. Österle, H. Rooch, a. Pyzalla, and L. Wang, “Investigation of white etching layers on rails by optical microscopy, electron microscopy, X-ray and synchrotron X-ray diffraction,” *Mater. Sci. Eng. A*, vol. 303, no. 1–2, pp. 150–157, May 2001.

[46] J. Seo, S. Kwon, H. Jun, and D. Lee, “Numerical stress analysis and rolling contact fatigue of White Etching Layer on rail steel,” *Int. J. Fatigue*, vol. 33, no. 2, pp. 203–211, 2011.

[47] S. Pal, W. J. T. Daniel, and M. Farjoo, “Early stages of rail squat formation and the role of a white etching layer,” *Int. J. Fatigue*, vol. 52, pp. 144–156, 2013.

[48] H. W. Zhang, S. Ohsaki, S. Mitao, M. Ohnuma, and K. Hono, “Microstructural investigation of white etching layer on pearlite steel rail,” *Mater. Sci. Eng.*, vol. 421, no. 1–2, pp. 191–199, 2006.

[49] W. Callister and D. Rethwisch, *Materials science and engineering: an introduction*, vol. 9. 2007.

[50] K. Knothe and S. Liebelt, “Determination of temperatures for sliding contact with applications for wheel-rail systems,” *Wear*, vol. 189, no. 1–2, pp. 91–99, 1995.

[51] J. Takahashi, K. Kawakami, and M. Ueda, “Atom probe tomography analysis of the white etching layer in a rail track surface,” *Acta Mater.*, vol. 58, no. 10, pp. 3602–3612, 2010.

[52] D. Scott, D. I. Fletcher, and B. J. Cardwell, “Simulation study of thermally initiated rail defects,” *Proc. Inst. Mech. Eng. Part F J. Rail Rapid Transit*, vol. 228, no. 2, pp. 113–127, Dec. 2012.

[53] D. I. Fletcher, “Numerical simulation of near surface rail cracks subject to thermal contact stress,” *Wear*, vol. 314, no. 1–2, pp. 96–103, 2013.

[54] A. F. Bower, “The Influence of Crack Face Friction and Trapped Fluid on Surface Initiated Rolling Contact Fatigue Cracks,” *J. Tribol.*, vol. 110, no. 4, pp. 704–711, Oct. 1988.

[55] W. Daniel, “Final Report on the Rail Squat Project R3-105,” Brisbane, Australia, 2012.

[56] “Train Derailment at Hatfield: A Final Report by the Independent Investigation Board,” London, United Kingdom, 2006.

[57] J. E. Garnham and C. L. Davis, “The role of deformed rail microstructure on rolling contact fatigue initiation,” *Wear*, vol. 265, no. 9–10, pp. 1363–1372, 2008.

[58] E. Magel, P. Sroba, K. Sawley, and J. Kalousek, “Control of rolling contact fatigue of rails,” in *Proceedings of the AREMA 2004 Annual Conferences*, 2004, p. 29.

[59] J. R. Evans and M. C. Burstow, “Vehicle / track interaction and rolling contact fatigue in rails in the UK,” *Veh. Syst. Dyn.*, vol. 44, no. November, pp. 708–717, 2006.

[60] RSSB, “Management and Understanding of Rolling Contact Fatigue,” London, 2006.

[61] “Rolling contact fatigue in rails: a guide to current understanding and practice,” in *RT/PWG/001 Issue 1*, Railtrack PLC, 2001, p. 46.

[62] J. Tillberg, F. Larsson, and K. Runesson, “A study of multiple crack interaction at rolling contact fatigue loading of rails,” *Proc. Inst. Mech. Eng. Part F J. Rail Rapid Transit*, vol. 223, no. 4, pp. 319–330, 2009.

[63] D. T. Eadie, D. Elvidge, K. Oldknow, R. Stock, P. Pointner, J. Kalousek, and P. Klauser, “The effects of top of rail friction modifier on wear and rolling contact fatigue: Full-scale rail-wheel test rig evaluation, analysis and modelling,” *Wear*, vol. 265, no. 9–10, pp. 1222–1230, 2008.

[64] K. D. Van and M. H. Maitournam, “Rolling contact in railways: modelling, simulation and damage prediction,” *Fatigue Fract. Eng. Mater. Struct.*, vol. 26, no. 10, pp. 939–948, 2003.

[65] S. L. Grassie, “Rolling contact fatigue on the British railway system: treatment,” *Wear*, vol. 258, no. 7–8, pp. 1310–1318, Mar. 2005.

[66] U. Zerbst, R. Lundén, K.-O. Edel, and R. a. Smith, “Introduction to the damage tolerance behaviour of railway rails – a review,” *Eng. Fract. Mech.*, vol. 76, no. 17, pp. 2563–2601, Nov. 2009.

[67] J. J. Marais and K. C. Mistry, “Rail integrity management by means of ultrasonic testing,” *Fatigue Fract. Eng. Mater. Struct.*, vol. 26, no. 10, pp. 931–938, 2003.

[68] U. Olofsson and R. Lewis, “Tribology of the wheel-rail contact,” in *Handbook of Railway Vehicle Dynamics*, S. Iwnicki, Ed. CRC Press, 2006, p. 527.

[69] D. F. Cannon, K. O. Edel, S. L. Grassie, and K. Sawley, “Rail defects: An overview,” *Fatigue Fract. Eng. Mater. Struct.*, vol. 26, no. 10, pp. 865–886, 2003.

[70] “Some Rail Defects, their Characteristics, Causes and Control,” in *Rail Defects Handbook*, no. RC 2400, Australian Rail Track Corporation, 2006, p. 68.

[71] S. Pal, C. Valente, W. Daniel, and M. Farjoo, “Metallurgical and physical understanding of rail squat initiation and propagation,” *Wear*, vol. 284–285, pp. 30–42, Apr. 2012.

[72] Z. Li, “Squats on railway rails,” in *Wheel-rail Interface Handbook*, Woodhead P., R. Lewis and U. Olofsson, Eds. Elsevier Science, 2009, pp. 409–436.

[73] X. Zhao, “Dynamic Wheel/Rail Rolling Contact at Singular Defects with Application to Squats,” Delft University of Technology, 2012.

[74] S. L. Grassie, “Rolling contact fatigue on the British railway system: Treatment,” in *Wear*, 2005, vol. 258, no. 7–8, pp. 1310–1318.

[75] P. Clayton, M. B. . Allery, and P. J. Bolton, “Surface damage phenomena in rails,” in *Proceedings of the conference on Contact Mechanics and Wear of Rail/wheel Systems*, 1982, pp. 419–443.

[76] K. Kondo, K. Yoroizaka, and Y. Sato, “Cause, increase, diagnosis, countermeasures and elimination of Shinkansen shelling,” *Wear*, vol. 191, no. 1–2, pp. 199–203, Jan. 1996.

[77] P. Clayton, “Tribological aspects of wheel-rail contact: a review of recent experimental research,” *Wear*, vol. 191, no. 1996, pp. 170–183, 1995.

[78] M. Steenbergen and R. Dollevoet, “On the mechanism of squat formation on train rails – Part I: Origination,” *Int. J. Fatigue*, vol. 47, pp. 361–372, Feb. 2013.

[79] S. Bogdanski, M. Olzak, and J. Stupnicki, “Numerical stress analysis of rail rolling contact fatigue cracks,” *Wear*, vol. 191, no. 1–2, pp. 14–24, Jan. 1996.

[80] S. Bogdański and M. W. Brown, “Modelling the three-dimensional behaviour of shallow rolling contact fatigue cracks in rails,” *Wear*, vol. 253, no. 1–2, pp. 17–25, Jul. 2002.

[81] S. Bogdański, P. Lewicki, and M. Szymaniak, “Experimental and theoretical investigation of the phenomenon of filling the RCF crack with liquid,” *Wear*, vol. 258, no. 7–8, pp. 1280–1287, Mar. 2005.

[82] D. Fletcher, P. Hyde, and a Kapoor, “Investigating fluid penetration of rolling contact fatigue cracks in rails using a newly developed full-scale test facility,” *Proc. Inst. Mech. Eng. Part F J. Rail Rapid Transit*, vol. 221, no. 1, pp. 35–44, Jan. 2007.

[83] Z. Li, R. Dollevoet, M. Molodova, and X. Zhao, “Squat growth—Some observations and the validation of numerical predictions,” *Wear*, vol. 271, no. 1–2, pp. 148–157, May 2011.

[84] S. L. Grassie, D. I. Fletcher, E. A. Gallardo Hernandez, and P. Summers, “Studs: a squat-type defect in rails,” *Proc. Inst. Mech. Eng. Part F J. Rail Rapid Transit*, vol. 226, no. 3, pp. 243–256, 2012.

[85] Y. Ivanisenko, I. MacLaren, X. Sauvage, R. Z. Valiev, and H. J. Fecht, “Shear-induced alpha to gamma transformation in nanoscale Fe-C composite,” *Acta Mater.*, vol. 54, no. 6, pp. 1659–1669, 2006.

[86] W. J. T. Daniel, S. Pal, and M. Farjoo, “Rail squats: progress in understanding the Australian experience,” *Proc. Inst. Mech. Eng. Part F J. Rail Rapid Transit*, vol. 227, no. 5, pp. 481–492, 2013.

[87] A. Wilson, M. Kerr, S. Marich, and S. Kaewunruen, “Wheel/rail conditions and squat development on moderately curved tracks,” in *CORE 2012: Global Perspectives; Conference on railway engineering, 10-12 September 2012, Brisbane, Australia*, 2012, p. 223.

[88] D. Mallik, S. K. Ojha, S. Bansal, and B. Lakshminarasimham, “Probability of Detection of Online Ultrasonic Testing of Rail,” 2013. [Online]. Available: http://www.ndt.net/article/apcndt2013/papers/002.pdf. [Accessed: 16-Nov-2016].

[89] A. Kapoor and K. L. Johnson, “Plastic ratchetting as a mechanism of metallic wear,” in *Proceedings of the Royal Society of London A: Mathematical, Physical and Engineering Sciences*, 1994, pp. 367–384.

[90] F. J. Franklin, J. E. Garnham, D. I. Fletcher, C. L. Davis, and A. Kapoor, “The evolution and failure of pearlitic microstructure in rail steel: observations and modelling,” in *Wheel-rail Interface Handbook*, R. Lewis and U. Olofsson, Eds. Woodhead Publishing Limited and CRC Press, 2009, pp. 311–348.

[91] D. I. Fletcher, F. J. Franklin, and A. Kapoor, “Rail surface fatigue and wear,” in *Wheel-Rail Interface Handbook*, R. Lewis and U. Olofsson, Eds. Woodhead Publishing Limited and CRC Press, 2009, pp. 280–310.

[92] S. Way, “Pitting due to rolling contact,” *J. appl. Mech*, vol. 2, no. 2, pp. 49–58, 1935.

[93] S. Bogdanski, “A rolling contact fatigue crack driven by squeeze fluid film,” *Fatigue Fract. Eng. Mater. Struct.*, vol. 25, no. May, pp. 1061–1071, 2002.

[94] J. A. Williams, “Wear and surface damage,” in *Engineering tribology*, Cambridge University Press, 1994, pp. 166–199.

[95] P. N. Suh, “The delamination theory of wear,” *Wear*, vol. 25, no. 1, pp. 111–124, 1973.

[96] J. F. Archard, “Contact and rubbing of flat surfaces,” *J. Appl. Phys.*, vol. 24, no. 8, pp. 981–988, 1953.

[97] P. J. Bolton and P. Clayton, “Rolling-sliding wear damage in rail and tyre steels,” *Wear*, vol. 93, no. 2, pp. 145–165, 1984.

[98] R. Lewis and U. Olofsson, “Mapping rail wear regimes and transitions,” *Wear*, vol. 257, no. 7–8, pp. 721–729, 2004.

[99] R. Lewis and U. Olofsson, *Wheel-rail interface handbook*. Woodhead Publishing Limited, 2009.

[100] D. Fletcher, “Equilibrium of crack growth and wear rates during unlubricated rolling-sliding contact of pearlitic rail steel,” *F J. Rail Rapid Transit*, vol. 214, pp. 93–105, 2000.

[101] G. Donzella, M. Faccoli, A. Ghidini, A. Mazzù, and R. Roberti, “The competitive role of wear and RCF in a rail steel,” *Eng. Fract. Mech.*, vol. 72, no. 2, pp. 287–308, 2005.

[102] “1954: ‘Metal fatigue’ caused Comet crashes,” *BBC News*, 19-Oct-2005. [Online]. Available: http://news.bbc.co.uk/onthisday/hi/dates/stories/october/19/newsid_3112000/3112466.stm. [Accessed: 17-Nov-2016].

[103] B. Hayes, “Six case histories of pressure vessel failures,” *Eng. Fail. Anal.*, vol. 3, no. 3, pp. 157–170, 1996.

[104] V. Esslinger, R. Kieselbach, R. Koller, and B. Weisse, “The railway accident of Eschede - technical background,” *Eng. Fail. Anal.*, vol. 11, no. 4, pp. 515–535, 2004.

[105] A. A. Griffith, “The Phenomena of Rupture and Flow in Solids,” *Philos. Trans. R. Soc. London*, vol. 221, no. Series A, Containing Papers of a Mathematical or Physical Character, pp. 163–198, 1921.

[106] G. R. Irwin, “Analysis of Stresses and Strains Near the End of a Crack Traversing a Plate,” *J. Appl. Mech.*, vol. 24, no. September, pp. 361–364, 1957.

[107] P. P. Benham, R. J. Crawford, and C. G. Armstrong, *Mechanics of engineering materials*. New York: John Wiley and Sons, 1987.

[108] A. Liu, “Summary of stress Intensity Factors,” *ASM International*. ASM International, USA, pp. 980–1000, 1996.

[109] J. E. Srawley, “Wide range stress intensity factor expressions for ASTM E 399 standard fracture toughness specimens,” *Int. J. Fract.*, vol. 12, no. 3, pp. 475–476, 1976.

[110] H. Nisitani, “The two-dimensional stress problem solved using an electric digital computer,” *Bull. JSME*, vol. 11, no. 43, pp. 14–23, 1968.

[111] M. Kaneta, M. Suetsugu, and Y. Murakami, “Mechanism of surface crack growth in lubricated rolling/sliding spherical contact,” *J. Appl. Mech.*, vol. 53, no. 2, pp. 354–360, 1986.

[112] S. Bogdanski, M. Olzak, and J. Stupnicki, “Numerical Modelling of a 3D Rail Rcf ‘ Squat ’ -Type Crack,” *Fatigue Fract. Eng. Mater. Struct.*, vol. 21, no. 8, pp. 923–935, 1998.

[113] M. Farjoo, W. Daniel, and P. A. Meehan, “Modelling a squat form crack on a rail laid on an elastic foundation,” *Eng. Fract. Mech.*, vol. 85, pp. 47–58, 2012.

[114] M. Kerr, A. Wilson, and S. Marich, “The epidemiology of squats and related defects,” Railway Technical Society of Australasia: Engineers Australia, JOUR, 2008.

[115] S. Bogdanski, “Quasi-static and dynamic liquid solid interaction in 3D squat-type cracks,” *Wear*, vol. 314, pp. 20–27, 2013.

[116] M. Akama and T. Mori, “Boundary element analysis of surface initiated rolling contact fatigue cracks in wheel/rail contact systems,” *Wear*, vol. 253, no. 1–2, pp. 35–41, 2002.

[117] D. I. Fletcher, L. Smith, and A. Kapoor, “Rail rolling contact fatigue dependence on friction, predicted using fracture mechanics with a three-dimensional boundary element model,” *Eng. Fract. Mech.*, vol. 76, no. 17, pp. 2612–2625, Nov. 2009.

[118] D. I. Fletcher, P. Hyde, and A. Kapoor, “Modelling and full-scale trials to investigate fluid pressurisation of rolling contact fatigue cracks,” *Wear*, vol. 265, no. 9–10, pp. 1317–1324, 2008.

[119] E647-00, “Standard Test Method for Measurement of Fatigue Crack Growth Rates,” *ASTM Int.*, p. 43, 1999.

[120] S. L. Wong, P. E. Bold, M. W. Brown, and R. J. Allen, “Fatigue crack growth rates under sequential mixed-mode I and II loading cycles,” *Fatigue Fract. Eng. Mater. Struct.*, vol. 23, no. 8, pp. 667–674, 2000.

[121] A. Otsuka, K. Mori, and T. Miyata, “The condition of fatigue crack growth in mixed mode condition,” *Eng. Fract. Mech.*, vol. 7, no. 3, pp. 429–439, Sep. 1975.

[122] H. L. Whittemore and S. N. Petrenko, *Technologic Papers Bureau of Standards*, Technologi. National Bureau of Standards, 1921.

[123] C. Rasmussen, “Special Diolkos remains near Corinth,” 2016. [Online]. Available: https://holylandphotos.wordpress.com/tag/corinth/. [Accessed: 25-Oct-2016].

[124] “Length of cast-iron fish-belly rail with two chairs, 19th century,” *Getty Images Science & Society Page Library*, 1995. [Online]. Available: http://www.gettyimages.co.uk/detail/news-photo/length-of-cast-iron-fish-belly-rail-with-two-chairs-found-news-photo/90747781#length-of-castiron-fishbelly-rail-with-two-chairs-found-at-east-picture-id90747781. [Accessed: 23-Nov-2016].

[125] “Rail profile.” [Online]. Available: http://www.railsystem.net/rail-profile/. [Accessed: 27-Oct-2016].

[126] S. Thornton, “Using simulation approach to move from manual to real time autonomous scheduling for a batch heat treatment process,” 2014. [Online]. Available: http://slideplayer.com/slide/4630326/. [Accessed: 27-Oct-2016].

[127] “Metallurgy of rail steel,” *Institue of Rail Welding*. [Online]. Available: http://www.iorw.org/jobknow4.html. [Accessed: 28-Oct-2016].

[128] N. Weinzapfel, F. Sadeghi, and V. Bakolas, "An Approach for Modeling Material Grain Structure in Investigations of Hertzian Subsurface Stresses and Rolling Contact Fatigue," *J. Tribol.*, vol. 132, no. 4, p. 41404, 2010.

[129] R. S. Dwyer-Joyce, Ed., "Contact Mechanics," in *Tribological Design Data*, First edn., vol. 1, London: The Tribology Group of The Institution of Mechanical Engineers, 1997, pp. 1–17.

[130] D. Fletcher, "Lecture 6 Friction & braking," in *Mechanical Engineering of Railways*, 2012, pp. 1–17.

[131] H. E. McGannon, H. H. Uhlig, E. Aguilar, A. Lacaton, J. P. Vassal, J. P. V. Anne Lacaton, K. Kuma, K. Kuma, M. Aguirre, and P. Aguirre, *The making, shaping and treating of steel*. Pittsburg: United States Steel Corporation, 1971.

[132] P. E. Bold, M. W. Brown, and R. J. Allen, "Shear mode crack growth and rolling contact fatigue," *Wear*, vol. 144, no. 1–2, pp. 307–317, Apr. 1991.

[133] D. I. Fletcher, P. Hyde, and a Kapoor, "Growth of multiple rolling contact fatigue cracks driven by rail bending modelled using a boundary element technique," *Proc. Inst. Mech. Eng. Part F J. Rail Rapid Transit*, vol. 218, no. 3, pp. 243–253, 2004.

[134] G. Mathers, "Compact tension and J integral tests," *The Welding Institute*. [Online]. Available: http://www.twi-global.com/technical-knowledge/job-knowledge/compact-tension-and-j-integral-tests-077/. [Accessed: 21-Nov-2016].

[135] S. L. Grassie, "Investigation of Squats -Preliminary Findings." Sydney Trains / Transport for NSW, Cambridge, p. 33, 2013.

[136] Y. Ivanisenko, I. MacLaren, X. Sauvage, R. Z. Valiev, and H. J. Fecht, "Phase transformations in pearlitic steels induced by severe plastic deformation," *Solid State Phenom.*, vol. 114, pp. 133–144, 2006.

[137] Y. Jin and M. Ishida, "Analysis of white etching layer generated on rail surface," *RTRI Rep.*, vol. 19, no. 9, pp. 17–22, 2005.

[138] D. I. Fletcher, “Numerical simulation of near surface rail cracks subject to thermal contact stress,” *Wear,* Nov. 2013.

[139] K. D. Cole, C. M. Tarawneh, A. A. Fuentes, B. M. Wilson, and L. Navarro, “Thermal models of railroad wheels and bearings,” *Int. J. Heat Mass Transf.*, vol. 53, no. 9–10, pp. 1636–1645, 2010.

[140] “BEASY Boundary Element software.” [Online]. Available: www.beasy.com. [Accessed: 04-Aug-2016].

[141] V. Raghavan, *Physical metallurgy: principles and practice*. PHI Learning Pvt. Ltd., 2012.

[142] V. K. Sharma, N. N. Breyer, N. Abe, and L. H. Schwartz, “Effects of plastic deformation on the density of a medium carbon martensite,” *Scr. Metall.*, vol. 8, no. 6, pp. 699–701, 1974.

[143] J. Miettinen, “Calculation of solidification-related thermophysical properties for steels,” *Metall. Mater. Trans. B*, vol. 28, no. 2, pp. 281–297, 1997.

[144] M. Narazaki, G. E. Totten, and G.M. Webster, *Handbook of Residual Stress and Deformation of Steel*. Ohio: ASM International, 2002.

[145] J. M. Moyer and G. S. Ansell, “The Volume Expansion Accompanying the Martensite Transformation in Iron-Carbon Alloys,” *Metall. Trans.*, vol. 6A, pp. 1785–1791, 1975.

[146] N. Giordano, *College physics: reasoning and relationships*, First. Cengage Learning, 2010.

[147] D. I. Fletcher and J. H. Beynon, “The effect of intermittent lubrication on the fatigue life of pearlitic rail steel in rolling-sliding contact,” *Proc. Inst. Mech. Eng. Part F J. Rail Rapid Transit*, vol. 214, no. 3, pp. 145–158, 2000.

[148] AFS, “Understanding Porosity,” *American Foundary Society*, 2016. [Online]. Available: http://www.afsinc.org/content.cfm?ItemNumber=6933. [Accessed: 17-Oct-2016].

[149] R. D. Pehlke, “Formation of Porosity During Solidification of Cast Metals,” in *Foundry Processes: Their Chemistry and Physics*, S. Katz and C. F. Landefeld, Eds. Boston, MA: Springer US, 1988, pp. 427–445.

[150] S. Kumar, S. Gupta, B. Ghodrati, and U. Kumar, “An approach for risk assesment of rail defects,” *Int. J. Reliab. Qual. Saf. Eng.*, vol. 17, no. 4, pp. 291–311, 2010.

[151] A. Gholami, S. Saharkhiz, M. Samadi, and F. Honarvar, “Ultrasonic Flaw Detection Systems for Testing Rails in Iran Railways (RAI),” in *Proceedings of the 3rd Iranian International NDT Conference*, 2016, p. 6.

[152] D. Hauser, “Welding of Railroad Rails — A Literature and Industry Survey ’,” *Am. Soc. Test. Mater.*, pp. 118–141, 1978.

[153] Sperry Rail Service, “Rail Defect Manual,” Danbury, 1968.

[154] E. Jasi and E. Žukauskas, “The ultrasonic wave interaction with porosity defects in welded rail head,” *Ultrasound*, vol. 65, no. 1, pp. 12–18, 2010.

[155] C. P. Lonsdale, “Thermite rail welding: history process developments, current practice and outlook for the 21st century.,” in *Proceedings of the AREMA 1999 Annual Conferences*, 1999, vol. 1895, no. C, p. 18.

[156] M. Papaelias, C. Roberts, and C. L. Davis, “A review on non-destructive evaluation of rails: state-of-the-art and future development,” *Proc. Inst. Mech. Eng. Part F J. Rail Rapid Transit*, vol. 222, no. 4, pp. 367–384, 2008.

[157] H. Y and Z. Öztürk, “Investigation of rail defects using an ultrasonic inspection method : a case study of Aksaray-Airport Light Rail Transit Line in Istanbul,” in *Urban Transport XXI*, vol. 146, W. C.A. Brebbia and J. L. M. i Garcia, Eds. WITPress, 2015, pp. 687–698.

[158] G. T. Fry, F. V. Lawrence, and A. R. Robinson, “A Fatigue Model for Thermite Rail Welds,” *Fatigue Fract. Eng. Mater. Struct.*, vol. 19, no. 170, pp. 655–668, 1995.

[159] Federal Railroad Administration, “Track Inspector Rail Defect Reference Manual,” 2015.

[160] S. Jahanmir and N. P. Suh, “Mechanics of subsurface void nucleation in delamination wear,” *Wear*, vol. 44, no. 1, pp. 17–38, 1977.

[161] A. R. Rosenfield, “Criteria for ductile fracture of two-phase alloys,” *Metall. Rev.*, vol. 13, no. 1, pp. 29–40, 1968.

[162] I. L. Mogford, “The deformation and fracture of two-phase materials,” *Metall. Rev.*, vol. 12, no. 1, pp. 49–68, 1967.

[163] A. S. Argon, J. Im, and R. Safoglu, “Cavity formation from inclusions in ductile fracture,” *Metall. Trans. A*, vol. 6, no. 4, p. 825, 1975.

[164] H. K. Jun, J. W. Seo, I. S. Jeon, S. H. Lee, and Y. S. Chang, “Fracture and fatigue crack growth analyses on a weld-repaired railway rail,” *Eng. Fail. Anal.*, vol. 59, pp. 478–492, 2016.

[165] D. M. Fegredo, M. T. Shehata, A. Palmer, and J. Kalousek, “The effect of sulphide and oxide inclusions on the wear rates of a standard C-Mn and a Cr-Mo alloy rail steel,” *Wear*, vol. 126, no. 3, pp. 285–306, 1988.

[166] Z. Mouallif, B. Radi, and I. Mouallif, “The thermomechanical modeling of aluminothermic welds affected by different defects Summary :,” *Int. J. Eng. Res. Develoment*, vol. 11, no. 10, pp. 44–48, 2015.

[167] Z. Mouallif, B. Radi, and I. Mouallif, “Effect of the Inclusion Defect on the Mechanical Behavior of Thermite Welds,” *Adv. Theor. Appl. Mech.*, vol. 9, no. 1, pp. 11–20, 2016.

[168] I. Mouallif, Z. Mouallif, A. Benali, and F. Sidki, “Finite element modeling of the aluminothermic welding with internal defects and experimental analysis,” in *MATEC Web of Conferences*, 2012, vol. 1, p. 12.

[169] J. E. Garnham, R.-G. Ding, and C. L. Davis, “Ductile inclusions in rail, subject to compressive rolling–sliding contact,” *Wear*, vol. 269, no. 11–12, pp. 733–746, Oct. 2010.

[170] H. P. Bassindale, “Railway rail rolling contact fatigue modelling,” University of Sheffield, 2014.

[171] G3data, “G3data,” 2010. [Online]. Available: https://github.com/pn2200/g3data.

[172] A. Kapoor, D. I. Fletcher, and F. J. Franklin, “The role of wear in enhancing rail life,” *Tribol. Res. Des. Eng. Syst. Proc. 29th Leeds-Lyon Symp. Tribol.*, vol. Volume 41, no. 0, pp. 331–340, 2003.

[173] G. Vasić, F. J. Franklin, and D. I. Fletcher, “Influence of partial slip and direction of traction on wear rate in wheel-rail contact,” *Wear*, vol. 270, no. 3–4, pp. 163–171, 2011.

[174] D. I. Fletcher, A. Kapoor, F. J. Franklin, L. Smith, and P. Hyde, “Comparison of the Hatfield and alternative UK rails using models to assess the effect of residual stress on crack growth from rolling contact fatigue,” Newcastle, 2006.

[175] S. Kumar, U. Espling, and U. Kumar, “Holistic procedure for rail maintenance in Sweden,” *J. Rail Rapid Transit*, vol. 222, no. 4, pp. 331–344, 2008.

[176] R. A. Smith, “The wheel-rail interface - Some recent accidents,” *Fatigue Fract. Eng. Mater. Struct.*, vol. 26, no. 10, pp. 901–907, 2003.

[177] J. W. Ringsberg, H. Bjarnehed, A. Johansson, and B. L. Josefson, “Rolling contact fatigue of rails - finite element modelling of residual stresses , strains and crack initiation,” *Proc. Inst. Mech. Eng. Part F*, vol. 214, no. October 1999, pp. 7–19, 2000.

[178] J. K. Kim and C. S. Kim, “Fatique crack growth behavior of rail steel under mode I and mixed mode loadings,” *Mater. Sci. Eng.*, vol. 338, no. 1–2, pp. 191–201, 2002.

[179] U. Olofsson and R. Nilsson, “Surface cracks and wear of rail: a full-scale test on a commuter train track,” *Proc. Inst. Mech. Eng. Part F J. Rail Rapid Transit*, vol. 216, no. 4, pp. 249–264, 2002.

[180] Z. Li, X. Zhao, C. Esveld, R. Dollevoet, and M. Molodova, “An investigation into the causes of squats—Correlation analysis and numerical modeling,” *Wear*, vol. 265, no. 9–10, pp. 1349–1355, Oct. 2008.

[181] S. Kumar, “A Study of the Rail Degradation Process to Predict Rail Breaks,” Lulea University of Technology, 2006.

[182] W. J. Wang, J. Guo, Q. Y. Liu, M. H. Zhu, and Z. R. Zhou, “Study on relationship between oblique fatigue crack and rail wear in curve track and prevention,” *Wear*, vol. 267, no. 1–4, pp. 540–544, 2009.

[183] S. L. Grassie, “Rail corrugation: characteristics, causes, and treatments,” *Proc. Inst. Mech. Eng. Part F-Journal Rail Rapid Transit*, vol. 223, no. 6, pp. 581–596, 2009.

[184] W. Zhong, J. J. Hu, Z. B. Li, Q. Y. Liu, and Z. R. Zhou, “A study of rolling contact fatigue crack growth in U75V and U71Mn rails,” *Wear*, vol. 271, no. 1–2, pp. 388–392, 2011.

[185] J. Grum and J. Viktor, “Ultrasonic Testing of Axle sets of Diesel- Engine trains,” in *Proceedings of the 15th World Conference on Non-Destructive Testing, Rome, Italy.*, 2000, pp. 1–8.

[186] H. M. Thomas, B. A. M. Berlin, F. Bureau, S. Rühe, and P. Linke, “Pioneering Inspection of Railroad Rails with Eddy Currents,” in *Proceedings of the 15th World Conference on Non-Destructive Testing, Rome, Italy.*, 2000, pp. 1–6.

[187] M. Junger, H. M. Thomas, R. Krull, and S. RÜhe, “The Potential of Eddy Current Technology Regarding Railroad Inspection and its Implementation,” in *Proceedings of the 16th World Conference on Non - Destructive Testing, Montreal, Canada*, 2004.

[188] D. Urata and R. Clark, “Groundwork for Rail Flaw Detection Using Phased Array Inspection,” *Am. Inst. Phys.*, vol. 22, pp. 799–805, 2003.

[189] M. P. Papaelias, C. Roberts, and C. L. Davis, “A review on non-destructive evaluation of rails : state-of-the-art and future development,” *J. Rail Rapid Transit*, vol. 222, pp. 367–384, 2008.

[190] N. McCormick and J. Lord, “Digital image correlation,” *Mater. Today*, vol. 13, no. 12, pp. 52–54, 2010.

[191] H. Qiu, J. Yan, O. Kwon, and M. A. Sutton, "Crack Detection by Digital Image Correlation," in *Proceedings of the XIth International Congress and Exposition*, 2008.

[192] J. Réthoré, F. Hild, and S. Roux, "Extended digital image correlation with crack shape optimization," *Int. J. Numer. Methods Eng.*, vol. 73, no. 2, pp. 248–272, 2008.

[193] S. Roux, J. Réthoré, and F. Hild, "Digital image correlation and fracture: an advanced technique for estimating stress intensity factors of 2D and 3D cracks," *J. Phys. D. Appl. Phys.*, vol. 42, no. 21, p. 214004, 2009.

[194] W. P. Leser, N. Carolina, N. Carolina, J. A. Newman, and W. M. Johnston, "Fatigue crack closure analysis using digital image correlation," *Nasa/Tm–2010-216695*, no. May, 2010.

[195] F. Mathieu, F. Hild, and S. Roux, "Identification of a crack propagation law by digital image correlation," *Int. J. Fatigue*, vol. 36, no. 1, pp. 146–154, 2012.

[196] J. D. Carroll, W. Abuzaid, J. Lambros, and H. Sehitoglu, "High resolution digital image correlation measurements of strain accumulation in fatigue crack growth," *Int. J. Fatigue*, vol. 57, pp. 140–150, 2013.

[197] J. L. Evans, "Creep-Fatigue Crack Growth Using Digital Image Correlation," in *13th International Conference on Fracture*, 2013, pp. 1–6.

[198] A. F. Cinar, S. M. Barhli, D. Hollis, R. A. Tomlinson, T. J. Marrow, and M. Mostafavi, "Autonomous surface discontinuity detection method with Digital Image Correlation." [Online]. Available: http://www.bssm.org/uploadeddocuments/Conference 2015/2015papers/Autonomous_surface_discontinuity_detection_method_with_Digital_Image_Correlation.pdf. [Accessed: 02-Aug-2016].

[199] M. Malesa, D. Szczepanek, M. Kujawińska, a. Świercz, and P. Kołakowski, "Monitoring of civil engineering structures using Digital Image Correlation technique," *EPJ Web Conf.*, vol. 6, p. 31014, 2010.

[200] C. Murray, “Dynamic Monitoring of Rail and Bridge Displacements using Digital Image Correlation,” Queen’s University, Kingston, Ontario, Canada, 2013.

[201] C. A. Murray, W. A. Take, and N. A. Hoult, “Measurement of vertical and longitudinal rail displacements using digital image correlation,” *Can. Geotech. J.*, vol. 52, no. 2, pp. 141–155, 2014.

[202] D. I. Fletcher, P. Hyde, and a Kapoor, “Growth of multiple rolling contact fatigue cracks driven by rail bending modelled using a boundary element technique,” *Proc. Inst. Mech. Eng. Part F J. Rail Rapid Transit*, vol. 218, no. 3, pp. 243–253, Jan. 2004.

[203] S. Kaewunruen and M. Ishida, “Field monitoring of rail squats using 3D ultrasonic mapping technique,” 2014. [Online]. Available: http://works.bepress.com/sakdirat_kaewunruen/49/. [Accessed: 01-Aug-2016].

[204] “Vic-3D software,” *Correlated Solutions Inc.*, 2016. [Online]. Available: http://correlatedsolutions.com/vic-3d/. [Accessed: 03-Aug-2016].

[205] M. Olzak, P. Pyrzanowski, and J. Stupnicki, “Rolling contact problem - fatigue crack propagation in a surface layer,” *J. Theor. Appl. Mech.*, vol. 39, no. 3, pp. 589–620, 2001.

[206] D. Peng and R. Jones, “Finite Element Method Study on the Squats Growth Simulation,” *Appl. Math.*, vol. 4, no. 5, pp. 29–38, 2013.

[207] B. Pan, Z. Wang, and Z. Lu, “Genuine full-field deformation measurement of an object with complex shape using reliability-guided digital image correlation.,” *Opt. Express*, vol. 18, no. 2, pp. 1011–1023, 2010.

[208] G. J. Pataky, “High resolution fatigue crack growth analysis of crack closure and slip irreversibility using digital image correlation,” University of Illinois, 2011.

[209] J. Herian and K. Aniolek, “Modelling of structure and properties of pearlitic steel and abrasive wear of the turnout frog in the cyclic loading conditions,” *J. Achiev. Mater. Manuf. Eng.*, vol. 49, no. 1, pp. 71–81, 2011.

[210] R. S. Shekhar, P. Shekhar, and P. Ganesan, “Automatic Detection of Squats in Railway Track,” in *IEEE Sponsored 2nd International Conference on Innovations in Information Embedded and Communication Systems*, 2015, pp. 1–5.

[211] M. Kaneta, H. Yatsuzuka, and Y. Murakami, “Mechanism of Crack Growth in Lubricated Rolling / Sliding Contact,” *ASLE Trans.*, vol. 28, no. 3, pp. 407–414, 1985.

Appendix

Contents lists available at ScienceDirect

Wear

journal homepage: www.elsevier.com/locate/wear

The potential for suppressing rail defect growth through tailoring rail thermo-mechanical properties

David I. Fletcher*, Shahmir H. Sanusi

Department of Mechanical Engineering, University of Sheffield, UK

A R T I C L E I N F O

Article history:
Received 5 October 2015
Received in revised form
21 June 2016
Accepted 22 June 2016

Keywords:
Railway
Rail–wheel
Contact
Crack
Thermal

A B S T R A C T

Thermal damage of rails can occur through brake lock-up, or traction control system failure to prevent wheel spin. In most cases the damage produced is shallow and takes the form of a “white etching layer”, usually thought to have a martensitic structure, formed as the steel is heated above its eutectoid temperature and then rapidly cooled as the wheel moves away. In many cases such layers are benign, but there is evidence of crack initiation at their interface with the sub-surface layers of the rail in “stud” defects. The metallurgical transformation during the formation of white etching layers leads to a volume change for the steel, leaving not only a transformed microstructure, but also locked-in stress. The influence of this additional locked-in stress on development of an initiated crack is studied in this paper, and the work extended to consider how alternative materials which react differently to the thermal input may offer a means to suppress crack development through locking in beneficial rather than problematic stresses.

1. Introduction

This paper presents an extension to previous research investigating thermal influence on crack growth in rails. The origin of the work is in building understanding of “stud” type defects which have been identified on railways and metros worldwide [1]. These have superficial similarities to squat defects, but are almost always associated with severe thermal input evidenced through the presence of thin (∼100 μm) white etching layer at the rail surface above the defects. Fig. 1 shows the morphology of a typical defect of this type.

White etching layer on the rail surface can be formed either through extreme mechanical work [2] or by a thermal process [3] often due to brake lock-up, or traction control system failure to prevent wheel spin. Evidence from defects cut open for examination is that plastic damage is almost completely absent in stud defects [4], so thermal input in the generation of the WEL has been examined. Severe thermal input has three main consequences, which last over different durations: (i) temporary thermal expansion of the steel, (ii) permanent metallurgical transformation of the steel to WEL, and (iii) permanent locked-in stress produced by the change of material volume associated with the metallurgical transformation. In the previous investigation [5] only additional stress due to cause (i) was considered for its effect on stress intensity factors (SIFs) describing growth of an already initiated defect. In this paper the change of volume (cause iii) is brought in as an additional phenomena in the modelling, opening up two routes of investigation. First, taking expansion characteristic of current rail steels undergoing transformation to WEL and examining the influence of the additional stress produced by this expansion. Second, using the same model in a design capacity to assess the most beneficial expansion (or contraction) which a heat affected area may exhibit if it is to suppress crack growth, i.e. assuming that initiation of damage still occurs, how can a future rail material be created to suppress the growth of the initiated defect. A wheel running temperature of 300 °C is considered, separate to the prior severe thermal event [6].

2. Modelling method and conditions

Modelling was conducted using a boundary element (BE) analysis in the Beasy software package [7] and considered cracks of 1 mm to 15 mm long, 1 mm deep, parallel to the surface of a rail. This crack configuration was chosen as a simplified representation of the “stud” crack type shown in Fig. 1. This type of crack is found in undeformed steel, and the crack sizes modelled were large relative to the microstructure dimensions, hence the model was of stress controlled crack growth, which was quantified by fracture mechanics. Microstructural anisotropy which would be important if there was extensive shear of the steel (typically affecting cracks much closer to the rail surface) was absent. The model (Fig. 2) used

---

* Corresponding author.
E-mail address: D.I.Fletcher@Sheffield.ac.uk (D.I. Fletcher).

http://dx.doi.org/10.1016/j.wear.2016.06.022
0043-1648/© 2016 Elsevier B.V. All rights reserved.

Please cite this article as: D.I. Fletcher, S.H. Sanusi, The potential for suppressing rail defect growth through tailoring rail thermo-mechanical properties, Wear (2016), http://dx.doi.org/10.1016/j.wear.2016.06.022

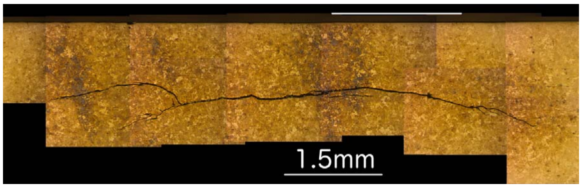

Fig. 1. Example of "stud" defect morphology below the running band in a longitudinal cross-section from a high speed mixed traffic line. The central portion of the crack is close to horizontal and lies at approximately 1 mm below the rail surface in an undeformed microstructure. The white marker above the rail surface indicates the location of a patch of white etching layer on the rail surface. The surface depression and plastic deformation characteristic of a "squat" defect are absent.

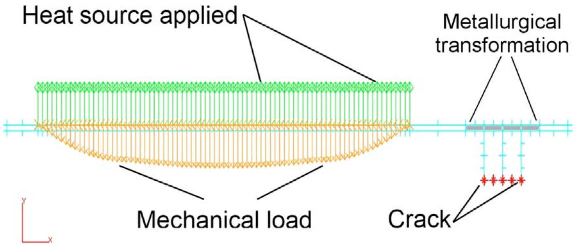

Fig. 2. BE model of rail–wheel contact with horizontal crack of 1 mm located 1 mm below the rail surface. 2 mm length of metallurgically transformed layer with 100 μm thickness from a previous thermal event is shown grey. The heat source moves together with the contact load traversing the rail surface.

Table 1
Conditions modelled.

Case	Expansion due to transformation (%)	Rail–wheel contact temperature rise (°C)
1	0	0
2	0.8	0
3	0.8	300
4	1.3	0
5	1.3	300
6	−0.8	0
7	−0.8	300

a 2D plane strain representation of the rail–wheel contact, with a maximum Hertzian contact pressure of 1014 MPa. Surface and crack face friction coefficient was taken as 0.3, with a contact half-width of 5 mm. This pressure and contact size correspond to a wheel of 780 mm diameter and 6.5 t axle load running on a UIC60 rail worn to a slightly flatter than new condition crown radius. The 2D model was able to represent vertical and longitudinal stresses that characterise wheel motion in straight track, but could not represent the lateral forces or lateral crack growth that can be significant in curved track. This disadvantage was set against significantly lower solution times, enabling a wider range of conditions and crack sizes to be studied. The contact was taken to be fully sliding, with shear traction distribution across the contact defined by the product of Hertzian normal load distribution multiplied by friction coefficient. The conditions modelled are shown in Table 1. Metallurgical transformation of the pearlite to martensite was simulated on a macro scale through bulk expansion or contraction of the heat affected zone, not by modelling the thermo-mechanical behaviour of the microstructure itself. The expansion depends on the specific alloy composition of the steel, with two different cases considered in the paper alongside the 'artificial' contraction cases used for the design study.

2.1. *Density based calculation of volume change*

Values for the metallurgical transformation volume change of the heat affected area can be generated using either a density or an atomic volume based approach. To assess the change based on density, the density of pearlite was calculated by taking the density of its constituents ferrite (α iron, 7870 kg/m^3) and cementite (Fe_3C, 7700 kg/m^3) and their weight percentage, assuming a eutectoid composition steel with 0.77% carbon for which the weight fractions of ferrite to cementite are 8:1 [8]. This gives a density of pearlite with 0.77% C as 7851.1 kg/m^3, although this takes no account of the effect of other alloying elements on the density. The density of martensite is available from literature [9], although its value is sensitive to plastic deformation. This is particularly relevant to rail steel surfaces where plastic deformation of pearlite is common, although the increased hardness of martensite after transformation may protect it from further deformation. Density prior to plastic deformation [9] is 7790 kg/m^3, but may drop to 7785 kg/m^3 with 5% plastic deformation. Assuming the value for zero plastic deformation applies, the change from pearlite to martensite reduces density to 7790/7851.1 = 99.22% through an expansion of 0.78% in volume. The expansion would be greater after plastic work. A value of 0.8% is used in Table 1 to capture this process.

2.2. *Atomic volume change approach*

An alternative to the bulk density based approach is to use atomic volume data for steel microstructures [10]. Taking carbon as a weight percentage (C) and atomic volume in Angstroms cubed, values are pearlite (11.916), austenite (11.401 + 0.329C), and martensite (11.789 + 0.370C). Considering a carbon fraction of 0.77% this indicates a change of atomic volume from 11.916 Å^3 to 12.0739 Å^3 with the transformation from pearlite to martensite i.e. a volume expansion of just over 1.3%. Following similar reasoning the change from austenite to martensite is predicted to give an atomic volume increase of around 3.6%, which is in agreement with literature data for this transformation [11]. A value of 1.3% is used in Table 1 to capture this approach for the pearlite to martensite volume change.

2.3. *Implementation of volume change in modelling*

The exact value of volume change with transformation will depend on the steel chemistry, and also the exact thermal path taken as the steel is heated and cooled, but the methods outlined above gave a reasonable range for which modelling could be conducted to investigate the effect on cracks in a rail. To represent the expansion and contraction through transformation of a surface layer in the BE model a thermal body load was applied to the whole of the transformed layer (regardless of contact size or position) using a temperature calculated to achieve the required volumetric expansion [12]:

$$\frac{\Delta V}{V_0} = 3\alpha\Delta T \tag{1}$$

where $\Delta V/V_0$ is the volume change ratio, α is the thermal linear expansion coefficient for the material and ΔT is the temperature difference. It should be noted that this is simply a convenient way to implement expansion or contraction within an existing structure without modelling microstructural change or applying a mechanical load. It is an artificial temperature value, distinct from the thermal boundary condition applied to represent the passing of a hot wheel over the rail with which it is combined using superposition.

Please cite this article as: D.I. Fletcher, S.H. Sanusi, The potential for suppressing rail defect growth through tailoring rail thermo-mechanical properties, Wear (2016), http://dx.doi.org/10.1016/j.wear.2016.06.022

For the case with a rail–wheel contact temperature rise, it was assumed that the rail surface was heated in the wheel contact area, and was elsewhere at 20 °C. This was intended to simulate 'flash' heating of the rail surface followed by rapid cooling as the contact moves away. The properties of the rail steel were Young's modulus, 210 GPa, Poisson's ratio, 0.3, and thermal linear expansion coefficient of 13 μm/mK. To identify the peak and range of stress intensity factors during the passage of a wheel, contact positions at 2.5 mm increments were examined up to 15 mm either side of the crack centre. No crack growth rate law exists specific to the loading and crack configuration used in the current investigation. Therefore, indicative crack growth rates were calculated using the lower bound method developed for inclined surface breaking cracks in rail steel [13,14]. Although the crack configuration differs this growth law was generated using a normal grade rail steel and there is similarity in the combination of mode I and II loading for a crack under compression. A more specific growth law for modern rail steels would be a useful area of future research.

3. Results & discussions

All the cases listed in Table 1 were investigated for a 1 mm crack length to examine a crack which has already initiated but not yet grown significantly. Modelling was also performed for a range of crack lengths from 2 to 15 mm but for economy of modelling these cases exclude conditions 4 and 5 (1.3% expansion due to transformation) since trends are visible from the baseline case and for ±0.8% expansion cases. For each condition modelled the range of stress intensity factor was assessed by considering the movement of a wheel incrementally across the crack (Fig. 3), generating a series of SIFs. The combined action of traction and normal stress is indicated in the figure, and results in asymmetry of the results for left and right crack tips. Results are presented as stress intensity factors in Figs. 4–6, in which the origin is at the centre of the crack, hence crack tips will lie to the left or right of the origin according to crack size. Stress intensity factors are converted to indicative crack growth rates shown in Fig. 7. As an addition to the SIF data, Table 2 shows stress calculated for a point 1 mm below the centre of the contact and white etching layer region, but without a crack present. This indicates that thermal expansion is particularly influential on longitudinal stress, and to a lesser extent on lateral stress, while metallurgical transformation has a strong influence on longitudinal and vertical stress in the rail. These stresses are for just a single location, and it is their combination throughout the rail during passage of the wheel that determines the SIFs for each case considered.

3.1. Stress intensity factor dependence on crack size

Fig. 4 shows the trends observed in K_I and K_{II} values for the left and right crack tips. These plots are for condition 1 (no expansion/contraction, no thermal input). For the left crack tip (Fig. 4a), K_I shows a rise with increasing crack size, but is small even for a 15 mm crack. For comparison a threshold stress intensity factor of 6 MPa m$^{1/2}$ for tensile growth of cracks in carbon steel is available from Otsuka et al. [15] and has been applied in previous work on crack growth in rail steel [16,17]. The mode II data for the left crack tip (Fig. 4b) shows much larger stress intensity factor values, but a low sensitivity to crack size of the total range during passage of the contact. The values for shear mode growth comfortably exceed the 1.5 MPa m$^{1/2}$ shear mode threshold given by Otsuka et al. [15].

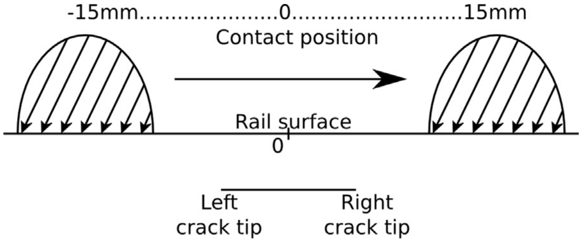

Fig. 3. A series of analyses are performed with incremental movement of the contact across the crack. The origin of the position is measured from the crack centre.

At the right crack tip both mode I and II SIF ranges show rising trends with increasing crack size (Fig. 4c and d). The mode I values are very small, but the mode II values are comfortably above threshold. Assuming applicability of the crack growth law previously developed for inclined surface breaking cracks, Fig. 7 and Table 3 show the outcome of mixed mode growth. There is a plateau in growth rate with increasing crack size for the left tip, but raising rates with increasing size at the right tip. This reflects similar trends in peak mode II SIF with increasing crack size for the left and right cracks (Fig. 4b and d) and its strong influence over predicted crack growth rate. In crack growth for inclined surface breaking cracks it is thought that a small mode I crack opening stress (even if itself below threshold) can "unlock" mode II growth through helping to overcome crack face friction [18]. In the current results high values of mode II are predicted even with almost zero K_I at the right tip, although larger K_I values are predicted at the left. This may influence the tendency of the right side crack to branch (the usual mode II growth behaviour), whereas prolonged co-planar growth may be possible with the higher mode I levels at the left tip. This is an aspect of the growth which requires further investigation, to better understand if and how the inclined surface breaking crack behaviour translates to these horizontal embedded cracks, and how they branch and propagate.

3.2. Effect of expansion and contraction of a thin surface layer

Fig. 5 shows the effect on mode I and II stress intensity factor of expansion or contraction of a surface layer due to metallurgical transformation, focusing on just the 1 mm length crack left tip. These data are generated without additional thermal stress as the wheel passes. Results for the right crack tip and at other crack sizes exhibit similar behaviour. The baseline case 1 is also included. Values of K_I rise well above the baseline when expansion of a thin surface layer is considered. Positive K_I values are present when the contact is absent, i.e. the crack becomes subject to a static mode I stress which is relieved as the compressive contact passes, producing a stress cycle. This is the case for the 1 mm crack which is short relative to the 2 mm transformed layer considered, but this effect diminishes as the crack exceeds the size of the transformed region. The values of K_I are low, in part because this is a small crack size, but they rise in proportion to the degree of expansion of the surface layer, representing possible reactions of different steel metallurgies (case 2 and 4, 0.8% and 1.3% expansion respectively). For the case of a 0.8% contraction of the surface layer (case 6) K_I is maintained at zero whatever the contact position.

For mode II under the same conditions moderate changes take place in the peak values determining stress intensity factor range during passage of the contact, but the overall form of the curves is similar for all cases. Inset graphs (Fig. 5b) enable the order of the peak values to be identified. It can be seen that expansion of the surface layer increases the magnitude of both positive and negative peaks (dependent also on the level of expansion). Furthermore, contraction of the surface layer reduces the peak magnitudes, and hence the stress intensity factor range. Although the number of contact positions examined is limited, the relative size of the contact and crack mean the peak position is known in

Please cite this article as: D.I. Fletcher, S.H. Sanusi, The potential for suppressing rail defect growth through tailoring rail thermo-mechanical properties, Wear (2016), http://dx.doi.org/10.1016/j.wear.2016.06.022

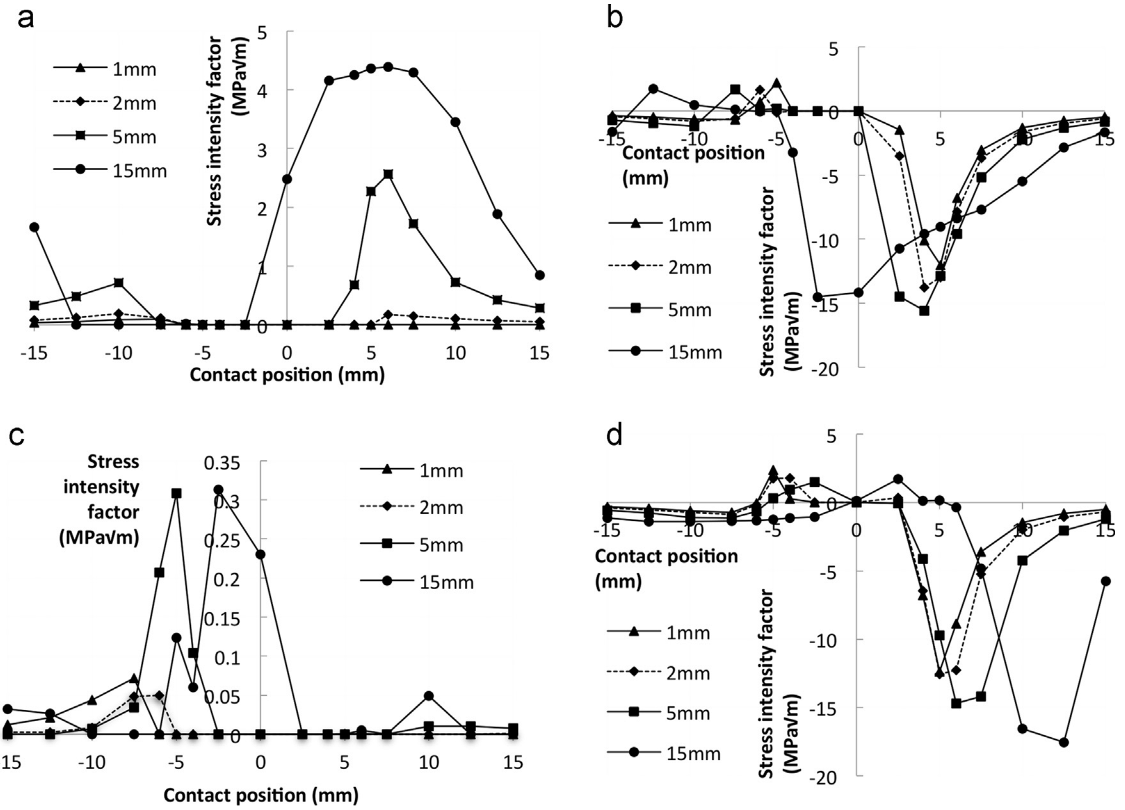

Fig. 4. Stress intensity factor dependence on contact position. (a) left tip mode I, (b) left tip mode II, (c) right tip mode I, and (d) right tip mode II.

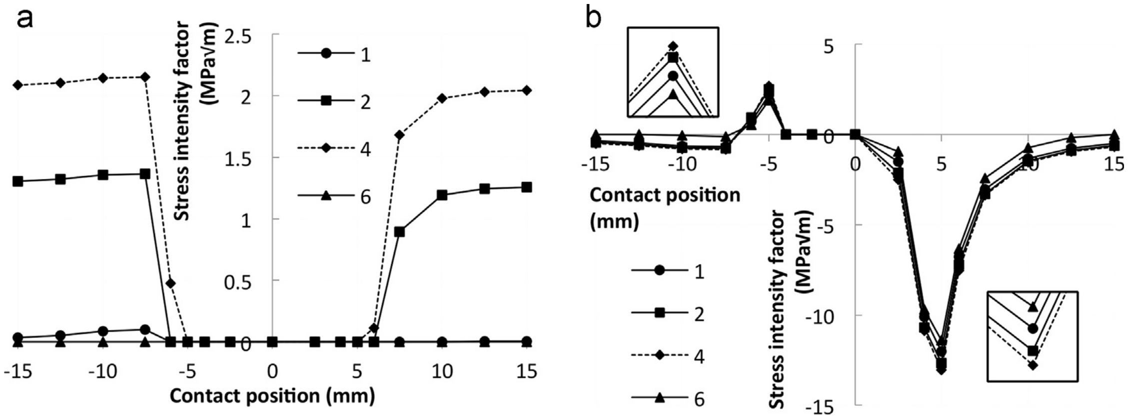

Fig. 5. Effect of metallurgical expansion and contraction (represented as density change) on stress intensity factor for 1 mm crack, left crack tip. (a) Mode I, and (b) mode II. Legend entries refer to cases in Table 1.

advance and can be accurately captured. The ranges can be seen numerically in Table 4. The changes are small, but when converted to crack growth rates (assuming applicability of the crack growth law), they raise or lower the crack growth rate relative to the baseline case across the range of crack sizes investigated, as indicated in Fig. 7 and Table 3.

3.3. *Effect of thermal input from passing wheels*

Fig. 6 shows a selection of cases to highlight the effect of additional thermal input from warm wheels passing a site of previous thermal damage with metallurgical transformation. Expansion and contract by 0.8% is considered, but the 1.3% cases are excluded from the plot for clarity. From Fig. 6a for mode I it can be seen that the thermal input considered (dotted lines) makes insignificant changes to the stress intensity factor. The behaviour is dominated by the effect of metallurgical expansion relative to the base case (producing a rise in K_{I} values), or contraction (for which K_{I} is maintained at zero). As discussed above, the values of K_{I} are all very small, but it is the trends that are of significance.

For K_{II} (Fig. 6b) the overall form of the curves for variation of stress intensity factor during the passage of the contact is insensitive to the differences between cases with and without additional thermal input. Dotted lines in the plot represent the cases with additional thermal input. At negative contact positions there is some sensitivity of K_{II} to thermal input. At positive contact positions there is almost no effect from thermal input, with K_{II} for metallurgical expansion or contraction cases being above or below baseline values irrespective of the additional thermal input.

The effect of thermal input on SIF range is shown numerically in Table 4. For both metallurgical expansion (cases 2, 3) and

Please cite this article as: D.I. Fletcher, S.H. Sanusi, The potential for suppressing rail defect growth through tailoring rail thermo-mechanical properties, Wear (2016), http://dx.doi.org/10.1016/j.wear.2016.06.022

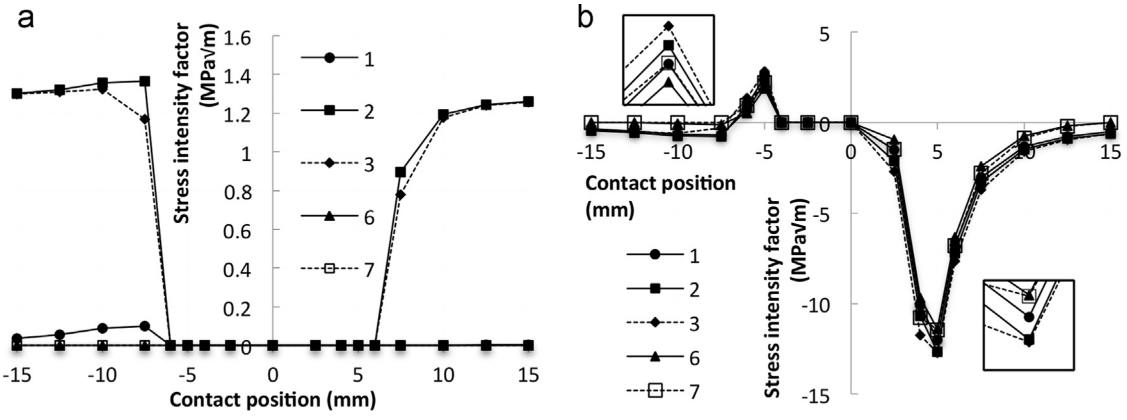

Fig. 6. Effect of additional thermal stress (warm wheels) on stress intensity factor for 1 mm crack, left crack tip. (a) Mode I, and (b) mode II. Legend gives case number from Table 1.

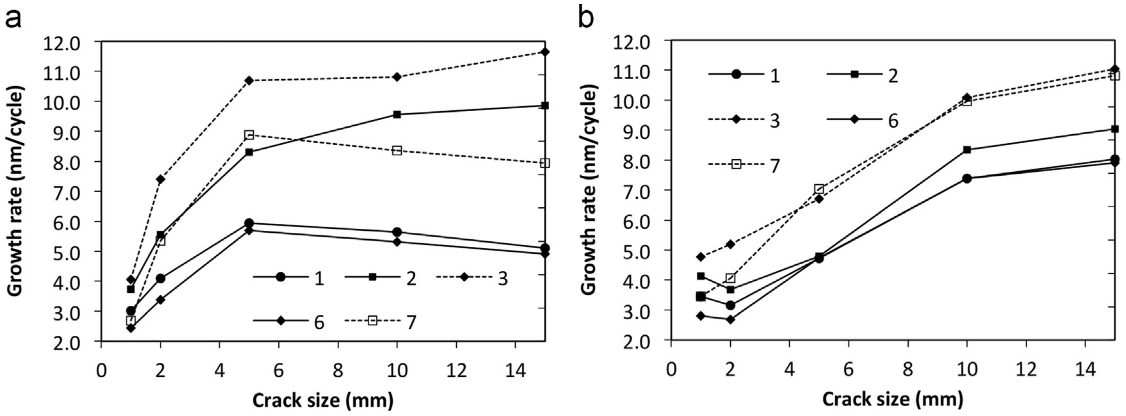

Fig. 7. Crack growth rate dependence on crack size for cases 1, 2, 3, 6, and 7. (a) Left crack tip, and (b) right crack tip. Case 6 is equal to the baseline case 1 for cracks of 5 mm length an over.

Table 2
Stress (MPa) at 1 mm from the rail surface, centrally below the contact and transformed layer.

Case	Longitudinal	Vertical	Lateral	Shear
1	−661.2	−995.6	−497	−209.1
2	−632.8	−968.7	−480.5	−212.5
3	−604.4	−965.1	−470.8	−213.2
6	−688.9	−1022	−513.2	−205.7
7	−660.4	−1018	−503.6	−206.5

Table 3
Crack growth rates (nm/cycle) for all the cases and sizes of cracks modelled.

Case	1 mm		2 mm		5 mm		10 mm		15 mm	
	L	R	L	R	L	R	L	R	L	R
1	3.0	3.4	4.1	3.2	5.9	4.7	5.6	7.4	5.1	8.0
2	3.8	4.2	5.6	3.7	8.3	4.8	9.6	8.3	9.9	9.0
3	4.1	4.7	7.4	5.2	10.7	6.7	10.8	10.1	11.6	11.0
4	4.5	4.8	–	–	–	–	–	–	–	–
5	4.5	5.0	–	–	–	–	–	–	–	–
6	2.4	2.8	3.4	2.7	5.7	4.7	5.3	7.4	4.9	7.9
7	2.6	3.3	5.0	3.8	8.2	6.5	7.7	9.2	7.3	9.9

contraction (cases 6, 7) the trend emerges that thermal input produces (i) minor or no change in ΔK_I, and (ii) an increase in ΔK_{II}.

The crack growth predictions (Fig. 7) show that a contracting microstructure is beneficial in suppressing crack growth (growth rate in case 6 is close to or reduced below the baseline case). However, this benefit is negated by surface heating from a warm wheel (case 7) for all but very small cracks which are wholly below the 2 mm wide transformed expansion/contraction region. For an expanding microstructure (case 2) the crack growth rate is always above the baseline case, and is made even higher when a warm wheel is considered (case 3).

3.4. Microstructure design

The research presented in this paper has considered a range of crack sizes at 1 mm below the surface, and indicates suppression of crack growth is possible if metallurgical transformation through thermal input produces contraction rather than expansion of the microstructure (considering this separately from temporary thermal expansion). This indicates it would be beneficial to study steel chemistry that can achieve this behaviour, or to undertake tests on a range of existing rail steels to see if some types already have this beneficial property. Beyond comparison of crack growth predictions with the physical evidence for existing rail defects (Fig. 1), validation depends on identifying such a material, and developing a crack growth law specific to mixed mode non-inclined sub-surface cracks. When considering new rail coating technologies [19] there is also the possibility of choosing a coating with this crack suppressing property. Even if contraction cannot be achieved, there would be benefit in selecting steel metallurgy able to reduce levels of expansion when metallurgical transformation takes place following thermal input. In further work a crack closer to the surface will be considered to understand the very earliest stage in growth of a defect near thermal damage, and whether

Please cite this article as: D.I. Fletcher, S.H. Sanusi, The potential for suppressing rail defect growth through tailoring rail thermo-mechanical properties, Wear (2016), http://dx.doi.org/10.1016/j.wear.2016.06.022

Table 4
Mode I and II stress intensity factor range for all cases modelled.

Case	1 mm				2 mm				5 mm				10 mm				15 mm			
	L		R		L		R		L		R		L		R		L		R	
	ΔK_{I}	ΔK_{II}	ΔK_{I}	ΔK_{II}	ΔK_{I}	ΔK_{II}	ΔK_{I}	ΔK_{II}	ΔK_{I}	ΔK_{II}	ΔK_{I}	ΔK_{II}	ΔK_{I}	ΔK_{II}	ΔK_{I}	ΔK_{II}	ΔK_{I}	ΔK_{II}	ΔK_{I}	ΔK_{II}
1	0.1	14.2	0.1	14.8	0.2	15.6	0.0	14.4	2.6	17.3	0.3	16.3	4.2	16.7	0.3	18.7	4.4	16.1	0.3	19.2
2	1.4	15.1	1.2	15.6	2.2	17.0	1.7	15.0	3.4	19.1	1.5	16.3	5.5	19.5	2.2	19.3	6.2	19.5	2.9	19.7
3	1.3	15.5	1.2	16.3	2.1	18.6	1.7	16.7	3.4	20.7	1.5	18.1	5.6	20.3	2.1	20.5	6.3	20.6	2.8	21.0
4	2.1	15.7	1.9	16.1	–	–	–	–	–	–	–	–	–	–	–	–	–	–	–	–
5	2.1	15.8	1.9	16.3	–	–	–	–	–	–	–	–	–	–	–	–	–	–	–	–
6	0.0	13.3	0.0	13.9	0.0	14.7	0.0	13.7	2.4	17.1	0.8	16.3	4.1	16.4	0.7	18.7	4.4	15.9	0.5	19.1
7	0.0	13.6	0.0	14.6	0.0	16.6	0.0	15.3	2.2	19.2	0.6	18.0	4.2	18.5	0.5	20.0	4.6	18.1	0.3	20.5

there is a prospect of “designing out” growth of cracks from this damage type.

4. Conclusions

Evidence of severe thermal loading (white etching layer, WEL) is often associated with rail defects. Severe thermal input has three main consequences, which last over different durations: (i) temporary thermal expansion of the steel, (ii) permanent metallurgical transformation of the steel to WEL, and (iii) permanent locked-in stress produced by the change of material volume associated with the metallurgical transformation. The modelling in this paper focuses on area (iii) and predicts that WEL can accelerate growth of cracks below it through locked in stress due to metallurgical transformation from pearlite to martensite which causes a local increase in volume of the rail steel. Conversely, taking a hypothetical case in which thermal damage leads to a permanent contraction of the steel microstructure it is predicted that crack growth rate can be reduced. The changes predicted in crack growth rate are small, but point to the interesting possibility that if a material (new steel chemistry or a clad layer of a non-steel material) were to contract locally in response to thermal damage it could suppress any subsequent crack growth close to this damage, or at the interface between the clad layer/repair and the underlying rail which is a crucial position prone to defects. Validation against physical samples depends on the creation of a suitable rail surface material offering contraction in response to thermal transformation. This, along with investigation to better understand if and how existing understanding of inclined surface breaking crack behaviour translates to horizontal embedded cracks, are the subject of future research.

Acknowledgements

The authors would like to thank SBB and Dr Stuart Grassie for initiating the project which led to this research. This research was supported by a scholarship from Universiti Tun Hussein Onn Malaysia (UTHM) (grant number 02482).

References

[1] S.L. Grassie, Squats and squat-type defects in rails: the understanding to date, IMechE J. Rail Rapid Transit. 226 (2012) 235–242.
[2] J. Ivanisenko, I. MacLaren, X. Sauvage, R. Valiev, H. Fecht, Phase transformations in pearlitic steels induced by severe plastic deformation, Solid State Phenom. 114 (2006) 133–144.
[3] W.D. Callister, Materials Science and Engineering: An Introduction, John Wiley & Sons, New York, USA, 2007.
[4] S.L. Grassie, D.I. Fletcher, E.A. Gallardo Hernandez, P. Summers, Studs: a squat-type defect in rails, IMechE J. Rail Rapid Transit. 226 (3) (2011) 243–256.
[5] D.I. Fletcher, Numerical simulation of near surface rail cracks subject to thermal contact stress, Wear 314 (2014) 96–103.
[6] K.D. Cole, C.M. Tarawneh, A.A. Fuentes, B.M. Wilson, L. Navarro, Thermal models of railroad wheels and bearings, Int. J. Heat Mass Transf. 53 (9) (2010) 1636–1645.
[7] BEASY Boundary Element software. 〈www.beasy.com〉, (accessed 8.6.16.).
[8] V. Raghavan, Physical Metallurgy Principles and Practice, PHI Learning Private Limited, New Delhi, India, 2012.
[9] V.K. Sharma, N.N. Breyer, N. Abe, L.H. Schwartz, Effects of plastic deformation on the density of a medium carbon martensite, Scr. Metall. 8 (1974) 699–702.
[10] M. Narazaki, G.E. Totten, G.M. Webster, Handbook of Residual Stress and Deformation of Steel, ASM International, Ohio (2002), p. 248–295.
[11] J.M. Moyer, G.S. Ansell, The volume expansion accompanying the martensite transformation in iron-carbon alloys, Metall. Trans. 6A (1975) 1785–1791.
[12] N.J. Giordano, College Physics: Reasoning and Relationships, 1st ed., Brooks/Cole Cengage Learning, Boston, USA (2010), p. 448.
[13] P.E. Bold, M.W. Brown, R.J. Allen, Shear mode crack growth and rolling contact fatigue, Wear 144 (1–2) (1991) 307–317.
[14] S. Bogdański, M.W. Brown, Modelling the three-dimensional behaviour of shallow rolling contact fatigue cracks in rails, Wear 253 (1) (2002) 17–25.
[15] A. Otsuka, K. Mori, T. Miyata, The condition of fatigue crack growth in mixed mode condition, Eng. Fract. Mech. 7 (1975) 429–439.
[16] M. Kaneta, M. Suetsugu, Y. Murakami, Mechanism of surface crack growth in lubricated rolling/sliding spherical contact, J. Appl. Mech. 53 (2) (1986) 354–360.
[17] D.I. Fletcher, J.H. Beynon, The effect of intermittent lubrication on the fatigue life of pearlitic rail steel in rolling-sliding contact, in: Proceedings of the IMechE Part F, 214, 3, 2000, pp. 145–158.
[18] A.F. Bower, The influence of crack face friction and trapped fluid on surface initiated rolling contact fatigue cracks, Journal of Tribology, Transactions of the ASME 110 (1988) 704–711.
[19] S.R. Lewis, R. Lewis, D.I. Fletcher, Assessment of laser cladding as an option for repairing/enhancing rails, in: Proceedings of the 20th International Conference on Wear of Materials, Toronto, Canada, April 12–16th 2015.

Please cite this article as: D.I. Fletcher, S.H. Sanusi, The potential for suppressing rail defect growth through tailoring rail thermo-mechanical properties, Wear (2016), http://dx.doi.org/10.1016/j.wear.2016.06.022